

Development of a microfluidic-based platform for delayed vaccine delivery

Thesis submitted for the degree of Doctor of Philosophy

Hillary Term 2023

Romain Guyon

Lady Margaret Hall College

Word count: ~35000 (excluding References and Appendix I)

Development of a microfluidic-based platform for delayed vaccine delivery

Romain Guyon, Lady Margaret Hall College, Hillary Term 2023

Thesis submitted for the degree of Doctor of Philosophy

Abstract

Incomplete vaccination poses a significant challenge to disease eradication efforts, resulting in approximately 1.5 million preventable deaths each year. A single-injection method for administering a full course of immunisation would help to improve global coverage, reduce preventable deaths, and alleviate logistical and cost burdens during outbreaks. Biodegradable polymer microparticles have been studied previously for controlled vaccine release, but traditional manufacturing methods lead to particles with inconsistent size, vaccine loading, and release rates, preventing the development of encapsulated delayed release or single-dose vaccines.

The goal of this thesis was to develop and assess a delayed vaccine delivery system using microfluidics. Firstly, a microfluidic emulsification system within a chip was designed for the production of double emulsion formulations by introducing a step in the height in the microfluidic channel. This enabled reliable production of double emulsions required for creating uniform liquid core – solid shell particles (LCSS particles). The system produced fully loaded particles of varying size and thickness, suitable for the application by injection delivery, with throughput rates of 300Hz and higher. Compared to previously reported systems, this microfluidic system offers

significant advantages, including better emulsification reliability and uniformity, postproduction quality control of particles, and scale-up potential.

The ability of particles to achieve delayed release was studied in vitro demonstrating pulsatile release after a lag phase. Duration of the lag phase was determined by the molecular weight and L:G ratio of the PLGA polymer used as the shell and could be extended from a couple of weeks to months. Finally, in vivo proof-of-concept of the utility of the particles was demonstrated in the context of a leading malaria candidate vaccine R21 in a mouse challenge model. Changing the particle formulation enabled to achieve different immune response delays. Moreover, a single injection of a priming vaccine with the booster dose encapsulated within particles resulted in higher immunogenicity and efficacy than a dose-matched priming vaccine alone. These findings provide key evidence for the potential of this system to achieve high vaccine efficacy with a single injection.

Acknowledgements

First and foremost, I would like to thank my supervisors, Dr. Anita Milicic, Prof. Eleanor Stride, and Prof. Adrian Hill. Anita, you gave me the opportunity 5 years ago to come to Oxford and have always helped me since, professionally and personally, something I will never forget. You and Eleanor have been both such an inspiration for me, letting me develop this project while challenging me and bringing extremely valuable support, advice, and expertise. Thanks for being patient with my English level, tolerating my moments of impatience and stubbornness about the research and my occasional craziness about the statistics. These PhD years have been for me an amazing experience, an opportunity for me to grow as a researcher and learn more about myself and my interests, and I am looking forward to continuing this promising research project with you both. Adrian, I will always be grateful for your brilliant guidance throughout the project and for giving me this opportunity to carry out this exciting research.

I would like to thank all the members of the Jenner Institute for their support with my work and for the great moment I had there with you, especially the famous Christmas parties! Special thanks also go to Dr. Ahmed Salman for his support with the insectary and malaria challenge work.

I would like to thank all the people from the Vaccine Formulation and Adjuvants group in the Jenner, especially Rik van der Veen and Alexandra Sanchez Martinez (“el minion Bob del patrón”) for your friendliness and help with this project. Special thanks go to Dr. Sören Reinke, for your help with all this never-ending ELISA plates,

and immunology work in general, for the crazy mouse shaving moment we spent together, and simply for your friendship, you are my big bro from the Jenner!

I would like to thank all the members of the BUBBL lab in IBME for their help with my work and for the fun moments at the pub. Special thanks go to Dr. Luca Bau, you have been extremely supportive and a great scientific inspiration for me throughout this whole PhD and I would have not developed this project nor this love for statistics without your precious guidance and advice.

I would like to thank all my amazing friends and family for their support during this insane period of the PhD, especially my basketball teammates for all the times we beat Cambridge, Max for all the suffering we shared on the track doing running sessions, and Nikos for the amazing kitesurf riding we had together, these things kept me sane during these 4 years. Thanks to all my friends from Montélimar and from INSA de Lyon for being there for me, especially Vincent (le fils à papou), for his help on the project as my microfluidic components expert advisor. Thanks to Matt, Sandy and James, my roommates, friends, and fearsome board game opponents, living with you in Oxford was amazing. Thanks to Zara, you have been such an amazing support throughout my work on the PhD, someone I could rely on, trust and with whom I had my best moments here in Oxford.

Pour finir j’aimerais remercier ma maman, pour avoir toujours été là pour moi, pour ta patience, ton soutien inconditionnel toutes ces années de doctorat, et ton amour. Je n'aurais jamais pu faire cette thèse sans toi, merci pour tout maman!

Table of contents

Abstract 2

Acknowledgements 4

Table of contents 6

List of Figures 13

List of Tables 19

Abbreviations 21

Publications and Patent 24

Contributions 25

1 Introduction 26

1.1 Overview of immunisation benefits 26

1.2 The need for vaccination compliance 27

1.3 Double batch emulsification and its limitations in single-dose immunisation 30

1.4 Benefits and challenges of core-shell particle architecture 33

1.5 Aims of the thesis 36

2 Materials and Methods 38

2.1 Microfluidic Manufacturing 38

2.1.1 Microfluidic channel design 38

2.1.2 SU-8 mould 40

2.1.3 Chip manufacturing 41

2.1.4 Surface treatment coating 41
2.2 Emulsification process 42
2.2.1 Fluid formulations 42
2.2.2 Microfluidic platform 44
2.2.3 Microfluidic double emulsification 45
2.2.4 Batch emulsification 46
2.2.5 Microfluidic video processing 47
2.3 *In vitro* Release 47
2.3.1 *In vitro* incubation 47
2.3.2 Release quantification 48
2.4 Particle characterisation 49
2.4.1 Microscopy image processing 49
2.4.2 Monitoring of the pH inside the LCSS particles 50
2.4.3 SEM characterisation 51
2.5 *In vivo* methods 52
2.5.1 R21 vaccine 52
2.5.2 R21 fluorescent labelling 53
2.5.3 LMQ adjuvant 54
2.5.4 Preparation of R21 loaded LCSS particles 54
2.5.5 Quality control and loading quantification of R21 loaded LCSS particles 55
2.5.6 Formulation of the R21 vaccine regimens 56

2.5.7 Animal immunisations 57
2.5.8 Live imaging of *in vivo* particle localisation 58
2.5.9 ELISA for measuring antigen-specific antibody titres 58
2.5.10 Production of transgenic sporozoites for malaria challenge 59
2.5.11 Malaria challenge 60
2.6 Statistical Analysis 61
2.6.1 Production and *in vitro* experiments 61
2.6.2 *In vivo* experiments 61
3 Microfluidic production 65
3.1 Introduction 65
3.2 Results 69
3.2.1 Identifying the correct parameters to produce double emulsions 69
3.2.1.1 PVA treatment enables the hydrophilic coating of PDMS 69
3.2.2 DMC solvent and PLGA with an ester end cap are compatible with the microfluidic double emulsification process 72
3.2.2.1 A stepped channel design is essential in forming loaded, monodispersed, liquid core – solid PLGA shell particles 76
3.2.3 Understanding the mechanism of double emulsification in the stepped chip design 84
3.2.4 Evaluating the achievable size range and loading of double emulsions 91
3.2.5 Optimising the double emulsion throughput 96

3.2.5.1 Changing the position of the step in the microfluidic design increases the throughput 97

3.2.5.2 Decreasing the outer flow surfactant concentration increases the throughput above a certain core diameter 99

3.2.5.3 Increasing the outer flow salt concentration increases the throughput 102

3.2.6 Particle size can be tuned during the collection process 104

3.3 Discussion and Summary 110

4 Characterisation of the release kinetics 114

4.1 Introduction 114

4.2 Release analysis 116

4.3 Results 119

4.3.1 Comparison of the release kinetics between LCSS and BE particles 119

4.3.2 Mechanism of Particle Degradation 122

4.3.3 The effect of LCSS particles shell thickness on their release is explained by autocatalysis 128

4.3.4 Influence of the Mw of the Payload 136

4.3.5 Effect of polymer formulation on the payload release of LCSS particles 139

4.3.5.1 Increasing the PLGA Mw in LCSS particles increases the Peak time by order of days 139

4.3.5.2 Increasing the PLGA Lactide:Glycolide ratio in LCSS particles increases the Peak time by order of weeks to months 144
4.3.6 Additional relevant parameters for vaccine delivery..... 149
4.3.6.1 Refrigeration..... 149
4.3.6.2 Small variations of incubation pH extend the delay..... 152
4.3.6.3 Particle properties are conserved *in vivo* 155
4.4 Discussion..... 160
5 *In vivo* use with R21 malaria vaccine 163
5.1 Introduction 163
5.1.1 The Case for Malaria as the target disease 163
5.1.2 The R21 vaccine and LMQ adjuvant..... 165
5.2 Results 167
5.2.1 R21 immunogenicity is preserved when encapsulated inside particles 167
5.2.2 Adjuvant effect of LMQ is maintained when co-encapsulated inside particles..... 171
5.2.3 Different particle formulations affect immunogenicity and immune response delay..... 176
5.2.4 Prime + Particle formulation provides superior immunogenicity to Prime alone 184
5.2.4.1 Immunogenicity in the Short particle release study..... 186
5.2.4.2 Immunogenicity in the Medium particle release study..... 188

5.2.5 Encapsulation improves the efficacy of a single vaccine dose 192
5.2.5.1 Short release delay particles 193
5.2.5.2 Medium release delay particles 194
5.3 Discussion 196
5.3.1 R21 remains immunogenic following encapsulation 196
5.3.2 Delay in the Cterm-specific response can be tuned by the LCSS particle formulation 197
5.3.3 NANP-specific response from Particle only regimens is hindered with longer delay release formulations 198
5.3.4 The addition of encapsulated booster to the Prime regimen increases both NANP and Cterm-specific immune responses 200
5.3.5 Protection against malaria was increased by the addition of the encapsulated booster dose to a soluble prime 200
6 Concluding remarks 203
6.1 Summary of findings 203
6.2 Limitations and future directions 205
6.2.1 Improving production reproducibility 205
6.2.2 Increasing production rates 206
6.2.3 Exploration of new particle formulations 207
6.2.4 *In vivo* release quantitative kinetics characterisation 208
6.2.5 Improvement of the single-dose R21 towards Prime/Boost equivalence 209

6.3 Final Conclusion 210

References 212

Appendix I 240

List of Figures

Figure 1-1: W/O/W double emulsification manufacturing technique. 31

Figure 1-2: PLGA microparticles produced by W/O/W double batch emulsification exhibit a wide range of sizes. 32

Figure 1-3: 3D assembly of liquid core – solid PLGA shell rectangular particles reported by McHugh et al. 34

Figure 2-1: General design and features of the channels for the microfluidic double emulsification chip. 39

Figure 2-2: Microfluidic flow control setup to perform microfluidic emulsification. 45

Figure 2-3: Calibration curve for the use of dextran-FITC/TRITC to monitor the pH evolution inside LCSS particles. 51

Figure 2-4: Mechanical homogenization of LCSS particles breaks up the solid PLGA shell and allows full release of the liquid core payload. 56

Figure 2-5: Estimation of peak titre and time to 50% peak titre by GAM posterior sampling simulations 64

Figure 3-1: PVA treatment of PDMS surface provides a long-lasting hydrophilic coating. 71

Figure 3-2: Dimethyl carbonate (DMC) is compatible with single and double emulsification in PDMS microfluidic chips, unlike dichloromethane (DCM). 73

Figure 3-3: PLGA with an ester end cap was found to generate spherical droplets unlike acid end cap PLGA. 75

Figure 3-4: Flat microfluidic channel design for double emulsification fails to produce efficient loading of liquid core - solid PLGA shell particles. 78

Figure 3-5: Flat microfluidic design induces burst and splitting of double emulsions that result in a wide particle size distribution and poor loading. 81

Figure 3-6: Stepped microfluidic design allows production of highly monodispersed and fully loaded liquid core - solid shell PLGA particles. ... 83

Figure 3-7: Stepped microfluidic design produces double emulsions by jetting and induction of Rayleigh-Plateau instability. 86

Figure 3-8: The absence of passing core results in an uninterrupted jet in step designs. 86

Figure 3-9: Core droplet diameter is responsible for the triggering of the Rayleigh-Plateau instability, resulting in the double emulsion formation. ... 89

Figure 3-10: Liquid core – solid PLGA shell particle production remains stable with time. 90

Figure 3-11: Inner fluid pressure during manufacturing controls fine tuning of particle dimensions and core loading. 93

Figure 3-12: Middle fluid pressure during manufacturing controls fine tuning of particles dimensions and core loading. 96

Figure 3-13: The position of the step in the microfluidic design facilitates the triggering of the double emulsion formation, enhancing generation frequency. 99

Figure 3-14: The surfactant concentration in the outer flow changes the double emulsification regimen. 101

Figure 3-15: The addition of salt in the outer flow allows higher frequency of double emulsion generation. 102

Figure 3-16: Passing cores trigger higher jet instabilities when salt is added to the outer flow in a W/O/W double emulsification. 103

Figure 3-17: The addition of salt in the collection media prevents the swelling of cores and results in thicker shell LCSS particles. 106

Figure 3-18: Adding NaCl after production results in buckled liquid core solid - shell particles. 107

Figure 3-19: The addition of salt in the outer flow slows down the extraction of the DMC solvent, and hence hardening of the particle shell. 109

Figure 4-1: Typical example of measured release profile indicating the parameters used for analysis. 117

Figure 4-2: **LCSS particles produced by microfluidics or BE particles, before in vitro incubation.** 120

Figure 4-3: Comparison of release kinetics between LCSS and BE particles. 122

Figure 4-4: Loading and diameter distribution evolution with in vitro degradation of core-shell particles. 123

Figure 4-5: Fluorescent microscopy imaging of LCSS particle populations to assess morphology and loading across time during in vitro release. 124

Figure 4-6: SEM imaging of LCSS particle morphology evolution with in vitro incubation. 125

Figure 4-7: Fluorescence in the LCSS particles shell increases with time. 127

Figure 4-8: Diameter variation of LCSS particles depending on the loading status after 30 days of in vitro degradation. 128

Figure 4-9: Initial thickness of different batches of LCSS particles produced by microfluidics before in vitro release study. 130

Figure 4-10: Effect of the shell thickness on the release kinetics of LCSS particles. 132

Figure 4-11: SEM imaging of LCSS particles with different initial thicknesses following 30 days of in vitro incubation. 133
Figure 4-12: Internal pH evolution with in vitro degradation of LCSS particles of different initial shell thickness. 134
Figure 4-13: Microscopy images of the internal pH of particles with different initial thicknesses at different timepoints of in vitro degradation. 136
Figure 4-14: Effect of the payload size on the release kinetics of LCSS particles. 139
Figure 4-15: Effect of the PLGA molecular weight on the release kinetics of LCSS particles. 142
Figure 4-16: Loading and diameter distribution evolution with in vitro degradation of High Mw core-shell particles. 143
Figure 4-17: SEM imaging of particles with high Mw PLGA at different times of in vitro incubation 144
Figure 4-18: Effect of a 75:25 L:G ratio on release kinetics of LCSS particles. 147
Figure 4-19: Effect of a 100:00 L:G ratio on release kinetics of LCSS particles. 149
Figure 4-20: LCSS particle populations produced by microfluidics stored in fridge for 2 months before in vitro incubation. 150
Figure 4-21: Effect of the fridge storage of LCSS particles on their release kinetics. 152
Figure 4-22: SEM imaging of LCSS particles incubated for 30 days in vitro at different incubation pH 153

Figure 4-23: Effect of the incubation pH of LCSS particles on their release kinetics. 155

Figure 4-24: In vivo release kinetics of Short formulation LCSS particles.. 157

Figure 4-25: In vivo release kinetics of Medium formulation LCSS particles 158

Figure 4-26: In vivo kinetic release of Long formulation LCSS particles 159

Figure 5-1: Design summary of the in vivo experiment testing for preservation of R21 immunogenicity following encapsulation. 168

Figure 5-2: Immune response kinetics of vaccination regiments including encapsulated R21 compared to the unencapsulated vaccine. 169

Figure 5-3: Peak antibody response of encapsulated non-adjuvanted R21 is non-inferior to the non-encapsulated vaccine. 170

Figure 5-4: Summary of the in vivo experimental design to evaluate adjuvant potency following encapsulation. 172

Figure 5-5: Effect of the addition of LMQ adjuvant on the immune response kinetics of encapsulated R21 regimens compared to unencapsulated controls. 173

Figure 5-6: Peak antibody response of encapsulated R21 with LMQ adjuvant is noninferior to the unencapsulated control. 175

Figure 5-7: Design summary of the in vivo experiment testing the delay in immunogenicity induced by different particle formulations. 177

Figure 5-8: Longitudinal NANP-specific immune kinetic profiles for different LCSS particle formulations. 178

Figure 5-9: Longitudinal Cterm-specific immune kinetic profiles for different LCSS particle formulations. 179

Figure 5-10: Estimates of the peak titre and time to 50% peak titre. 180

Figure 5-11: Fold change of peak antibody titres and additional immune response delay for different LCSS particle formulations compared to unencapsulated control. 183

Figure 5-12: Design summary of the in vivo immunogenicity and malaria challenge experiment comparing the efficacy of the Prime + Particles regimen with Prime only. 185

Figure 5-13: **Immune response kinetics of different R21/LMQ regimens in the Short study challenge** 186

Figure 5-14: Peak antibody Cterm-specific response in the Prime and Short PAR regimen is superior to nonencapsulated Prime and Prime/Boost regimens. 188

Figure 5-15: Immune response kinetics of different R21/LMQ regimens in the Short study challenge. 189

Figure 5-16: Peak antibody Cterm-specific response of Prime and Medium PAR regimen is superior to nonencapsulated Prime regimen. 191

Figure 5-17: Prime + Short PAR is more protective and delays time to malaria infection compared to Prime only. 194

Figure 5-18: Prime + Medium PAR is more effective at delaying time to malaria infection compared to Prime only. 195

List of Tables

Table 1-1: Routine childhood immunisation schedule in the UK in 2022..... 28

Table 2-1: Summary of the dimensions of the features in the microfluidic chip design..... 40

Table 2-2: Summary of the concentrations of PLGA used in the middle fluid formulation...... 44

Table 2-3: Summary of immunisation regimen composition..... 57

Table 4-1: In vitro release Peak characteristics for different thicknesses .. 130

Table 4-2: In vitro release Peak characteristics for different payload sizes 137

Table 4-3: In vitro release Peak characteristics for different PLGA molecular weights..... 140

Table 4-4: In vitro release Peak characteristics for a PLGA with 75:25 L:G ratio 145

Table 4-5: In vitro release Peak characteristics for a PLA with 100:0 L:G ratio 147

Table 4-6: In vitro release Peak characteristics with fridge pre-storage 150

Table 4-7: In vitro release Peak characteristics for incubation pH 152

Table 5-1: Geometric mean estimates of peak antibody titres for unadjuvanted R21 regimens...... 171

Table 5-2: **Geometric mean estimates of peak antibody titres for the adjuvanted R21 regimens.**..... 175

Table 5-3: Estimates of peak antibody titres and time to 50% peak titre for NANP-specific and Cterm-specific responses for the different particle formulations and the unencapsulated control...... 181

Table 5-4: Geometric mean estimates of peak antibody titres for Short and Medium formulations studies...... 192

Abbreviations

Abbreviations	Description
AF	Alexa Fluor
ANOVA	Analysis of Variance
AP	Alkaline Phosphatase
API	Active Pharmaceutical Ingredient
BCA	Bicinchoninic acid Assay
BE	Batch Emulsification (method or particles)
BSA	Bovine Serum Albumin
CAD	Computer-Aided Design
CDC	Center for Disease Control
CI	Confidence Interval
CMC	Carboxymethylcellulose
CS	Core-Shell
CSP	Circumsporozoite Protein
CV	Coefficient of Variation
DCM	Dichloromethane
DI Water	Deionized Water
DMC	Dimethyl Carbonate
DMSO	Dimethyl Sulfoxide
DMV	Droplet Morphometry and Velocimetry (software)
DNA	Deoxyribonucleic Acid
DOPC	1,2-dioleoyl-sn-glycero-3-phosphocholine
DPBS	Dulbecco's Phosphate-Buffered Saline
DTP	Diphtheria-Tetanus-Pertussis (vaccine)

EDTA	Ethylenediaminetetraacetic acid
ELISA	Enzyme-Linked Immunosorbent Assay
EPI	Extended Programme on Immunization
Er	Erythrocyte
ESI	Elveflow Smart Interface (software)
EU	ELISA Units
FEG	Field Emission Gun
FF	Flow Focussing
FITC	Fluorescein Isothiocyanate
FM	Fluorescence Microscopy
GAM	General Additive Model
GFP	Green Fluorescent Protein
IM	Intramuscular
IPA	Isopropanol
IV	Intravenous
IVIS	In Vivo Imaging System
LCSS	Liqui core – solid shell (particle or structure)
L:G	Lactide:Glycolide ratio
LMIC	Low- and Middle-Income Country
LUT	Look-Up Table
MFI	Mean Fluorescence Intensity
MM	Matrix-M
MMR	Measles-Mumps-Rubella (vaccine)
MW	Molecular Weight
NHS	National Health Service
OD	Optical Density
PAR	Particles
Pb	*Plasmodium berghei*
PBS	Phosphate-Buffered Saline
PCR	Polymerase Chain Reaction

PDMS	Polydimethylsiloxane
Pf	*Plasmodium falciparum*
PLA	Polylactic Acid
PLGA	Polylactic-co-glycolic Acid
PTFE	Polytetrafluoroethylene
PVA	Polyvinyl Alcohol
QS	Quillaja Saponaria
SD	Standard Deviation
SEM	Scanning Electron Microscopy
TLR	Toll Like Receptor
TMCS	Trimethylchlorosilane
TRITC	Tetramethylrhodamine Isothiocyanate
TT	Tetanus Toxoid
UK	United Kingdom
VFI	Vaccine Formulation Institute
VLP	Virus-Like Particle
WHO	World Health Organisation

Publications and Patent

Manuscript: Two manuscripts arising from this work are in preparation: one describing the development of the technology and its application to the R21 vaccine in a mouse model of malaria as a proof-of concept, the second one about the mechanism of the double emulsification technology developed and its throughput optimisation for at scale encapsulation.

Patent:

Guyon R, Hill A, Milicic A, Stride E

Encapsulation Method and Particle

UK patent application No. 2205123.9

Contributions

All experimental conception, execution and analysis presented in this thesis have been performed by the author, Romain Guyon. Valuable help has been provided by the following additional contributors:

- Dr Sören Reinke performed the intramuscular injections in mice and provided training and advice for *in vivo* experiments, including the ELISA and malaria challenge.
- Dr Luca Bau provided training, advice and feedback on the statistical analysis and presentation of the *in vivo* results.
- Dr Ahmed Salman produced the *P. berghei* transgenic sporozoites for malaria challenges, helped with mosquito dissections and performed the intravenous injection of parasites in malaria challenge experiments.
- Adam Truby took care of the insectary work for sporozoites production.
- Dr Errin Johnson provided training on scanning electron microscopy.

1 Introduction

1.1 Overview of immunisation benefits

Vaccination is widely considered to be one of the most successful medical interventions in human history. Vaccines have contributed substantially to the control of infectious diseases in modern medicine, with numerous examples of their impact, most notably the eradication of smallpox in 1977 [1]. Since the introduction of routine vaccination in the United States, the incidence and death toll of diseases such as diphtheria, pertussis and tetanus, have been reduced by 80% or more by routine immunization [2], preventing 42,000 deaths annually [3]. Globally, immunisation has reduced the incidence of poliomyelitis by 99% [4], and mortality due to measles was reduced by more than 80% between 2000 and 2017 according to the World Health Organisation (WHO) [5]. Similarly, neonatal mortally rates due to tetanus have dropped by 90% globally, since 1990, thanks to immunisation campaigns [6]. The incidence and consequences of many other diseases have also been drastically reduced by vaccination [7], [8], providing protection both for the vaccinated individual, and at the population level by herd immunity, haltering disease transmission when high levels of vaccination are achieved [9].

The benefits of vaccination are not limited to improving health, their impact can also be measured at the economic and social level. By reducing the need for later interventions, vaccines reduce the cost of medical treatment, and help maintain the productivity of the working population [3], [10]. Importantly, in many parts of the world vaccines can ensure better health equity across social classes, as low-income households are at a greater risk of experiencing unaffordable health costs. As an

example, the introduction of measles vaccines in low and middle-income countries (LMICs) is predicted to prevent 12.5 million cases of catastrophic health costs and medical impoverishment for cohorts born between 2016 and 2030, of which a majority, 75% in the case of measles, would have affected the lowest income quintile [11]. The same trend was observed for rotavirus and pneumococcal vaccines, highlighting their ability to balance out unequal access to healthcare. Finally, Influenza vaccination in children in the United States has decreased missed schooldays by 50% [12], emphasising the contribution of vaccines to school attendance, another target marker for social equity.

The numerous benefits of vaccination, and the success of smallpox eradication, led to the establishment of the Extended Programme on Immunization (EPI) in 1974 by the WHO, with the aim of providing universal access to vaccines against diphtheria, pertussis, tetanus, poliomyelitis, measles and tuberculosis in children. The program has achieved tremendous progress in worldwide coverage, raising it above 77% globally for these vaccines [13]. However, the WHO still estimates the annual number of children's deaths that could be prevented by vaccination to around 1.5 million, a high toll partially due to lack of access but also lack of compliance with vaccination [14].

1.2 The need for vaccination compliance

Vaccines are mostly administered in a prime/boost regimen to achieve high efficacy and durable protection against infectious diseases. Injection of multiple doses enhances the cellular and humoral immune response in intensity, quality and longevity, constituting a strong immunological memory [15]. The number of boosters

required and the timing between doses differ for each vaccine [16], making compliance with vaccination a major challenge.

The UK routine childhood immunisation schedule comprises a multitude of vaccines and boosters for children below 14 years of age (**Table 1-1**), similar to other European countries and in accordance with the WHO recommendations [17]. As a result, and in addition to the oral vaccine for rotavirus and hexavalent vaccines, a baby receiving the recommended schedule will experience 12 vaccinations in its first year, of which 10 are given intramuscularly.

Table 1-1: Routine childhood immunisation schedule in the UK in 2022

Vaccine	UK immunisation schedule (2022)
Diphtheria-Tetanus-Pertussis (DTP)	**5 injections** month 2 - 3 - 4, year 3.5 - 14
Meningococcal group B (MenB)	**3 injections** month 2 - 4, year 1
Meningococcal group C (MenC)	**2 injections** year 1 - 14
Rotavirus	**2 injections** month 2-3
Polio	**5 injections** month 2 - 3 - 4, year 3.5 - 14
Measles-Mumps-Rubella (MMR)	**2 injections** year 1 - 3.5
Human papilloma virus	**2 injections** year 12 - 12.5
Haemophilus influenzae type b (Hib)	**3 injections** month 2 - 3 - 4
Pneumococcal disease	**2 injections** month 3, year 1

Data from the NHS [18]

The need to administer a large number of vaccines over a relatively short time can lead parents to delay or refuse immunisation and this is defined as vaccine hesitancy by the WHO. A study conducted in 2019 in the US demonstrated that

more than 23% of parents reported vaccine hesitancy, attributed to a variety of causes, including lack of knowledge, misinformation, negative attitude towards vaccination, demographic characteristics, or socio-economic status [19], [20]. Interestingly, vaccine hesitancy in high income countries does not necessarily translate to vaccine refusal but rather to a temporary or permanent under-immunisation by deferring or rejecting subsequent vaccine injections following the prime dose administration. Taking the case of the Diphtheria-Tetanus-Pertussis (DTP) vaccine, for example, in 2019 in Canada, the proportion of completely unvaccinated 2-year-old children was as low as 1.7% but compliance with the schedule of 4 recommended doses was only 78%, well below the WHO coverage goal of 95% [21], [22]. Low compliance for the DTP vaccine is observed worldwide, with 6.8 million infants not receiving required 3 doses of the DTP vaccine in 2021 [14]. In LMICs, lower socio-economic conditions and reduced access to healthcare are major factors behind the limited vaccination compliance. In a study conducted in rural areas of Pakistan, only 39% of infants, having received the first dose of DTP, completed the full 3 dose schedule. Lack of compliance was found to significantly correlate with household income and distance to the healthcare centre [23]. Similarly, a study of infants in a low-resource community in Zambia reported a 62% rate of complete vaccination [24]. These trends are also seen with other childhood vaccines, as highlighted by a recent analysis of immunisation data in Tanzania [25], with significant rural-urban disparities in vaccine coverage and timeliness, and delay in vaccination due to increased distance to the health facilities.

Overall, incomplete vaccination and non-compliance with vaccination schedules have been major obstacles for disease eradication, leading the WHO to initiate a Special Programme for Vaccine Development [26]. This programme aimed to

produce single-dose vaccines using delayed antigen delivery systems, thus reducing the number of required injections, and alleviating the compliance burden on the patient while facilitating the implementation and success of global vaccination campaigns.

1.3 Double batch emulsification and its limitations in single-dose immunisation

The possibility of delivering vaccine antigens by sustained release from polymer-based particles, triggering long lasting antibody responses, was first demonstrated in a mouse model in 1979 [27]. Following these early cutting-edge results, biodegradable microparticles, already used for the delivery of hormones [28], emerged as the solution in the development of single dose vaccines. The idea was based on the encapsulation of the antigen inside a hydrophobic polymer matrix (poly lactic acid, PLA, or polylactic-co-glycolic acid, PLGA) that could degrade with time by hydrolysis and release the contents. The microsphere shape was chosen to facilitate manufacturing and intramuscular injection, and release timing tuned by varying the chemical properties of the polymer.

In order to produce antigen loaded PLGA microparticles, the main manufacturing technique still used today in both academic research laboratories and the industry is the water-in-oil-in-water (W/O/W) double batch emulsification (BE) technique [29]. The antigen is first suspended in an aqueous phase, emulsified with the polymer and organic solvent by magnetic stirring to form water-in-oil (W/O) droplets, and subsequently re-emulsified in a water phase to create the W/O/W emulsion (**Figure 1-1**). These emulsions are converted into solid particles, by evaporation or extraction of the solvent.

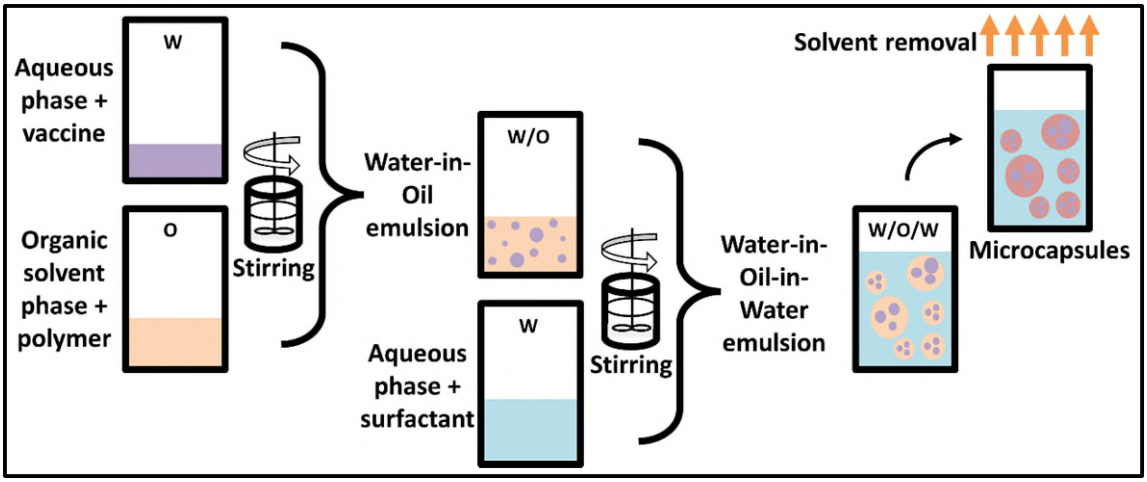

Figure 1-1: W/O/W double emulsification manufacturing technique.

Reproduced from [29].

Using this method, and following the objectives defined by the Special Programme for Vaccine Development, the initial target defined by the WHO was the encapsulation of the Tetanus Toxoid (TT) vaccine, [26]. A long-lasting immune response in mice was reported, and numerous studies conducted between 1990 and 2000 in mice, rats and guinea pigs, showed that TT-loaded microparticles could match the long-term TT-specific antibody response, comparable to two or even three injections of TT vaccine [30]–[32]. However, a major limitation of these studies was the substantial dose of TT required to produce similar immune response in a single dose regimen by itself, without encapsulation [31], [32]. Regimens with lower TT doses remained inconclusive due to the partial loss of antigenicity of the toxoid during the encapsulation process [32].

In addition to the absence of clear preclinical evidence compared to non-encapsulated controls, many factors have hindered the progress of vaccine encapsulation technology [33], [34]. For example, the W/O/W double BE technique produces a wide size range of particle sizes [35](**Figure 1-2**). Microparticles smaller

than 10µm are subject to phagocytosis [36], while larger ones are likely to remain intact at the injection site until the release of the payload. These differences in the uptake limit the comprehension of the delivery mechanism and produce batch-to batch variation in the immune response [34].

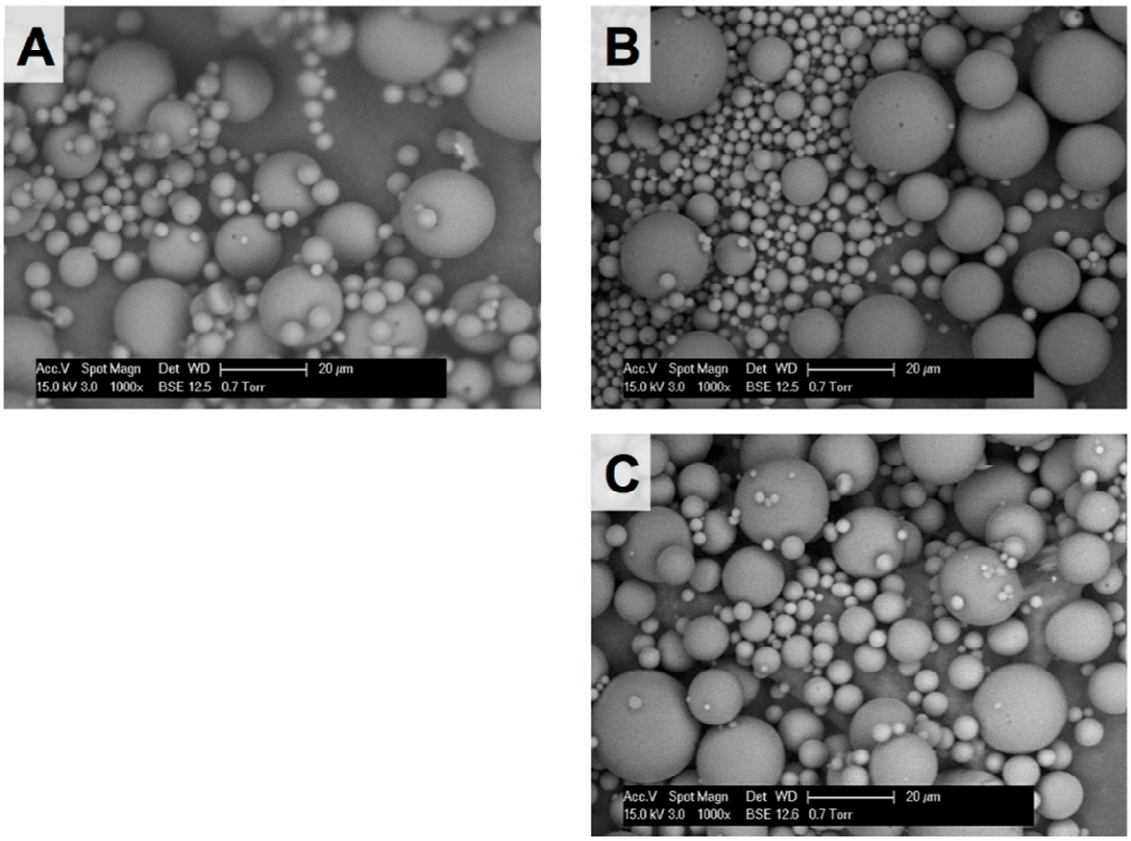

Figure 1-2: PLGA microparticles produced by W/O/W double batch emulsification exhibit a wide range of sizes.

SEM images of different formulations of PLGA microparticles produced by W/O/W double BE and encapsulating the polio vaccine with different excipients (A – gelatine, B- sucrose, monosodium glutamate, magnesium chloride, C- maltodextrin, monosodium glutamate, magnesium chloride). Reproduced from [35].

Quality control of microparticles generated by this method is also very limited, with no methods currently available to precisely quantify the antigen content [37]. Characterisation of antigen release *in vitro* is significantly hindered by the instability

of proteins inside the particles. This is both due to the exposure to harsh conditions during manufacturing, including high shear stirring and solvent interaction [38], and to the exposure to acidic conditions during microsphere degradation [39]. Moreover, lack of control over particle size and loading results in a low encapsulation efficiency (~50%) [40], and an early “burst release” effect so that substantial amounts of the payload are released shortly after injection [41].

Since these early results of microparticle systems based on W/O/W double BE, formulation improvements have been made to stabilise the encapsulated proteins, reduce the burst effect and increase the encapsulation efficiency [42]–[44]. However, the combination of between-study result variability, lack of reliable quality control methods and irregular delivery profile with no clear pulsatile release mimicking the booster vaccination have remained major obstacles that prevented testing these delivery systems in a clinical trial [45].

1.4 Benefits and challenges of core-shell particle architecture

In 2017, a novel system for vaccine encapsulation was reported based on a 3D assembly of PLGA particles presenting a liquid core – solid shell structure (LCSS) and demonstrating proof of concept of delayed pulsatile delivery to mimic the booster vaccination [46]. The assembly process was based on the hot embossing of a PLGA film onto a PDMS mould fabricated by soft-lithography (**Figure 1-3.A**), followed by the filling of the resulting cavity with aqueous core content using a picolitre dispensing apparatus (**Figure 1-3.B**) before sealing by precise alignment and hot pressing of the caps (**Figure 1-3.C**). The resulting cuboid particles had a highly reproducible architecture (400 x 400 x 300µm).

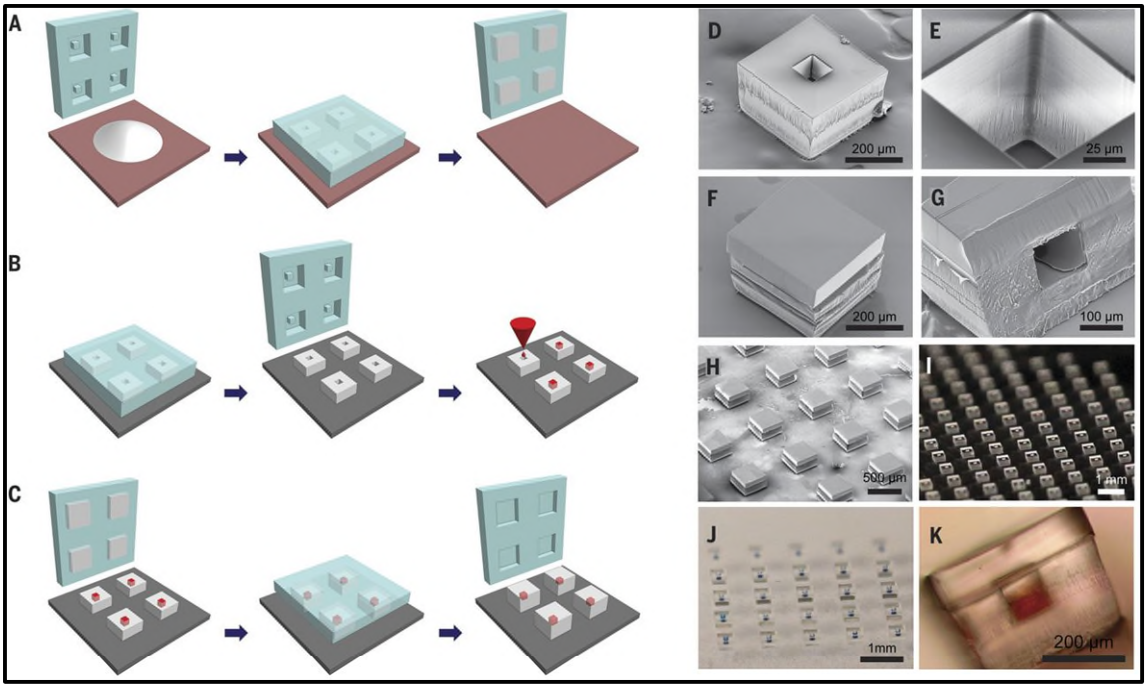

Figure 1-3: 3D assembly of liquid core – solid PLGA shell rectangular particles reported by McHugh et al.

Description of the manufacturing process, including, the hot embossing moulding (A), filling (B) and sealing (C) of the particles. SEM (D-H) and optical microscopy (I-K) images of the resulting particles produced by this process. Reproduced from [46].

When administered *in vitro* and *in vivo* in mice, these particles displayed pulsatile release kinetics with tuneable delay [46], [47] which could be explained by the homogeneous and exclusive localisation of the encapsulated payload in the core [47]. Hence, the uniformity and precise architecture of this system represented a significant advantage over the double BE-based particles, in the development of a single dose vaccine technology.

However, due to the complexity of the manufacturing process and large size incompatible with standard intramuscular injection, this technology has limited development potential for scale-up and mass production. The manufacturing process is discontinuous by nature, with the mould footprint restraining the scaling-

up of the hot embossing. The filling rate is dependent on the picolitre dispensing apparatus to ~2 seconds per particle [46] and required precise micrometric alignment similar to the sealing step. In addition, mechanical scraping using a razor blade was required for the collection of the hot embossed particles that could lead to deformation and destruction [48].

Furthermore, the particles were large for subcutaneous injection through a needle constraining the administration by tip loading in 18-gauge (G) needles, a needle size not recommended in mice [49]. A new syringe design was proposed more recently by the same research group, aiming to increase the injection success [50]. This design limited the sedimentation of the particles and clogging, achieving up to 80% injectability with a 18G needle, and 20% in 25G needles. This complex administration would constitute a major barrier in the context of a vaccination campaign, constraining the injection to specific syringes, large gauge needles and skilled practicians to ensure successful immunisation. Indeed, the recommendation of the Center for Disease Control (CDC) for vaccine administration are 23-25G for subcutaneous and 22-25G for intramuscular routes, respectively [51]. In addition to this logistical constraint, fear of needles has been associated with vaccine hesitancy [52], adding value to the preferential use of small gauge needles.

In this respect, single dose vaccine technology would benefit from the convenient injectability and scale-up potential of micro spherical particles with a controlled and precise delayed pulsatile release provided by a defined core-shell geometry.

1.5 Aims of the thesis

This thesis aims to explore microfluidic droplet emulsification techniques to produce uniform liquid core – solid PLGA shell particles (LCSS particles) in a continuous, reproducible manner, and their application for single dose vaccine delivery. The specific objectives are as follows:

- Structure objective: The particles must provide a LCSS structure with high uniformity in terms of both core and shell diameter, (coefficient of variation (CV) < 10% and < 5% respectively[1]).
- Size objective: The outer diameter of the particles should be between 40 and 100µm to ease injection while preventing their phagocytosis in the body [36]
- Production objective: The particles must be produced continuously via a process that is stable over multiple hours, offering a tuneable size and high loading and encapsulation efficiency.
- Kinetics objective: The particles should exhibit *in vitro* a delayed pulsatile release, without significant burst release.
- Vaccine application objective: Used in a murine model, the antigen loaded particles, given alongside a priming dose of antigen in a single injection, should provide better immune response and protection than a dose-matched priming regimen without particles and non-inferior immune response and protection to a dose-matched prime/boost regimen.

These different objectives are investigated in the following research chapters:

[1] chosen arbitrarily to contrast with the high polydispersity of existing methods with CV >25%

- **Chapter 3** focuses on the development of the microfluidic platform to produce LCSS particles, exploring different processing parameters to change the particle size and increase manufacturing rate.
- **Chapter 4** reports the *in vitro* kinetic release of the LCSS particles for different formulations and incubation parameters and investigates the mechanism of release using microscopy techniques.
- **Chapter 5** describes the study of a malaria candidate vaccine loaded in the LCSS particles in a murine model to assess the immune response and resulting protection in malaria challenges of particle-based single injection regimen. Efficacy is compared to dose-matched prime and to prime/boost injection to evaluate the performance of the particles.

2 Materials and Methods

All chemicals used are listed in the relevant section below, and were purchased from Sigma Aldrich, unless stated overwise.

2.1 Microfluidic Manufacturing

2.1.1 Microfluidic channel design

Microfluidic channels were designed using a computer-aided design software (AutoCAD, AutoDesk). The general design and features are presented in **Figure 2-1**. The corresponding dimensions of the features are listed in **Table 2-1**. Flow resistors were added to reduce the backflow risks during the microfluidic process operation, triangular expansions at the intersections were added to produce a velocity gradient as reported in [53], and the step, i.e. change in height, was added to stabilise the double emulsion, as explained in Chapter 3.

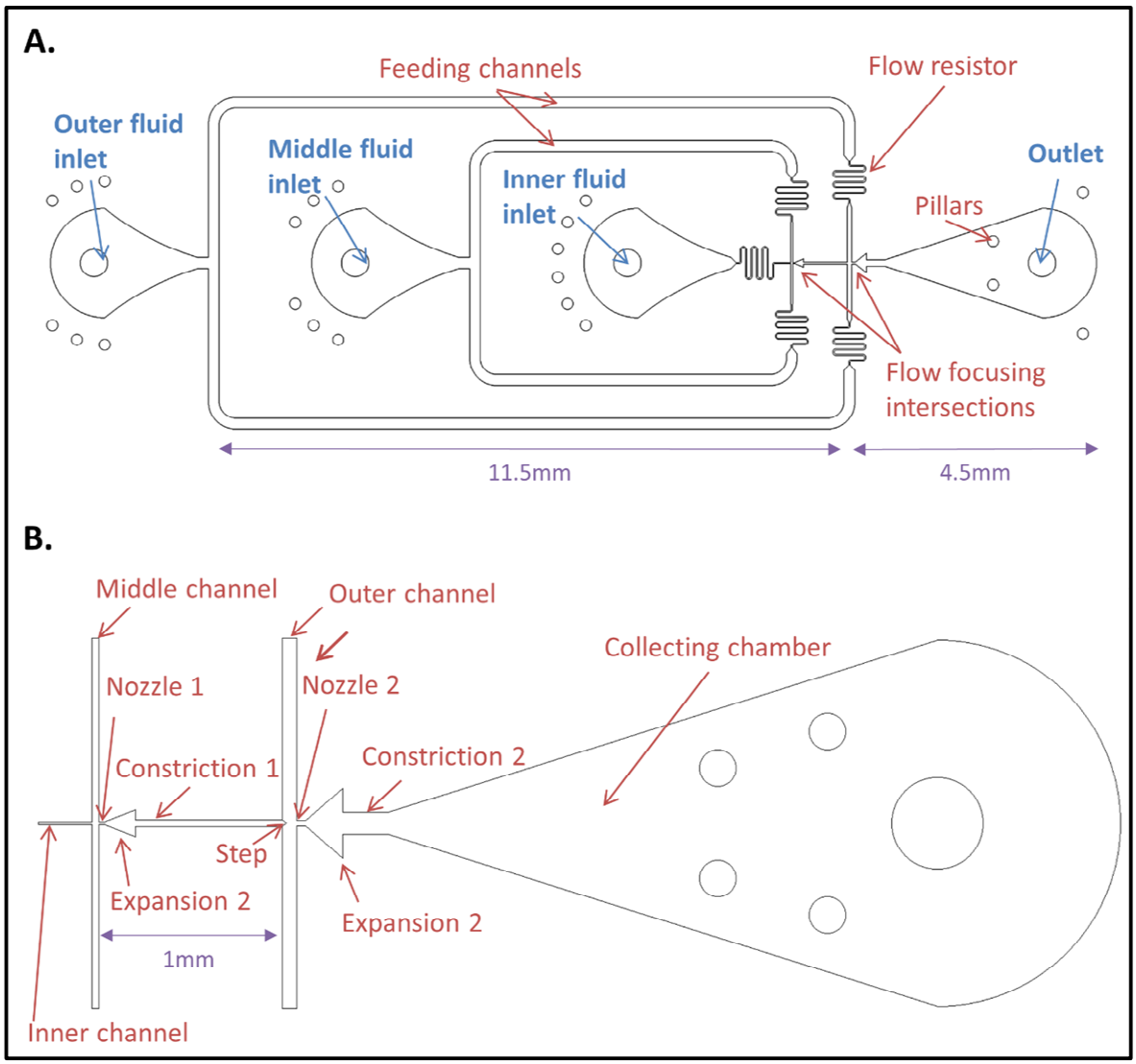

Figure 2-1: General design and features of the channels for the microfluidic double emulsification chip.

A. General chip design with inlets and outlets indicated in blue, and features in red.

B. Enlarged view of the flow focusing design with specific features indicated in red.

Table 2-1: Summary of the dimensions of the features in the microfluidic chip design

Regimen	Width (µm)	Height (µm)	Length (µm)
Nozzle 1	15	50	40
Nozzle 2	50	100	70
Expansion 1	150 (max)	50	200
Expansion 2	360 (max)	100	200
Constriction 1	50	50	800
Constriction 2	120	100	350
Inner channel	20	50	290
Middle channel	40	50	700
Outer channel	80	100	1000
Flow resistor	20	50	3700
Feeding channel	200	100	variable

2.1.2 SU-8 mould

SU-8 soft lithography positive moulds, corresponding to the design described above, were manufactured externally by Micrux Technologies using soft lithography techniques, as described in the literature [54]. Once received, to enable the silicon replication, the moulds were treated to make them hydrophobic by vapour deposition of trimethylchlorosilane (TMCS, Sigma-Aldrich). The moulds were left for 1 hour inside a sealed glass petri dish surrounded by a few drops of TMCS. The remaining TMCS was then left to evaporate, and the mould cleaned with isopropanol (IPA, Sigma-Aldrich) and dried under a flow of nitrogen gas.

2.1.3 Chip manufacturing

The microfluidic chips were produced by the widely used silicon replication method [54]. Briefly, polydimethylsiloxane (PDMS) was mixed at 10:1 ratio of pre-polymer: curing agent (SYLGARD 184, Dow) and poured on a positive SU-8 mould, hydrophobized to prevent any sticking of the prepolymer. After degassing in a vacuum chamber until no visible air bubbles were left, the PDMS was cured overnight in an oven at 65°C. The PDMS layer was peeled off the mould and each chip design cut out separately with a razor blade. Inlets and outlets were punched with a blunt 18G needle, the chips were then cleaned with IPA, dried with nitrogen, and bonded to a flat PDMS slab by exposure to O_2 plasma in a plasma chamber (HPT-200, Henniker plasma) for 3 min at 100% power. After plasma exposure the PDMS chip design and PDMS slab were pressed together for 30 seconds, and their bonding strengthened on a hot plate at 115°C for 30 seconds.

2.1.4 Surface treatment coating

Sealed chips were used with fully hydrophobic, partially hydrophobic (from the second intersection) or fully hydrophilic channels, depending on the experiments, as described in Chapter 3.

Hydrophobic: Without surface treatment, PDMS is naturally hydrophobic.

Partially hydrophilic: To create partially hydrophilic channels, a protocol was adapted from [55]. Briefly, immediately after plasma bonding, a coating solution of 1% (w/v) polyvinyl alcohol (PVA, 30-70k Mw, 87-90% hydrolysed, Sigma-Aldrich) in deionized water (DI water) was injected from the outer inlet at 100 mbar while air was continuously flushed through the inner and middle inlet at 50 mbar to protect

the first intersection from the coating solution. The treatment was performed for 5 minutes before flushing the channels with air and drying the entire chip for 5 minutes at 115°C on a hot plate. The process was repeated 3 times to ensure durable and reliable partial hydrophilic coating.

Hydrophilic: Immediately after plasma bonding, the channels were filled with a coating solution of 1%(w/v) PVA (30-70k Mw, 87-90% hydrolysed, Sigma-Aldrich) in deionized water (DI water) and left for 5 minutes before flushing the channels with air and drying the entire chip for 5 minutes at 115°C on a hot plate. The process was repeated 3 times to ensure durable and reliable hydrophilic coating, using plastic syringes (5mL, BD), needles (23G, Terumo) and PTFE tubing (1/32" outer diameter, 300µm inner diameter, Darwin microfluidics) to inject the fluids.

Following coating, the microfluidic chips were left at 60°C for a minimum of 48 hours to allow any uncoated parts to recover its hydrophobicity. Chips were then stored at room temperature and used for microfluidic emulsification within 3 months following their manufacturing.

2.2 Emulsification process

2.2.1 Fluid formulations

Three different fluid composition were used to achieve W/O/W double emulsification.

Inner fluid: The aqueous inner fluid was made by dissolving the relevant payload in PBS (1X, Sigma-Aldrich). For *in vitro* applications (Chapter 3 and 4) dextran-

TRITC (40 kDa, Sigma-Aldrich) was used at a concentration of 50mg/mL. For *in vivo* the vaccine formulation is detailed in section 2.5.4.

Middle fluid: The organic middle fluid was made by dissolving different type of PLGA (Resomer, Evonik) in either dimethyl carbonate (DMC, Sigma-Aldrich) or dichloromethane (DCM, Sigma-Aldrich) solvent, in a glass vial at room temperature. The glass vials were kept 2 hours on a rolling shaker to ensure complete dissolution of the polymer. The PLGA concentration used depending on the polymer's characteristics, corresponding to the maximum compatible concentration with the microfluidic setup before clogging, are reported in **Table 2-2**.

Outer fluid: The aqueous outer fluid comprised 3%(w/v) PVA (9-10k Mw, 80% hydrolysed, Sigma-Aldrich) in DPBS (1X, Gibco). For specific experiments described in Chapter 3, the concentration of PVA was varied from 0.03 to 10% (w/v), and/or supplemented with 1% (w/v) NaCl.

Table 2-2: Summary of the concentrations of PLGA used in the middle fluid formulation.

Polymer name	Mw (kDa)	End cap	Lactide:Glycolide ratio	Concentration %(w/v)
Resomer® 502	7-17	ester	50:50	17.75
Resomer® 502H	7-17	acid	50:50	17.75
Resomer® 503	24-38	ester	50:50	12
Resomer® 504	38-54	ester	50:50	10.75
Resomer® 505	54-69	ester	50:50	7.5
Resomer® 753 S	24-38	ester	75:25	12
Resomer® 202 S	7-17	ester	100:00	17.75

Produced by Evonik, ordered from Sigma-Aldrich

2.2.2 Microfluidic platform

To perform microfluidic emulsification, a pressure-driven microfluidic setup was assembled. Compressed air was generated from a compressor (6-4 quiet running compressor, Jun-Air) and fed to a pressure controller (OB1, Elveflow). Separated reservoirs (Darwin Microfluidics) containing the inner middle and outer fluid were precisely pressurised by the pressure controller and the liquids pumped into the microfluidic chip through PTFE tubing (1/32” outer diameter, 300µm inner diameter, Darwin microfluidics). Solenoid 3-way valves (Elveflow) were added as required on the fluidic path to switch between formulations. The emulsification process was monitored using an inverted microscope (DMi8, Leica) in brightfield illumination

mode and a high-speed camera (Hx-3 from NAC, or Nova S16 from Phantom). The injection pressures were set using the pressure controller dedicated software (ESI, Elveflow) and adjusted as described in section 2.2.3. A diagram of the microfluidic setup is shown in **Figure 2-2**.

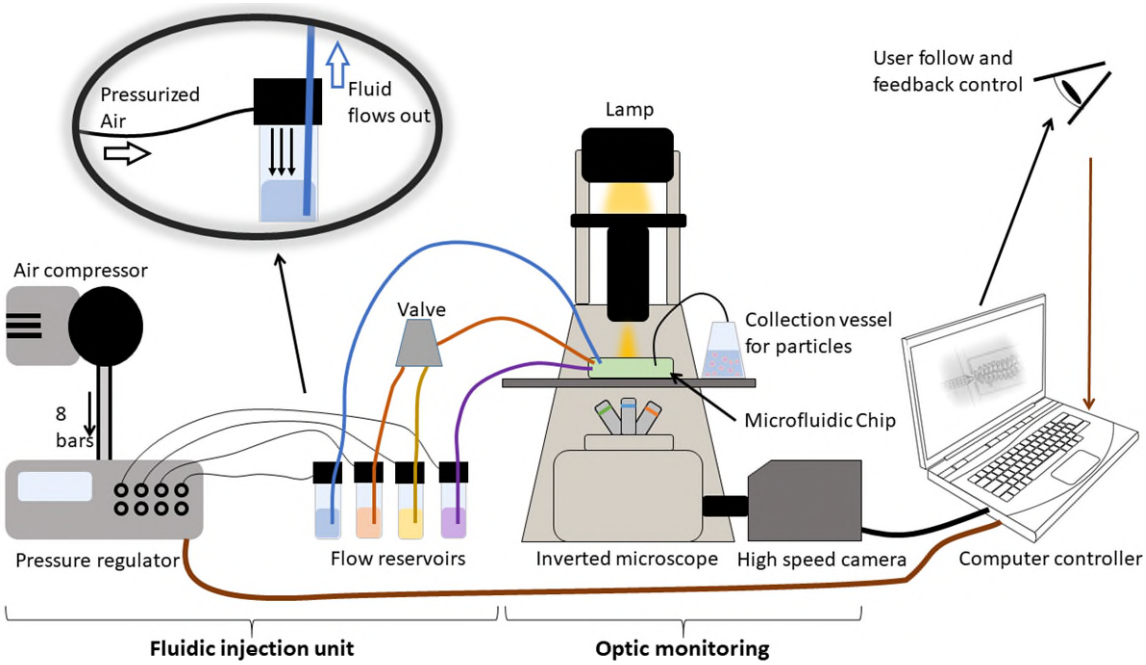

Figure 2-2: Microfluidic flow control setup to perform microfluidic emulsification.

2.2.3 Microfluidic double emulsification

Microfluidic emulsification was performed with the platform described in section 2.2.2. The formulation of the injected fluid is described in section 2.2.1. The reservoirs containing the inner, middle, and outer fluids were connected to their respective chip inlet using the appropriate microfluidic fittings (1/4-28”, Darwin microfluidics) and PTFE tubing (1/32” outer diameter, 300µm inner diameter, Darwin microfluidics). Tubing was also used to connect the outlet to a collecting glass petri dish filled with outer fluid. Inner, middle, and outer flow pressures were set respectively to 200, 300, and 400 mbar, to prefill all channels and reduce risk of

backflow. After 2 minutes the flow pressures were changed to the required levels for double emulsification and monitored using a high-speed camera. Videos of production were recorded, and the core and outer droplet diameter, and frequency of particle formation were measured by a dedicated software (DMV, developed at Wayne State University [56]). The pressures were adjusted manually to obtain the desired diameter and/or maximum frequencies (see Chapter 3 for more details). Double emulsions were collected in a glass petri dish. Extraction of the solvent was performed over 48 hours at room temperature on a roller shaker, replacing the PBS extraction media every 12 hours. Particles were then filtered using mini cell strainers (100µm, pluriSelect) and stored in 2mL of PBS in Eppendorf tubes (2mL-size LoBind) at 4°C.

2.2.4 Batch emulsification

To produce particles by batch emulsification (BE) with the same fluids as used in the microfluidic double emulsion, two different ratios of inner to middle fluid were tried as described in Chapter 4. For BE 1:10, 30µL of inner fluid was pipetted in 300µL of middle fluid, and for BE 1:5, 100µL of inner fluid was pipetted in 500µL of middle fluid. The middle fluid was formulated as 17.75% (w/v) PLGA R 502 in DMC solvent. The mix was vortexed at 3000rpm for 1 minutes in a 2mL-size LoBind Eppendorf. The resulting water-in-oil emulsion was transferred by pipetting into 10mL of the outer fluid (3% (w/v) PVA in DPBS) contained in a 15mL-size glass vial, and vortexed at 2500rpm for 1minute. The resulting water-in-oil-in-water emulsion was left to rest for 15 minutes. Extraction of the solvent was performed over 48 hours at room temperature on a roller shaker, replacing the PBS extraction media

every 12 hours. Particles were then filtered using mini cell strainers (100µm, pluriSelect) and stored in 2mL of PBS in Eppendorf tubes (2mL-size LoBind) at 4°C.

2.2.5 Microfluidic video processing

In addition to the video processing during production to measure the core and outer droplet features, as described in section 2.2.3, postproduction video analysis was performed to measure the variation of the jet diameter across different core sizes flowing (see experiment described in section 3.2.4). High-speed videos of the microfluidic emulsification transition were recorded as before. The jet diameter variation with time was measured frame by frame at a fixed cross section, by setting a threshold to identify the interface between the jet and the outer phase, using Fiji (ImageJ). The jet diameter variation was plotted against the diameter of the core and outer droplet produced, measured on the same video with the DMV software (**Figure 3-9**).

2.3 *In vitro* Release

2.3.1 *In vitro* incubation

To measure the release from particles under simulated *in vivo* conditions, particles encapsulating 50mg/mL of dextran-TRITC in PBS (40kDa, Sigma-Aldrich) and produced either by BE or microfluidic emulsification were divided equally into sets of 4 samples suspended in 0.01%(w/v) Tween 80 (Sigma-Aldrich) in PBS in Eppendorf tubes (2mL-size LoBind). The replicates were incubated in a rotating incubator (Roto-Therm, Benchmark Scientific) kept at 37°C at 20rpm. The combination of the rotation and the presence of Tween 80 surfactant in the release

media prevented aggregation of the particles. At selected timepoints (depending on the PLGA formulation used), particles were sedimented by centrifugation for 30 seconds at 50xg, and 1mL of supernatant was replaced with fresh releasing media to provide sink conditions, preventing saturation effects of the released dextran. A fraction (200µL) of the removed media was used for quantification of the release. Particles were then resuspended by simple inversion of the tube, before being placed back in the rotating incubator. A small amount (20µL) of resuspended particles were imaged (see section 2.4.1) before being returned to the tube. Occasionally an additional 10µL of resuspended particles were taken out for SEM imaging (see section 2.4.3), in these cases the particles were not returned.

2.3.2 Release quantification

Release quantification was performed by fluorescent spectroscopy (FLUOstar Omega, BMG Labtech). The concentration of dextran-TRITC at each timepoint was determined by measuring the TRITC fluorescence intensity and interpolating the concentration using a previously obtained standard curve. The release was computed from the measured concentration and normalised to the initial total encapsulated content for each sample by measuring the remaining encapsulated dextran-TRITC at the end of the experiment The amount of unreleased dextran-TRITC at the end point was measured in the supernatant after mechanically breaking up the particles using a cell homogenizer (Cole-Parmer) for 30 seconds, and isolation from PLGA debris by centrifugation at 15000xg for 10 minutes. At each timepoint concentration was corrected for the dilution resulting from the partial replacement of the releasing media.

2.4 Particle characterisation

2.4.1 Microscopy image processing

For postproduction quality control and to study the degradation and release of the produced particles *in vitro*, an image processing protocol was developed. An aliquot (20µL) of particles were suspended in 200uL of 0.01% (w/v) Tween 80 in PBS in Cellview slides (Greiner) and multi-tile imaging was performed with an inverted microscope (TiE2, Nikon) and 10X objective. The brightfield and the relevant fluorescent channel images were recorded and processed with a custom MATLAB script (Appendix I). Each image was first smoothed by applying a bilateral filter or a gaussian filter for the brightfield and fluorescence channels respectively. Background fluorescence was removed, and contrast enhanced for the brightfield. Individual particles were detected using a Hough transform algorithm and, if necessary, separated from each other by watershed segmentation. Masking techniques were used to associate each particle observed in the brightfield images with their cores in the fluorescence images. Thus, different features were measured for each particle, including the fluorescence intensities of the whole particle, the core and the shell, the diameter of the core and the particle, and the eccentricity between the core and the shell centroids. In addition to individual features, the loading of the batch (postproduction or at different timepoints of the *in vitro* release) was determined as the ratio between the number of particles with a fluorescent signal above 500 mean fluorescence intensity (MFI) and the total number of particles released. The described detection process applied both to BE and microfluidic double emulsification productions was limited to particles above 10µm, as the

microfluidic emulsification production generated small satellite (<10μm) droplets [57] that did not contain any core and hence were not relevant to this research.

2.4.2 Monitoring of the pH inside the LCSS particles

To monitor the evolution of the pH inside the LCSS particle, dextran-FITC/TRITC (70kDa, Sigma-Aldrich) was used at a concentration of 10mg/mL in PBS as the payload, and LCSS particles made using the microfluidic process described in section 2.2.3. The FITC fluorescent signal is sensitive to pH whereas the TRITC signal is not. Hence, the ratio of fluorescence from the core of particles at different timepoints was imaged by fluorescent microscopy and analysed by image processing, described in section 2.4.1. The pH was computed using a calibration curve (**Figure 2-3**) made with dextran-FITC/TRITC suspended in different citrate and phosphate buffers with pH spanning from 2.1 to 7.4.

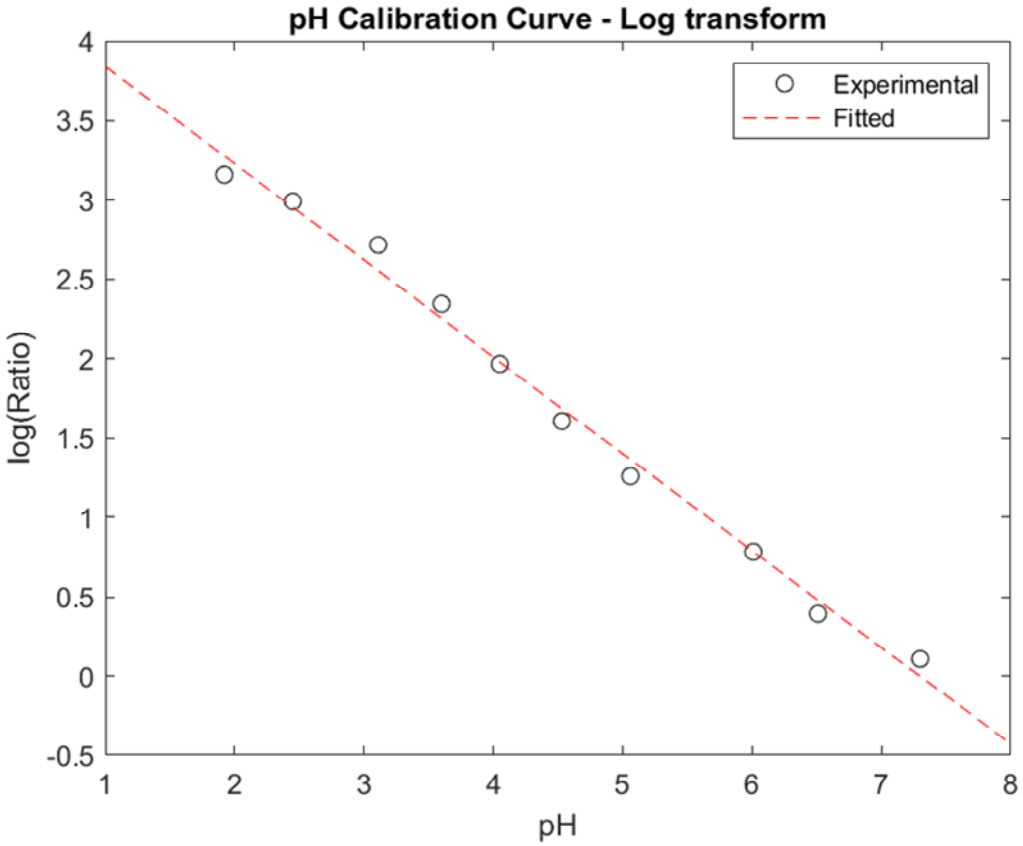

Figure 2-3: Calibration curve for the use of dextran-FITC/TRITC to monitor the pH evolution inside LCSS particles.

Dextran-FITC/TRITC (70kDa) was suspended at a concentration of 10mg/mL in citrate or phosphate buffer with a pH range spanning from 2.1 to 7.4. The fluorescence ratio between the TRITC and FITC signal was measured from image pixels of wells filled with the solutions, taken by fluorescent microscopy, to be comparable in size to particle images. The mean of 4 image ratios for a given pH are log transformed and plotted as circles. The linear fit is represented as a red dotted line.

2.4.3 SEM characterisation

The morphology of particles immediately after production or at different timepoints of *in vitro* degradation was imaged using a field emission gun scanning electron microscope (FEG-SEM, Zeiss Sigma 300) with an acceleration voltage of 2kV. Before imaging, 10µL of particles in suspension in PBS or release media were

spread on a conductive adhesive carbon tape attached to a SEM pin stub and a thin film of Pd/Au coating was sputtered onto the sample (Q150R ES Dual Carbon/Sputter Coater, Quorum Technologies).

2.5 *In vivo* methods

2.5.1 R21 vaccine

The virus-like particle R21 vaccine was generated as described previously [58]. The R21 DNA sequence codon optimised for optimal expression in yeast was synthesised by GeneArt. The R21 expression plasmid was constructed by inserting the R21 DNA sequence into the pPink-HC (high copy) expression plasmid from the PichiaPink Expression System (Invitrogen) by restriction cloning using EcoR1 and Kpn1. The presence of the insert in the plasmid was confirmed by PCR. The R21.pPink-HC expression plasmid was linearized by Afl II and integrated into the genome of the PichiaPink™ yeast strain 4 (Invitrogen) using electroporation. Positive transformants were then selected by growth on adenine deficient media and genomic DNA was isolated and sequenced to confirm the correct insert in the yeast. Transformed yeast were grown in glycerol-containing media and protein expression induced with 0.5% methanol for 3 days. Yeasts were harvested by centrifugation and the pellets resuspended in a lysis buffer containing 10 mM Tris (pH 7.8), 0.1%Triton X-100, 1 mM EDTA and 250U/mL benzonase. Acid washed glass beads (0.425–600µm) were added, samples were vortexed and yeast cell debris removed by centrifugation for 5 minutes at 1500 ×g. The supernatant was clarified by ultracentrifugation at 13000 ×g for 20 minutes and layered onto a discontinuous CsCl gradient containing equal parts of 1.1g/mL CsCl layered on top

of 1.3g/mL CsCl. Following ultracentrifugation (2 hours, 268000 ×g) the fraction containing the virus-like particles was collected and applied to a PD10 column containing Sephadex G100. The sample was eluted in 10 mM Tris and the particle containing fractions pooled and added to an isopycnic CsCl gradient containing 1.2g/mL CsCl. Following another ultracentrifugation (20 hours, 13000 ×g) the particle containing fraction was collected and applied to a Hiprep 16/60 Sephacryl S-500 HR gel filtration column and eluted in 10 mM Tris buffer.

2.5.2 R21 fluorescent labelling

R21 was labelled with Alexa Fluor 647 (AF-R21) to enable the loading and core size measurement post microfluidic encapsulation, adapting steps from the supplier's protocol [59]. Buffer exchange of a 0.5mL R21 stock solution (0.38mg/mL in Tris Buffer) was performed using an ultra-centrifugal filter unit (30kDa cut-off, Amicon, Sigma-Aldrich) centrifuged 3 times at 10000 ×g for 10 minutes at 4°C, using PBS as the replacing buffer. R21 in PBS was then mixed in a 0.5mL Eppendorf tube with 50µL of 4mg/mL Alexa Fluor 647 NHS ester suspended in DMSO (ThermoFischer), and vortexed for 30 seconds at 500 ×g. The labelling reaction was left to incubate on a rotating shaker for 1.5 hours at 30 rpm mix mode, at 28°C, protected from light. Removal of unreacted dye and washing of the labelled product was done by centrifugation 6 times with an ultra-centrifugal filter unit (30kDa cut-off, Amicon, Sigma-Aldrich) at 10000 ×g for 10 minutes at 4°C, using PBS. Labelled R21 was stored at -80°C.

2.5.3 LMQ adjuvant

The LMQ adjuvant used in this study was manufactured at the Vaccine Formulation Institute as described previously [60]. Briefly, LMQ adjuvant was prepared by incorporating QS21 saponin (Desert King International) and the synthetic TLR4 ligand 3D-6-acyl-PHAD (Merck-Avanti) to neutral liposomes composed of 1,2-dioleoyl-sn-glycero-3-phosphocholine (DOPC, Merck-Avanti) and cholesterol. LMQ was supplied in solution at fixed concentration of 80µg/mL of TLR4 agonist 3D6AP and 200µg/mL of QS21 saponin.

2.5.4 Preparation of R21 loaded LCSS particles

To produce R21 loaded LCSS particles, 200µL of AF-R21 solution was mixed with 800µL of R21 solution, reaching a final concentration of 0.3mg/mL unlabelled R21 in PBS. In the case of R21+LMQ loaded LCSS particles, 500µL of the previously described R21:AF-R21 solution was added to 500µL of LMQ reaching a final concentration of 0.15mg/mL unlabelled R21 in PBS. Either of these solutions were used as the inner core fluid for microfluidic double emulsification production. The inner core fluid was kept on ice in the dark during production. Middle and outer fluid formulations were identical to those described in section 2.2.1. Particles were collected in an open glass petri dish and transferred postproduction to 24mL glass vials filled with PBS to extract the DMC solvent. Extraction was performed over 48 hours at room temperature on a roller shaker, replacing the PBS extraction media every 12 hours. Particles were then filtered using mini cell strainers (100µm, pluriSelect) and stored in 4mL of PBS in Eppendorf tubes at 4°C.

2.5.5 Quality control and loading quantification of R21 loaded LCSS particles

Quality control of the produced particles was performed by microscopy image analysis described in section 2.4.1, measuring the loading percentage, core and particle diameters, eccentricity, and shell thickness of the batch, using the AF-R21 as the fluorescent marker inside the core.

Quantification of the encapsulated R21 was performed by mechanically breaking the LCSS particles after combining 300μL of the produced LCSS particle batch with 700μL of PBS. R21 loading was released from the LCSS particles by 30 seconds homogenisation with a cell homogenizer (Cole-Parmer) as illustrated in **Figure 2-4**. Released R21 was isolated from the PLGA particles debris by centrifugation at 15000 ×g for 10 minutes, and the supernatant concentration was determined using the micro–BCA Protein assay (ThermoFischer) by interpolation against a standard curve of R21.

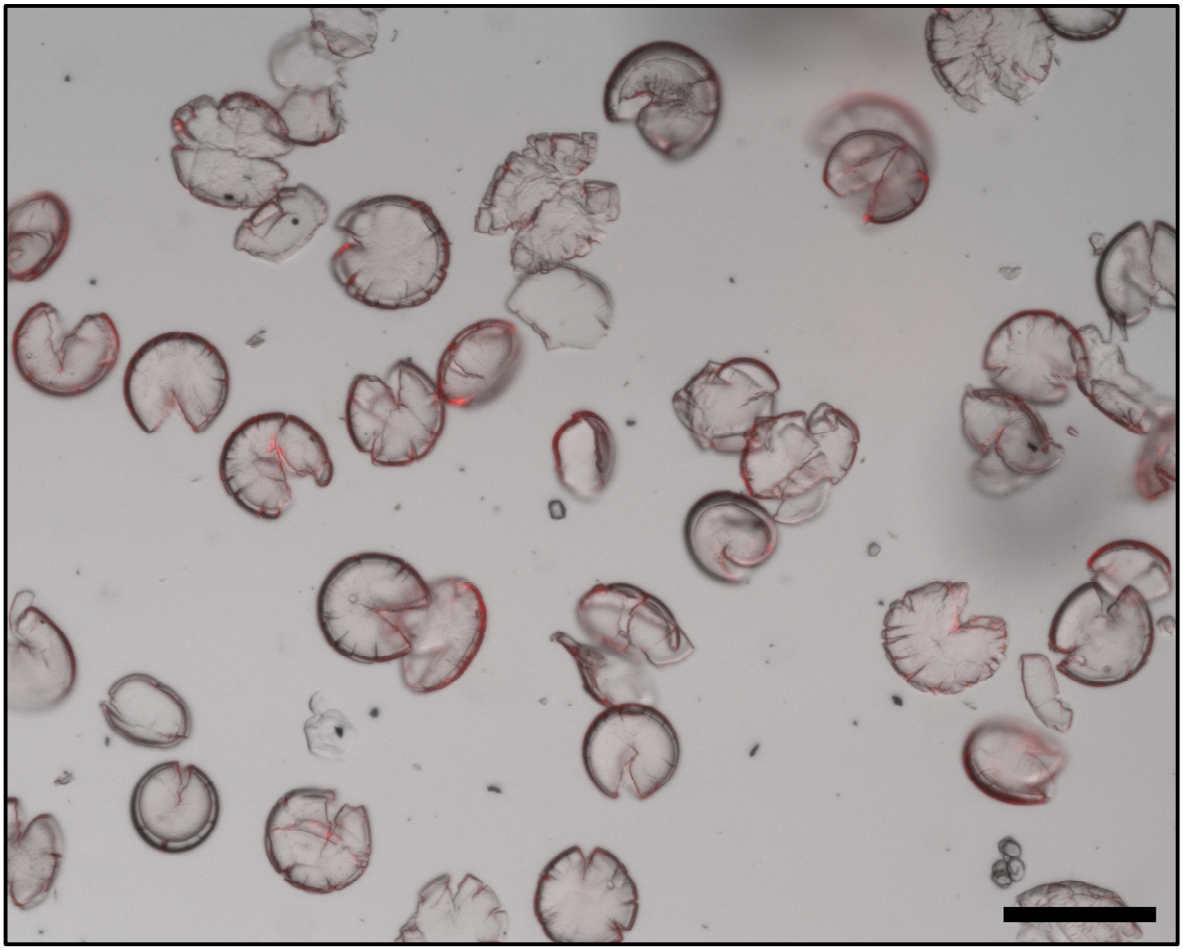

Figure 2-4: Mechanical homogenization of LCSS particles breaks up the solid PLGA shell and allows full release of the liquid core payload.

Microscopy image of LCSS particles loaded with a mix of AF-R21 and R21 (10X objective, AF and brightfield channels overlayed), produced by microfluidic double emulsification, and mechanically broken by 30 seconds of homogenisation. Black scale bar = 100µm.

2.5.6 Formulation of the R21 vaccine regimens

For R21 studies, vaccination doses were prepared by suspending the correct number of LCSS particles encapsulating the booster dose of R21 with the soluble antigen and adjuvant (LMQ) as the soluble priming dose) in 0.25% (w/v) medium viscosity carboxymethylcellulose (CMC, ref C4888, Sigma-Aldrich) depending on

the regimen. CMC was added as a viscoenhancer to prevent the early sedimentation of particles as described previously [61].

The different regimen contents are summarised in **Table 2-3**, and designated as soluble (sol) when suspended in media, or encapsulated (caps) when loaded in the particle core. In a Prime/Boost regimen the mice received two injections of soluble vaccine separated by a certain time interval, each of them corresponding to the Prime composition described in **Table 2-3**.

Table 2-3: Summary of immunisation regimen composition

Regimen	**R21 vaccine**	**LMQ adjuvant** *(optional)*	
		QS21	**TLR4 agonist**
Prime	1µg (sol.)	5µg (sol.)	2µg (sol.)
Prime - dose matched *(with Prime + Particle)*	2µg (sol.)	5.67µg (sol.)	2.27µg (sol.)
Particle	1µg (caps.)	0.67µg (caps.)	0.27µg (caps.)
Prime + Particle	1µg (sol.) 1µg (caps.)	5µg (sol.) 0.67µg (caps.)	2µg (sol.) 0.27µg (caps.)

2.5.7 Animal immunisations

For all experiments, mice were maintained at the animal facility either the Wellcome Centre for Human Genetics or the John Radcliffe Hospital, University of Oxford. Animals were housed under Specific Pathogen Free conditions and in accordance with the recommendations of the UK Animals (Scientific Procedures) Act 1986. Protocols were approved by the University of Oxford Animal Care and Ethical Review Committee for use under Project Licenses P9804B4F1 (Anita Milicic), or PP0984913B (Adrian Hill) granted by the UK Home Office.

Six to ten-week-old female inbred BALB/c mice (Envigo, UK) were immunised intramuscularly (IM) with a total volume of 50µL in the right tibialis muscle under 3% isoflurane anaesthesia. All injections were performed with 100µL Gas Tight glass syringes (ref 81020, Hamilton), with 1.40mm barrel inner diameter to improve the particle injectability, as previously described [50]. Glass syringes were sterilized with ethanol before use.

2.5.8 Live imaging of *in vivo* particle localisation

Following IM immunisation of BALB/c mice with ~ 50,000 LCSS particles loaded with 50mg/mL dextran-TRITC (40kDa, Sigma-Aldrich), mice were imaged at different timepoints to follow the evolution of the fluorescence coming from the site of injection using the IVIS imaging system (IVIS Spectrum in vivo imaging system, PerkinElmer). Mouse lower body fur which emits autofluorescence under IVIS imaging was removed before each imaging session by applying hair removal cream (Veet). Images were taken under 3% isoflurane anaesthesia, using excitation and emission filters of 520-550nm and 570-590nm, respectively.

2.5.9 ELISA for measuring antigen-specific antibody titres

Antigen-specific IgG ELISA to detect antibodies against the central repeat (NANP) or the C-terminal (C-term) regions of CSP was performed as previously described [58]. Serum was obtained by collecting blood from the lateral tail vein in a microcuvette tube. Blood was allowed to clot at 2 hours at room temperature before centrifugation at 10000 ×g for 4 minutes and sera removed and stored at −20 °C until use. Nunc-Immuno Maxisorp 96 well plates were coated with 2µg/mL $NANP_6$

peptide (Mimotopes, NANPNANPNANPNANPNANPNANPC) or 1µg/mL C-term peptide (ProImmune, EPSDKHIKEYLNKIQNSLSTEWSPCSVTCGNGIQVRIKPGSANKPKDELDYANDIE KKICKMEKCS) in carbonate-bicarbonate coating buffer overnight at 4 °C. Plates were washed with PBS-Tween (0.05% v/v) and blocked with 2% BSA in PBS-Tween for 1 hour at room temperature. Sera were serially diluted by 3-fold, between 1:100 and 1:24,300 in 1% BSA in PBS-Tween and added to plate in duplicates at the appropriate dilution for the vaccine regimen and timepoint. Plates were incubated for 1.5 hour at room temperature and washed as before. Fc-specific goat anti-mouse IgG conjugated to alkaline phosphatase (AP) (1:5000, Sigma-Aldrich, A1418), was added for 1 hour at room temperature. Following a final wash, plates were developed by adding p-nitrophenylphosphate at 1 mg/mL in diethanolamine buffer and OD was read at 405 nm. NANP or Cterm-specific IgG concentration in the sera were calculated as ELISA Units (EU) by interpolation against a standard curve of monoclonal 2A10 (MR4, MRA-183A) for NANP-specific or a serum pool of previously R21-immunised mice for C-term specific ELISA. Sera from naïve mice were used as negative control.

2.5.10 Production of transgenic sporozoites for malaria challenge

Malaria challenge of mice vaccinated with the R21 vaccine which encodes the *Plasmodium falciparum (Pf)* CSP was performed using previously constructed *Plasmodium berghei* (*Pb)* parasites carrying a copy of the *Pf* CSP gene. The *Pf* CSP is inserted into at the 230p locus under the control of the *Pb* UIS4 promoter

(*PfCSP(r)PbCSP* + *GFP::Luc@Pbeef1a_230p*), using the “gene insertion/marker out’ technology”[62].

Pb transgenic sporozoites for malaria challenge were produced by the Jenner Institute insectary as previously described [58]. In brief, starved female *Anopheles stephensi* mosquitoes were fed on BALB/c mice infected with the transgenic *Pb* parasites for approximately 10 minutes. The mosquitoes were maintained on Fructose/PABA solution at 19–21 °C in a humidified incubator on a twelve-hour day-night cycle.

Approximately 21 days after feeding, the mosquitoes were dissected, and the salivary glands removed and placed in RPMI-1640 media. The glands were disrupted with a tissue homogeniser to release the sporozoites which were then counted using a haemocytometer.

2.5.11 Malaria challenge

Malaria challenge was performed as described previously [58]. For all experiments 1,000 transgenic *Pb* sporozoites (described above) were injected intravenously (IV) in the total volume of 100 µL into the lateral tail vein of each mouse. From day 5 post challenge mice were monitored for parasitaemia in blood by thin-film blood smears, fixed in methanol and stained in 10% Giemsa for 30 min. Mice were sacrificed when >1% parasitaemia was observed. If no parasites were detected on day 12 after challenge, mice were considered sterilely protected.

2.6 Statistical Analysis

All statistical analysis was performed in R (version 4.2.1). Results were deemed to be statistically significant if $p<0.05$.

2.6.1 Production and *in vitro* experiments

Size distributions were represented by computing and plotting kernel density estimates. Coefficients of variation (CV) were computed as the ratio between standard deviation and mean of a distribution.

Relationship between set flow pressures and droplets/particles diameter were assessed by linear regression.

***In vitro* release longitudinal data** were analysed as described in section 4.2.

2.6.2 *In vivo* experiments

Non-inferiority was declared if the 95% confidence interval for a fold change was entirely above the non-inferiority threshold, which was set at 0.5 as reported in the literature [63], [64].

Analysis of observed peak antibody titres. Estimates of observed peak titre (geometric mean and geometric mean fold change), were obtained, with their CIs, from the corresponding bootstrap distributions. Geometric mean fold changes were calculated by bootstrapping differences of log-transformed titres and back-transforming the mean and CI of the bootstrap distributions. Bootstrapping was performed using the *boot* package (version 1.3-28) with 10000 resamples.

Permutation ANOVA was performed using the *lmPerm* package (version 2.1.0) for non-parametric comparison of multiple factors.

Analysis of immune kinetic profiles. As reported in the literature [65], [66] and advised for biological longitudinal studies [67], longitudinal antibody titres were fitted, after log-transformation, with a generalised additive model (GAM), using the *mgcv* package (version 1.8-40). Penalised cubic regression splines were used as smoother of the weekly timepoint covariate for each regimen with 10 knots placed evenly throughout the weekly values. Regimen was modelled as a fixed effect. Random intercept for each mouse and random effect of mice by week were also included to account for biological variability. In *mgcv* syntax:

```
Regimen + s(Week, by='Regimen', bs='cr') + s(ID, bs='re') + s(ID,
          Week, bs='re')
```

Estimates of peak antibody titres (geometric mean and geometric mean fold change) and time to 50% peak titre (mean and mean additional delay) were obtained, with their CIs, from the corresponding simulated sampling distributions. The sampling distributions were generated for each regimen, following [68], by repeatedly: 1) sampling from the multivariate normal posterior distribution of model coefficients, 2) predicting log titres at 0.01 week steps, 3) finding peak log titre and time to 50% peak titre on the predicted curve, and 4) where required, calculating differences between regimens (**Figure 2-5**). This process was repeated 10,000 times per regimen.

Time to infection analysis. Time to infection was determined by linear interpolation of parasitaemia between the last blood sample below 1% and the first blood sample above, to find the time corresponding to 1% parasitaemia. The time to infection data

were analysed by Cox regression using regimen and challenge session as covariates. Hazard ratios are adjusted for challenge session. Cox regression was performed using the *survival* package (version 3.2-13), Kaplan Meier plots were generated using the *survminer* package (version 0.4.9).

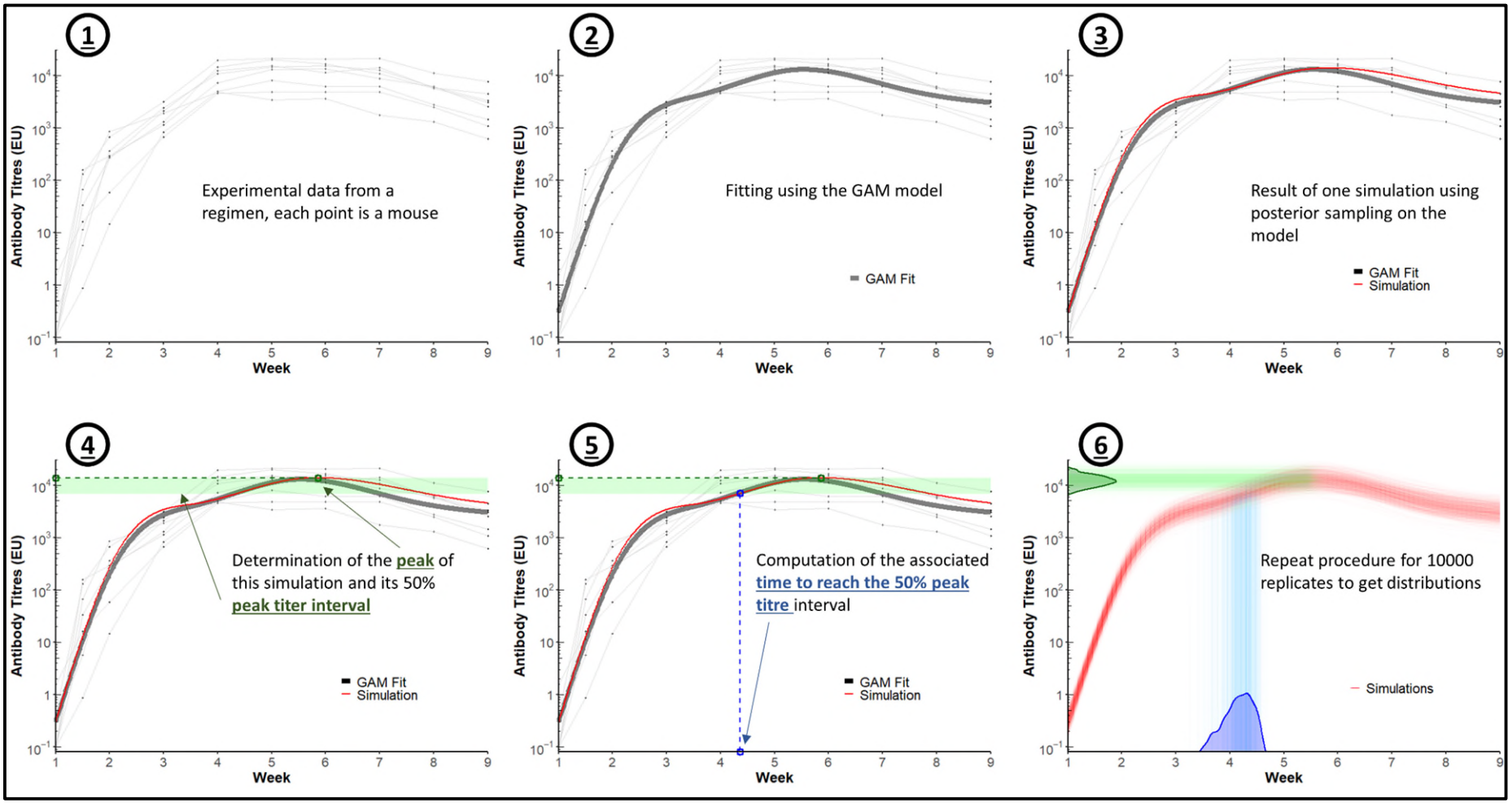

Figure 2-5: Estimation of peak titre and time to 50% peak titre by GAM posterior sampling simulations

3 Microfluidic production

3.1 Introduction

The production of uniform micrometre sized droplets is desirable for numerous applications in the food [69] and pharmaceutical industries [70], and in particular for drug delivery [71]. Droplet microfluidic techniques have emerged to fulfil this need [72].

Microfluidics refers to the movement and manipulation of small volumes of fluids, typically inside channels with dimensions scaling from a few micrometres to a millimetre [72]. Laminar flow is a key characteristic of microfluidic systems, due to the dominance of viscous forces over inertial forces. The Reynold number (Re):

$$Re = \frac{Inertial\ forces}{Viscous\ forces} = \frac{\rho\ * V * L}{\mu}$$

is used to describe the ratio of these forces, where ρ is the fluid density, μ is the fluid viscosity, V is the fluid velocity and L is the characteristic length. Due to microscopic channel dimensions in microfluidic chips, Re <2000 ensures laminar flow conditions [73] thus facilitating fluid manipulation. Multiple applications of microfluidics are derived from this property, in particular droplet fabrication.

Droplets can be formed by flowing two immiscible or partially miscible fluids so that they meet at an intersection. The droplet fluid is then named the “dispersed” phase while the surrounding phase is called “continuous” phase. Droplet generation requires favourable wettability between the channel walls and the continuous phase to ensure proper emulsification, meaning that microfluidic channels need to be

hydrophobic for Water-in-Oil (W/O) emulsions and hydrophilic for Oil-in-Water (O/W) emulsions [74].

Multiple systems to form droplets by microfluidics have been reported, but they can be categorised as two main strategies, capillary-based microfluidics and chip-based microfluidics.

Capillary-based droplet microfluidics require the radial alignment of glass capillaries, shaped to the correct dimensions e.g. by micropipette pullers [75]. During emulsification, the dispersed fluid is flown through a capillary embedded within a larger one carrying the continuous phase. Droplets are produced at the tip of the inner capillary when the two phases meet [76]. Due to the geometry and use of glass material, the emulsification process is robust for different flow formulations, and the wettability of the capillary surfaces can be chemically modified relatively easily [77]. Thus, these systems can produce single and double emulsions [78]–[80] as templates for polymeric particles and liquid core-solid shell capsules, e.g. using PLGA polymers commonly employed in drug delivery [80]–[83]. However, they suffer from several manufacturing limitations [77]. First, capillary-based systems require precise alignment making mass production challenging; second, they are very fragile due to the thin diameter of the capillaries used. Consequently, these systems offer poor reproducibility and scale-up potential, which limits their use to dedicated research laboratories.

Chip-based microfluidics use glass or more commonly polydimethylsiloxane (PDMS) blocks to house channels created via lithography and/or moulding techniques [84], [85]. To form droplets in PDMS chips, different intersection designs have been reported, flow focusing (FF) being one of the most frequently used,

offering control over a wide particle size range and rate of generation. In FF, droplet formation can occur when the viscous shear strain applied by the continuous phase temporarily overcomes the interfacial tension of the dispersed phase, resulting in a periodic break-up of the dispersed fluid stream. This is the so called “dripping” regime [86], [87]. A “jetting” regime can also be observed when the viscous drag of the continuous phase or the inertia of the dispersed phase overcomes interfacial tension. The dispersed flow no longer drips at the intersection but forms a jet that eventually breaks into droplets as a result of Rayleigh Plateau instabilities [87]. These instabilities occur when a perturbation at the interface between the dispersed phase jet and the surrounding continuous phase produces tiny fluctuations of the jet diameter, forming thinner and larger diameter regions. Due to the increased Laplace pressure in the thinner regions, the dispersed phase is pushed toward the lower pressure larger regions, accentuating the thinning of the high-pressure regions and the amplitude of the fluctuations. Ultimately, a neck, that cannot withstand the interfacial tension with the continuous phase, breaks, forming droplets at a certain distance of the jet [88], [89].

Such systems have been extensively used to produce W/O and O/W droplets and adding successive FF intersections with appropriate channel wettability enables the production of Water-in-Oil-in-Water (W/O/W) double emulsions [90]–[92]. Due to the highly reproducible manufacturing process, chip-based system can be easily parallelised to achieve kilo-scale throughput of emulsions [93]–[95]. However, whist the production of single phase PLGA particles from single emulsions in PDMS microfluidic chips has been widely reported [96], [97], the production of liquid core - solid PLGA shell particles from double emulsions with similar techniques remains

challenging. The use of PLGA dissolved in organic solvents as the middle fluid in the W/O/W emulsification adds several constraints:

- The higher viscosity of the middle fluid due to the polymer can inhibit droplet formation[98].
- The tendency of organic solvents to swell PDMS channels which shrink and clog, preventing droplet formation [99], [100].
- Hardening of the middle phase due to solvent extraction can cause clogging of the microfluidic chips.

For these reasons, no consistent method has been reported to produce W/O/W emulsions in a PDMS chip-based microfluidic system to produce aqueous LCSS particles. This has prevented their evaluation in delayed delivery applications such as vaccination.

In this chapter, the experimental development of a system that overcomes these constraints is presented, together with the evaluation of achievable size, loading and generation frequency of the double emulsions, and the resulting LCSS particles. The optimisation of different parameters to stabilise the process and increase the production rate is also reported.

3.2 Results

3.2.1 Identifying the correct parameters to produce double emulsions

In this section, the different parameters affecting the microfluidic production of double emulsions are investigated, including the surface treatment of PDMS, the selection of the correct solvent/PLGA combinations and the geometry of the microfluidic chip.

3.2.1.1 PVA treatment enables the hydrophilic coating of PDMS

Crosslinked PDMS is hydrophobic, which allows the generation of W/O emulsions in PDMS chips but in the case of W/O/W emulsions, the second FF intersection and downstream channels need to be hydrophilic. A polyvinyl alcohol (PVA) treatment protocol has been reported in the literature [55] and its ability to achieve hydrophilic coating of PDMS was verified by measuring contact angle with a 10µL drop of water (**Figure 3-1**) at different times following the treatment.

Untreated PDMS demonstrated a constant high contact angle, >100°, throughout the experiment, while O_2-Plasma treatment (a necessary step to bond and seal the PDMS chip during manufacturing) resulted in a temporary hydrophilic PDMS surface (22 +/- 5° at 3 hours following treatment) that subsequently recovered its hydrophobic properties (95 +/- 7° at 96 hours following treatment). In contrast, additional treatment with PVA following O_2-plasma (see protocol in Methods) resulted in a PDMS surface that retained its hydrophilicity after 96 hours, with a contact angle of 38 +/- 5° at 96 hours following treatment (**Figure 3-1.B**).

In the subsequent sections of this chapter, the PVA treatment was used to coat the second intersection of all W/O/W PDMS chips using flow containment (see section 2.1.4, partially hydrophilic surface treatment).

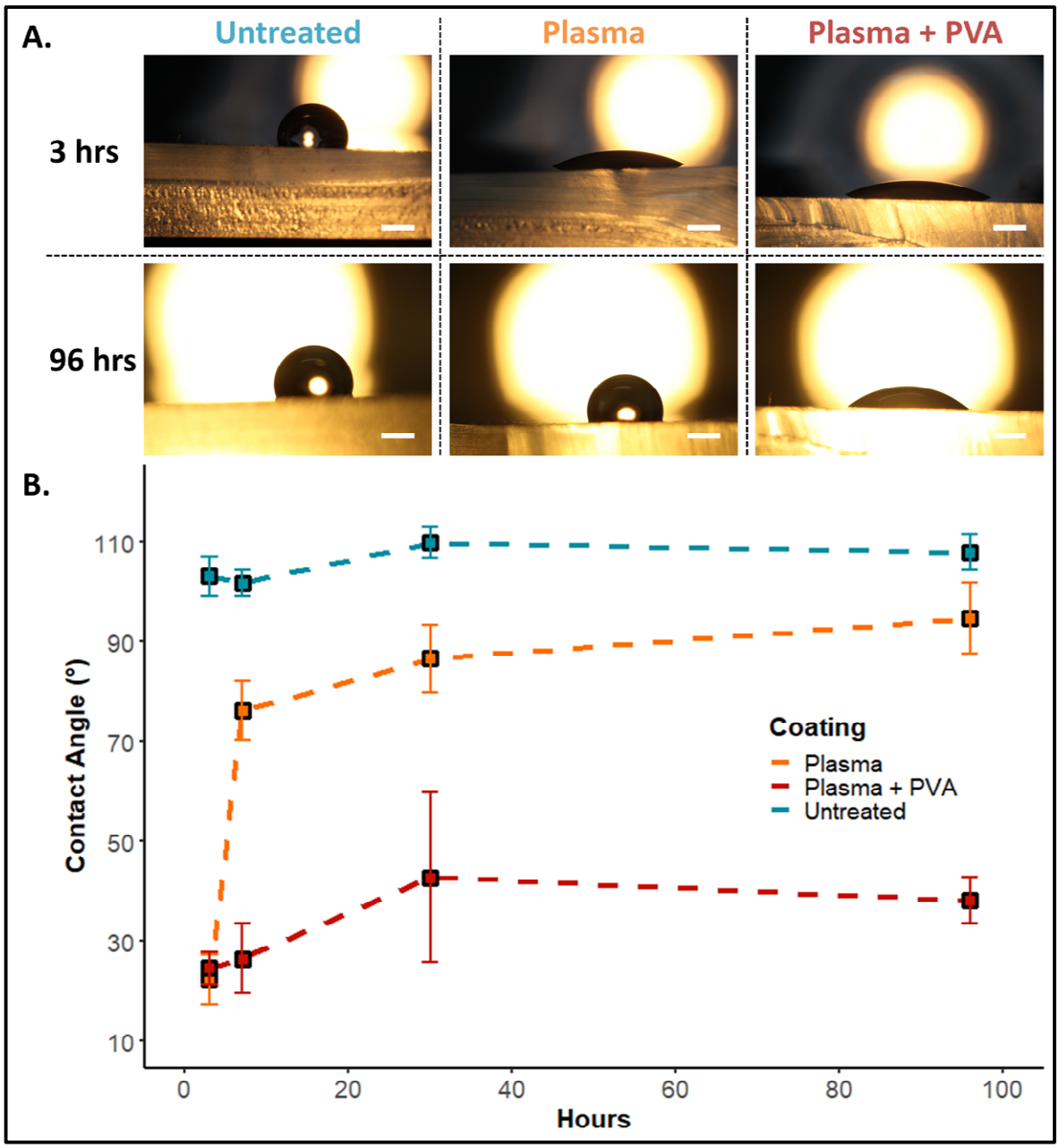

Figure 3-1: PVA treatment of PDMS surface provides a long-lasting hydrophilic coating.

(A) Images (Nikon photography camera) of 10µL water drop on PDMS slabs taken 3 hours (first row) or 96 hours (second row) following different treatments (untreated, O2-plasma treated, or O2-plasma + PVA treated), using a backlight as contrast enhancer for contact angle measurements (white scale bar = 1mm). (B) Evolution of the contact angle of a 10µL water drop with PDMS measured manually by image processing (Fiji) at different times following different treatments (n=4 per time and treatment, square markers show the mean of replicates, error bars indicate +/- SD).

3.2.2 DMC solvent and PLGA with an ester end cap are compatible with the microfluidic double emulsification process

Organic solvents are essential to dissolve the water insoluble PLGA polymer that will ultimately constitute the hard-shell surrounding the liquid core in LCSS particles, but these solvents also tend to swell PDMS, hindering the emulsification process [99]. Hence the choice of organic solvent was a key parameter for the development of this process. Dichloromethane (DCM) has been extensively used in capillary-based microfluidics, and in the production of single phase PLGA particles in single O/W emulsion PDMS-based microfluidics [81], due to its immiscibility with water, ability to dissolve PLGA and volatility that facilitates solvent removal. For both applications, the glass material of the capillaries or the coating of PDMS required for O/W emulsion prevented the swelling. However, in the case of a W/O/W emulsification in a PDMS chip, the first intersection, where the W/O emulsion occurs, remains uncoated. Thus, when testing W/O/W with DCM as the solvent, deformation and swelling of the channels at the first intersection was observed, impairing the formation of the water core (**Figure 3-2.A** -DCM**).** In a W/O emulsification using an uncoated PDMS chip, DCM diffusion was visible inside the channel walls when Nile Red dye was added to the organic phase, causing the channels to shrink, and the PLGA to harden inside the chip (**Figure 3-2.B** -DCM). In contrast, when using dimethyl carbonate (DMC), a green solvent (i.e. non-toxic and biodegradable in the atmosphere) partially miscible with water that can also dissolve PLGA and is extractible [97], both W/O and W/O/W were successfully produced in PDMS chips (**Figure 3-2** -DMC). When combined with Nile red dye,

DMC did not display any signs of diffusion. Thus, DMC was chosen as the solvent for the development of the double emulsification process.

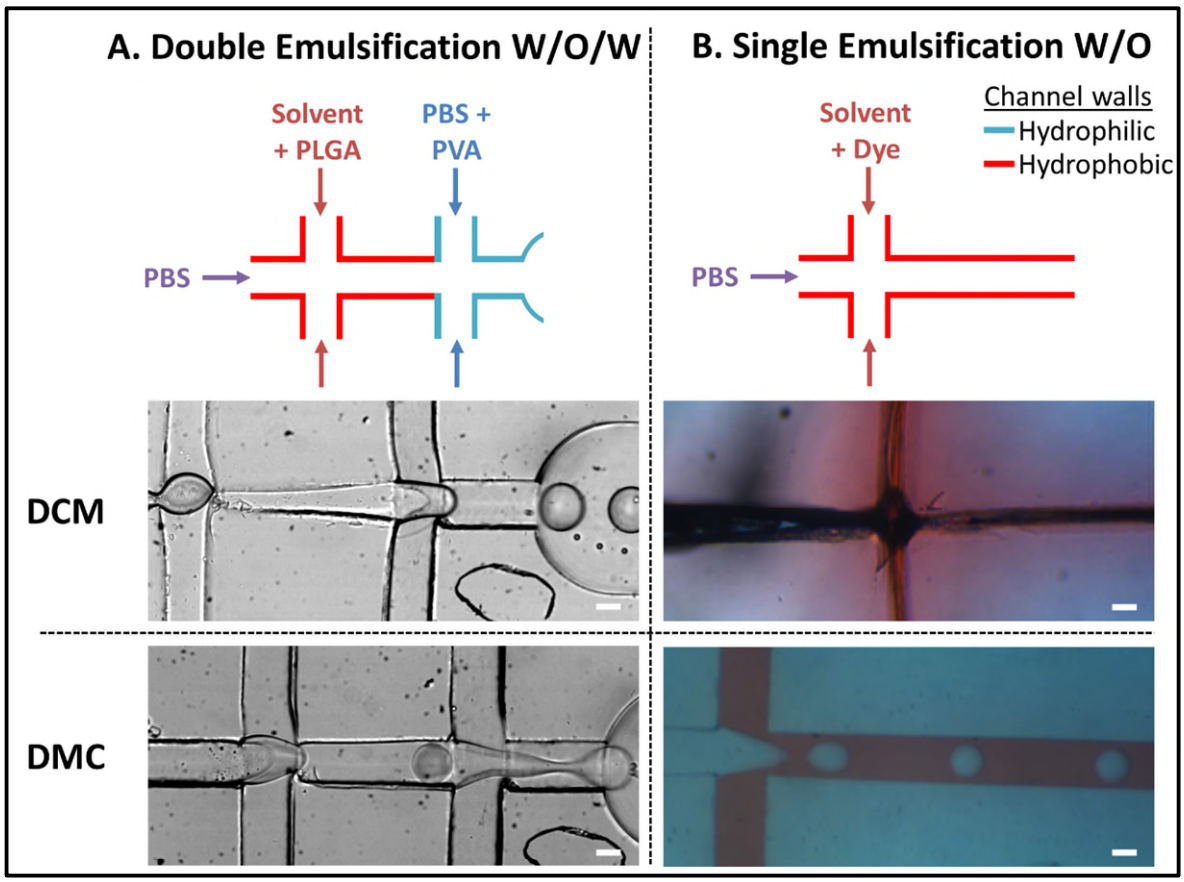

Figure 3-2: Dimethyl carbonate (DMC) is compatible with single and double emulsification in PDMS microfluidic chips, unlike dichloromethane (DCM).

Microfluidic process of (A) double Water-in-Oil-in-Water (W/O/W) emulsification and (B) single Water-in-Oil (W/O) emulsification. First row illustrates the design of the microfluidic channels, the coating pattern and the flow composition and direction. Microscopic brightfield images (inverted Nikon microscope, colour camera) of the running microfluidic emulsification process using dichloromethane (DCM, second row) or dimethyl carbonate (DMC, third row) as the oil phase solvent with 5% (w/v) PLGA. Nile red dye was added to the outer phase for the W/O single emulsification to highlight solvent diffusion in PDMS and swelling. White scale bar = 100µm.

PLGA, the polymer of interest for the elaboration of the LCSS particles, has 3 main tuneable characteristic that modify its degradation rate: molecular weight (Mw), Lactide:Glycolide ratio (L:G) and the “end cap” (a molecular moiety which can be a

carboxylic acid or an ester) [101] . Different PLGA types were used in a O/W single emulsification process to characterise the effects of these parameters on the ability to perform microfluidic emulsification. Changes in L:G did not impact the emulsification, and the higher viscosity of higher Mw solutions could be overcome by reducing the PLGA concentration. However, when testing PLGAs of identical Mw and L:G but different end cap, the acidic end cap was found to produce emulsions that lost their sphericity in the channel, forming long tails and adopting a cylindrical shape that would be detrimental to maintaining a core inside in the case of a W/O/W emulsification (**Figure 3-3.B**). On the other hand, the ester end cap PLGA could form spherical droplets that kept their shape through the microfluidic process (**Figure 3-3.C**). Hence, ester end cap PLGA polymers were used for the work in this thesis.

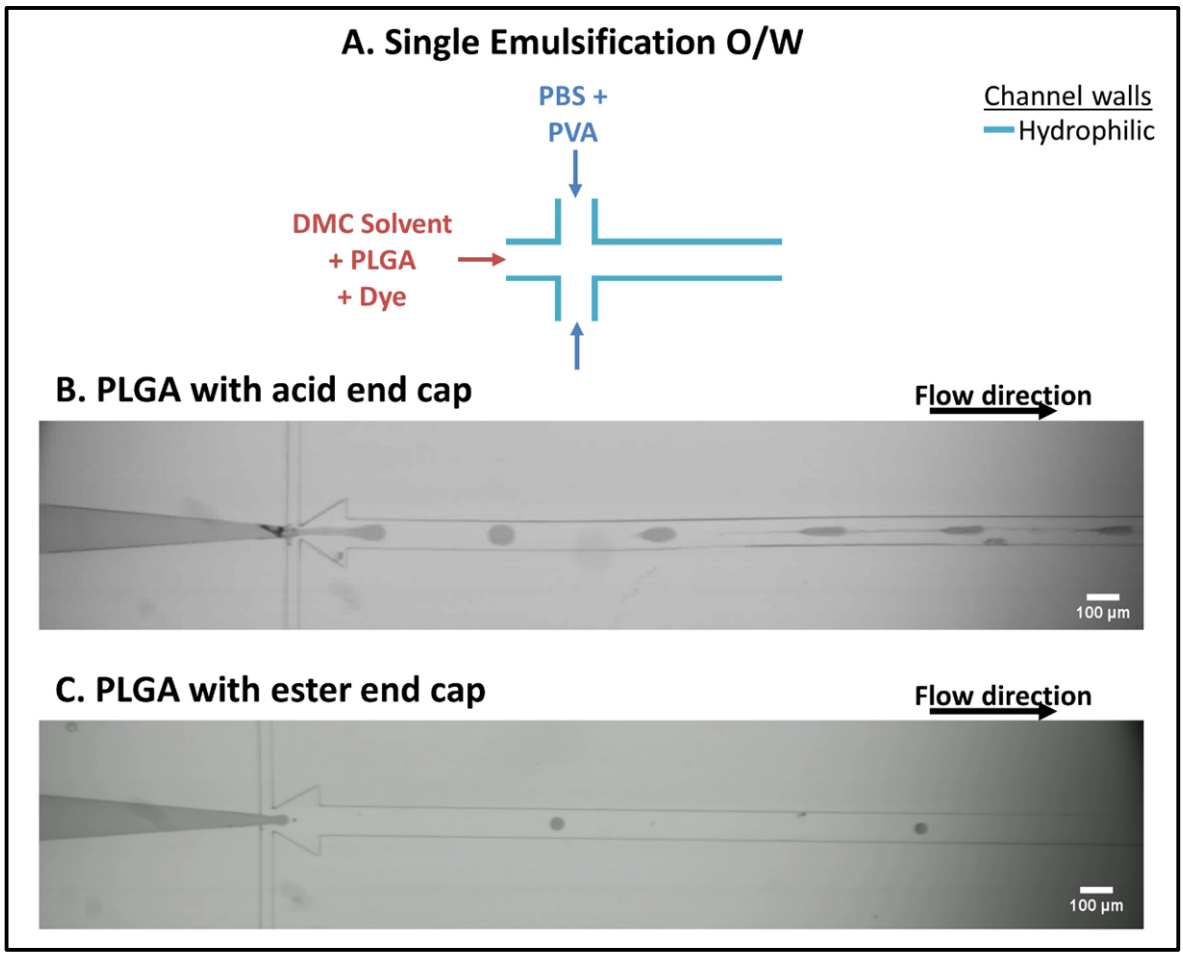

Figure 3-3: PLGA with an ester end cap was found to generate spherical droplets unlike acid end cap PLGA.

(A) Design, coating pattern and flow composition used for single Oil-in-Water (O/W) microfluidic emulsification.

(B-C) Microscopic brightfield images of the running microfluidic O/W emulsification process using 10%(w/v) (B) acid end cap PLGA, or (C) ester end cap PLGA as the polymer in the DMC solvent oil phase (high-speed camera, 4X objective, 5000fps). Nile red dye was added to the solvent oil phase to enhance imaging contrast.

3.2.3 A stepped channel design is essential in forming loaded, monodispersed, liquid core – solid PLGA shell particles

Using the above identified parameters, double W/O/W emulsification was first tested in a PDMS chip device using a conventional flat design [102] with sequential FF geometries (**Figure 3-4.A**). The double emulsion process appeared stable, producing consistent single core loaded droplets (**Figure 3-4.B**). However, once encapsulated, the water cores were seen to migrate towards the rear of the outer droplet (**Figure 3-4.B** -higher magnification). This was attributed to internal flow inside the compressed outer droplet as reported in the literature [103]–[105]. Once collected and solidified by DMC extraction, only 10% of the resulting particles exhibited a LCSS architecture, the rest being single phase PLGA particles (**Figure 3-4.C**). This indicates that the aqueous core was lost during the process, potentially pushed out of the outer droplet by the internal flows whilst flowing through the channel (**Figure 3-4.B** -higher magnification).

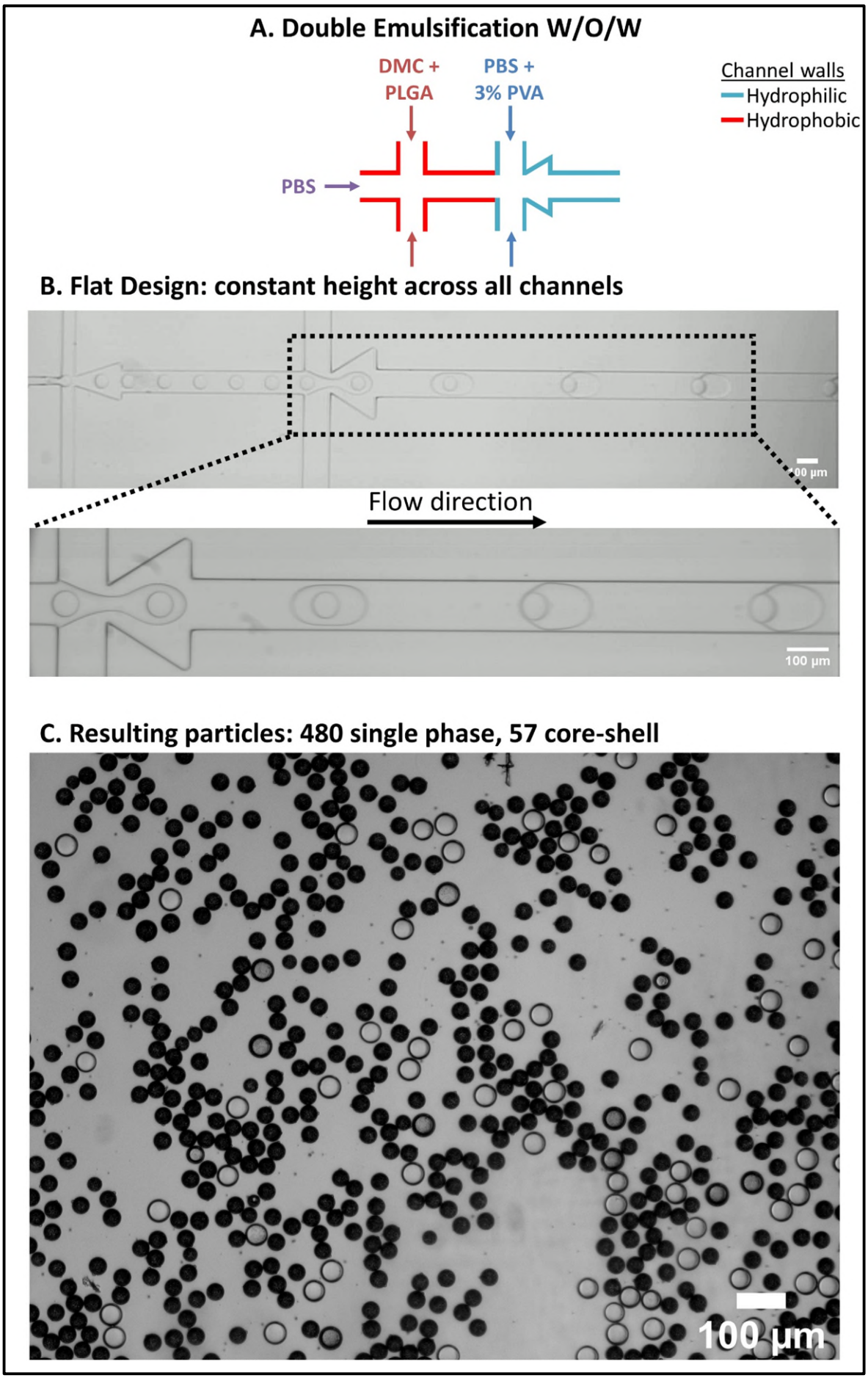
A. Double Emulsification W/O/W
DMC + PLGA
PBS + 3% PVA
PBS
Channel walls
Hydrophilic
Hydrophobic
B. Flat Design: constant height across all channels
Flow direction
100 µm
C. Resulting particles: 480 single phase, 57 core-shell
100 µm

Figure 3-4: Flat microfluidic channel design for double emulsification fails to produce efficient loading of liquid core - solid PLGA shell particles.

(A) Design, coating pattern and flow composition used for the W/O/W emulsification process.

(B) Microscopic images of the running microfluidic W/O/W emulsification process (high-speed camera, 4X and 10X objectives, 5000fps). Inner, middle, and outer flows were formulated with PBS, 10% (w/v) PLGA in DMC and 3% (w/v) polyvinyl alcohol (PVA) in PBS, respectively. Flow direction is indicated by black arrows.

(C) Microscopic brightfield image (10X objective) of the resulting particles produced by the W/O/W process following DMC extraction and suspension in PBS. Single phase solid PLGA particles appear dark, while liquid water core - solid PLGA shell particles appear clear with a dark surrounding ring. White scale bars = 100µm.

In order to reduce the accumulation of the core at the rear of the double emulsion and to understand this unloading phenomenon, a W/O/W emulsification was conducted in flat design with a widening collection chamber, reducing the flow speed of the double emulsions and allowing monitoring of the process in real time (**Figure 3-5.A**). Dextran-TRITC was used in the core aqueous phase to enable separate sizing of the core and the particles postproduction, and quantification of loading (**Figure 3-5.B**).

It was found that even if both the core and outer droplet were formed in a stable dripping regime at both intersections (**Figure 3-5.C**), two phenomena were observed that impaired the loading and size distribution of the resulting particles: bursting (**Figure 3-5.C** -red square) and splitting (**Figure 3-5.C** -blue square).

In the case of bursting, the aqueous core migrated to the rear of the outer droplet until the interface could not prevent the core merging with the aqueous outer phase, leaving a solvent/PLGA droplet (**Figure 3-5.D**) that would become a single phase PLGA particle once the solvent was extracted.

In the case of splitting, the outer droplet was split before the bursting of the core, resulting in a thinner shell double emulsion and a separated solvent phase droplet (**Figure 3-5.E**). Both phenomena impacted the loading and size distribution of the resulting solidified particles (**Figure 3-5.F-G**). Thus, the observed loading was only 55.8%, meaning that half of the encapsulated core material was lost, and the particles presented a broad size distribution with coefficients of variation (CV) of 15.5% and 24.1% for the core and particle diameters, respectively.

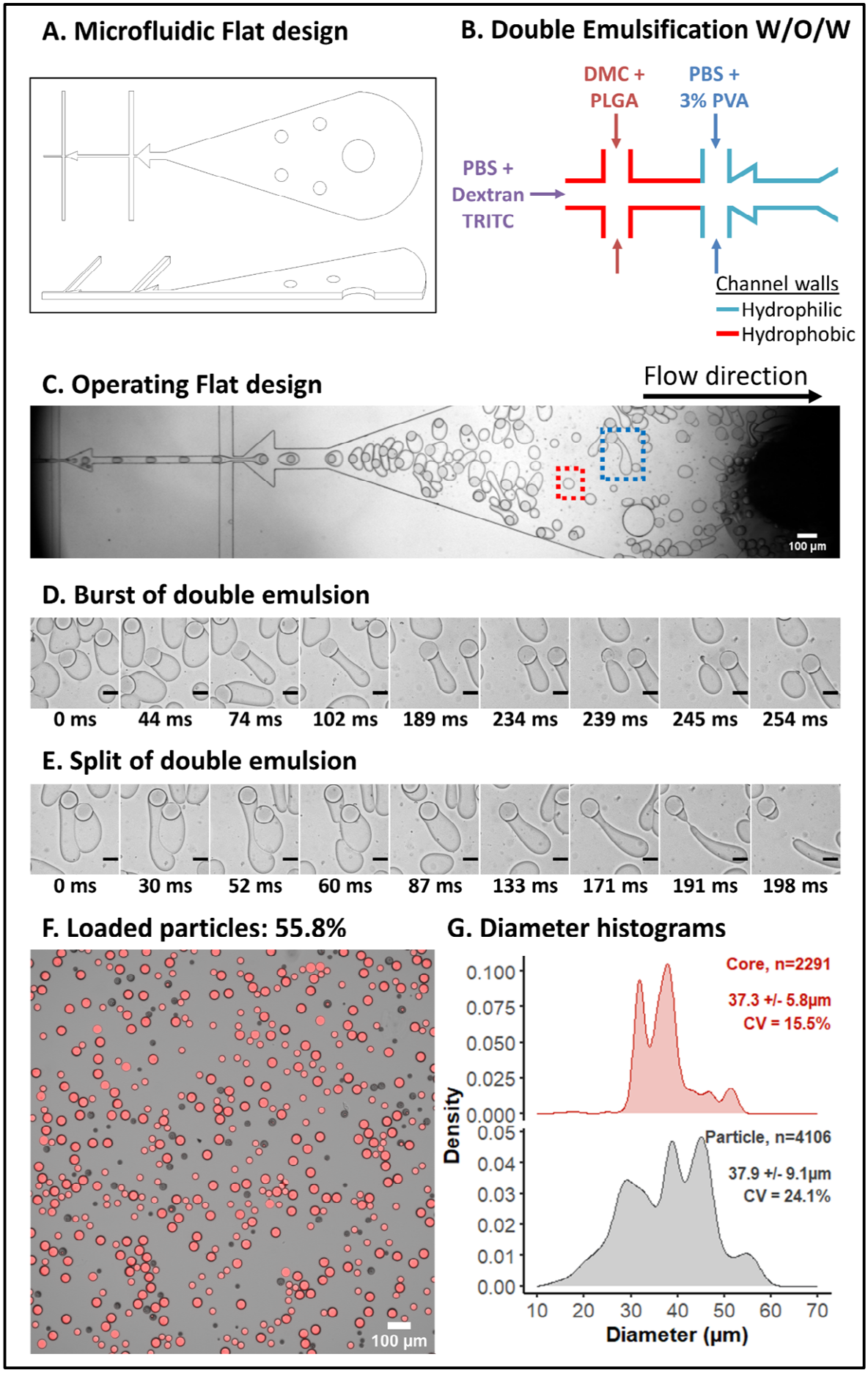
A. Microfluidic Flat design
B. Double Emulsification W/O/W
DMC + PLGA
PBS + 3% PVA
PBS + Dextran TRITC
Channel walls
Hydrophilic
Hydrophobic
C. Operating Flat design
Flow direction
100 µm
D. Burst of double emulsion
0 ms
44 ms
74 ms
102 ms
189 ms
234 ms
239 ms
245 ms
254 ms
E. Split of double emulsion
0 ms
30 ms
52 ms
60 ms
87 ms
133 ms
171 ms
191 ms
198 ms
F. Loaded particles: 55.8%
100 µm
G. Diameter histograms
Core, n=2291
37.3 +/- 5.8µm
CV = 15.5%
Particle, n=4106
37.9 +/- 9.1µm
CV = 24.1%
Density
Diameter (µm)

***Figure 3-5: Flat microfluidic design induces burst and splitting of double emulsions that result in a wide particle size distribution and poor loading**.*

(A) Top view and cross section of the flat W/O/W design used.

(B) Design, coating pattern and flow composition used for the W/O/W emulsification process.

(C) Microscopic image of the running microfluidic W/O/W emulsification process (high-speed camera, 4X objective, 5000fps). Inner, middle, and outer flows were formulated with dextran-TRITC in PBS, 17.5% (w/v) PLGA in DMC and 3% (w/v) polyvinyl alcohol (PVA) in PBS, respectively. Red and blue dotted squares illustrate bursting and deformation events respectively.

(D-E) Time sequential microscopic images following the (D) bursting or (E) splitting of an individual double emulsion during the microfluidic W/O/W process in a flat design, taken by high-speed camera (5000fps). Time indicated in milliseconds (ms), black scale bar = 50µm.

(F) Microscopic fluorescent image (10X objective) of the resulting particles produced by the W/O/W process and encapsulating dextran-TRITC following DMC extraction and suspension in PBS. TRITC and brightfield channels are overlayed.

(G) Corresponding collected LCSS particles features distribution (core - red, outer particle – grey) at different production times. Data was measured from 9 fluorescent microscopy images of the liquid core - solid PLGA shell particles population by MATLAB custom script (see Methods), plotted as kernel density estimation plots (R). Number of particles n used for distribution kernels are displayed for both features. Core size was measured for loaded particles only (fluorescence level above 500MFI threshold).

To overcome these issues, in particular the compression of the droplets inside the microfluidic chip, a step up in the channel height was introduced at the second FF intersection (**Figure 3-6.C** -red square), creating an asymmetric geometry (**Figure 3-6.A**). Using this new design, aqueous cores were formed in a dripping regime at the first FF intersection and outer droplets were formed in a jetting regime at the second FF intersection (**Figure 3-6.C**). As highlighted by the sequential image monitoring of producing a double emulsion (**Figure 3-6.D**), the absence of compression due to the change in height after the step allowed the particles to conserve their sphericity and prevented the core from bursting out. As a result, the

collected and solidified particles had the desired, uniform, LCSS architecture (**Figure 3-6.E**) with loading efficiency of 99.9% and high monodispersity (**Figure 3-6.F**) with CV of 5.4% and 1.3% for the core and particle diameters respectively. Accordingly, step designs were used for the rest of the work presented in this thesis.

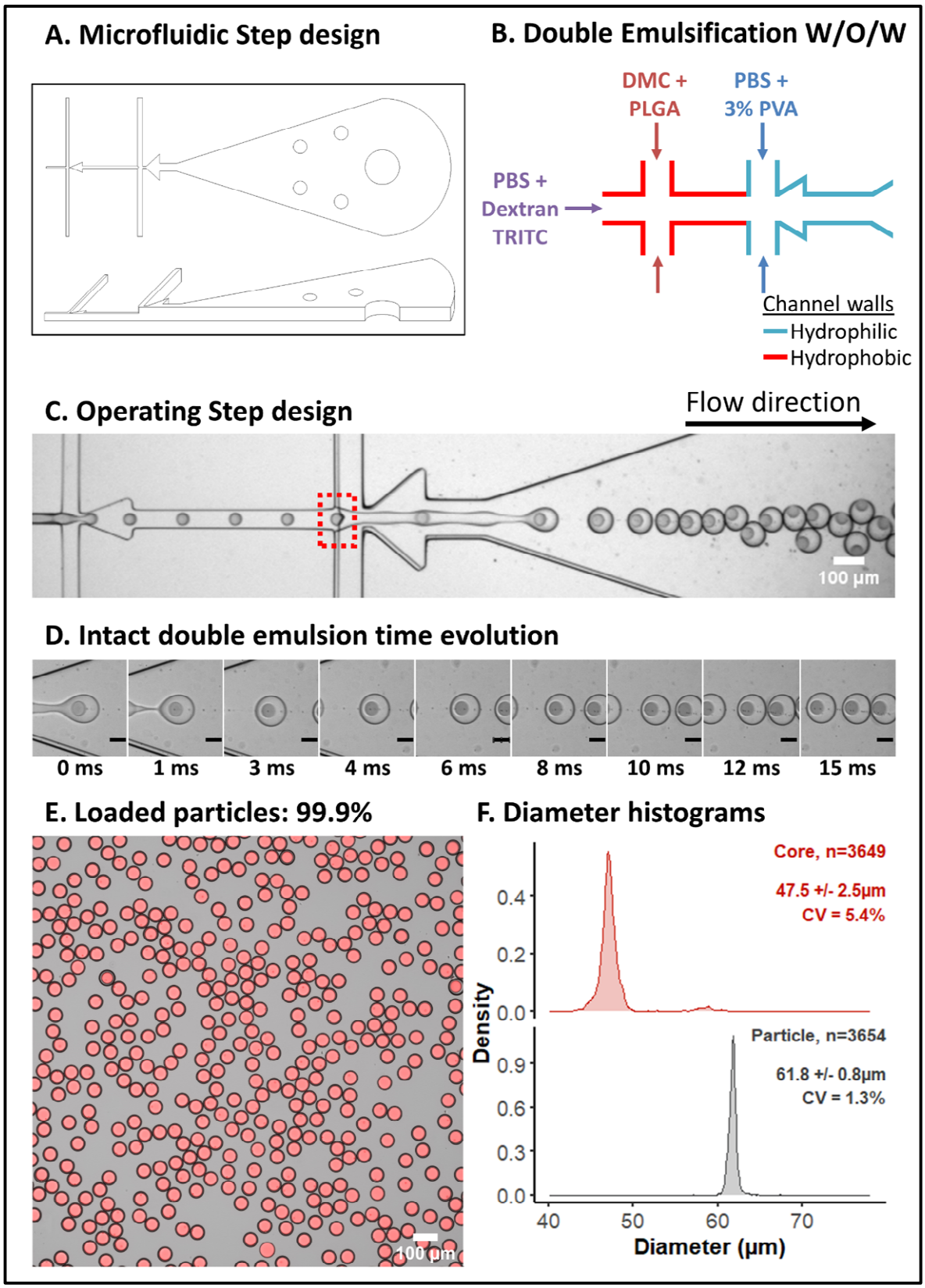

Figure 3-6: Stepped microfluidic design allows production of highly monodispersed and fully loaded liquid core - solid shell PLGA particles.

(A) Top view and cross section of the height asymmetric, stepped W/O/W design.

(B) Design, coating pattern and flow composition used for the W/O/W emulsification process.

(C) Microscopic image of the microfluidic W/O/W emulsification process (high-speed camera, 4X objective, 5000fps). Inner, middle, and outer flows were formulated with dextran-TRITC in PBS, 17.5% (w/v) PLGA in DMC and 3% (w/v) polyvinyl alcohol (PVA) in PBS, respectively. Red dotted square indicates the position of the step (change in height) in the channel.

(D) Time sequential microscopic images (high-speed camera, 10X objective, 5000fps) following an individual double emulsion during the microfluidic W/O/W process in a step design. Time indicated in milliseconds (ms), black scale bar = 50µm.

(E) Microscopic fluorescent image (10X objective) of the resulting LCSS particles produced by the W/O/W process and encapsulating dextran-TRITC following DMC extraction and suspension in PBS. TRITC and brightfield channels are overlayed.

(F) Size distribution (core - red, outer particle – grey). Data were measured from 9 fluorescent microscopy images of the liquid core - solid PLGA shell particles population by MATLAB custom script (see Methods), plotted as kernel density estimation plots (R). Number of particles n used for distribution kernels are displayed for both features. Core size was only measured for loaded particles (fluorescence level above 500MFI threshold).

3.2.4 Understanding the mechanism of double emulsification in the stepped chip design

To further investigate the double emulsification mechanism in the stepped chip design, high speed videos were used to monitor the emulsification at the second FF intersection.

As shown in **Figure 3-7** , the middle flow (DMC + PLGA) formed a jet containing the aqueous cores produced at the first FF intersection, arising from the inertial force of the middle flow overcoming the interfacial tension with the outer aqueous flow. As detailed in the Introduction of this Chapter, in the jetting regime, growing Rayleigh-Plateau instabilities ultimately induce the formation of droplets downstream of the intersection, with higher dispersity than the dripping regime. However, in the case of the stepped design, the arrival of a core droplet (**Figure 3-7** -blue dot) at the

intersection at t=0ms, and its passing through the nozzle, triggered an instability across the jet. Thinner regions of high pressure (**Figure 3-7** -red arrow) and larger regions of low pressure (**Figure 3-7** -green arrow) were formed across the jet and induced the necking and breaking of the jet to form a double emulsion containing the preceding core at t=7ms. Due to the periodic arrival of cores, the instabilities induced were regular and the formation of the double emulsion uniform.

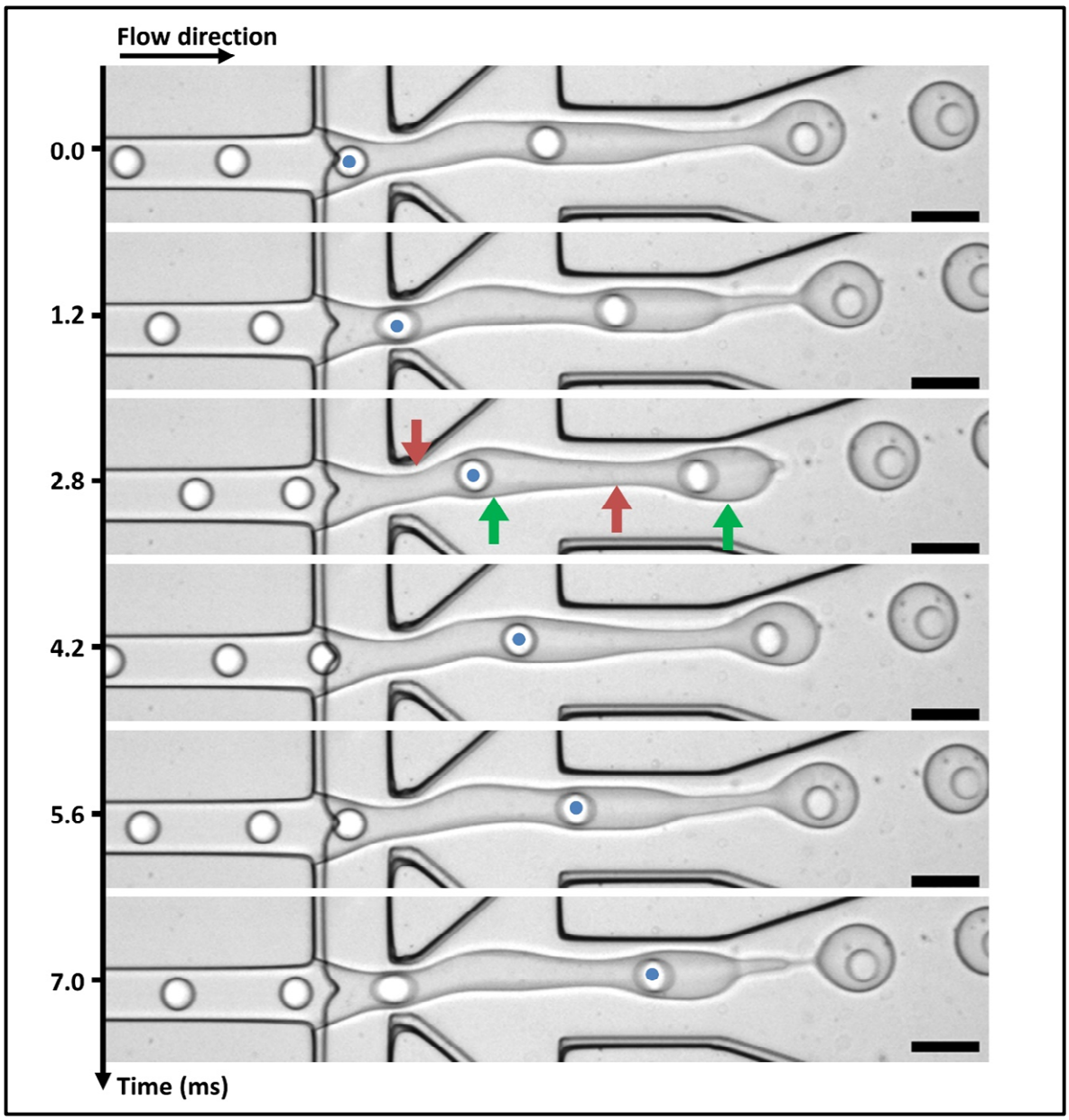

Figure 3-7: Stepped microfluidic design produces double emulsions by jetting and induction of Rayleigh-Plateau instability.

Time sequential microscopic images (high-speed camera, 10X objective, 5000fps) of the formation of the second emulsion in the W/O/W process in a step design. Inner, middle, and outer flows were formulated with dextran-TRITC in PBS, 17.5% (w/v) PLGA in DMC and 3% (w/v) polyvinyl alcohol (PVA) in PBS, respectively. Blue dots identify an individual core, red and green arrows indicate thinner and thicker regions of high and low pressure, respectively. Black scale bar = 100µm.

To confirm that the formation of double emulsion was triggered by the passing of the inner core, a similar W/O/W emulsification was conducted, but the inner fluid pressure was reduced in order to prevent the formation of cores at the first intersection (inner fluid pressure of 46.5 mbar in this case). As a result, the middle flow formed an uninterrupted jet (**Figure 3-8**).

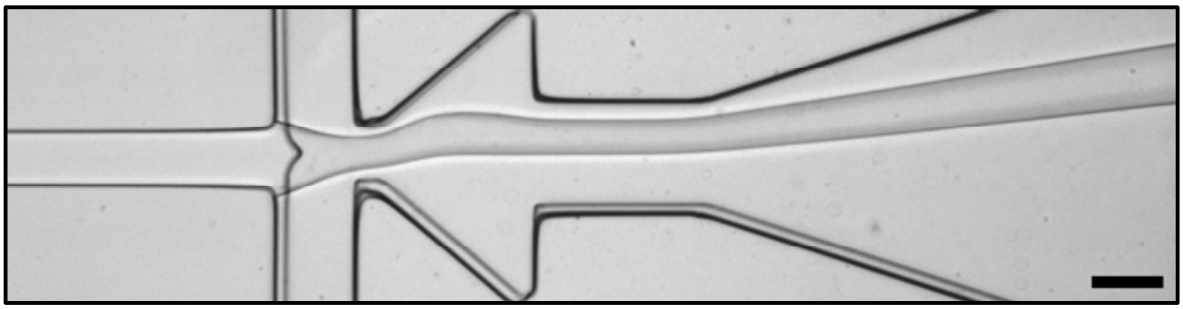

Figure 3-8: The absence of passing core results in an uninterrupted jet in step designs.

Microscopic images (high-speed camera, 10X objective, 5000fps) of the jetting occurring during the W/O/W process in a step design when no cores are passing. Inner, middle, and outer flows were formulated with dextran-TRITC in PBS, 17.5% (w/v) PLGA in DMC and 3% (w/v) polyvinyl alcohol (PVA) in PBS, respectively. Inner, middle, and outer fluid pressures were 46.5, 155 and 300 mbar respectively. Black scale bar = 100µm.

Then the inner fluid pressure was increased to a known working pressure for double emulsification (52.5 mbar in these conditions) and the transition was monitored with a high-speed camera. During this transition, the evolution of the inner core diameter,

the resulting outer droplet diameter (during double emulsification) and the jet variation (i.e. the difference in jet diameter between the narrower and wider regions of the perturbation, as identified in **Figure 3-7**), were measured. These are plotted in **Figure 3-9.A**.

There was no perturbation of the jet for the first 200ms of the transition, as no cores reached the intersection during this time. When the first cores arrived, due to their small diameter (starting around 35μm), they only induced small variations of about 5μm in the jet which quickly recovered its stability (**Figure 3-9.B**). As the frequency and diameter of passing cores increased (diameter = 45μm), however, the jet perturbation also increased and became permanent, although not sufficient to induce the breakup of the jet into a double emulsion (**Figure 3-9.C**). For this diameter of jet, the double emulsification only occurred once the cores reached diameters >50μm, and the jet perturbation exceeded a threshold of 20μm, triggering permanent necking and break up (**Figure 3-9.D**).

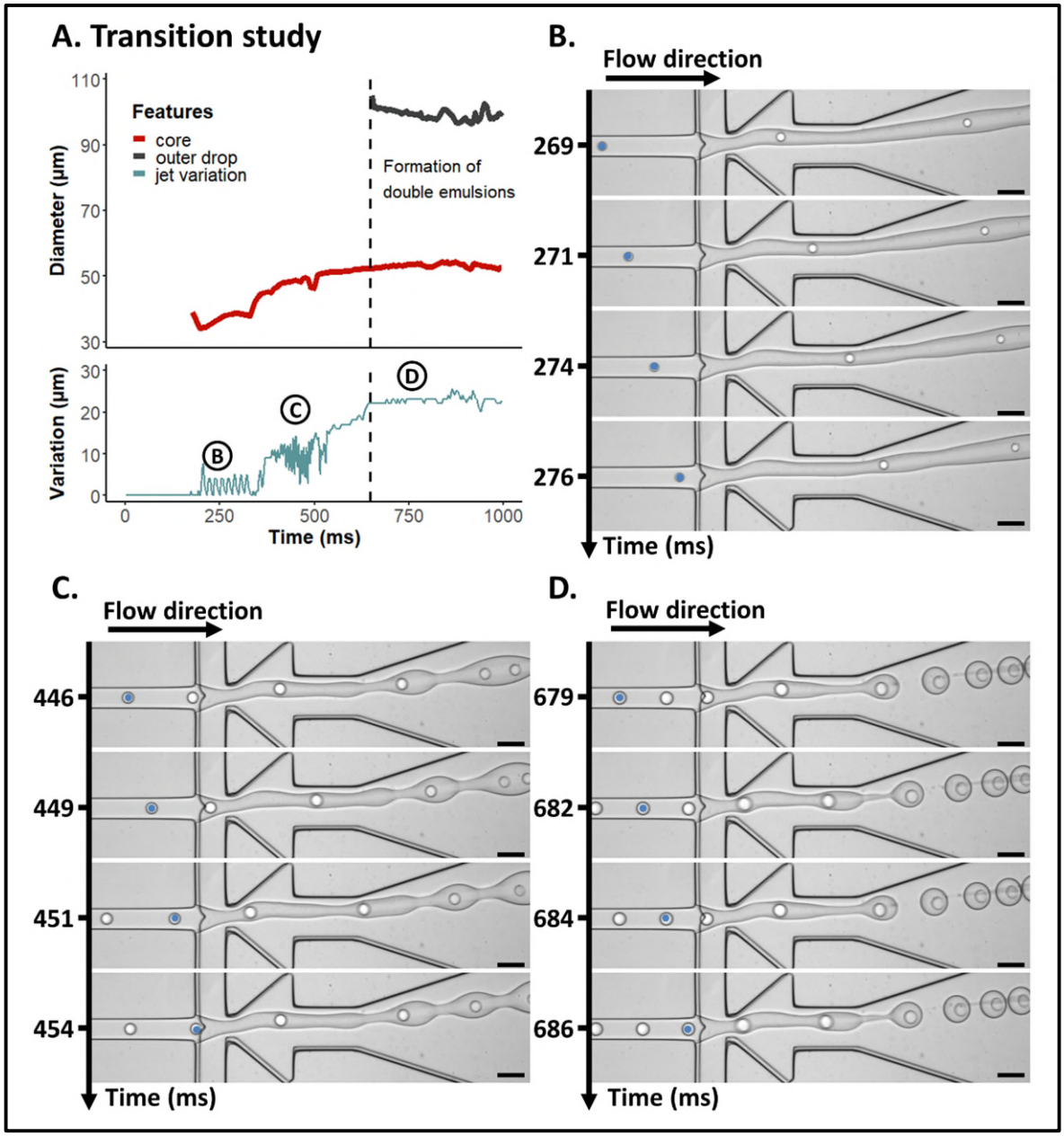
A. Transition study
Features
core
outer drop
jet variation
Formation of
double emulsions
Diameter (µm)
110
90
70
50
30
Variation (µm)
30
20
10
0
B
C
D
0
250
500
750
1000
Time (ms)
B.
Flow direction
269
271
274
276
Time (ms)
C.
Flow direction
446
449
451
454
Time (ms)
D.
Flow direction
679
682
684
686
Time (ms)

Figure 3-9: Core droplet diameter is responsible for the triggering of the Rayleigh-Plateau instability, resulting in the double emulsion formation.

A stepped design microfluidic chip was used. Inner, middle, and outer flows were formulated with dextran-TRITC in PBS, 17.5% (w/v) PLGA in DMC and 3% (w/v) polyvinyl alcohol (PVA) in PBS, respectively. Transition state and instabilities induced by the passing of core droplets of increasing diameters were monitored by high-speed camera and analysed (DMV software).

(A) Evolution of the core (red line) and outer droplet (grey line) diameter with time during the transition from a stable solvent + PLGA jet to the formation of a double emulsion. Jet variations are plotted below (blue lines), measured frame by frame (high speed camera, 10X objective, 5000fps) by a custom Fiji script as the difference in diameter between high-pressure narrower and low-pressure wider regions of the jet at a given time; variation of 0µm indicates a straight jet. Lines are drawn by linear interpolation from experimental points for visualisation.

(B-C-D) Time sequential microscopic images (high-speed camera, 10X objective, 5000fps) of the different states of the transition, as defined in (A). Blue dots identify an individual core flowing, black scale bar = 100µm.

The above results show that the generation of the Rayleigh-Plateau instability responsible for the double emulsification requires the uniform and stable production of core droplets of sufficient diameter interacting with the jet. Because the cores were formed in a stable, dripping regime, this conferred high stability to the process during the production, illustrated by **Figure 3-10**. During a 12-hour W/O/W double emulsification, the diameter of the core and outer droplet remained consistent throughout, with an overall core diameter of 41.9 +/- 1µm and total particle diameter of 86.4 +/- 2µm (**Figure 3-10.A**). Similar monodispersity was observed in the resulting collected and solidified particles across the entire production time, with the measured core diameter of 43.4 +/- 1.7µm and particle diameter of 59.9 +/- 2µm (**Figure 3-10.B**). High loading efficiency, over 99%, was ensured as the formation of double emulsion required a core to flow through the jet.

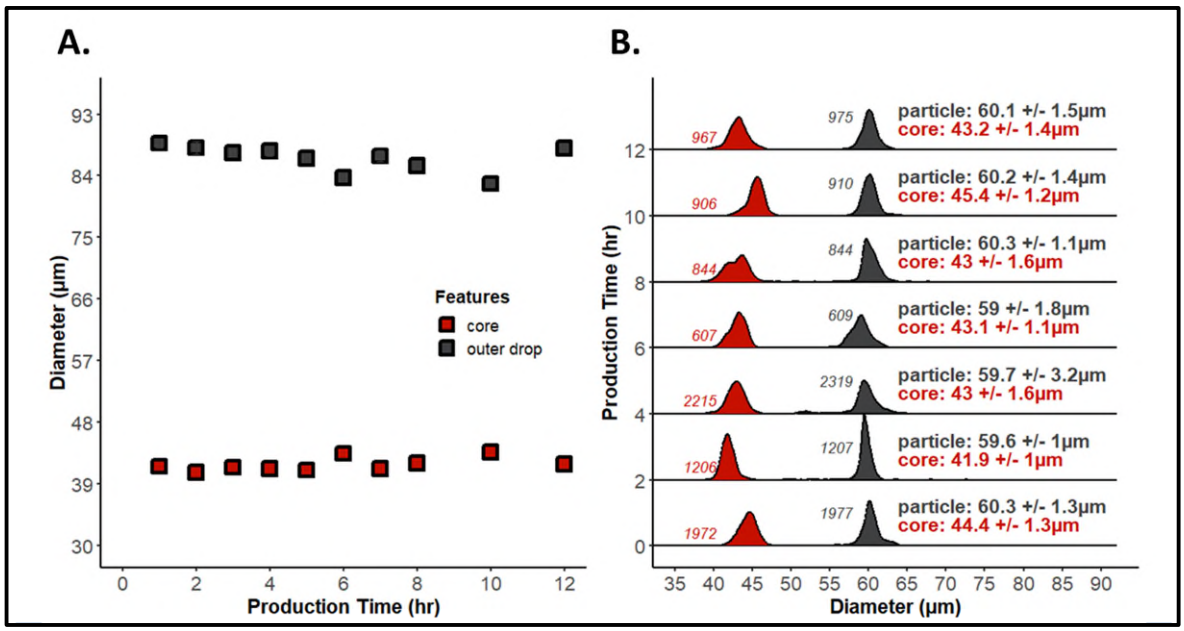

Figure 3-10: Liquid core – solid PLGA shell particle production remains stable with time.

Double emulsions were produced in a stepped design. Inner, middle, and outer flows were formulated with dextran-TRITC in PBS, 17.5% (w/v) PLGA in DMC and 3% (w/v) polyvinyl alcohol (PVA) in PBS, respectively. Evolution with production time of the features diameter for the liquid double emulsion inside the chip (A) and the corresponding collected LCSS particles (B) following solvent extraction, are plotted.

(A) Distribution of core and outer diameters of double emulsion (Mean +/- SD) measured at different production times. Data (n>90 per point) was measured from 0.5s lasting videos (high-speed camera, 4X objective, 5000fps) and analysed (DMV software). Error bars representing standard deviation are masked by the points, as <0.2µm for cores and <1µm for outer droplets.

(B) Distribution of core and outer diameters of collected LCSS particles (core - red, outer particle – grey) measured at different production times. Data was measured from 9 fluorescent microscopy images of the liquid core - solid PLGA shell particles population by MATLAB custom script (see Methods), plotted as kernel density estimation plots (R). Number of particles n used for distribution estimation are displayed in italic for both features. Core size was measured for loaded particles only (fluorescence level above 500MFI threshold).

3.2.5 Evaluating the achievable size range and loading of double emulsions

To measure the different sizes of particles and thicknesses of shell that can be produced using the presented stepped design, W/O/W emulsification was performed, setting the outer fluid pressure higher (370 mbar in this experiment) to create a thinner jet, where smaller cores can induce the formation of the double emulsion. **Figure 3-11** and **Figure 3-12** show the effect of inner and middle fluid pressure on the produced double emulsion diameters, core loading, frequency and the size distribution of the resulting collected and solidified particles. In both cases, the core and outer droplet diameters of the double emulsions were found to be linearly dependant on the fluid pressure (linear regression, p-values $<2x10^{-16}$ for all).

When the inner pressure was increased and the outer and middle fluid pressures kept constant, the core diameter increased while the outer droplet diameter decreased (**Figure 3-11.B**) as a consequence of the increased frequency and reduced space between the successive cores (**Figure 3-11.C**) . Ultimately, at an inner fluid pressure of 88mbar, 2 cores could pass passing before the jet necking and breaking occurred (**Figure 3-11.A** -88mbar) and uniform multi-core particles were created. The resulting collected and solidified LCSS particles were uniform (**Figure 3-11.D**) and demonstrated a range of shell thicknesses between 14.3 and 5.7µm while maintaining the core loading higher than 99.3%.

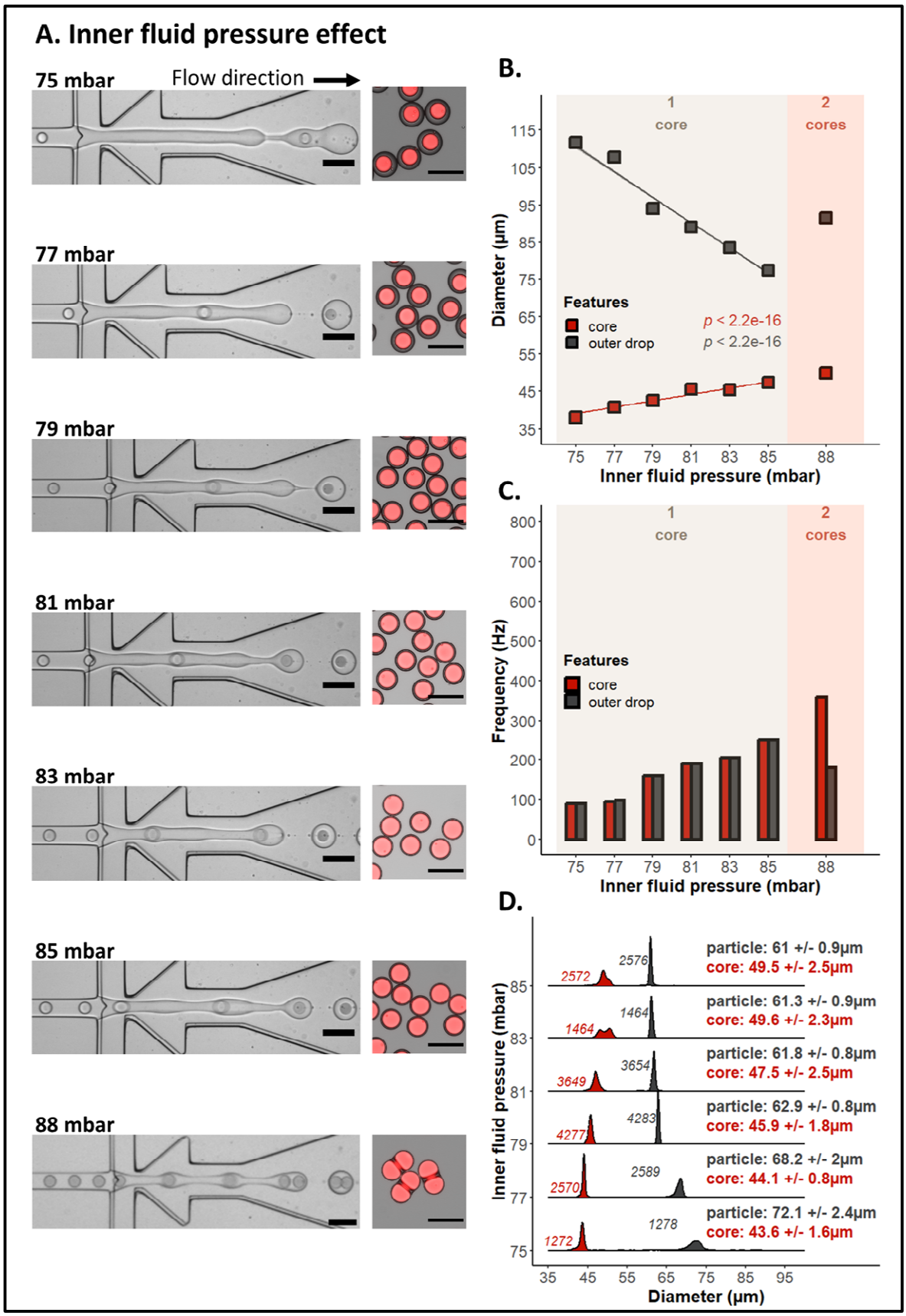
A. Inner fluid pressure effect
75 mbar
Flow direction
77 mbar
79 mbar
81 mbar
83 mbar
85 mbar
88 mbar
B.
1
core
2
cores
Diameter (µm)
Features
core
outer drop
p < 2.2e-16
p < 2.2e-16
Inner fluid pressure (mbar)
C.
Frequency (Hz)
Features
core
outer drop
Inner fluid pressure (mbar)
D.
Inner fluid pressure (mbar)
2572
2576
particle: 61 +/- 0.9µm
core: 49.5 +/- 2.5µm
1464
particle: 61.3 +/- 0.9µm
core: 49.6 +/- 2.3µm
3649
3654
particle: 61.8 +/- 0.8µm
core: 47.5 +/- 2.5µm
4277
4283
particle: 62.9 +/- 0.8µm
core: 45.9 +/- 1.8µm
2570
2589
particle: 68.2 +/- 2µm
core: 44.1 +/- 0.8µm
1272
1278
particle: 72.1 +/- 2.4µm
core: 43.6 +/- 1.6µm
Diameter (µm)

Figure 3-11: Inner fluid pressure during manufacturing controls fine tuning of particle dimensions and core loading.

(A) Microscopic images of the microfluidic W/O/W emulsification process for different inner fluid pressures (high-speed camera, 4X objective, 5000fps), and corresponding microscopic fluorescent images of the resulting liquid core - solid PLGA shell particles (10X objective, TRITC and Brightfield channels overlayed). Inner, middle, and outer flows were formulated with dextran-TRITC in PBS, 17.5% (w/v) PLGA in DMC and 3% (w/v) polyvinyl alcohol (PVA) in PBS, respectively. Middle and outer flow were kept constant at 170 and 370 mbar respectively. Black scale bar = 100µm.

(B) Measure of core and outer droplet diameters of double emulsions (Mean +/- SD) for different inner fluid pressures during production. Data (n>10 per point) was measured from 0.2s long videos (high-speed camera, 4X objective, 5000fps) and analysed (DMV software). Loading regimens (single or multiple cores) are displayed as faded rectangles. Linear regression and corresponding slope p-values are shown for single core regimens. Error bars representing standard deviation are masked by the points, as <0.5µm for all points.

(C) Observed frequency of core and outer droplet generation at different inner fluid pressures.

(D) Distribution of core and outer diameter of collected LCSS particles following production (core - red, outer particle – grey) for different inner fluid pressure used during production. Data was measured from 9 fluorescent microscopy images of the liquid core - solid PLGA shell particles population by MATLAB custom script (see Methods), plotted as kernel density estimation plots (R). Number of particles n used for distributions kernels are displayed in italic for both features. Core size was measured for loaded particles only (fluorescence level above 500MFI threshold).

When the middle fluid pressure was increased and the outer and inner fluid pressures kept constant, the core diameter decreased while the outer droplet diameter increased (**Figure 3-12.B**). From 160 mbar, the frequency and spacing between successive cores (**Figure 3-11.C**) was too high to trigger the break of the jet after one passing core, and double emulsions with 2 or 4 cores were created (see **Figure 3-12** -160 to 180mbar**)**. The resulting collected and solidified LCSS particles were also uniform (**Figure 3-12.D**) and demonstrated a smaller range of achievable shell thicknesses between 4.5 and 2.6µm with a core loading of 99.9% or higher. Dual core, and quadruple core solid structures could also be produced.

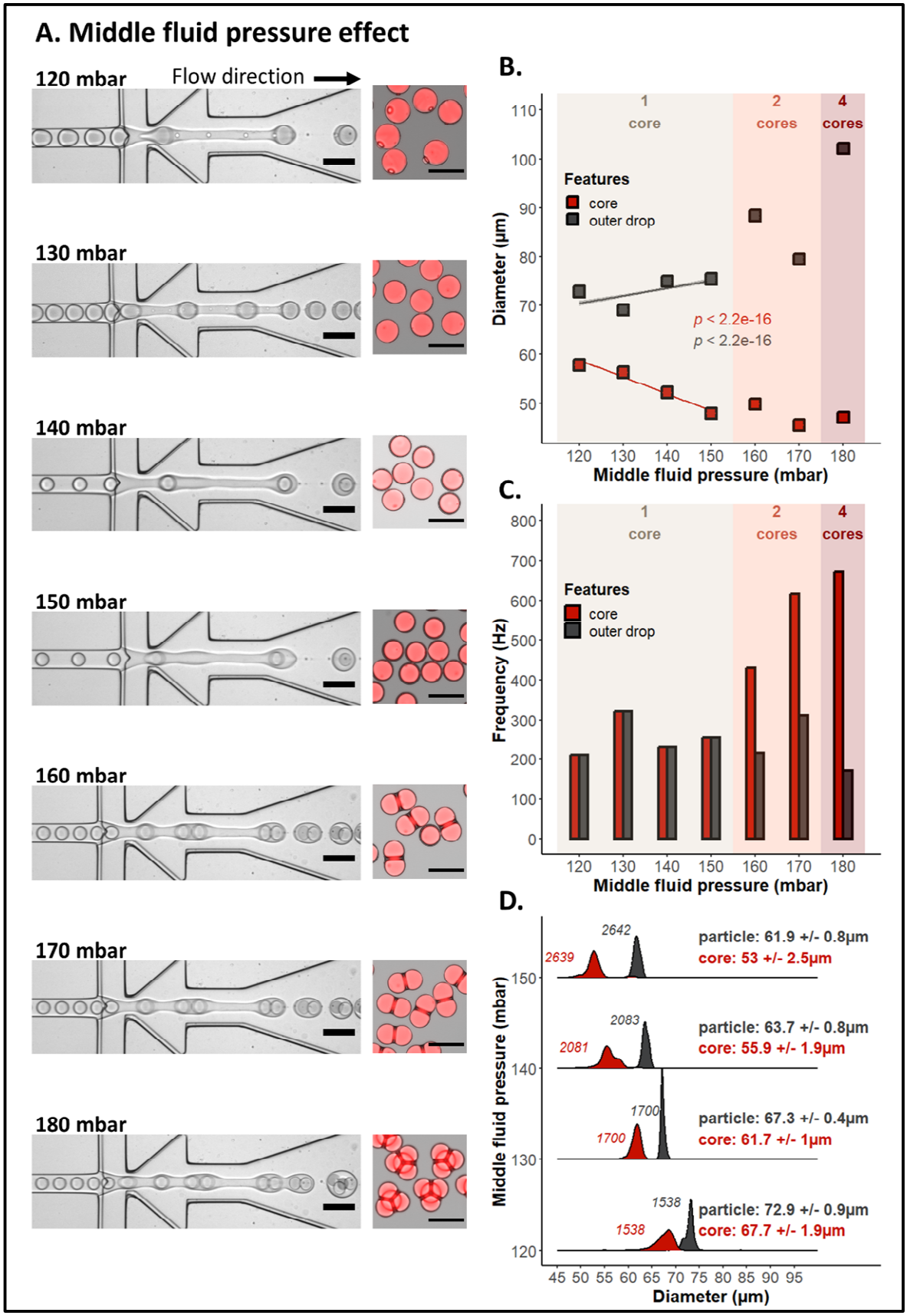
A. Middle fluid pressure effect
120 mbar
Flow direction
130 mbar
140 mbar
150 mbar
160 mbar
170 mbar
180 mbar
B.
1 core
2 cores
4 cores
Features
core
outer drop
p < 2.2e-16
p < 2.2e-16
Diameter (µm)
Middle fluid pressure (mbar)
C.
Frequency (Hz)
Middle fluid pressure (mbar)
D.
2642
2639
particle: 61.9 +/- 0.8µm
core: 53 +/- 2.5µm
2083
2081
particle: 63.7 +/- 0.8µm
core: 55.9 +/- 1.9µm
1700
1700
particle: 67.3 +/- 0.4µm
core: 61.7 +/- 1µm
1538
1538
particle: 72.9 +/- 0.9µm
core: 67.7 +/- 1.9µm
Middle fluid pressure (mbar)
Diameter (µm)

Figure 3-12: Middle fluid pressure during manufacturing controls fine tuning of particles dimensions and core loading.

(A) Microscopic images of the running microfluidic W/O/W emulsification process for different middle fluid pressures (high-speed camera, 4X objective, 5000fps), and corresponding microscopic fluorescent images of the liquid core - solid PLGA shell particles produced (10X objective, TRITC and Brightfield channels overlayed). Inner, middle, and outer flows were formulated with dextran-TRITC in PBS, 17.5% (w/v) PLGA in DMC and 3% (w/v) polyvinyl alcohol (PVA) in PBS, respectively. Inner and Outer flow were kept constant at 110 and 370 mbar respectively. Flow direction is indicated by a black arrow, black scale bar = 100µm.

(B) Measure of core and outer droplet diameters of double emulsions (Mean +/- SD) for different inner fluid pressures during production. Data (n>10 per point) was measured from 0.2s long videos (high-speed camera, 4X objective, 5000fps) and analysed (DMV software). Loading regimens (single or multiple cores) are displayed as faded rectangles. Linear regression and corresponding slope p-values are shown for single core regimens. Error bars representing standard deviation are masked by the points, as <0.3µm for all points.

(C) Observed frequency of core and outer droplet generation at different inner fluid pressures.

(D) Distribution of core and outer diameter of collected LCSS particles following production (core - red, outer particle – grey) for different inner fluid pressure used during production. Data was measured from 9 fluorescent microscopy images of the liquid core - solid PLGA shell particles population by MATLAB custom script (see Methods), plotted as kernel density estimation plots (R). Number of particles n used for distributions kernels are displayed in italic for both features. Core size was measured for loaded particles only (fluorescence level above 500MFI threshold).

3.2.6 Optimising the double emulsion throughput

Understanding the mechanism of double emulsification in the stepped microfluidic design allowed the tuning of certain parameters to increase the platform throughput. Indeed, being able to produce double emulsions faster is essential for this approach to be feasible for vaccine encapsulation. For the standard stepped design presented earlier, the limiting factor is the formation rate of the outer droplet at the second emulsion. The core formation at the first intersection is operating in a dripping regime that can be higher than 800Hz [92] but a high frequency of core

flowing in the jet at the second intersection and the high fluid velocity required for this frequency would stabilise the jet and its breakup after the passing of a single core, preventing the formation of single liquid core-solid shell particles. Different parameters, including the step position in the design, surfactant and salt concentration in the outer flow phase were tested to facilitate the jet destabilisation after the passing of a single core.

3.2.6.1 Changing the position of the step in the microfluidic design increases the throughput

Two additional positions of step in the microfluidic design were tested, either immediately after the nozzle ("Nozzle" step design, see **Figure 3-13.A**) or downstream, before the collection chamber ("Late" step design, see **Figure 3-13.C**). The objective was to use the step as an additional trigger of the Rayleigh plateau-instability (following reported work on single emulsification [106]), thus being able to increase the frequency of the double emulsification without loading multiple cores as seen before.

If the "Nozzle" step throughput was not quantitatively comparable to the standard step, as other dimensions were changed due to mould supplier constraints, the mechanism remained the same with the seeding of an instability in the jet induced by the passing of a core in the nozzle and through the step (**Figure 3-13.B**). The instability was seen to grow along the jet by forming thinner and larger regions resulting in the necking of the jet and formation of core-shell emulsion.

In contrast, the "Late" step design had identical channel dimensions to the standard design. In the case of the "Late" step, the double emulsification frequency was 830hz for emulsions with 37.8μm core diameter, almost 9 times higher than the

standard stepped design that produced double emulsion with a 38µm core diameter at a rate of 95 Hz (**Figure 3-11.C** -77mbar). Observation of the emulsification mechanism showed that the necking of the jet occurred immediately after the step, triggered by the passing of the core (**Figure 3-13.D**).

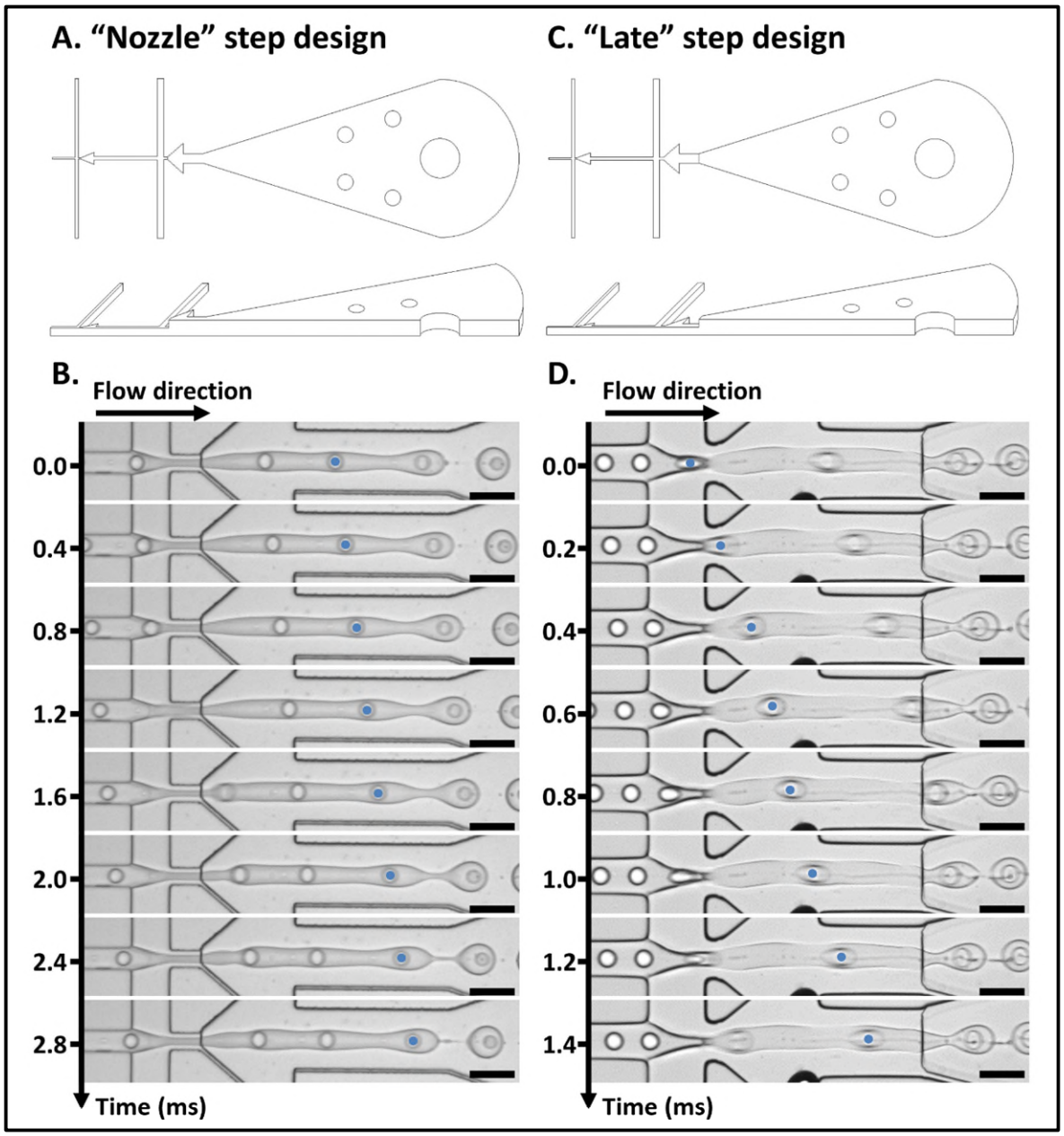

Figure 3-13: The position of the step in the microfluidic design facilitates the triggering of the double emulsion formation, enhancing generation frequency.

(A-C) Top view and cross section of the height-asymmetric, stepped W/O/W designs used, with a step position at the nozzle (A) or at the collection chamber (C).

(B-D) Time sequential microscopic images (high-speed camera, 10X objective, 5000 and 10000fps) of the formation of the second emulsion in the W/O/W process in the corresponding stepped design. Inner, middle, and outer flows were formulated with dextran-TRITC in PBS, 17.5% (w/v) PLGA in DMC and 3% (w/v) polyvinyl alcohol (PVA) in PBS, respectively. Blue dots identify an individual core, black scale bar = 100µm.

3.2.6.2 Decreasing the outer flow surfactant concentration increases the throughput above a certain core diameter

Using the standard stepped design, the effect of surfactant concentration in the outer flow on the double emulsion generation frequency and the resulting emulsification regimen was tested. Fluid pressures were adapted manually to achieve the highest generation frequency possible before multiple core loading, for different core diameters.

As illustrated in **Figure 3-14**, the surfactant concentration was found to affect the double emulsification process. For core diameters ~40.8µm, a concentration of 3% (w/v) of PVA in the outer phase was the only formulation able to generate double emulsions, with a frequency of 95Hz, while lower surfactant concentrations were seen to induce coalescence of the middle phase downstream (**Figure 3-14.B** -orange diamond), or incomplete loading (**Figure 3-14.B** -red diamond), for 0.03% (w/v) and 0.3% (w/v) PVA formulations respectively. The 3% PVA concentration condition was not tested for this core size range as it was already producing a jet with core diameters around 42.5µm (**Figure 3-14.B** -purple triangle). At this size range, the decrease of PVA resulted in an increase of highest double emulsion

generation frequency, with a jet break-up occurring closer to the intersection with lower PVA formulations (**Figure 3-14.C**). Thus, the maximum throughput reached by the 0.03%(w/v) PVA formulation was 450Hz, almost 3 times higher than the 3%(w/v) PVA formulation (160Hz).

Above 45µm core diameter (**Figure 3-14.D**), lower PVA concentrations in the outer flow also allowed to reach higher generation frequencies, however, no double emulsification could be operated with the 0.03%(w/v) formulation as the process resulted in heavy coalescence and clogging of the microfluidic chip.

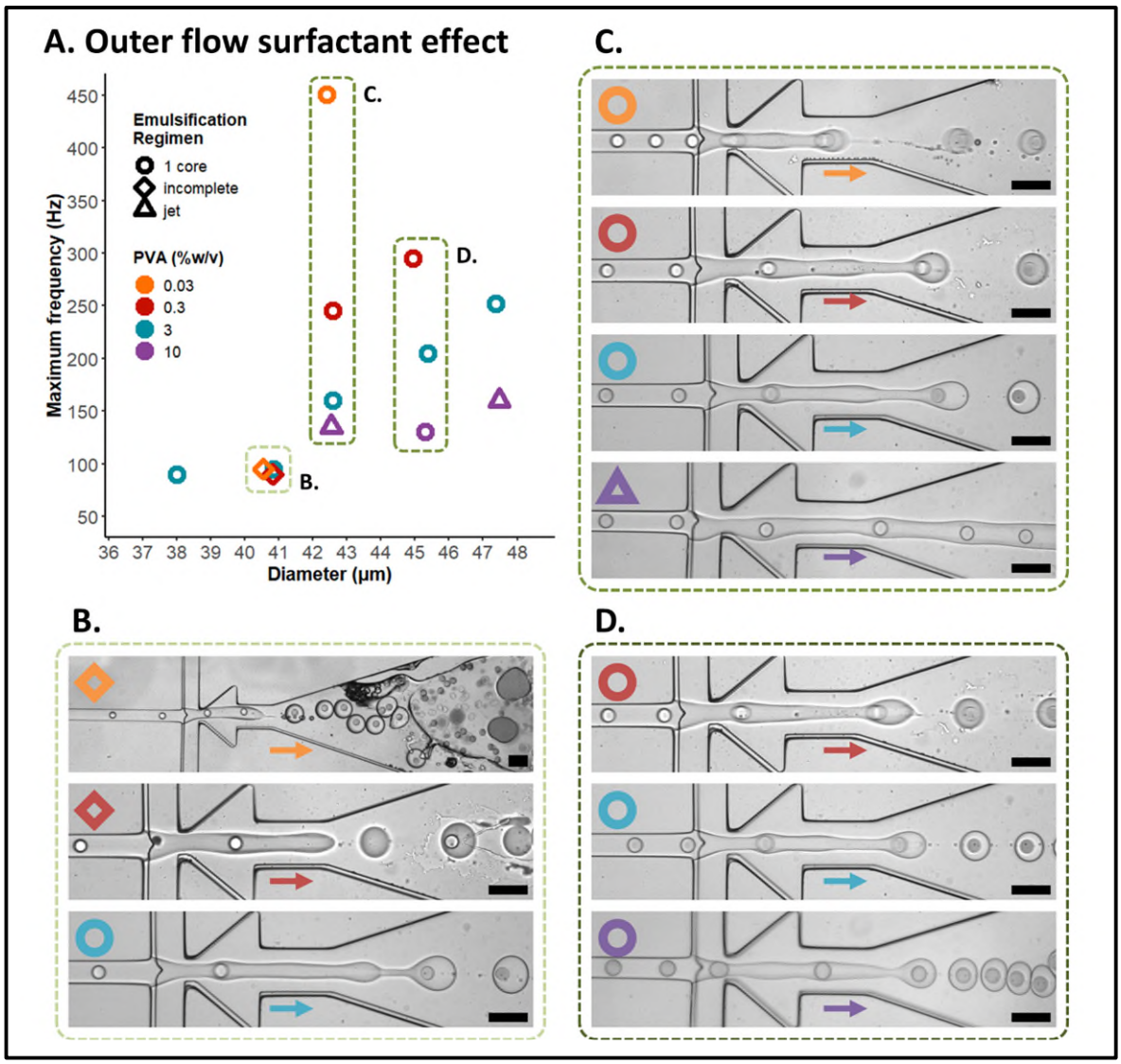

Figure 3-14: The surfactant concentration in the outer flow changes the double emulsification regimen.

(A) Observed double emulsification regimens (shapes) at a given core diameter and maximum reached generation frequency for different outer flow PVA surfactant concentrations in PBS (colours). Inner and middle flows were formulated with dextran-TRITC in PBS and 17.5% (w/v) PLGA in DMC, respectively. Fluid pressures were adapted to achieve the targeted core diameter.

(B-C-D) Microscopic images (high-speed camera, 4X or 10X objective, 5000fps) of the different emulsification regimens, as defined in (A). Outer flow formulation is indicated by the corresponding-coloured symbols, black scale bar = 100µm.

3.2.6.3 Increasing the outer flow salt concentration increases the throughput

The same analysis was conducted to determine the effect of addition of NaCl in the outer fluid, measuring the highest double emulsification generation frequency reached before multiple loading and jetting.

For the whole range of core diameters produced, the maximum frequency of double emulsion generation was systematically higher for the formulation containing NaCl (**Figure 3-15**).

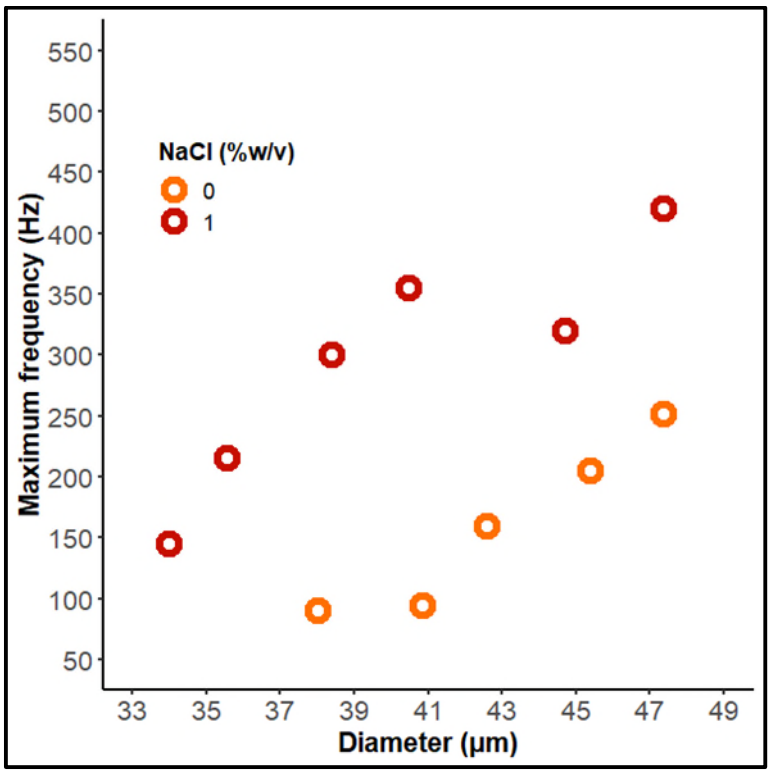

Figure 3-15: The addition of salt in the outer flow allows higher frequency of double emulsion generation.

Maximum reached double emulsification frequency at a given core diameter for different outer flow NaCl salt concentrations in PBS (colours). Inner and middle flows were formulated with dextran-TRITC in PBS and 17.5% (w/v) PLGA in DMC, respectively. Fluid pressures were adapted to achieve desired core diameter.

Looking at core diameters of 41µm, the addition of 1% (w/v) of NaCl in the outer flow increased the maximum reachable throughput of the double emulsification process from 95Hz to 355Hz. The increased amplitude of instability on the jet induced by the passing of the core for this core diameter was visible using the NaCl outer flow (**Figure 3-16**).

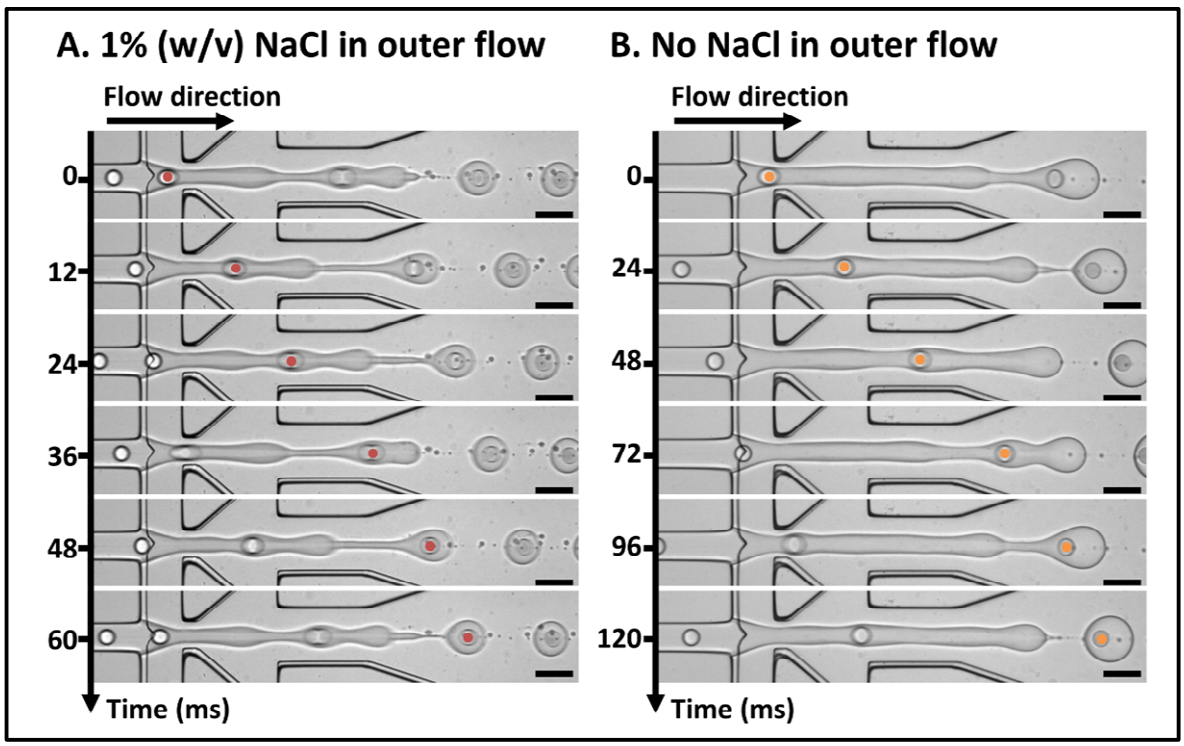

Figure 3-16: Passing cores trigger higher jet instabilities when salt is added to the outer flow in a W/O/W double emulsification.

Time sequential microscopic images (high-speed camera, 10X objective, 5000 fps) of the formation of the second emulsion in the W/O/W process with (A) or without (B) 1% (w/v) NaCl in the outer flow. Inner, middle, and outer flows were formulated with dextran-TRITC in PBS, 17.5% (w/v) PLGA in DMC and 3% (w/v) polyvinyl alcohol (PVA) in PBS, respectively. Incoming cores flowing were around 41µm in diameter. Coloured dots identify an individual core flowing for each formulation, black scale bar = 100µm.

3.2.7 Particle size can be tuned during the collection process

To determine whether the addition of salt was disturbing the postproduction transition of emulsion to LCSS particle, the double emulsions produced in **Figure 3-16.A** were collected in 3% (w/v) PVA in PBS with or without 1%(w/v) NaCl and imaged immediately after collection, and also 4 days later, after solvent extraction at room temperature (**Figure 3-17.A**). Before imaging at day 4, the particles were washed 5 times and resuspended in PBS. The shell thickness distribution of the double emulsions at day 0 (**Figure 3-17.B**) and of the LCSS particles at day 4 (**Figure 3-17.C**) were measured.

From the moment of collection, the double emulsions collected in the NaCl complemented media demonstrated a thicker shell in comparison to the double emulsions collected without NaCl in the media. After solvent extraction at day 4, the particles extracted in both media demonstrated a thinner shell than the double emulsion they were derived from. In addition, the resulting final particles collected in NaCl had a shell 2.5µm thicker than their counterparts collected without NaCl, with a much narrower distribution (3.9% CV for NaCl + PVA compared to 10.9% CV for PVA).

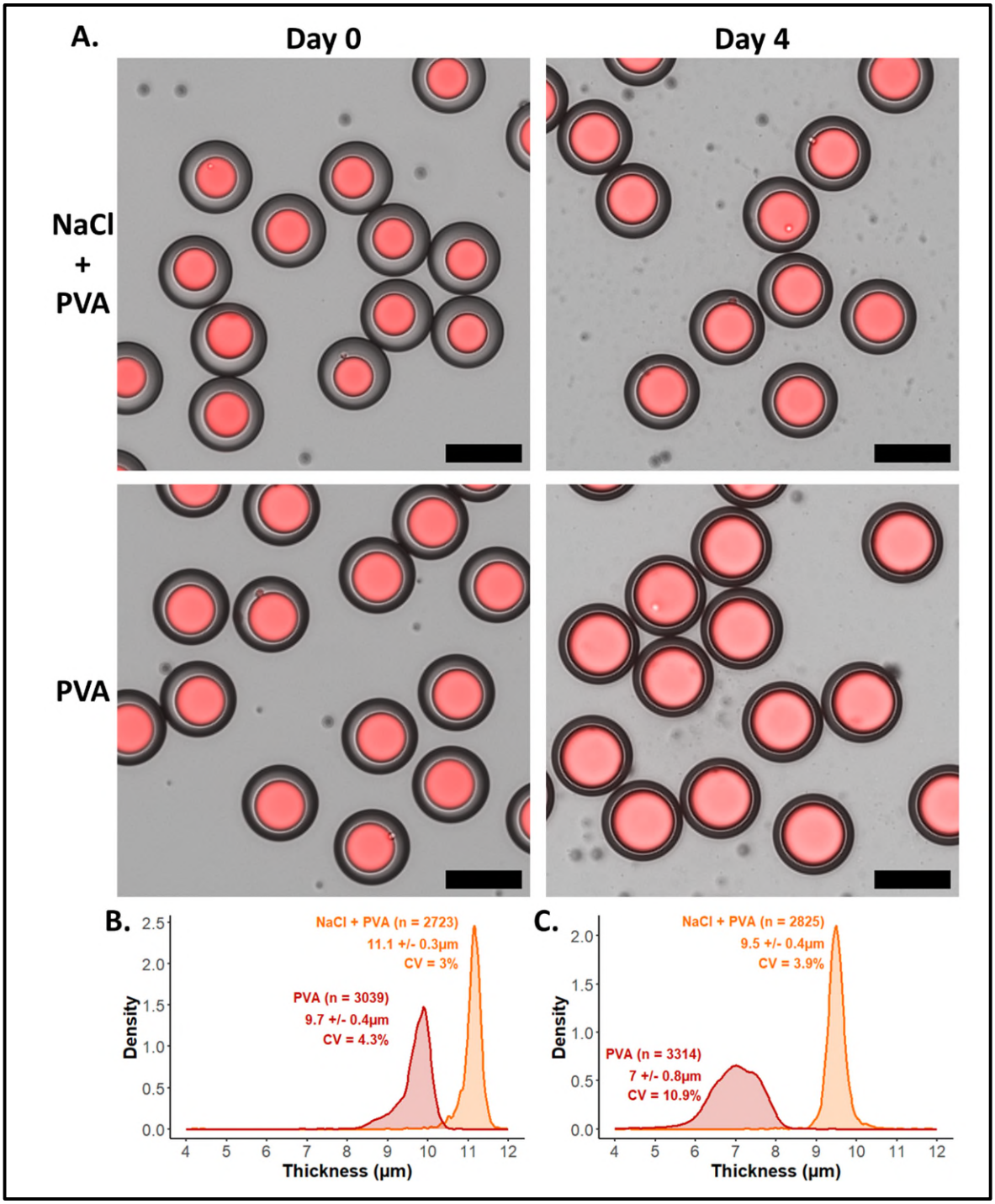
A.
Day 0
Day 4
NaCl + PVA
PVA
B.
NaCl + PVA (n = 2723)
11.1 +/- 0.3µm
CV = 3%
PVA (n = 3039)
9.7 +/- 0.4µm
CV = 4.3%
Density
Thickness (µm)
C.
NaCl + PVA (n = 2825)
9.5 +/- 0.4µm
CV = 3.9%
PVA (n = 3314)
7 +/- 0.8µm
CV = 10.9%
Density
Thickness (µm)

Figure 3-17: The addition of salt in the collection media prevents the swelling of cores and results in thicker shell LCSS particles.

(A) Microscopic images (10X objective, TRITC and Brightfield channels overlayed) of collected double emulsions in different media after different solvent extraction times, originating from the same emulsification process. NaCl + PVA media was 1% (w/v) NaCl and 3% (w/v) PVA in PBS, while PVA media was 3% (w/v) PVA in PBS only. Double emulsions were imaged immediately after collection (day 0) or 4 days after extraction at room temperature in corresponding media and subsequent wash in PBS at day 4. Black scale bar = 50µm.

(B-C) Corresponding collected LCSS particles thickness distributions, for different collection media (colours) at different time of extraction (B- day 0, C- day 4). Data were measured from 9 fluorescent microscopy images by MATLAB custom script (see Methods), plotted as kernel density estimation plots (R). Number of particles n used for distributions kernels are displayed.

Interestingly, when double emulsions were produced without NaCl in the outer flow but collected in media complemented with 1% (w/v) NaCl, the LCSS particles appeared more buckled (**Figure 3-18**), losing their sphericity due to the osmotic pressure resulting from the addition of NaCl outside of the particle. This finding is consistent with other studies in the literature [107].

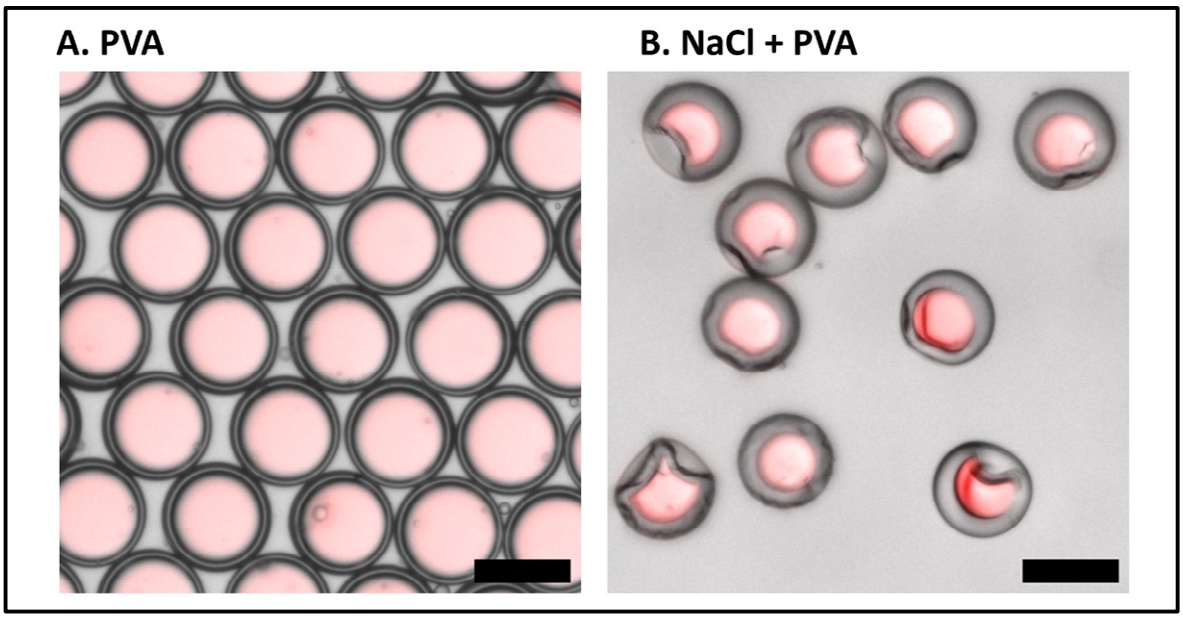

Figure 3-18: Adding NaCl after production results in buckled liquid core solid - shell particles.

Microscopic images (10X objective, TRITC and brightfield channels overlayed) of liquid core-solid shell particles produced with a 3% (w/v) PVA in PBS outer flow and collected in (A) the same media or (B) 1% (w/v) NaCl complemented media. Particles were imaged 4 days after extraction at room temperature and subsequent wash in PBS. Black scale bar = 50µm

This buckling was not observed for the LCSS particles produced and collected in NaCl, indicating that, in that case, the outer shell was able to adapt to the change of core diameter due to osmotic pressure. This phenomenon could be explained by the solvent extraction due to partial miscibility of the DMC solvent in water which started from the moment of generation inside the chip and was faster when the outer flow was not supplemented with NaCl.

To confirm the different rates of solvent extraction depending on the salt content of the outer flow, a W/O/W microfluidic emulsification was conducted in a chip with a serpentine channel located downstream of the intersection to be able to monitor the evolution of the double emulsion diameter after different flowing times in the channel (**Figure 3-19**).

The double emulsions were produced with or without 1%(w/v) NaCl in the outer flow, with similar initial diameters (channel position 1: 97.3 +/- 0.3µm and 98.6 +/- 0.2µm for the conditions with and without NaCl, respectively) and speed (47 +/- 3mm/s and 50 +/- 1mm/s for the conditions with and without NaCl, respectively). However, after flowing for 22mm and reaching the position 4 (**Figure 3-19**) of the channel, the outer diameter of double emulsion produced without NaCl in the outer flow was almost 10µm lower than the double emulsion produced with NaCl (channel position 4: 89.7 +/- 0.2µm and 81 +/- 0.4µm for the conditions with and without NaCl, respectively). As reported in the literature [108], the addition of NaCl decreased the partial miscibility of the DMC solvent in water, thus limiting its extraction inside the microfluidic chip.

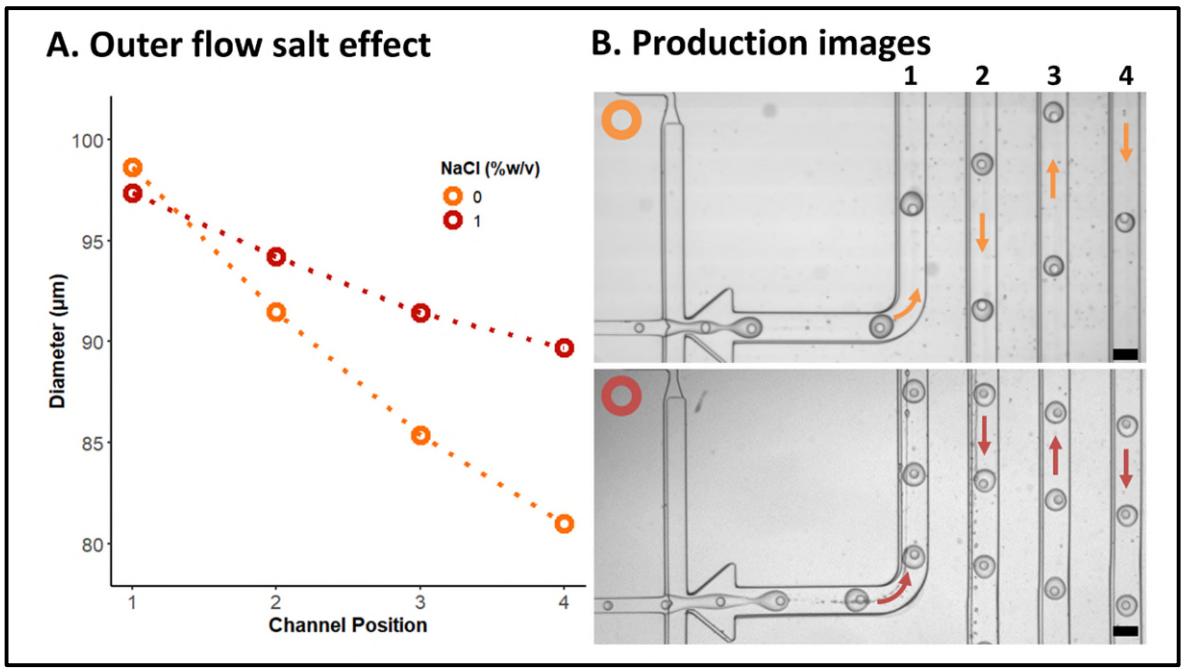

Figure 3-19: The addition of salt in the outer flow slows down the extraction of the DMC solvent, and hence hardening of the particle shell.

(A) Evolution of the double emulsion outer droplet diameter (Mean +/- SD) at different channel positions in a serpentine step design for different outer flow NaCl salt concentrations (colours). Inner, middle, and outer flows were formulated with dextran-TRITC in PBS, 17.5% (w/v) PLGA in DMC and 3% (w/v) polyvinyl alcohol (PVA) in PBS, respectively. Data (n>10 per point) was measured from (A) 0.4s and (B) 0.5s long videos (high-speed camera, 4X objective, 5000fps) and analysed (DMV software). Error bars representing standard deviation are masked by the points, as <0.4µm for all points. Linear interpolation of points is displayed with dotted lines for visualisation of the same production process.

(B) Microscopic images (high-speed camera, 4X objective, 5000fps) of the running W/O/W emulsification process and subsequent solvent extraction phenomena in the serpentine design for different outer flow NaCl salt concentrations, indicated by the corresponding-coloured symbols. Channel positions are annotated with numbers, black scale bar = 100µm.

3.3 Discussion and Summary

In this chapter, successful production of a double emulsion with a middle phase comprising PLGA in solvent in order to produce LCSS particles, was demonstrated using a PDMS chip-based microfluidic approach. Different key parameters were identified.

First, the DMC solvent was proven compatible with the PDMS material while being able to dissolve PLGA and being partially miscible with water so that it could be emulsified and subsequently extracted. However, this limited the choice of PLGA to ones with an ester end cap, as acid end cap formulations could not form spherical particles and deformed during the emulsification process. This deformation can be explained by the more hydrophilic property of acid end cap PLGA compared to ester ones [109] that decreases the surface tension between the solvent phase and the aqueous phase. Lower interfacial tension induces droplets deformations as the viscous drag exerted by the outer phase cannot be overcome [110], and combined with the DMC solvent being partially extracted, it leads to the deformed emulsion observed with the acid end cap PLGA.

Another indispensable feature for achieving double emulsification was the addition of a step up in the channel height. The absence of this feature in flat designs resulted in the bursting and splitting of the produced double emulsion, reducing both the loading and the uniformity of the resulting particles. It could be explained by the drag exerted by the compression of the core and outer droplet between the walls of the channel, as described in the literature [103], [105], [111]. This drag increases with the diameter of the emulsion, given the width and height of the channel. Hence a large, compressed, plug-shaped droplet will exhibit a higher drag than a non-

compressed spherical one. Thus, by adding the step - a sudden expansion in the channel height - the double emulsion can flow with minimal compression. The step feature was essential to achieve the successful production of LCSS particles with a loading efficiency above 99% and size CV inferior to 6%.

The narrow distribution of particle diameters resulted from the high uniformity and reproducibility of the emulsification process, generating double emulsion droplet with CV less than 2%. Interestingly, the jetting regime has been reported as generally producing droplets with higher polydispersity due to challenges in controlling Rayleigh plateau instabilities formation [112]. However, in this situation, high monodispersity was observed in the double emulsion generated by the jetting regime. This could be explained by the flowing of the inner cores inside the jet. Thus, by passing and blocking the flow of the middle phase, inner cores induce the formation of regions of larger and smaller diameters within the jet [113]. An instability is induced and growing, driven by the difference in Laplace pressure between the two regions, until the interfacial tension cannot be withstood, breaking the jet into a droplet containing the core. In the case of W/O/W emulsification with stepped designs, the inner cores were generated by dripping consistently at the first intersection, thus regularly seeding instabilities in the jet at the second intersection and extending the uniformity of the formation to the outer droplet formation. The induction of instability was dependent on the minimum diameter of the inner core for a given jet diameter, consistent with findings when solid spheres are flowing in a jet [113].

This mechanism of the second emulsification relying on the induction of the first one allowed the maximisation of the loading above 99%, as a droplet is systematically formed when a core flows, providing production reliability. In contrast, W/O/W

designs reported in the literature, which operate in dripping modes at both intersections and rely on the synchronisation of the inner core and outer droplet frequencies, can yield loading efficiencies ranging between 40 and 90% [114]. In addition, a planar W/O emulsification system triggering water droplet formation by flowing solid beads in a jet to trigger Rayleigh plateau instabilities reported throughputs above 20 kHz [115], illustrating a promising aspect of operating in a triggered, jetting, manner.

The step design demonstrated its versatility to achieve a wide range of resulting particle shell thickness, in addition to multicore encapsulation, when the generation frequency of cores was too high, preventing the necking of the jet at the second intersection, after the passing of a single core [116]. To increase the throughput and be able to generate double emulsions at higher frequencies of the passing core, the induction of the instability by passing cores was enhanced either by design, or formulation.

Hence, placing the step before the collecting chamber resulted in an additional element inducing jet instability [106]. Combined with the passing of the core, the late step double emulsification could withstand a frequency of passing cores 9 times higher than the standard step one, for a given core diameter.

The seeding of the instability by the flowing core was also enhanced by changing the formulation of the outer flow. Changing the salt or surfactant concentration resulted in an increased interfacial tension between the middle and outer fluids, facilitating the necking of the jet at a higher frequency.

Finally, the addition of salt in the outer fluid also reduced the partial miscibility of the DMC solvent with water [117], resulting in particles with thicker shells when the

double emulsions were collected, and the solvent extracted in a salt complemented environment. This phenomenon was due to a difference in osmotic pressure between the inner core and outer media and reported for double emulsions as osmotic annealing [83]. It was only possible when the double emulsions were produced with salt in the outer flow, to prevent early extraction of the solvent and buckling of the resulting particles. Using osmotic annealing can help to increase the throughput of thicker shell particles, taking advantage of the higher frequency of double emulsion generation with larger cores, before subsequently reducing their core diameter by osmotic pressure.

The LCSS particles produced by the stepped design process presented in this chapter were investigated in vitro to understand their mechanism of degradation and characterise the release of their payload for future vaccination applications. These results are presented in the next chapter.

4 Characterisation of the release kinetics

4.1 Introduction

Polylactic-co-glycolic acid (PLGA) has been extensively used for drug delivery due to its biocompatibility [118] and tuneable degradation rate [119]. PLGA is a copolymer of lactic and glycolic acid, susceptible to degradation by hydrolysis of the ester bonds between its monomers. It can be used to create multiple different types of structures, from films and scaffolds, to microparticles [120]–[122], and more recently core-shell 3D printed particles [46]. PLGA is a bulk eroding polymer [123]–[125], meaning that water diffuses faster through the polymer matrix than the polymer itself degrades [126]. There is consequently simultaneous random degradation across the whole polymer matrix volume, in contrast to surface eroding polymers, in which hydrolytic degradation occurs at the interface between the polymer and surrounding aqueous environment. Hydrolytic degradation is an autocatalytic process, whereby carboxylic acid ends are formed by ester bond cleavage, locally decreasing the pH [127], which accelerates the degradation process. As a result, pores of different sizes appear inside the matrix, forming a network that, in the case of drug delivery systems, facilitates diffusion of the payload [128]. Autocatalysis is driven by the lower molecular weight (Mw) chains of PLGA generated by the degradation process. However, once these acidic by-products can diffuse out of the polymer matrix, the autocatalysis effect is drastically reduced. Thus, there is a variation in the size of pores formed depending on the distance to the interface with the outside media [129]. The change in molecular weight across

the PLGA matrix also affects the crystallinity, mechanical characteristics, and the glass transition temperature of the system, all influencing its delivery properties.

In vitro characterisation of drug delivery systems is usually conducted by incubation with constant agitation of the particles in a buffer simulating *in vivo* physiological conditions by its composition and temperature. In the case of a single-phase microparticle system, the active pharmaceutical ingredient (API) payload is embedded homogeneously inside the PLGA matrix, and its release is dependent on its diffusion through the matrix, facilitated by the polymer degradation with time, leading to a continuous kinetic of release [130]. In contrast, in a recently described core-shell system the payload was suspended in a liquid aqueous core surrounded by a PLGA shell [46]. The system demonstrated a pulsatile release behaviour, explained by its LCSS architecture. With polymer degradation, a pore network is formed inside the shell, and release of the core content occurs once a continuous path connecting the inside to the outside of the particle is formed [47].

In this section, experimental *in vitro* results are presented for the LCSS particles manufactured using microfluidics as described in the previous chapter. The mechanism of a pore network driven release is confirmed and drug release from the microparticle population is monitored. Finally, the effect of different particle properties on the release kinetics *in vitro* is reported.

4.2 Release analysis

The different LCSS particle PLGA formulations (see **Table 2-2**) displayed similar triphasic release kinetic profiles, characteristic of PLGA systems [131]. First, an initial “burst” release phase was typically observed followed by a slower release or “lag” phase. Finally, a sharp release peak was seen (**Figure 4-1**). Non-LCSS particles produced by BE exhibited a biphasic release curve, with an initial burst release until a plateau is reached.

In order to compare the release characteristics of the different formulations, the cumulative release data were modelled by spline interpolation to obtain a derivative function. The derivative corresponds to the instantaneous rate of release. Peaks were detected by defining a threshold of 0.1%/day. For slower release formulations this threshold was lowered to 0.05%/day. For each peak, multiple characteristics were measured:

- **Proportion:** the proportion of the total payload released during the peak,
- **Time:** the time at which 50% of the payload lost during the peak was released,
- **Duration:** the duration of the peak,
- **Lag:** the time at which the peak started.

All these parameters are relevant in the context of vaccination: the **Proportion** represents the fraction of the vaccine dose delivered in lieu of a booster shot. The **Time** gives an estimate of the time needed to deliver a significant amount (50%) of the vaccine booster dose. The **Duration** and **Lag** indicate the length and the starting moment of the exposure to the vaccine booster dose. The highest proportion peaks were compared among different particle formulations, as the most

relevant for applying to vaccination. The analysis method is summarised in **Figure 4-1**.

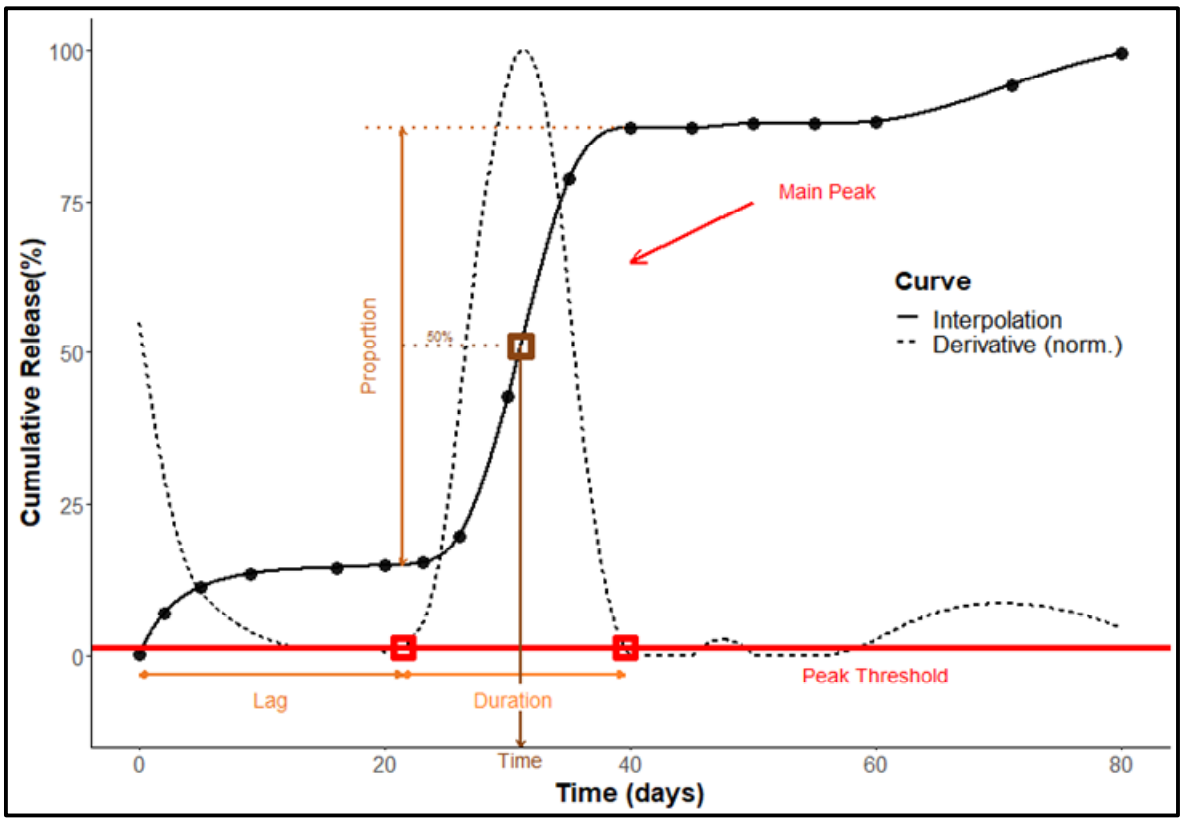

Figure 4-1: Typical example of measured release profile indicating the parameters used for analysis.

This figure describes the method used for the analysis of in vitro release kinetics of LCSS particles batches. Example of a cumulative release data experimentally measured is shown as circle points. A spline interpolation (solid line) is used to model the continuous cumulative release function and compute its derivative (dashed line), corresponding to the instantaneous rate of release. Using a threshold (red line) arbitrarily set to 0.1%/day in this example (0.05%/day for slower release formulations), detection of peaks in the derivative is performed (boundaries of the peak represented as red square points). Different characteristics are measured for each peak: its lag (time length before peak's left boundary) and duration (time length between peak's boundaries), the proportion of release (cumulative release occurring during the duration of the peak), and its time of release (brown square point - time where 50% of the peak's proportion is release).

Peak parameters are reported in the Figures and Tables in this chapter as the mean and 95% confidence interval (CI) values estimated from a Student's distribution.

Correlation between formulation molecular weight and the peak's time was established by a Jonckheere–Terpstra non-parametric permutation test [132]. Where relevant, comparisons were performed using a linear regression model to estimate the effect size and 95%CI.

4.3 Results

4.3.1 Comparison of the release kinetics between LCSS and BE particles

The effect on payload release of the LCSS architecture produced by microfluidics was evaluated against particles produced by standard batch emulsification (BE). The BE particles were made with two different volume ratios of the inner to the middle phase (1:5 and 1:10). All types of particles contained the same payload (40kDa Mw dextran-TRITC) in the same composition of polymer (PLGA R502 7-17kDa, 50:50 Mw). The size distribution of the LCSS particles was much narrower than the BE particles, as illustrated in **Figure 4-2**. LCSS particles had an outer diameter CV of 3.6% while BE particles had a CV of 24.5% and 32.5% respectively (BE 1:10 and BE 1:5).

Batches of different types of particles were incubated in the *in vitro* setup (see Material and Methods, section 2.3.1) and the monitoring of the release, demonstrated a clear booster-mimicking kinetic behaviour from the LCSS particles (**Figure 4-3**) with a lag of 14 days. During this period the release is negligible, followed by a bulk release of more than 85% of the total loading of the batch over the following 13 days. In contrast, both BE types of particles started to release from the beginning of the *in vitro* incubation (Lag = 0), displaying continuous release over 10 and 24 days for BE1:5 and BE1:10 respectively. Overall, in addition to a different kinetic profile of release, the time of release of the core shell formulation was around 21 days, higher than the BE particles, with a time of release at 3 days for the 1:5 formulation, and 15 days for the 1:10 formulation.

For all following results sections, these LCSS particle batch release data were used as reference to explore effects of different particle or polymer characteristics.

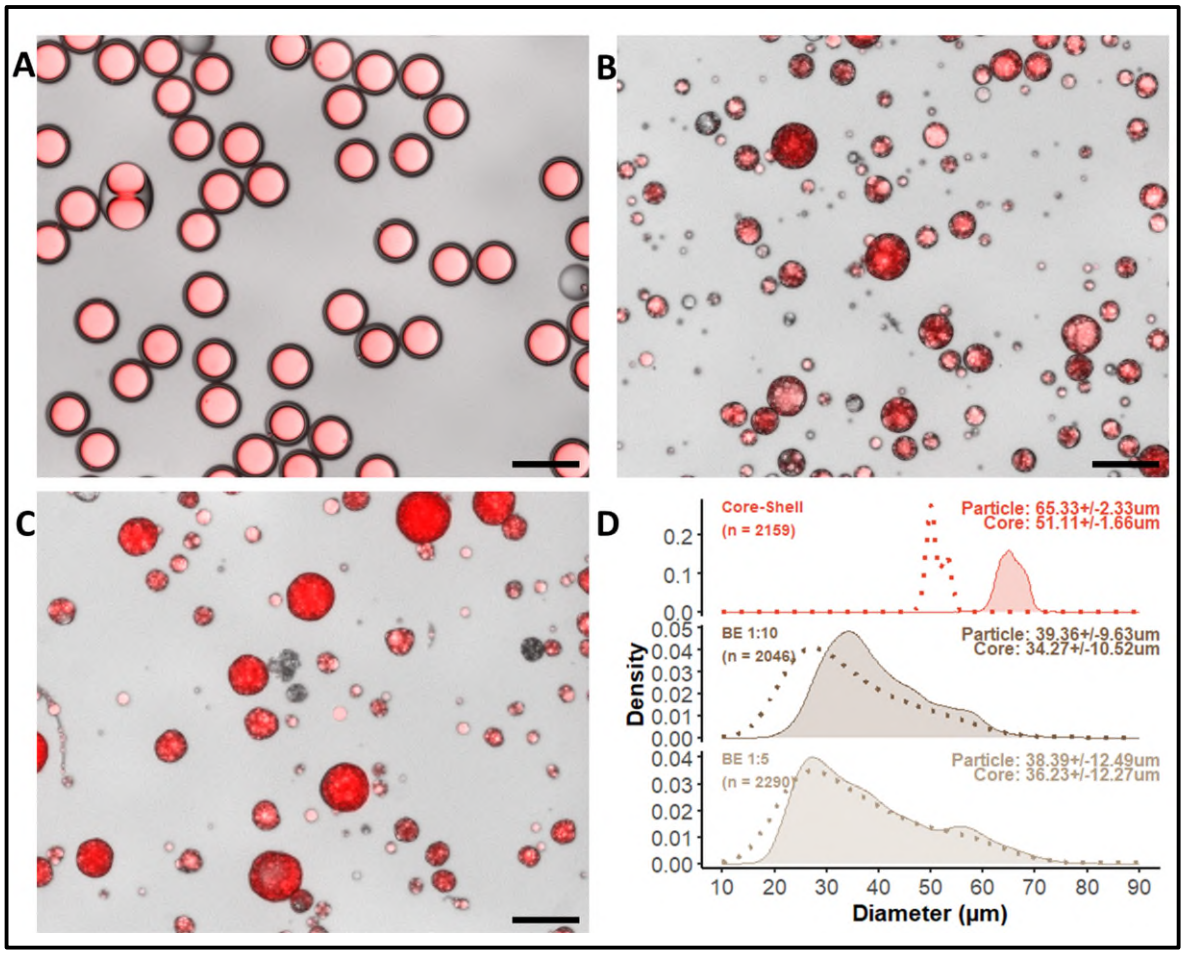

Figure 4-2**: **LCSS particles produced by microfluidics or BE particles, before in vitro incubation.

Microscopic images of different types of particles manufactured by microfluidics (forming LCSS structure) or BE techniques, encapsulating fluorescent dextran-TRITC and suspended in PBS at room temperature. (A) Core-Shell (LCSS) (B) BE 1:10, and (C) BE 1:5 particles were imaged with a 10X objective. TRITC and brightfield channels are overlayed, same LUT is applied for all images. (D) Outer diameter (solid filled line) and core diameter (dotted line) size distribution, plotted as kernel density estimations. Number of particles n used for distribution estimate are displayed and core size was measured for loaded particles only (fluorescence level above 500MFI threshold). The scale bar is 100µm.

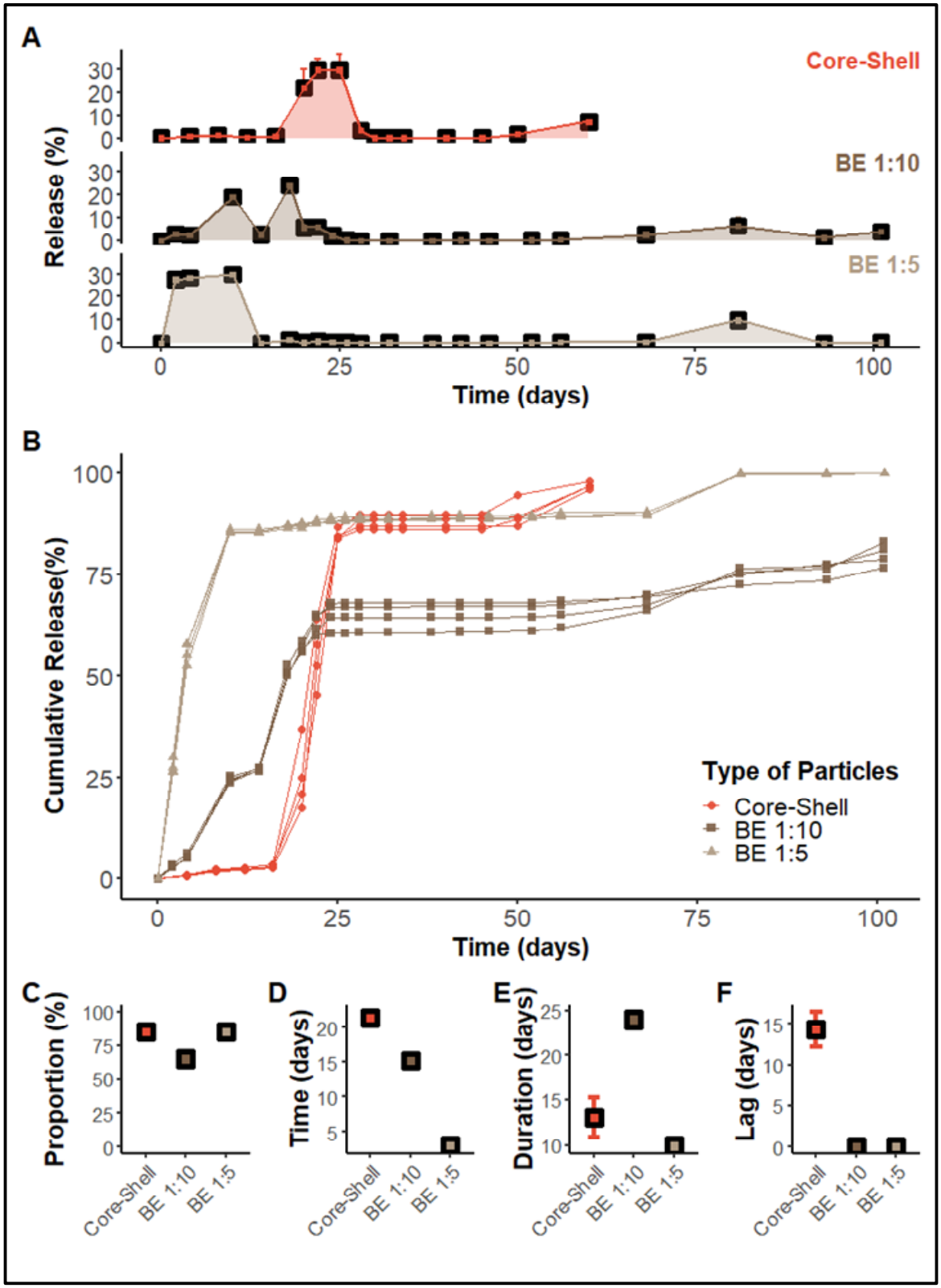
A
Core-Shell
BE 1:10
BE 1:5
Release (%)
Time (days)
B
Cumulative Release(%)
Time (days)
Type of Particles
Core-Shell
BE 1:10
BE 1:5
C
Proportion (%)
D
Time (days)
E
Duration (days)
F
Lag (days)
Core-Shell
BE 1:10
BE 1:5

Figure 4-3: Comparison of release kinetics between LCSS and BE particles.

Summary of in vitro release kinetics from different type of particles, manufactured by microfluidics (LCSS particles) or BE techniques, encapsulating fluorescent 40kDa dextran-TRITC. Each batch/type of particles (n=4 replicates by type) was incubated at 37°C in PBS, pH 7.4, with 0.01% Tween 80, under constant rotation of 20rpm. Dextran release was measured by spectrophotometry. Results are reported as (A) Measured release over time (Mean of replicates +/- SD), (B) Cumulative release of each replicate over time, and (C-F) main peaks characteristics for each particle type (Mean and 95%CI assuming student distribution) as described in section 4.2.

4.3.2 Mechanism of Particle Degradation

One replicate from the batch of LCSS particles reported in the previous section was monitored using different microscopic techniques, fluorescence microscopy (FM) and scanning electron microscopy (SEM) to observe the changes in morphology and payload release over time, to better understand the underpinning mechanisms. Image processing was performed by custom MATLAB script (see Appendix I) to independently measure the fluorescence and dimensions of the particles (64 images at day 0, then 36 images per timepoint). The changes in particle loading (fluorescence) and diameter over time are plotted in **Figure 4-4**. A sample of the FM images taken at different timepoints is displayed in **Figure 4-5**. These results indicate that most of the particles remained fully loaded for the first 16 days of the incubation, with a similar MFI distribution. Between days 20 and 25 the loading shifted abruptly, indicating a sharp release of fluorescent dextran from most particles, corresponding to the measured release reported in section 4.3.1. A few particles remained fully loaded on day 30 and beyond (**Figure 4-5**). The diameter of the particles did not change significantly for the first 20 days of *in vitro* release (day 0: 65.3 +/- 2.4µm, day 20: 69.6 +/- 4.1µm). However, the observed unloading

of the particles after day 20 coincided with an increase of outer diameter of the particles (day 40: 113.4 +/- 17.5µm).

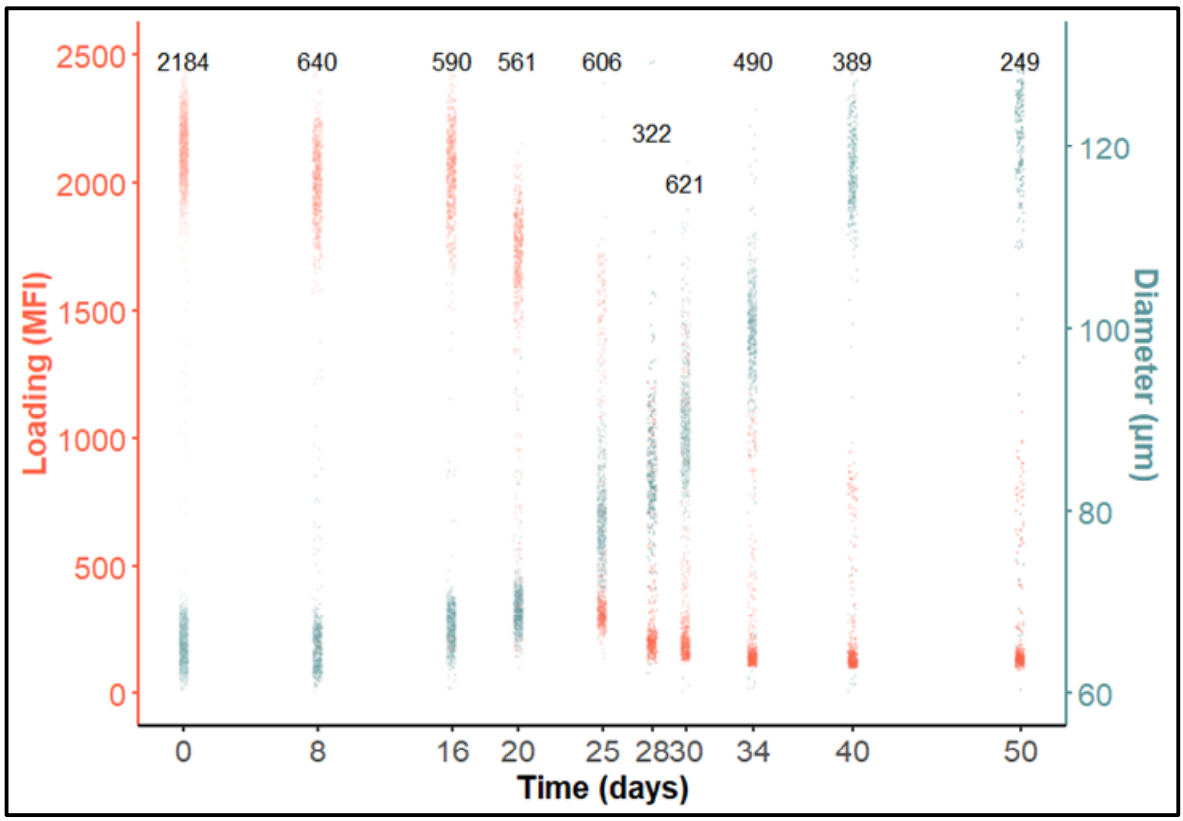

Figure 4-4: Loading and diameter distribution evolution with in vitro degradation of core-shell particles.

LCSS particles (PLGA 50:50 7-17kDa Mw) encapsulating dextran-TRITC were monitored by microscopy at different timepoints of vitro incubation (37°C in PBS, pH 7.4, with 0.01%Tween 80, under constant rotation of 20rpm). Image processing was performed automatically by MATLAB custom script and distributions of the loading and diameter are reported at different timepoints. Each dot represents one particle. Loading is represented by MFI from the encapsulated dextran-TRITC. Diameter is expressed in µm. The number of particles analysed for each timepoint is indicated in black font above.

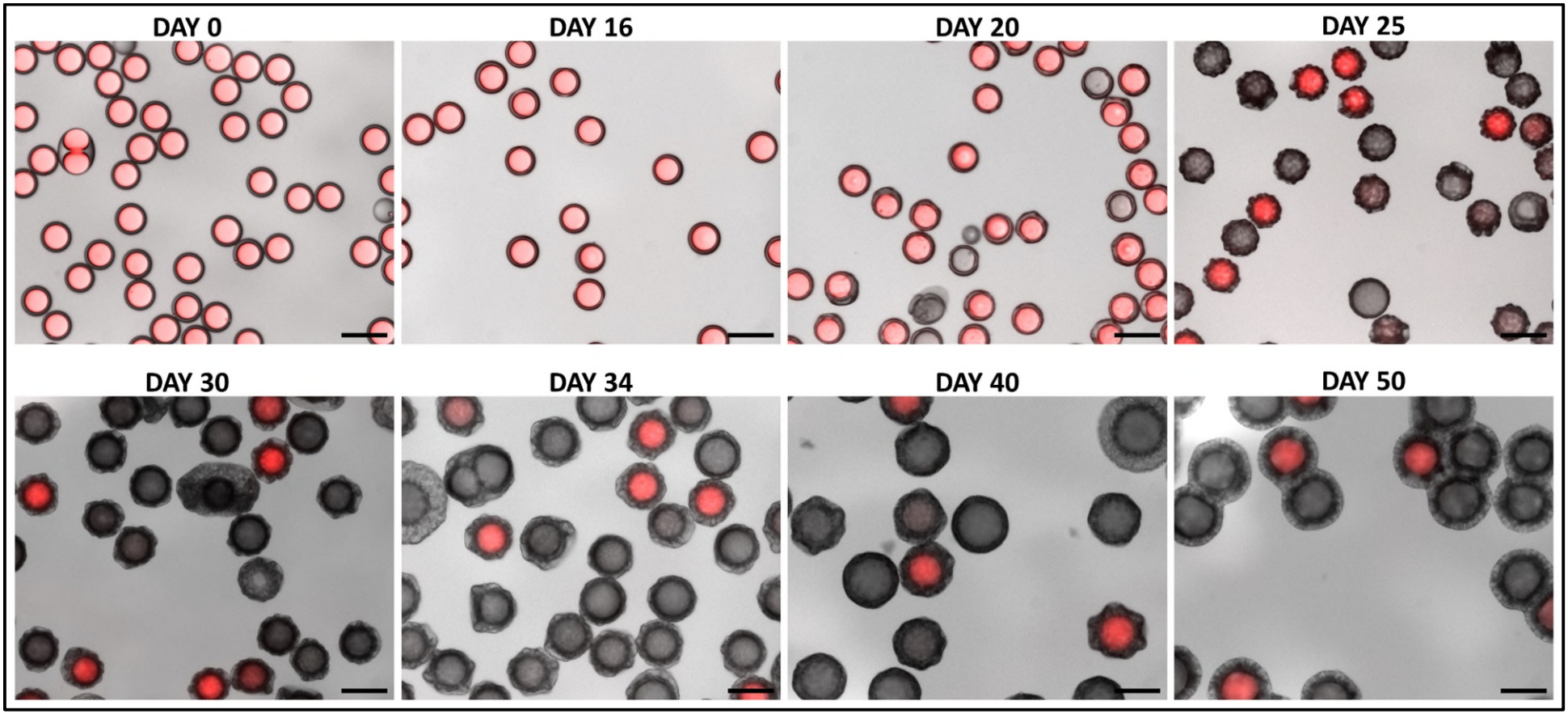

Figure 4-5: Fluorescent microscopy imaging of LCSS particle populations to assess morphology and loading across time during in vitro release.

Images of LCSS particles (PLGA 50:50 7-17kDa Mw) encapsulating dextran-TRITC were taken with 10X objective at different times of in vitro degradation (37°C in PBS, pH 7.4, with 0.01% Tween 80, under constant rotation of 20rpm). TRITC and brightfield channels are overlayed, same LUT is applied for all images. Black scale bar is 100µm.

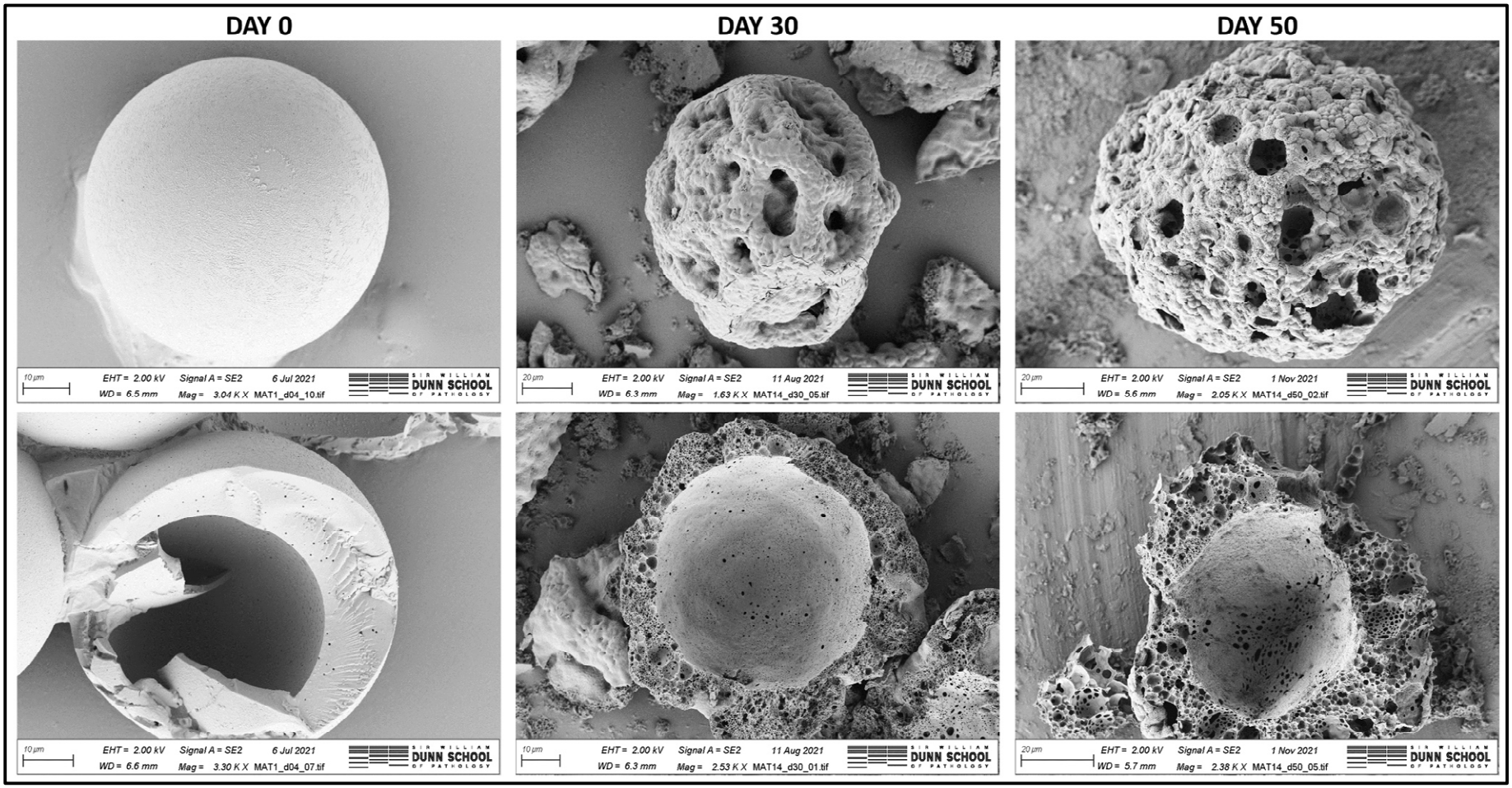

Figure 4-6: SEM imaging of LCSS particle morphology evolution with in vitro incubation.

SEM images of LCSS particles (PLGA 50:50 7-17kDa Mw) encapsulating dextran-TRITC taken at different time of in vitro degradation (37°C in PBS, pH 7.4, with 0.01%Tween 80, under constant rotation of 20rpm). Plain particles (upper row) and sectioned particles (lower row) are displayed. Magnification and scale bar are displayed in a detailed ribbon for each image.

The SEM images shown in **Figure 4-6** illustrate the process of bulk degradation of the polymer shell, evolving from a smooth appearance with few to none visible pores at day 0 to a rough, perforated appearance on days 30 and 50. A network of pores of up to a few micrometres in size forms in the swollen shell, creating a path that bridges the inside core to the outside of the particle, explaining the diameter increase shown in **Figure 4-4**. The pores are the result of the autocatalytic degradation of PLGA described earlier, whereby the acidic by-product remains trapped inside the polymer matrix, accumulates, reduces the local pH, and so increases the rate of hydrolysis, resulting in pore formation. By day 50, the integrity of the particles was drastically reduced with pores reaching 10μm in size. This pore network produced by degradation explains the observed increase in fluorescence in the shell of the particles (**Figure 4-7**).

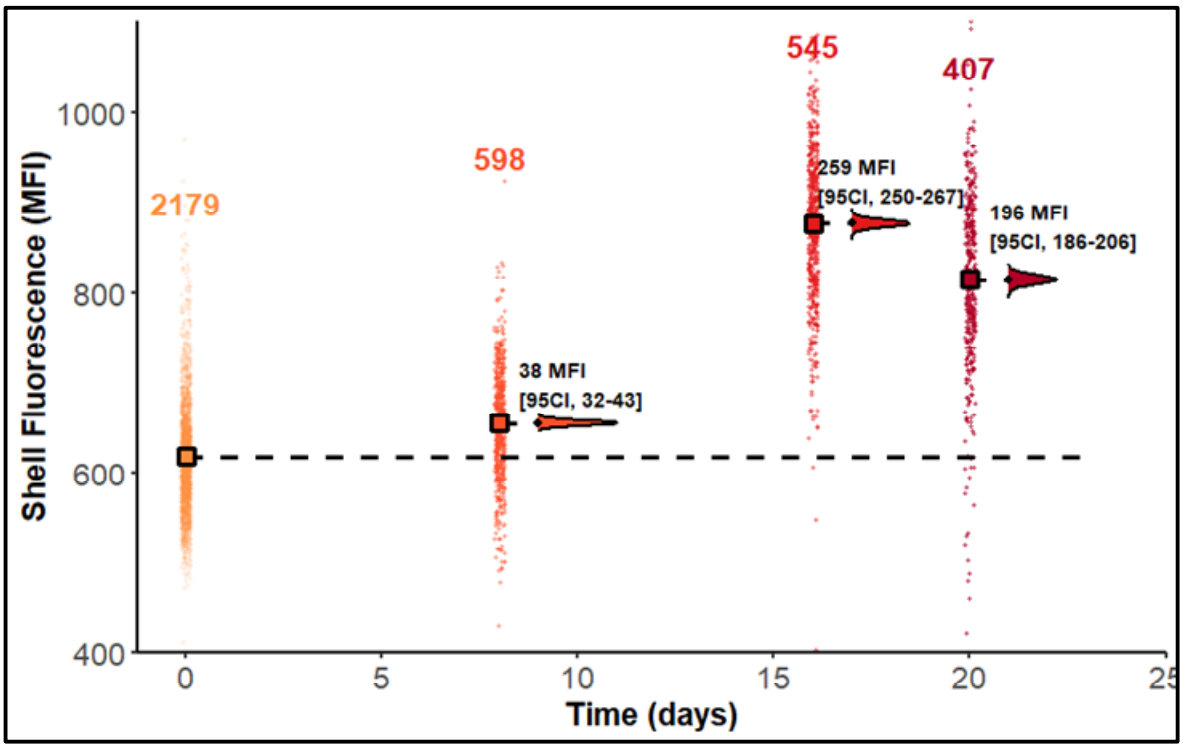

Figure 4-7: Fluorescence in the LCSS particles shell increases with time.

LCSS particles (PLGA 50:50 7-17kDa Mw) encapsulating dextran-TRITC taken with 10X objective at different timepoints of in vitro degradation (37°C in PBS, pH 7.4, with 0.01%Tween 80, under constant rotation of 20rpm). Evolution of the fluorescence signal (in MFI) in the shell was measured using a custom MATLAB script (Appendix I). All data were plotted as dots. Means are represented by the squares and bootstrap mean differences against the day 0 reference are displayed by a distribution histogram. Corresponding MFI mean difference and 95% CI are shown. The number n of particles analysed per timepoint is displayed above each marker.

Interestingly, some particles remained clearly loaded even after the observed release peak (**Figure 4-3**). When comparing the loading status of particles at an arbitrary MFI of 500 (based on **Figure 4-4**), the diameter of loaded and unloaded particles differed at day 30 of degradation, as displayed in **Figure 4-8**. Particles that released their content were significantly larger, by more than 5µm [95%CI, 4.3-6.4], suggesting a relationship between particle swelling and their ability to deliver the payload.

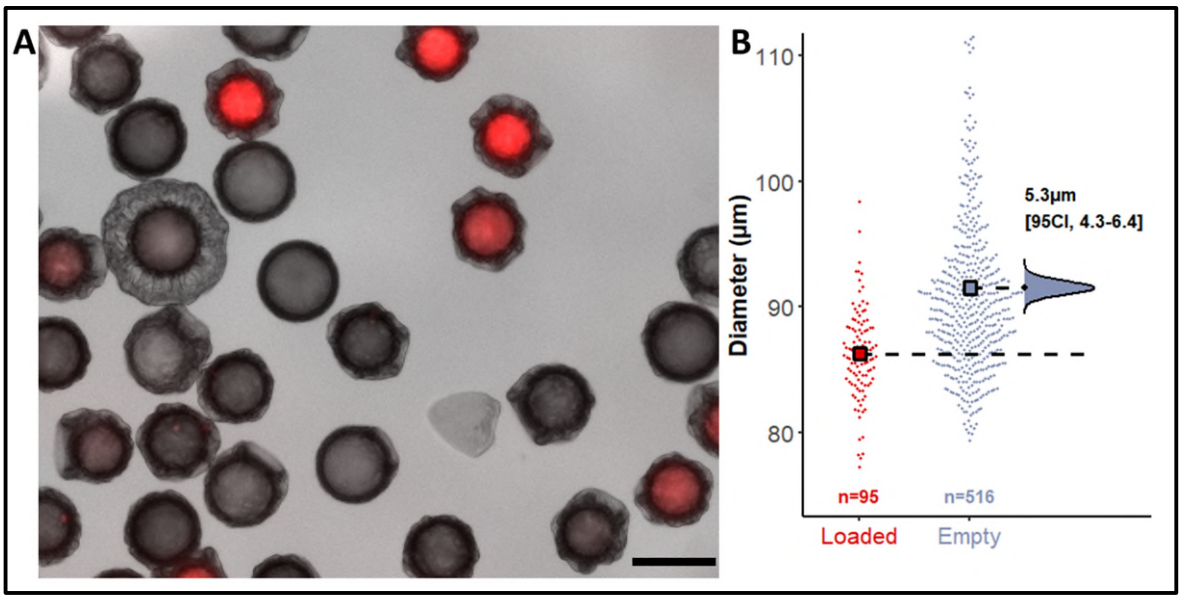

Figure 4-8: Diameter variation of LCSS particles depending on the loading status after 30 days of in vitro degradation.

LCSS particles (PLGA 50:50 7-17kDa Mw) encapsulating dextran-TRITC taken with 10X objective at day 30 of in vitro degradation (37°C in PBS, pH 7.4, with 0.01% Tween 80, under constant rotation of 20rpm). (A) Fluorescent microscopy images, TRITC and brightfield channels are overlayed, scale bar is 100µm. (B) Bee-swarm plot of diameter variation (µm) depending on loading status at day 30 of in vitro degradation. All data were plotted as dots. Means are represented by the squares and bootstrap mean differences against the loaded reference are displayed by a distribution histogram. Corresponding diameters mean difference and 95% CI are shown. The number n of particles analysed per timepoint is displayed for each population of particles.

4.3.3 The effect of LCSS particles shell thickness on their release is explained by autocatalysis

To further investigate the mechanism of release from LCSS particles, the effect of the shell thickness was investigated. Batches of particles were prepared with 3 distinct initial thicknesses of respectively 7.2µm, 6.1µm and 4.1µm (**Figure 4-9**) by varying the flow pressures during the microfluidic process (see Chapter 3). In this section, these batches are designated as “Thick”, “Medium” and “Thin” particles for

convenience. The Thick-shell batch corresponds to the LCSS particles studied in the previous sections.

The release characteristics for these three batches are presented in **Figure 4-10** and **Table 4-1**. The payload release was initiated after a lag of 14 days for Thick and 13 days for Medium LCSS particles. By day 21 (Thick) and 19 days (Medium) more than 80% of the payload had been released. Thin-shelled particles, however, exhibited a profile with two distinct peaks of release. The first peak occurred at 23 days, with an estimated 20% of the payload released at that time. The second release occurred at 85 days of the *in vitro* release, delivering 75% of the loaded content.

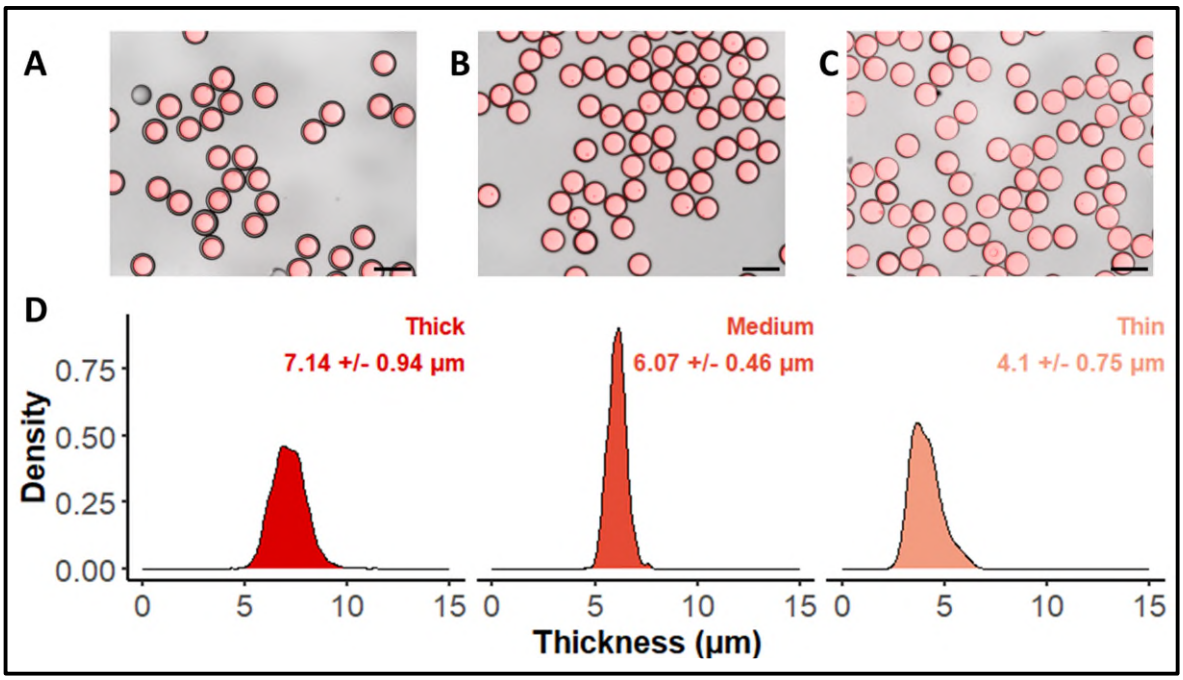

Figure 4-9: Initial thickness of different batches of LCSS particles produced by microfluidics before in vitro release study.

Microscopic images of particles with different thickness shells, manufactured by microfluidics, encapsulating fluorescent dextran-TRITC and suspended in PBS at room temperature. (A) Thick shell (B) Medium shell, and (C) Thin shell particle populations were imaged with a 10X objective. TRITC and brightfield channels are overlayed, same LUT is applied for all images, scale bar is 100 µm. (D) Thickness (µm) distribution as kernel plots of density estimates for each batch, with mean and SD reported.

Table 4-1: In vitro release Peak characteristics for different thicknesses

Thickness (µm)	**Peak Proportion** Mean % [95%CI]	**Peak Time** Mean days [95%CI]	**Peak Duration** Mean days [95%CI]	**Peak Lag** Mean days [95%CI]
7.2	**85.3** *[82.6-88.0]*	**21.4** *[20.5-22.3]*	**13.1** *[10.9-15.3]*	**14.4** *[12.2-16.5]*
6.1	**82.1** *[72.6-91.7]*	**18.6** *[18.3-18.9]*	**14.6** *[14.0-15.3]*	**13.0** *[12.9-13.1]*
4.1 *Peak1*	**20.7** *[7.8-33.7]*	**23.0** *[22.1-24.0]*	**11.9** *[9.6-14.2]*	**15.6** *[13.9-17.2]*
4.1 *Peak2*	**75.1** *[61.8-88.4]*	**84.8** *[84.5-85.1]*	**29.4** *[27.0-31.9]*	**60.6** *[58.1-63.0]*

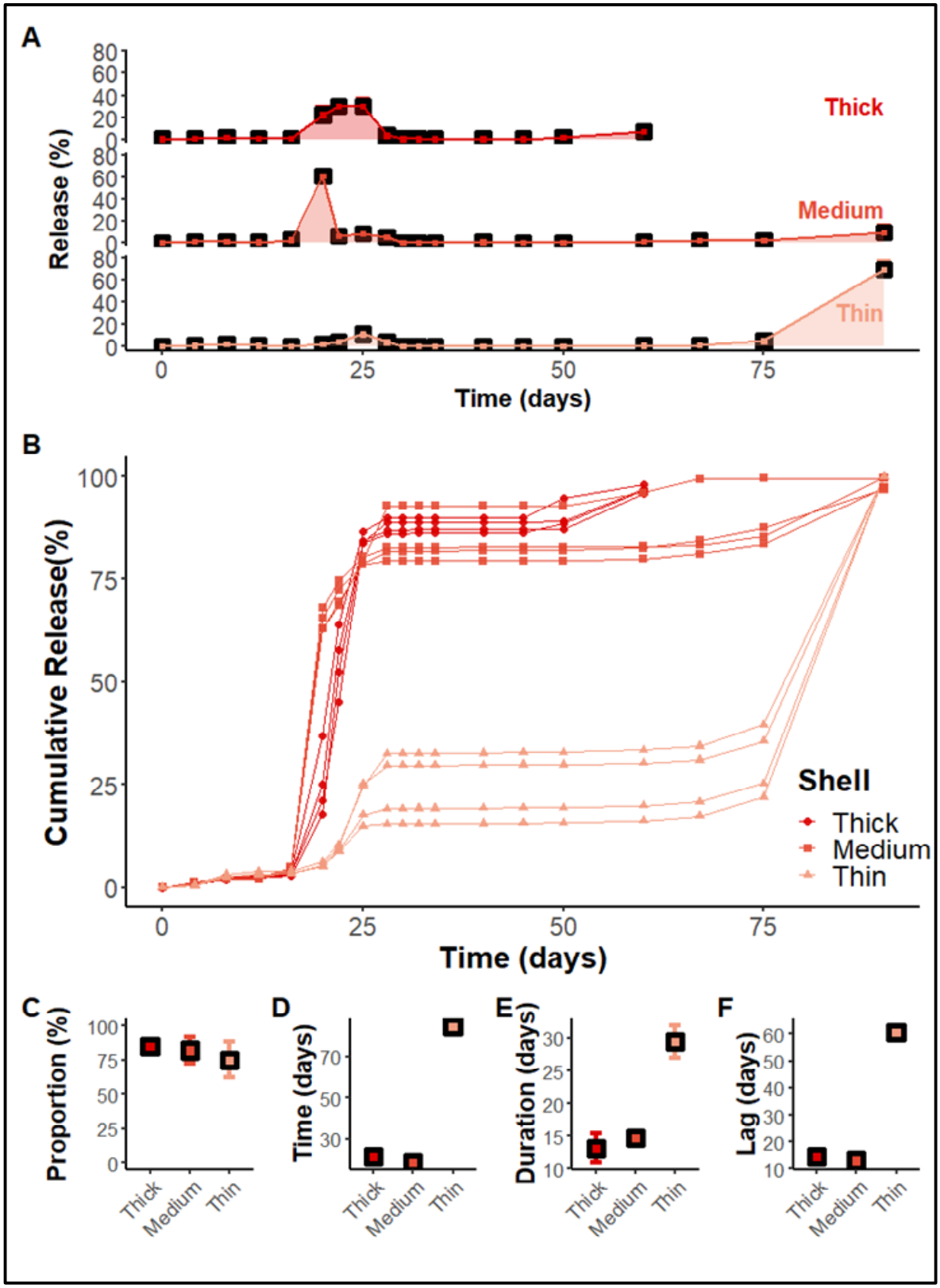
A
Release (%)
Thick
Medium
Thin
Time (days)
B
Cumulative Release(%)
Shell
Thick
Medium
Thin
Time (days)
C
Proportion (%)
D
Time (days)
E
Duration (days)
F
Lag (days)
Thick
Medium
Thin

Figure 4-10: Effect of the shell thickness on the release kinetics of LCSS particles.

Summary of in vitro release kinetics from LCSS particles with different initial shell thickness, manufactured by microfluidics, encapsulating fluorescent 40kDa dextran-TRITC. Each batch (n=4 replicates for each type) was incubated at 37°C in PBS, pH 7.4, with 0.01% Tween 80, under constant rotation of 20rpm. Dextran release was measured by spectrophotometry. Results are reported as (A) Measured release over time (Mean of replicates +/- SD), (B) Cumulative release of each replicate over time, and (C-F) Main Peaks characteristics for each particle type (Mean and 95%CI assuming student's distribution) as described in section 4.2.

The effect of the shell thickness on particle degradation was also visible in the SEM images (**Figure 4-11** for Medium and Thin, Thick can be seen in **Figure 4-6**, day 30). Thick and Medium-shell particles were in a more degraded state after 30 days of *in vitro* degradation, with visible shell perforations and a developed pore network across the polymer matrix, visibly reaching the core. In contrast, Thin-shell particles were smoother, less indented by degradation, and the pore network formed within the shell was less interconnected.

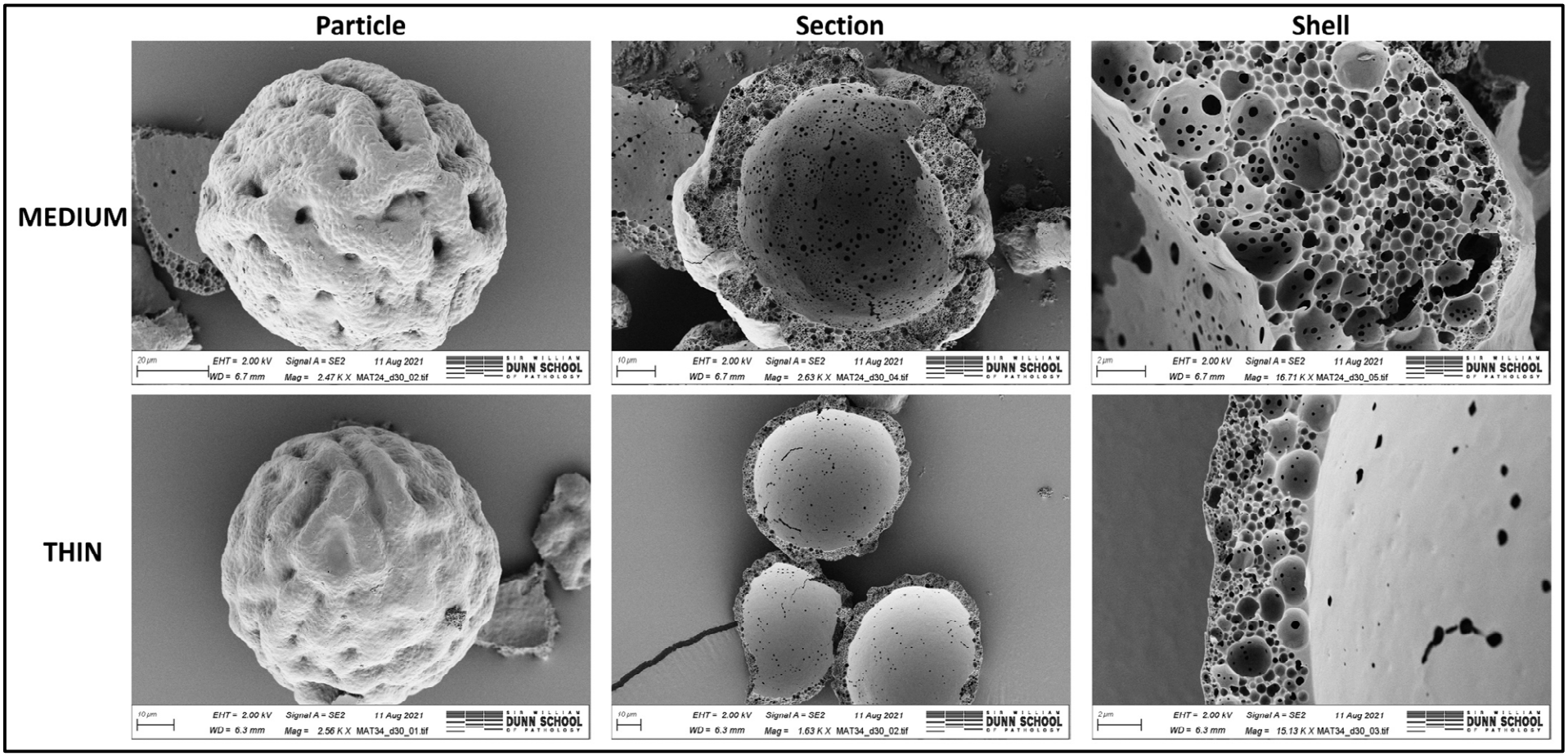

Figure 4-11: SEM imaging of LCSS particles with different initial thicknesses following 30 days of in vitro incubation.

SEM images of LCSS particles (PLGA 50:50 7-17kDa Mw) of Medium and Thin initial thickness encapsulating dextran-TRITC taken at day 30 of in vitro degradation (37°C in PBS, pH 7.4, with 0.01% Tween 80, under constant rotation of 20rpm). Full particles (left), sectioned particles (middle), and corresponding shell high magnifications (right) are displayed. Magnifications and scale bar are displayed in a detailed ribbon for each image.

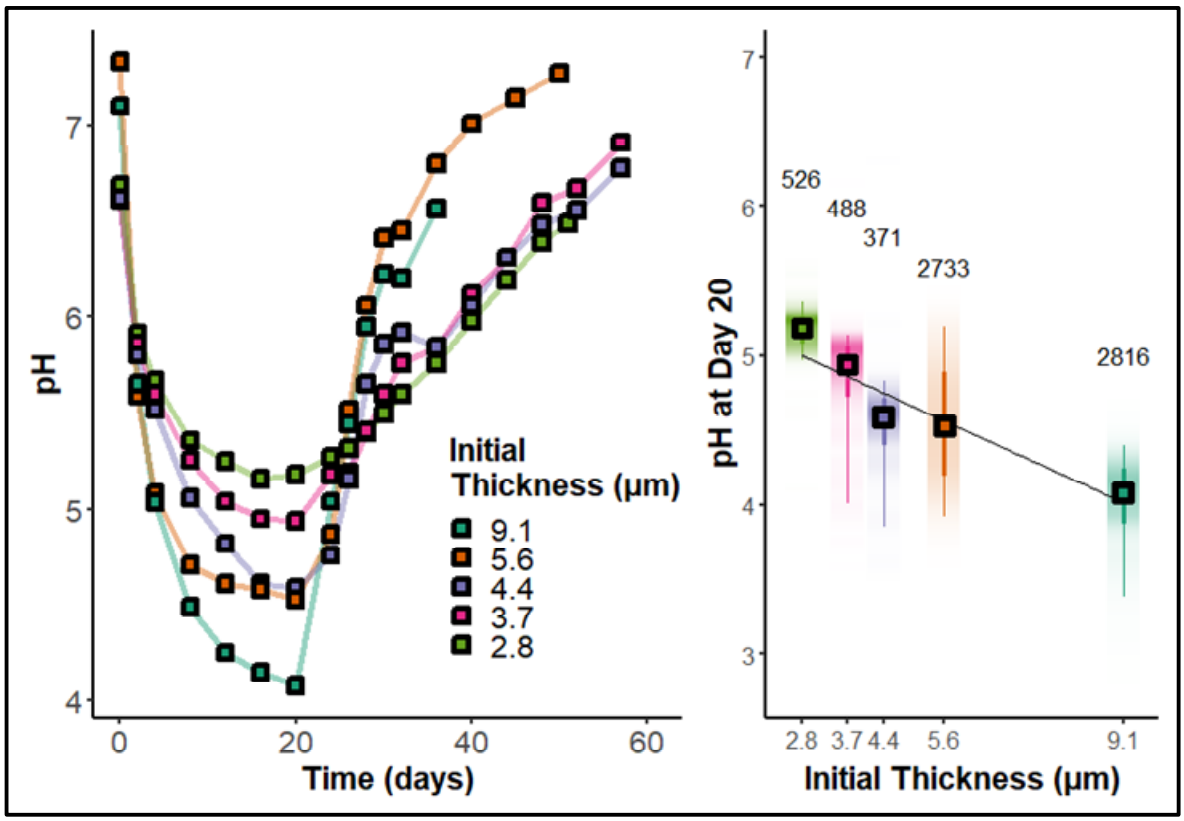

Figure 4-12: Internal pH evolution with in vitro degradation of LCSS particles of different initial shell thickness.

LCSS particles (PLGA 50:50 7-17kDa Mw) encapsulating dextran-TRITC/FITC were monitored by microscopy at different timepoints of vitro incubation (37°C in PBS, pH 7.4, with 0.01% Tween 80, under constant rotation of 20rpm). Image processing was performed automatically by a MATLAB custom script to determine (Left) internal pH from TRITC/FITC fluorescence at different timepoints depending on the initial thickness of the particle batch (Mean). (Right) Internal pH distribution at day 20 of in vitro degradation; each dot represents one particle analysed; the number of particles analysed for each timepoint is displayed in black above points; black line shows linear regression result.

To explain these morphological differences, and because the pore network was formed due to autocatalysis with acidic pH, the evolution of the pH inside the capsules at different timepoints and for different initial thicknesses was followed by encapsulating dextran TRITC/FITC as the payload. The pH was determined using a calibration curve, from the FITC/TRITC signal ratio from the core of the particles, since FITC fluorescence is sensitive to pH while TRITC is not. The evolution with

time of the internal pH for batches produced with 5 different initial shell thicknesses is presented in **Figure 4-12** and images illustrating the phenomenon are displayed in **Figure 4-13**. All particle batches presented the same profile: the pH inside the core initially dropped, as more acidic by-products were produced from the polymer degradation. The internal pH decreased more with the initial thickness of the different batches. Thus, the minimum was reached at day 20 and presented a linear trend with the initial shell thickness (linear regression slope = -0.156 pH-unit/μm [95%CI -0.159, -0.153]). After day 20, which corresponds to the release time for this PLGA formulation, the internal pH rose back towards pH7. The rate of pH rise was steeper for the initially thicker particles.

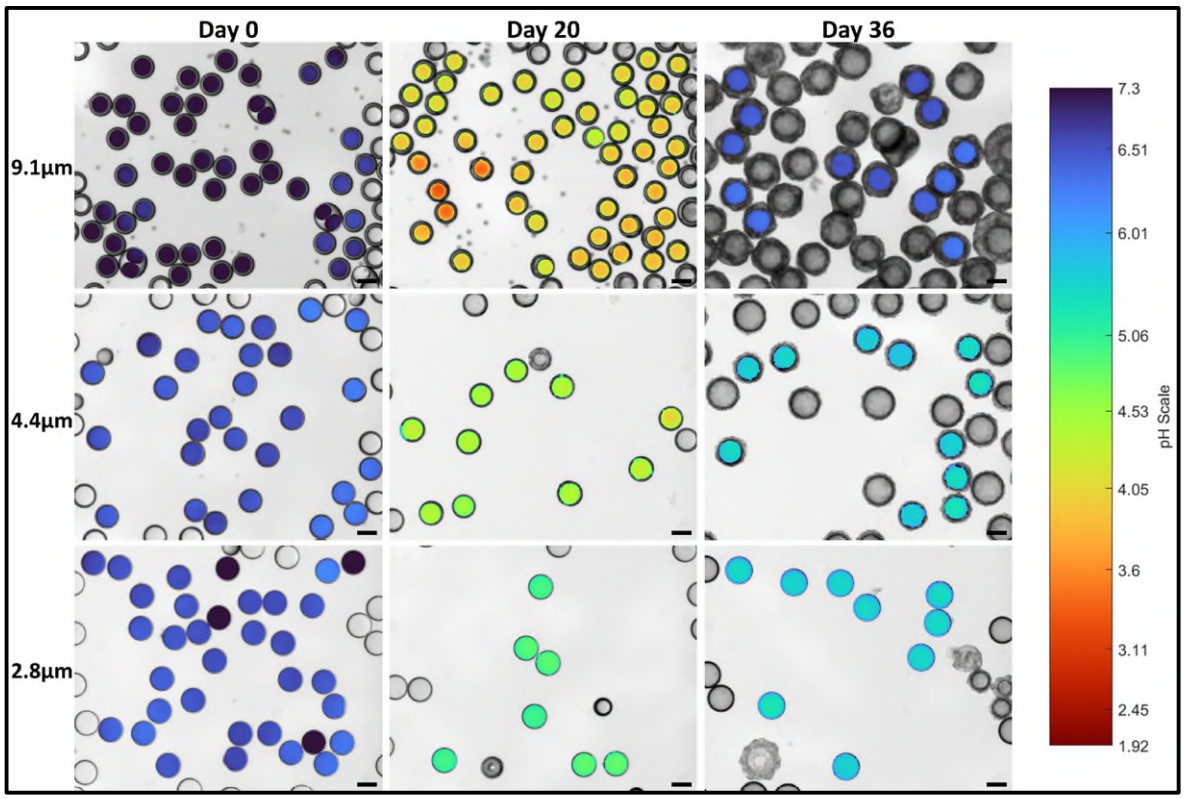

Figure 4-13: Microscopy images of the internal pH of particles with different initial thicknesses at different timepoints of in vitro degradation.

Microscopic images of particles with different thicknesses, manufactured by microfluidics, encapsulating fluorescent dextran-TRITC/FITC were incubated in vitro (37°C in PBS, pH 7.4, with 0.01% Tween 80, under constant rotation at 20rpm) and imaged using a 10X objective on an inverted microscope at different timepoints. Images are displayed for different initial thicknesses (row) at different timepoints (columns). The measured internal core pH computed from the TRITC/FITC signal ratio is overlayed (MATLAB). The pH value scale bar is displayed on the right, black scale bar = 50µm.

4.3.4 Influence of the Mw of the Payload

Using dextran payloads of different Mw, encapsulated inside the same formulation of PLGA (7-17 kDa Mw, 50:50 L:G), the effect of the hydrodynamic radius (Rh) of the dextran on the release characteristics was monitored (**Figure 4-14**). No large differences were observed. All 3 batches of particles containing different dextran solutions with Rh of 6.5, 4.8 and 1.8 respectively presented a triphasic release with a main peak of release occurring between 18 and 22 days. The release timing and

lag increased slightly with the Rh of the dextran. The proportion released during the peak was more variable between replicates for the batch with lowest Rh. Estimates for all peak characteristics are displayed in **Table 4-2**.

Table 4-2: In vitro release Peak characteristics for different payload sizes

Payload Rh (nm)	**Peak Proportion** Mean % [95%CI]	**Peak Time** Mean days [95%CI]	**Peak Duration** Mean days [95%CI]	**Peak Lag** Mean days [95%CI]
6.5	**79.4** *[68.5-90.4]*	**21.8** *[19.3-24.4]*	**7.4** *[2.7-12.2]*	**18.3** *[13.8-22.8]*
4.8	**85.3** *[82.6-88.0]*	**21.4** *[20.5-22.3]*	**13.1** *[10.9-15.3]*	**14.4** *[12.2-16.5]*
1.6	**72.1** *[49.2-95]*	**18.8** *[16.4-21.1]*	**8.2** *[6.8-9.5]*	**13.7** *[10.9-16.5]*

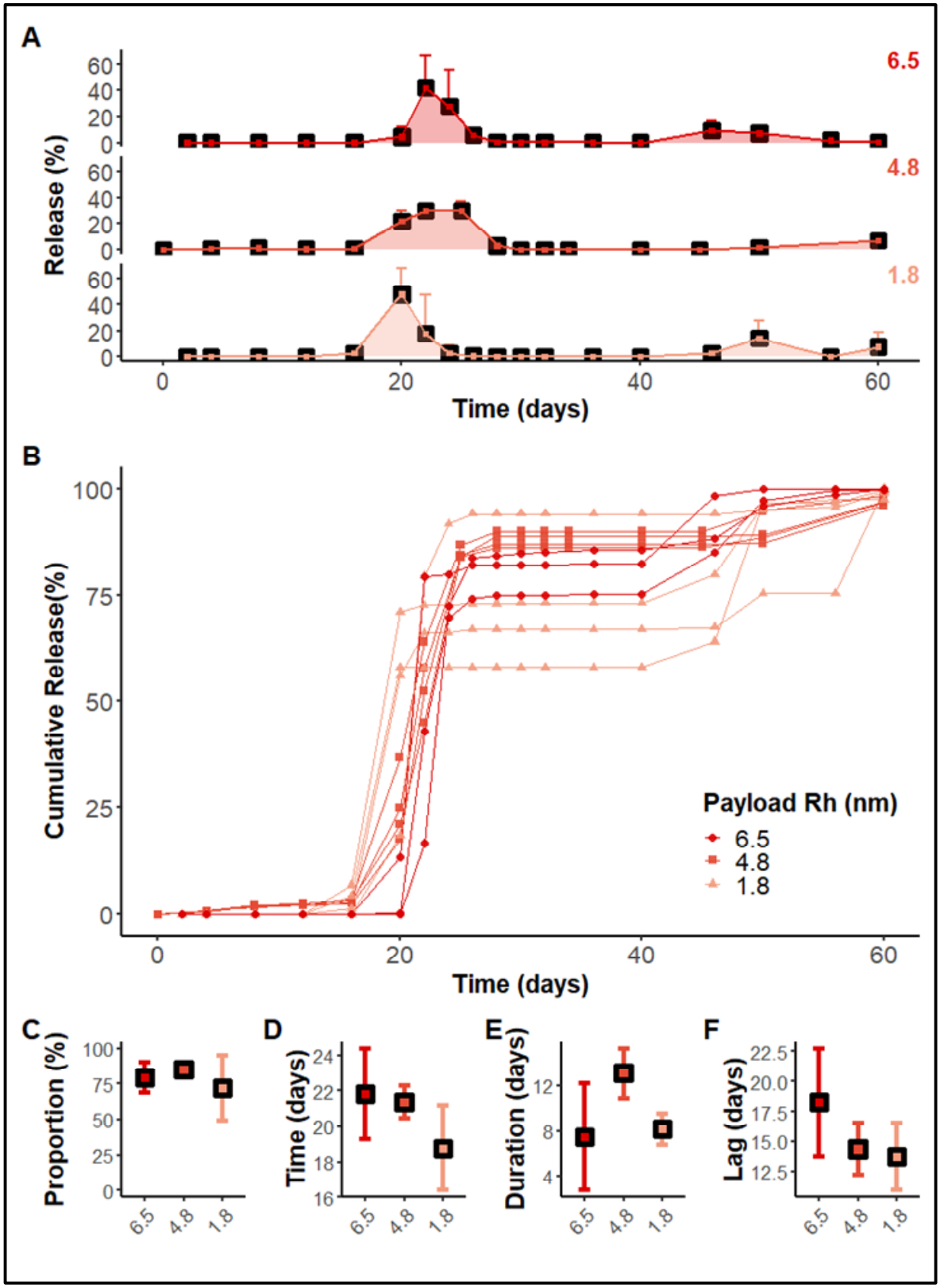
A
Release (%)
6.5
4.8
1.8
Time (days)
B
Cumulative Release(%)
Payload Rh (nm)
6.5
4.8
1.8
Time (days)
C
Proportion (%)
D
Time (days)
E
Duration (days)
F
Lag (days)

Figure 4-14: Effect of the payload size on the release kinetics of LCSS particles.

Summary of in vitro release kinetics from LCSS particles encapsulating different dextran-TRITC hydrodynamic radii (Rh), manufactured by microfluidics. Each batch (n=3 replicates for Rh=6.5, n=4 replicates for other) was incubated at 37°C in PBS, pH 7.4, with 0.01%Tween 80, under constant rotation of 20rpm. Dextran release was measured by spectrophotometry. Results are reported as (A) Measured release over time (Mean of replicates +/- SD), (B) Cumulative release of each replicate over time, and (C-F) Main Peak characteristics for each particle type (Mean and 95%CI assuming student distribution) as described in section 4.2.

4.3.5 Effect of polymer formulation on the payload release of LCSS particles

For the delayed release technology to be applicable to different vaccines, different timings of release are required, to correspond to different vaccine prime-boost intervals. As PLGA degradation is dependent on the molecular weight and Lactide:Glycolide (L:G) ratio of the polymer, their effect on the release profile of the LCSS particles was studied.

4.3.5.1 Increasing the PLGA Mw in LCSS particles increases the Peak time by order of days

By increasing the Mw of the PLGA, the polymer chains become longer and require more time to degrade [131]. This change in degradation time was translated in the release kinetics when PLGA with different Mw were used for the shell. Four different LCSS particles batches were produced by microfluidics using formulations of PLGA with MW of 7-17kDa, 24-38kDa, 38-54kDa, and 54-69kDa respectively. The resulting kinetic profile from their *in vitro* release is reported in **Figure 4-15**, with main release Peak characteristics detailed in **Table 4-3**.

Table 4-3: In vitro release Peak characteristics for different PLGA molecular weights

Molecular Weight (kDa)	**Peak Proportion** Mean % [95%CI]	**Peak Time** Mean days [95%CI]	**Peak Duration** Mean days [95%CI]	**Peak Lag** Mean days [95%CI]
7-17	**85.3** *[82.6-88.0]*	**21.4** *[20.5-22.3]*	**13.1** *[10.9-15.3]*	**14.4** *[12.2-16.5]*
24-38	**70.5** *[68.4-72.5]*	**22.4** *[20.1-24.7]*	**20.3** *[17.7-23.0]*	**8.2** *[7.2-9.2]*
38-54	**81.6** *[79.4-83-9]*	**26.2** *[25.0-27.4]*	**16.8** *[13.5-20.1]*	**16.3** *[15.7-16.9]*
54-69	**72.1** *[70.9-73.4]*	**32.8** *[30.7-35.0]*	**17.7** *[15.9-19.4]*	**23.0** *[20.5-25.5]*

All formulations presented a triphasic profile, with a larger initial burst release for the 24-38kDa batch. Their main peak of release yielded a high proportion of the payload, higher than 70% for all formulations. Both Times and Lags of the Peaks (**Figure 4-15** D and F) demonstrated a significant monotonic increase with the increase of polymer Mw (Jonckheere-Terpstra test, p-value = $3x10^{-6}$ for Time, p-value = 0.003 for Lag). Thus, release peak time ranged from 21 days for the lowest molecular weight (7-17kDa) up to 33 days for the highest molecular weight assessed (54-69kDa), demonstrating the ability to extend the release delay. Switching from the lowest molecular weight PLGA (7-17kDa) to the highest (54-69kDa) provided a significant increase in Lag time, estimated at 8.6 additional days [95%CI 7.0-10.3] using linear regression and contrasts. Therefore, the impact of this range of PLGA Mw on the release was of the order of days, extending the exposure to the payload (Lag) by a maximum of a week.

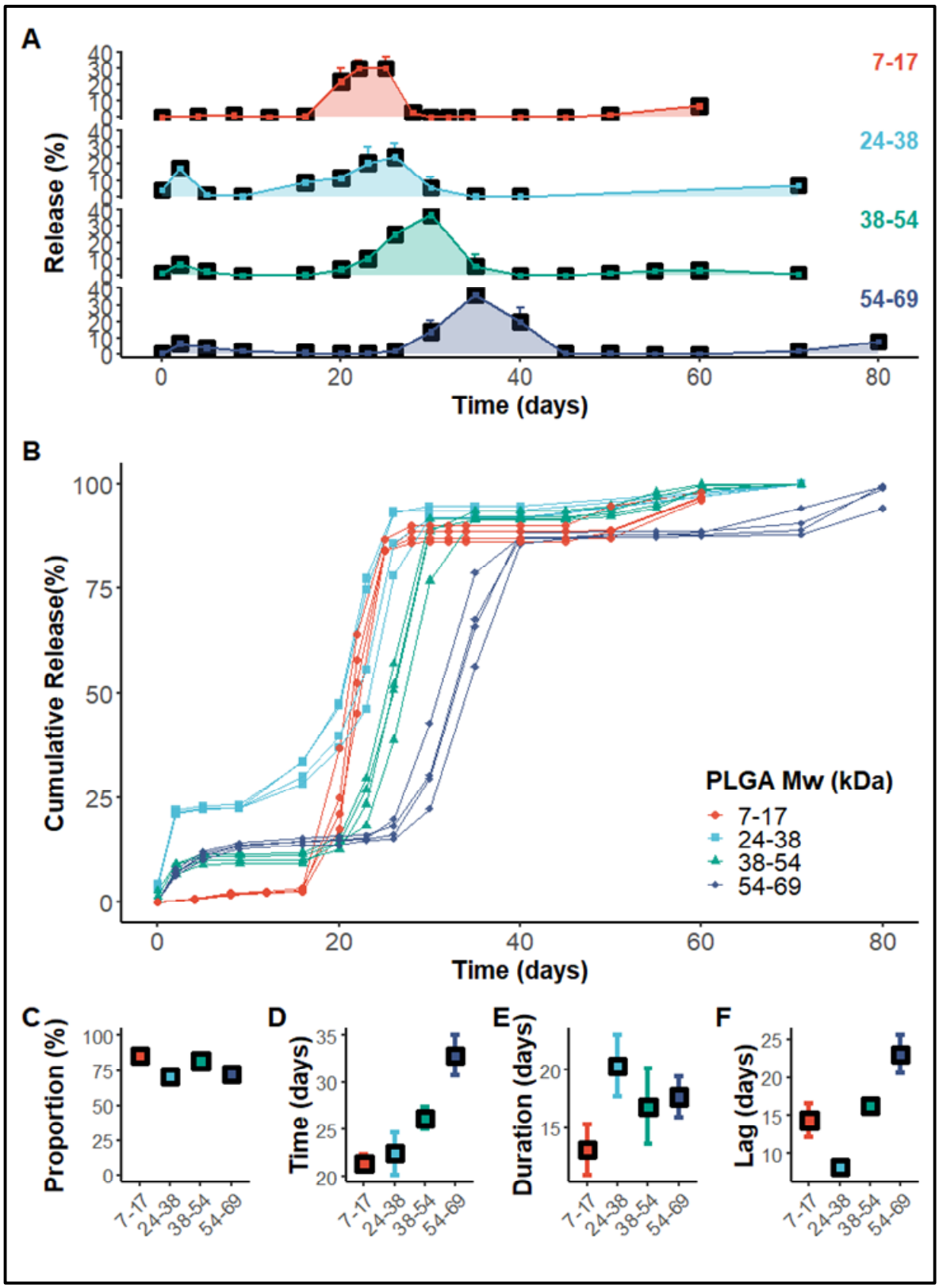
A
Release (%)
7-17
24-38
38-54
54-69
Time (days)
B
Cumulative Release(%)
PLGA Mw (kDa)
7-17
24-38
38-54
54-69
Time (days)
C
Proportion (%)
D
Time (days)
E
Duration (days)
F
Lag (days)

Figure 4-15: Effect of the PLGA molecular weight on the release kinetics of LCSS particles.

Summary of in vitro release kinetics from LCSS particles encapsulating 40kDa dextran-TRITC with the shell made of different Mw PLGA, manufactured by microfluidics. Each batch (n=4 replicates) was incubated at 37°C in PBS, pH 7.4, with 0.01% Tween 80, under constant rotation of 20rpm. Dextran release was measured by spectrophotometry. Results are reported as (A) Measured release over time (Mean of replicates +/- SD), (B) Cumulative release of each replicate over time, and (C-F) Main Peaks characteristics for each particle type (Mean and 95%CI assuming Student's distribution) as described in section 4.2.

Looking more specifically at the highest Mw PLGA formulation using fluorescence microscopy (**Figure 4-16**), there was no significant change in loading until day 30, after which there was a fall from 77.6% to 17.5% loaded particles by day 40 (considering a loading threshold of 500MFI). This implied a rapid content release between day 30 and 40, consistent with the release measured in **Figure 4-15**. The diameter of the particles also increased over this period, indicating that the mechanism of release for LCSS particles detailed in section 4.3.2 was the same for different PLGA Mw. The SEM imaging (**Figure 4-17**) revealed that the same network of pores was formed across the polymer matrix, connecting the core to the outside. However, this pore network was less developed at day 30 compared to the lower Mw PLGA formulation (**Figure 4-6**), illustrating the slower degradation of PLGA with a higher Mw.

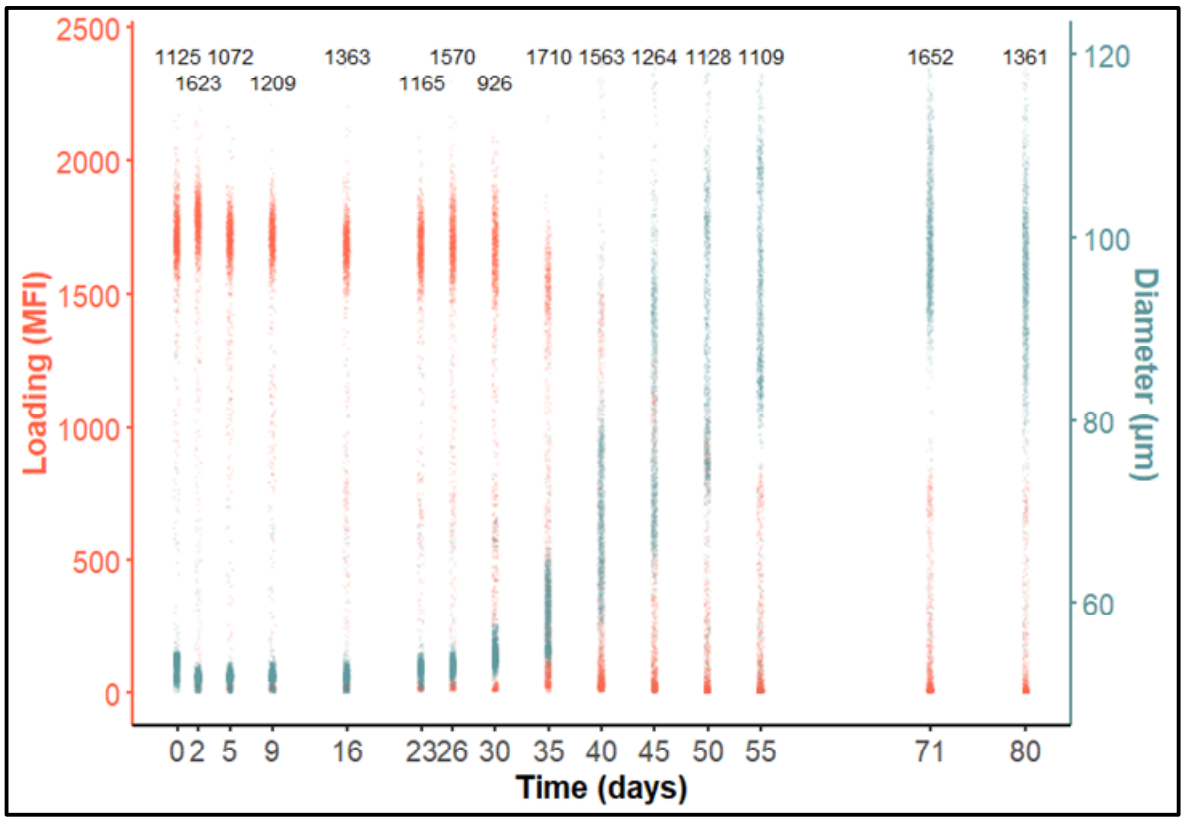

Figure 4-16: Loading and diameter distribution evolution with in vitro degradation of High Mw core-shell particles.

LCSS particles (PLGA 50:50 54-69kDa Mw) encapsulating dextran-TRITC were monitored by microscopy imaging at different timepoints of vitro incubation (37°C in PBS, pH 7.4, with 0.01% Tween 80, under constant rotation of 20rpm). Image processing was performed automatically by MATLAB custom script and distributions of the loading and diameter are reported at different timepoints. Each dot represents one particle analysed; loading is represented by Mean Fluorescence Intensity (MFI) from the encapsulated dextran-TRITC. Diameter is expressed in µm. The number of particles analysed for each timepoint is displayed in black above the points.

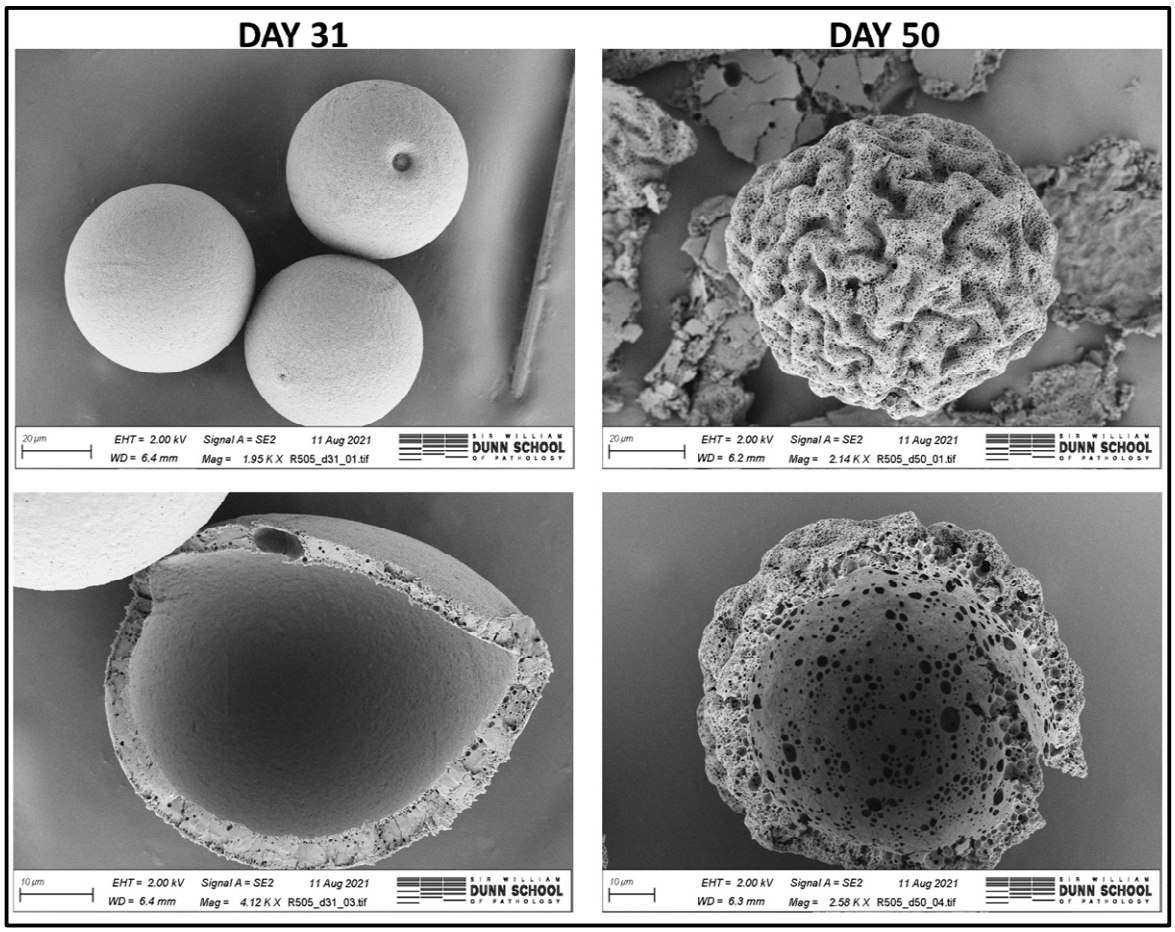

Figure 4-17: SEM imaging of particles with high Mw PLGA at different times of in vitro incubation

SEM images of LCSS particles (PLGA 50:50 54-69kDa Mw) encapsulating dextran-TRITC taken at day 31 (left) and 50 (right) of in vitro degradation (37°C in PBS, pH 7.4, with 0.01% Tween 80, under constant rotation of 20rpm. Full particles (top row), and sections (bottom row) are displayed. Magnifications and scale bar are displayed in a detailed ribbon for each image.

4.3.5.2 Increasing the PLGA Lactide:Glycolide ratio in LCSS particles increases the Peak time by order of weeks to months

The lactide content in the PLGA polymer chains is another factor influencing the degradation rate of the polymer [131], [133], as it affects the hydrophobicity of the matrix. Lactic acid contains an additional methyl group compared to glycolic acid

and water diffuses more slowly in a hydrophobic environment, thus reducing the rate of hydrolysis of the polymer ester groups.

The effect of increasing the lactide content of the PLGA was assessed by comparing LCSS particles formulations with same polymer Mw but different L:G ratios.

First batches of LCSS particles made with 24-38kDa PLGA of either 50:50 or 75:25 L:G ratio were produced by microfluidics and their release kinetics assessed *in vitro*. The release profiles were once again triphasic (**Figure 4-18**) and the Peak characteristics (**Table 4-4**) demonstrated that changing the L:G ratio to 75:25, substantially increased the Peak timing of release, from 22 days to more than 75 days. The proportion released with this higher L:G ratio formulation was more than 85% of the total loading, but the release was more widespread, over a period of 38 days.

Table 4-4: In vitro release Peak characteristics for a PLGA with 75:25 L:G ratio

L:G ratio	**Peak Proportion** Mean % [95%CI]	**Peak Time** Mean days [95%CI]	**Peak Duration** Mean days [95%CI]	**Peak Lag** Mean days [95%CI]
50:50	**70.5** *[68.4-72.5]*	**22.4** *[20.1-24.7]*	**20.3** *[17.7-23.0]*	**8.2** *[7.2-9.2]*
75:25	**85.5** *[79.4-91.6]*	**76.6** *[69.2-84.0]*	**38.1** *[33.3-42.8]*	**57.0** *[48.7-65.3]*

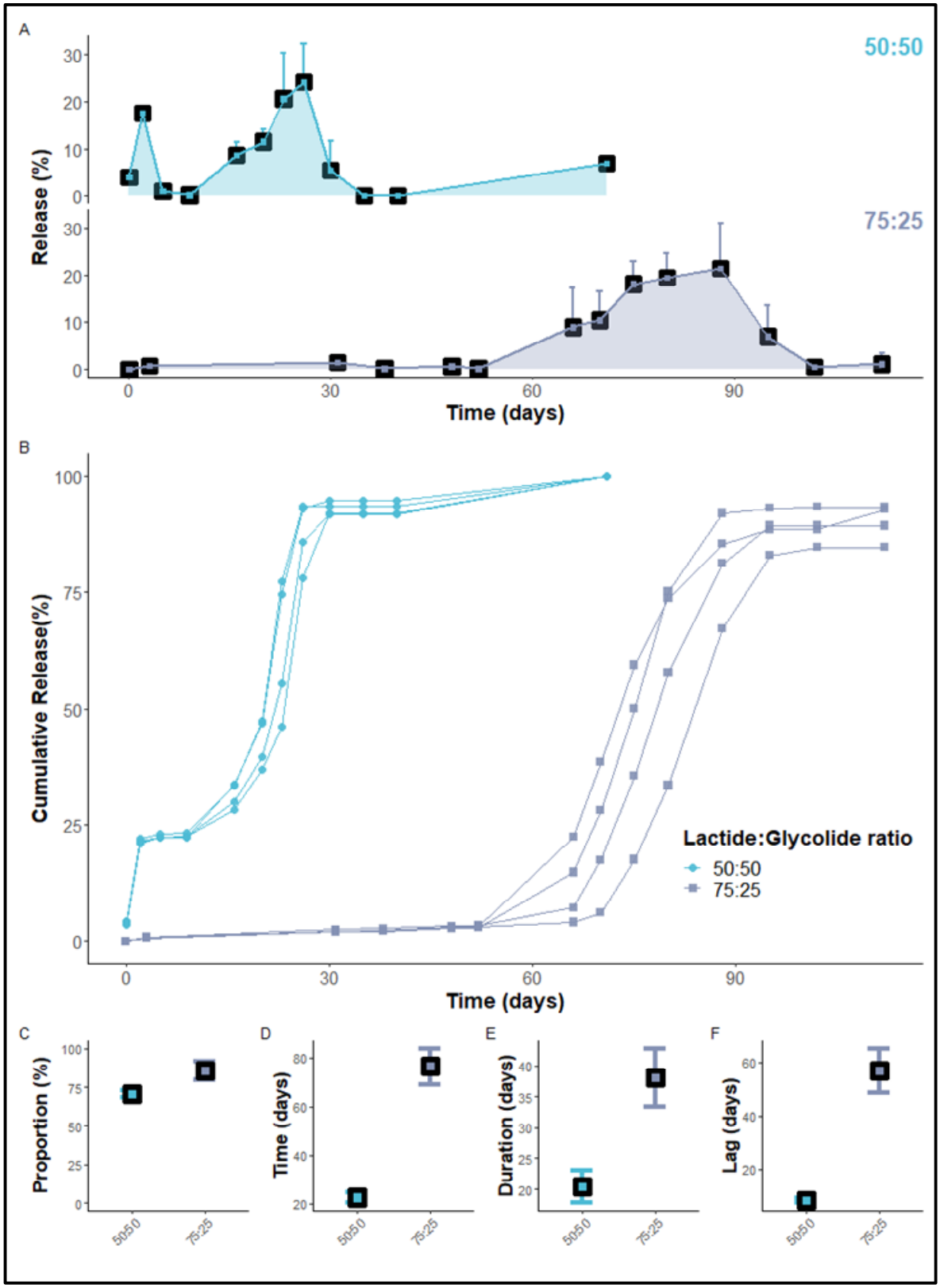
A
50:50
75:25
Release (%)
Time (days)
B
Cumulative Release(%)
Time (days)
Lactide:Glycolide ratio
50:50
75:25
C
Proportion (%)
D
Time (days)
E
Duration (days)
F
Lag (days)

Figure 4-18: Effect of a 75:25 L:G ratio on release kinetics of LCSS particles.

Summary of in vitro release kinetics from LCSS particles encapsulating 40kDa dextran-TRITC with PLGA (24-38kDa Mw) of different L:G ratio as shell, manufactured by microfluidics. Each batch (n=4 replicates) was incubated at 37°C in PBS, pH 7.4, with 0.01% Tween 80, under constant rotation at 20rpm. Dextran release was measured by spectrophotometry. Results are reported as (A) Measured release over time (Mean of replicates +/- SD), (B) Cumulative release of each replicate over time, and (C-F) Main Peak characteristics for each particle type (Mean and 95%CI assuming student distribution) as described in section 4.2.

Switching to the 75:25 L:G ratio formulation extended the lag time), i.e. the delay before first content release, a relevant parameter for vaccination, by 48.8 days [95%CI 42.4-55.2] (estimated by linear regression).

Another comparison was made using batches of particles with 7-17kDa PLGA and L:G ratios of 50:50 or 100:0 (pure polylactic acid - PLA). Triphasic release was also observed for the pure PLA formulation (**Figure 4-19**), the Peak time was close to 6 months, with the release spreading over 3 months (**Table 4-5**). The lag was extended by more than 3 months (linear regression - 97.5 days [95%CI 86.5-108.5]) using a L:G ratio of 100:0 compared to the 50:50 formulation.

Table 4-5: In vitro release Peak characteristics for a PLA with 100:0 L:G ratio

L:G ratio	**Peak Proportion** Mean % [95%CI]	**Peak Time** Mean days [95%CI]	**Peak Duration** Mean days [95%CI]	**Peak Lag** Mean days [95%CI]
50:50	**85.3** *[82.6-88.0]*	**21.4** *[20.5-22.3]*	**13.1** *[10.9-15.3]*	**14.4** *[12.2-16.5]*
100:00	**84.8** *[44.3-125.3]*	**171.8** *[130.3-213.2]*	**105.5** *[79.0-132.0]*	**111.5** *[97.4-125.6]*

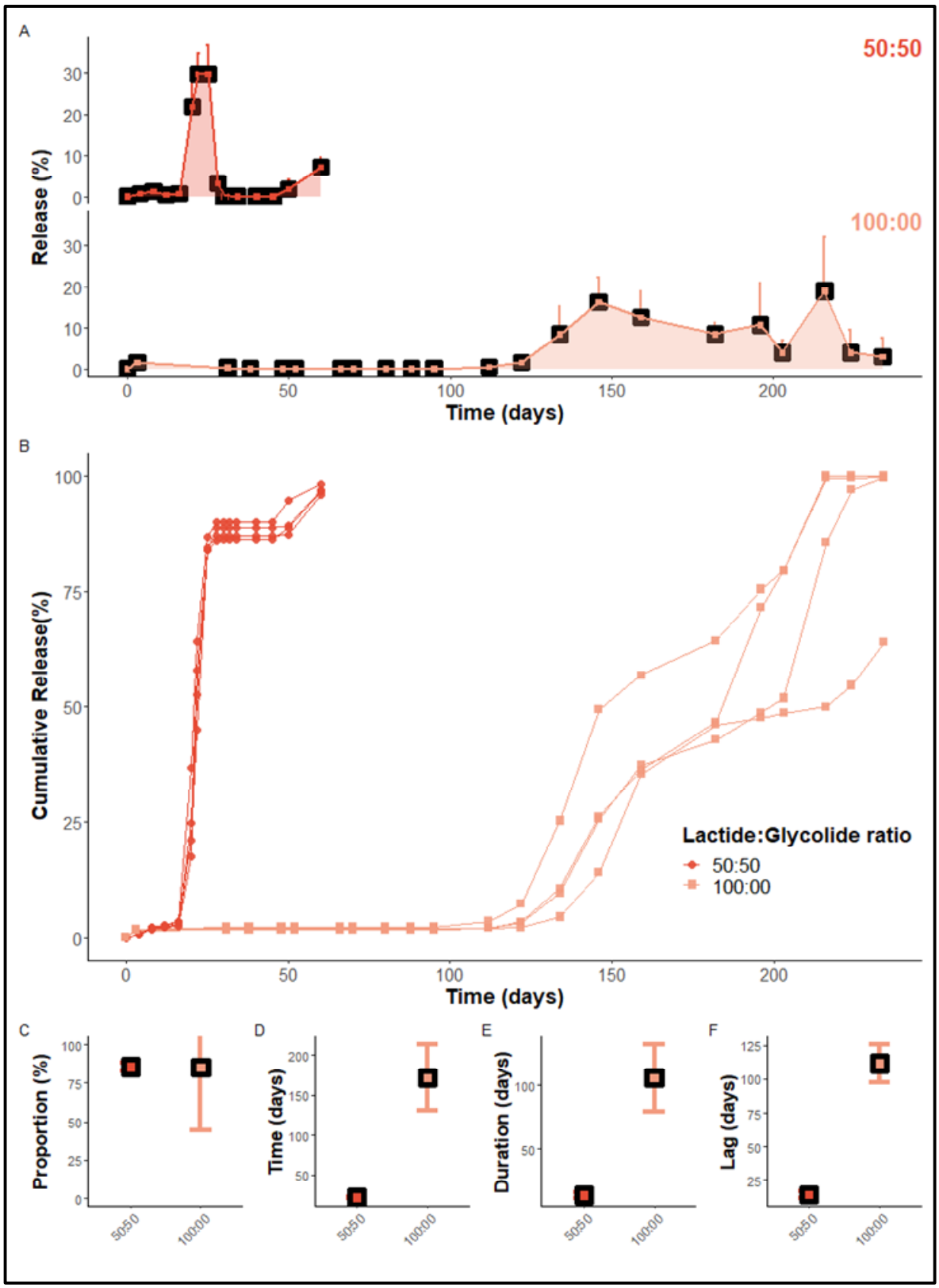
A
50:50
100:00
Release (%)
Time (days)
B
Cumulative Release(%)
Time (days)
Lactide:Glycolide ratio
50:50
100:00
C
Proportion (%)
D
Time (days)
E
Duration (days)
F
Lag (days)

Figure 4-19: Effect of a 100:00 L:G ratio on release kinetics of LCSS particles.

Summary of in vitro release kinetics from LCSS particles encapsulating 40kDa dextran-TRITC with PLGA (7-17kDa Mw) of different L:G ratio as shell, manufactured by microfluidics. Each batch (n=4 replicates) was incubated at 37°C in PBS, pH 7.4, with 0.01% Tween 80, under constant rotation at 20rpm. Dextran release was measured by spectrophotometry. Results are reported as (A) Measured release over time (Mean of replicates +/- SD), (B) Cumulative release of each replicate over time, and (C-F) Main Peaks characteristics for each particle type (Mean and 95%CI assuming student distribution) as described in section 4.2.

Overall, both the Mw of the polymer and L:G ratio were shown to significantly change the rate of release from LCSS particles while keeping the same release profile. Polymer Mw extended the lag in order of days to a week while polymer L:G ratio extended it by weeks to months.

4.3.6 Additional relevant parameters for vaccine delivery

4.3.6.1 Refrigeration

Vaccine storage is a key aspect in ensuring its successful deployment. To investigate whether refrigerating the particles affected their degradation or ability to release the payload, a fraction of the LCSS particles batch presented in section 4.3.1 (PLGA 50:50 L:G 7-17 kDa Mw, thick shell) was stored for 60 days at 4°C before assessing in vitro release. After storage, the particles retained the same appearance, with identical size distribution to that before storage (**Figure 4-20**).

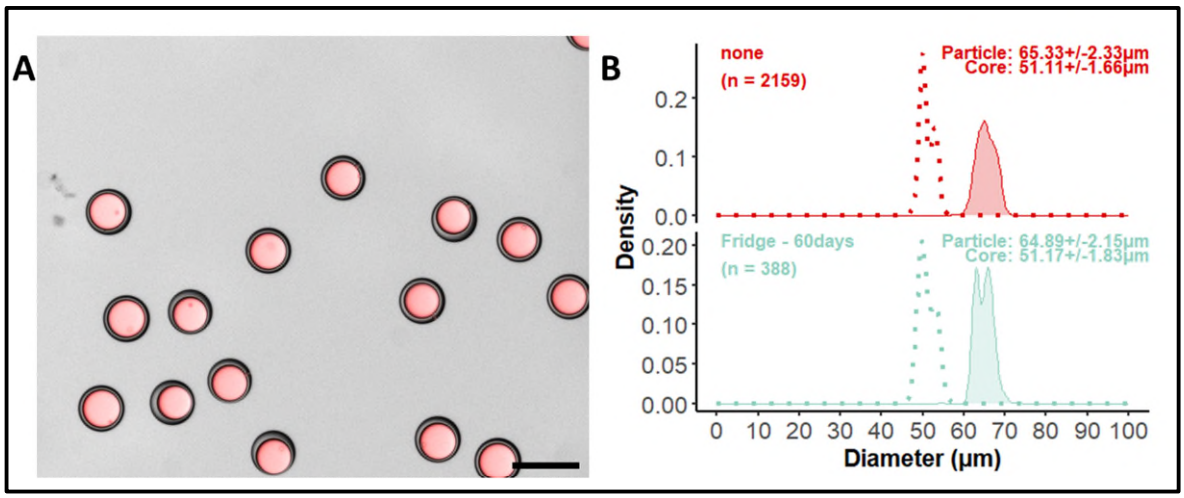

Figure 4-20: LCSS particle populations produced by microfluidics stored in fridge for 2 months before in vitro incubation.

Microscopic image of LCSS particles manufactured by microfluidics stored 60 days in fridge at 4 °C, encapsulating fluorescent dextran-TRITC and suspended in PBS at room temperature. (A) LCSS particle population was imaged with a 10X objective. TRITC and brightfield channels are overlayed. Scale bar is 100µm. (B) Outer diameter (solid filled line) and core diameter (dotted line) size distribution for particles without (none) or with fridge storage.

Storage had no significant impact on the release profile (**Figure 4-21**) or Peak characteristics (**Table 4-6**), indicating that particles can be refrigerated for 2 months without altering their release properties. Interestingly, the release kinetics for particles stored in the fridge was more reproducible across replicates, with smaller CIs for Peak duration and lag than non-stored particles.

Table 4-6: In vitro release Peak characteristics with fridge pre-storage

Storage Time *(days, at 4C)*	**Peak Proportion** Mean % [95%CI]	**Peak Time** Mean days [95%CI]	**Peak Duration** Mean days [95%CI]	**Peak Lag** Mean days [95%CI]
0	**85.3** *[82.6-88.0]*	**21.4** *[20.5-22.3]*	**13.1** *[10.9-15.3]*	**14.4** *[12.2-16.5]*
60	**89.6** *[88.4-90.8]*	**21.3** *[20.9-21.7]*	**10.5** *[9.3-11.6]*	**15.6** *[15.4-15.8]*

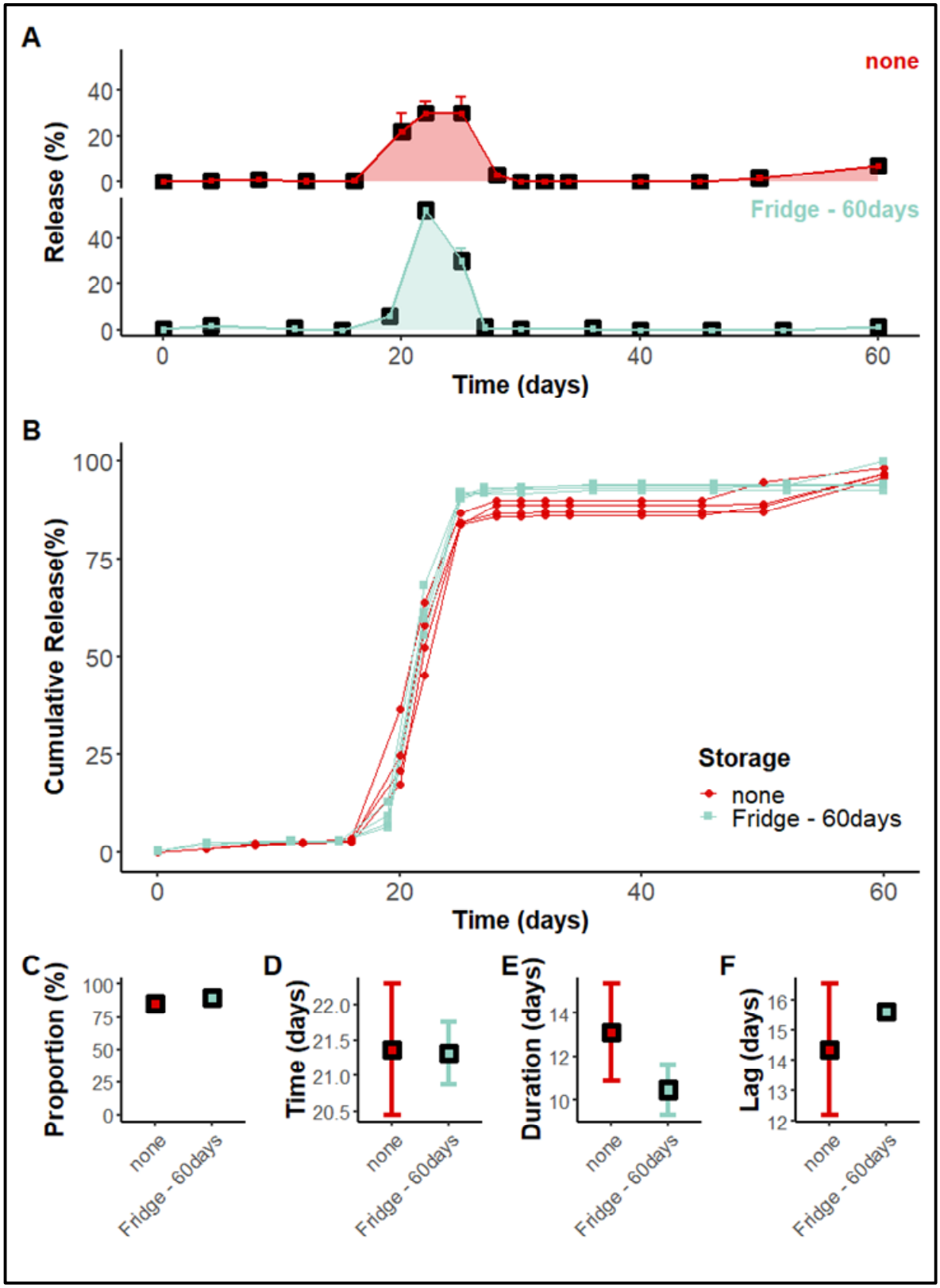
A
none
Fridge - 60days
Release (%)
Time (days)
B
Cumulative Release(%)
Time (days)
Storage
none
Fridge - 60days
C
Proportion (%)
D
Time (days)
E
Duration (days)
F
Lag (days)
none
Fridge - 60days

Figure 4-21: Effect of the fridge storage of LCSS particles on their release kinetics.

Summary of in vitro release kinetics from LCSS particles encapsulating 40kDa dextran-TRITC with PLGA (7-17kDa Mw 50:50 L:G ratio), manufactured by microfluidics with or without storage in fridge at 4°C before in vitro release. Each batch (n=4 replicates) was incubated at 37°C in PBS, pH 7.4, with 0.01% Tween 80, under constant rotation at 20rpm. Dextran release was measured by spectrophotometry. Results are reported as (A) Measured release over time (Mean of replicates +/- SD), (B) Cumulative release of each replicate over time, and (C-F) Main Peaks characteristics for each particle type (Mean and 95% CI assuming Student's distribution) as described in section 4.2.

4.3.6.2 Small variations of incubation pH extend the delay

Most vaccines are injected intramuscularly [134]. However, during physical activity, the interstitial pH of the muscle can drop below pH 7.4, due to accumulation of lactic acid, depending on the intensity of the activity [135]. In order to assess the impact of incubation pH on the release, fractions of the Thick-shell LCSS batch of particles presented in section 4.3.1 (PLGA 50:50 L:G 7-17kDa Mw, thick shell) were incubated for in vitro release at pH 7.2 and pH 6.8.

Table 4-7: In vitro release Peak characteristics for incubation pH

Incubation pH	**Peak Proportion** Mean % [95%CI]	**Peak Time** Mean days [95%CI]	**Peak Duration** Mean days [95%CI]	**Peak Lag** Mean days [95%CI]
7.4	**85.3** *[82.6-88.0]*	**21.4** *[20.5-22.3]*	**13.1** *[10.9-15.3]*	**14.4** *[12.2-16.5]*
7.2	**89.1** *[84.3-93.9]*	**25.1** *[23.9-26.4]*	**14.1** *[7.4-20.8]*	**16.9** *[13.3-20.4]*
6.8 *Peak1*	**48.9** *[41.6-56.2]*	**29.9** *[29.2-30.6]*	**8.1** *[7.8-8.4]*	**25.5** *[25.4-25.6]*
6.8 *Peak2*	**40.7** *[33.4-48.0]*	**44.0** *[40.1-47.9]*	**12.9** *[12.6-13.3]*	**37.5** *[31.5-43.5]*

The release profile presented in **Figure 4-23**, demonstrated that, despite preserving the same triphasic release profile, decreasing the incubation pH extended the release duration. In addition, batches of particles incubated at pH 6.8 also showed

2 successive release peaks at day 30 and day 44 (**Table 4-7**). Looking at the lag extension, a drop in pH delayed the release by almost 2 days per 0.1 pH unit (1.9 [95%CI 1.4-2.4] by linear regression). Hence the pH of the environment surrounding the LCSS particles can impact their release profile and extend the lag before content release, by order of days in this case.

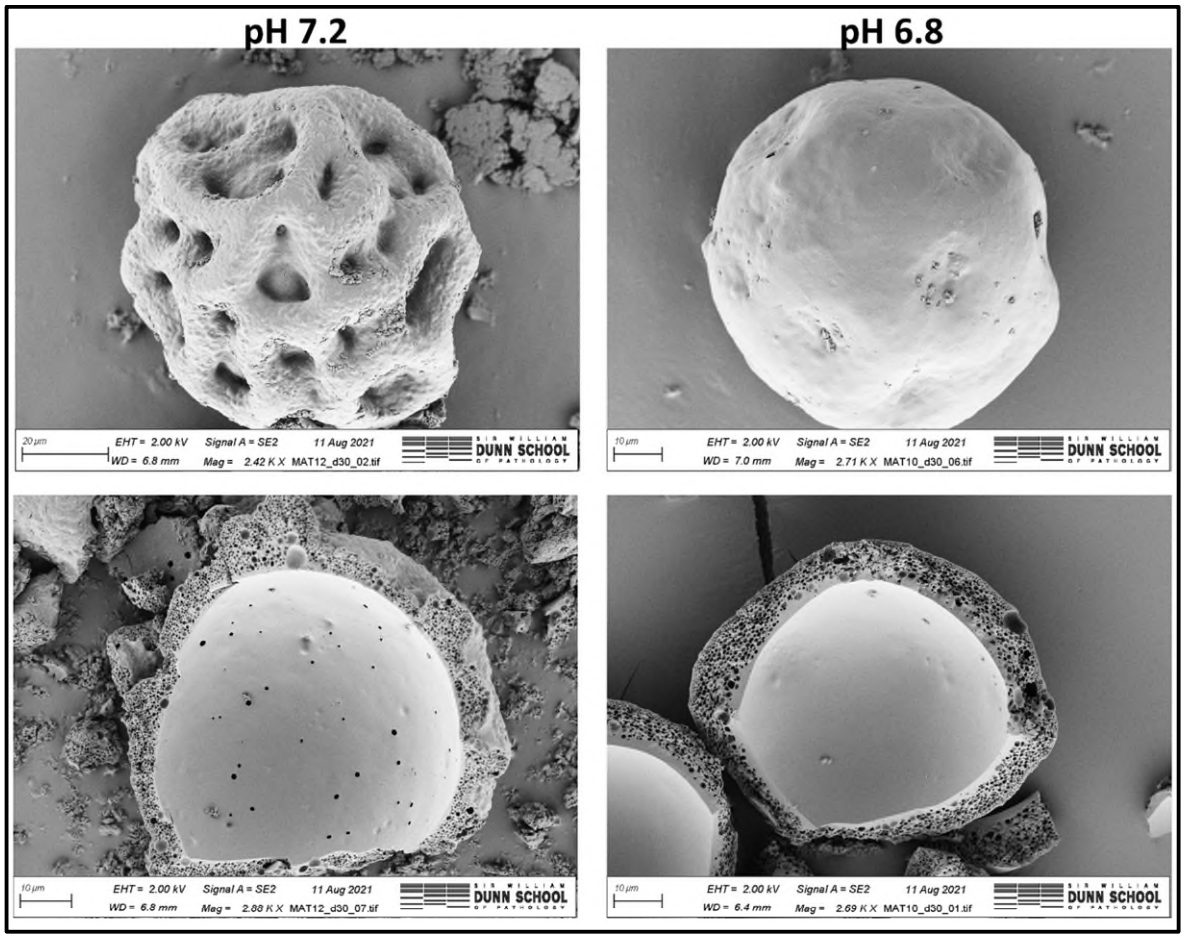

Figure 4-22: SEM imaging of LCSS particles incubated for 30 days in vitro at different incubation pH

SEM images of LCSS particles (PLGA 50:50 7-17kDa Mw) encapsulating dextran-TRITC, taken at day 30 of in vitro degradation (37°C in PBS, with 0.01% Tween 80, under constant rotation of 20rpm) at different incubation pH (7.2 – left, 6.8-right). Full particles (top row), and sections (bottom row) are shown. Magnifications and scale bar are displayed in a detailed ribbon for each image.

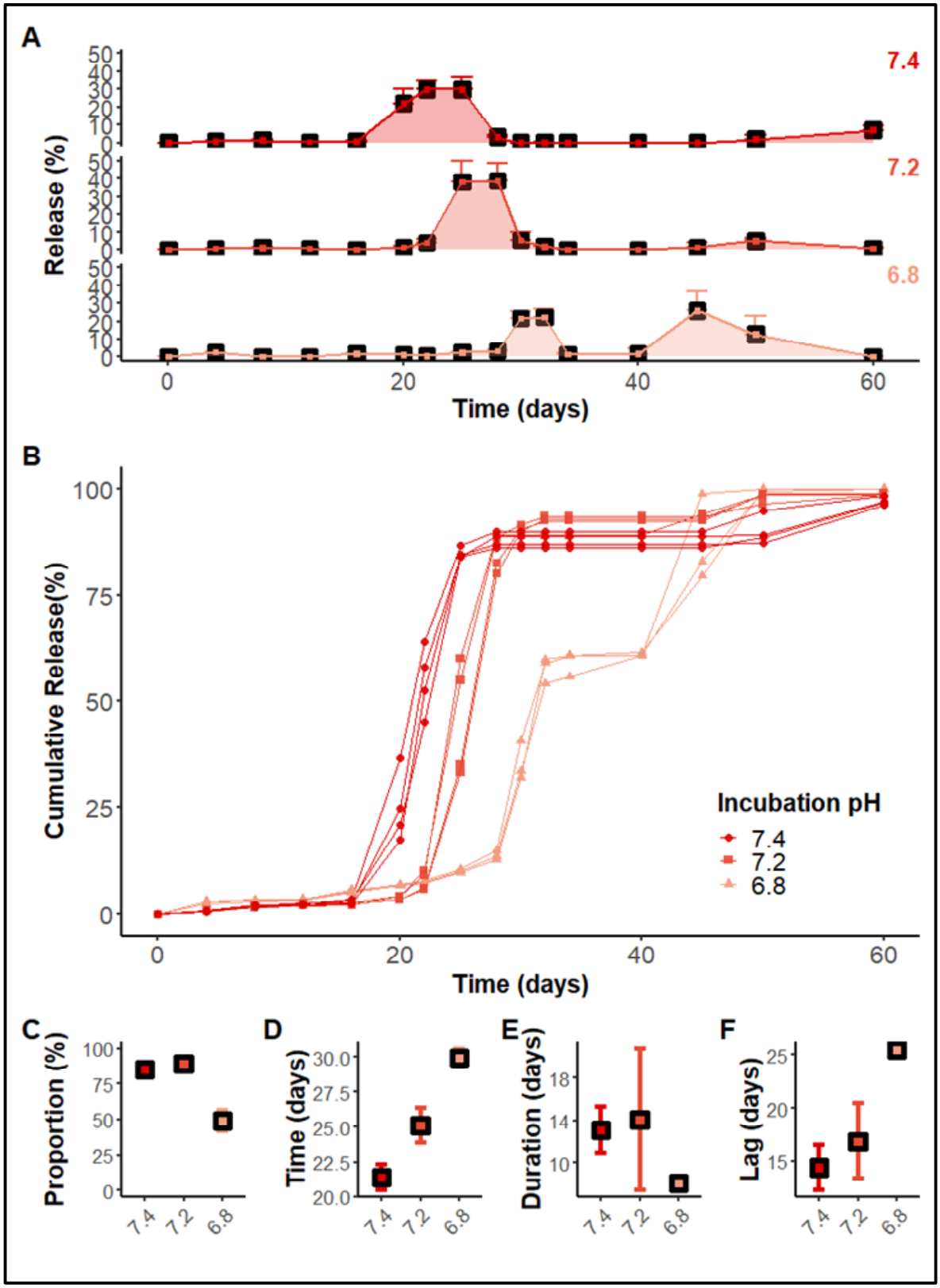
A
Release (%)
7.4
7.2
6.8
Time (days)
B
Cumulative Release(%)
Incubation pH
7.4
7.2
6.8
Time (days)
C
Proportion (%)
D
Time (days)
E
Duration (days)
F
Lag (days)

Figure 4-23: Effect of the incubation pH of LCSS particles on their release kinetics.

Summary of in vitro release kinetics from LCSS particles encapsulating 40kDa dextran-TRITC with PLGA (7-17kDa Mw 50:50 L:G ratio), manufactured by microfluidics. Each batch (n=3 replicates for pH=6.8, n=4 replicates for others) was incubated at 37°C in PBS with 0.01% Tween 80 at different pH, under constant rotation at 20rpm. Dextran release was measured by spectrophotometry. Results are reported as (A) Measured release over time (Mean of replicates +/- SD), (B) Cumulative release of each replicate over time, and (C-F) Main Peaks characteristics for each particle type (Mean and 95%CI assuming student distribution) as described in section 4.2. For

SEM images (**Figure 4-22**) show that the LCSS particles, despite displaying a pore network inside the shell as seen in **Figure 4-6**, had a much smoother outer surface when exposed to a lower pH of incubation. Thus, the LCSS particles incubated at pH 6.8, remained spherical after 30 days of in vitro degradation, without any sign of perforation of the shell. The pore network was located in the middle of the shell, due to homogeneous degradation.

4.3.6.3 Particle properties are conserved *in vivo*

To ensure that LCSS particles could be injected intramuscularly, remain in the muscle during degradation, and retain their payload, groups of BALB/c mice were injected with different batches of particles. The following batches that had shown different release times *in vitro* were injected at ~30000 particles/mouse:

- **Short**: PLGA R502, 7-17kDa Mw, 50:50 L:G, Peak time *in vitro* = 21 days.
- **Medium**: PLGA R505, 54-69kDa Mw, 50:50 L:G, Peak time *in vitro* = 33 days.
- **Long**: PLGA R753S, 24-38kDa Mw, 75:25 L:G Peak time *in vitro* = 77 days.

LCSS particles were loaded with 40kDa dextran-TRITC and imaged at different timepoints *in vivo* using an IVIS system, to follow the evolution of the fluorescent signal coming from the encapsulated payload.

The resulting images (**Figure 4-24**, **Figure 4-25**, **Figure 4-26**) demonstrated that the LCSS particles behaved as expected, remaining at the site of injection and retaining their payload for the expected time, as predicted from the *in vitro* release assays. The particles appear to have fully released their content in vivo by day 32, 55 and 136 for the Short, Medium and Long formulations, respectively. A shortcoming of this experiment was the absence of controls with non-encapsulated dextran. Also, irregular intervals in the measurement timepoints and unequal loading between groups prevented any detailed quantitative analysis of the results from this pilot study. It should be noted that mouse hair produces a non-specific fluorescent signal at this wavelength, visible in some of the images away from the injection site.

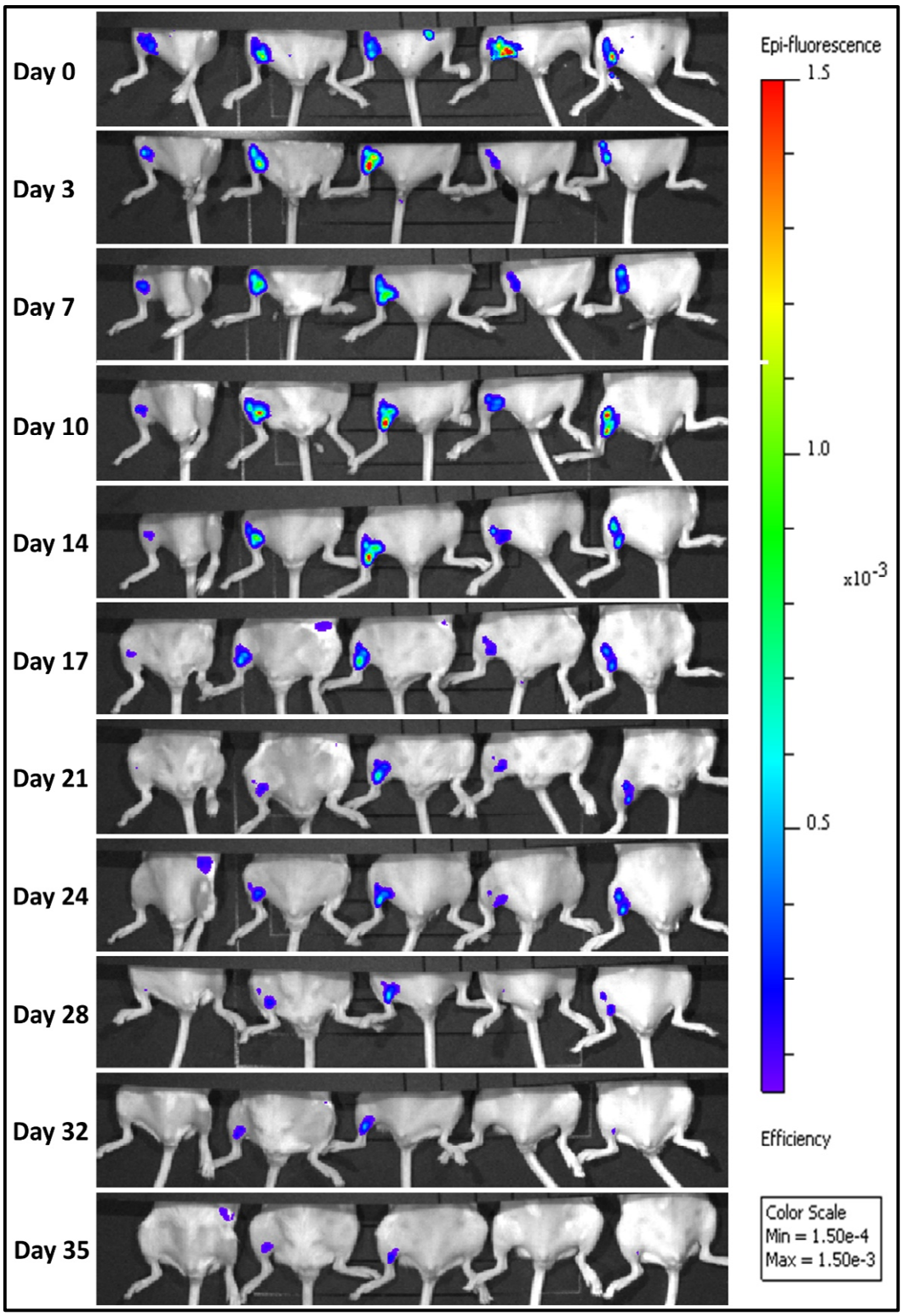

Figure 4-24: In vivo release kinetics of Short formulation LCSS particles

BALB/c mice (n=5) were injected intramuscularly in the right tibialis muscle with LCSS particles loaded with 40kDa dextran-TRITC. The polymer used for the core shell was the Short formulation (PLGA 7-17kDa Mw, 50:50 L:G). Images of the fluorescence from the encapsulated dextran-TRITC were taken at different timepoints using the IVIS. The scale colour bar is identical for all images.

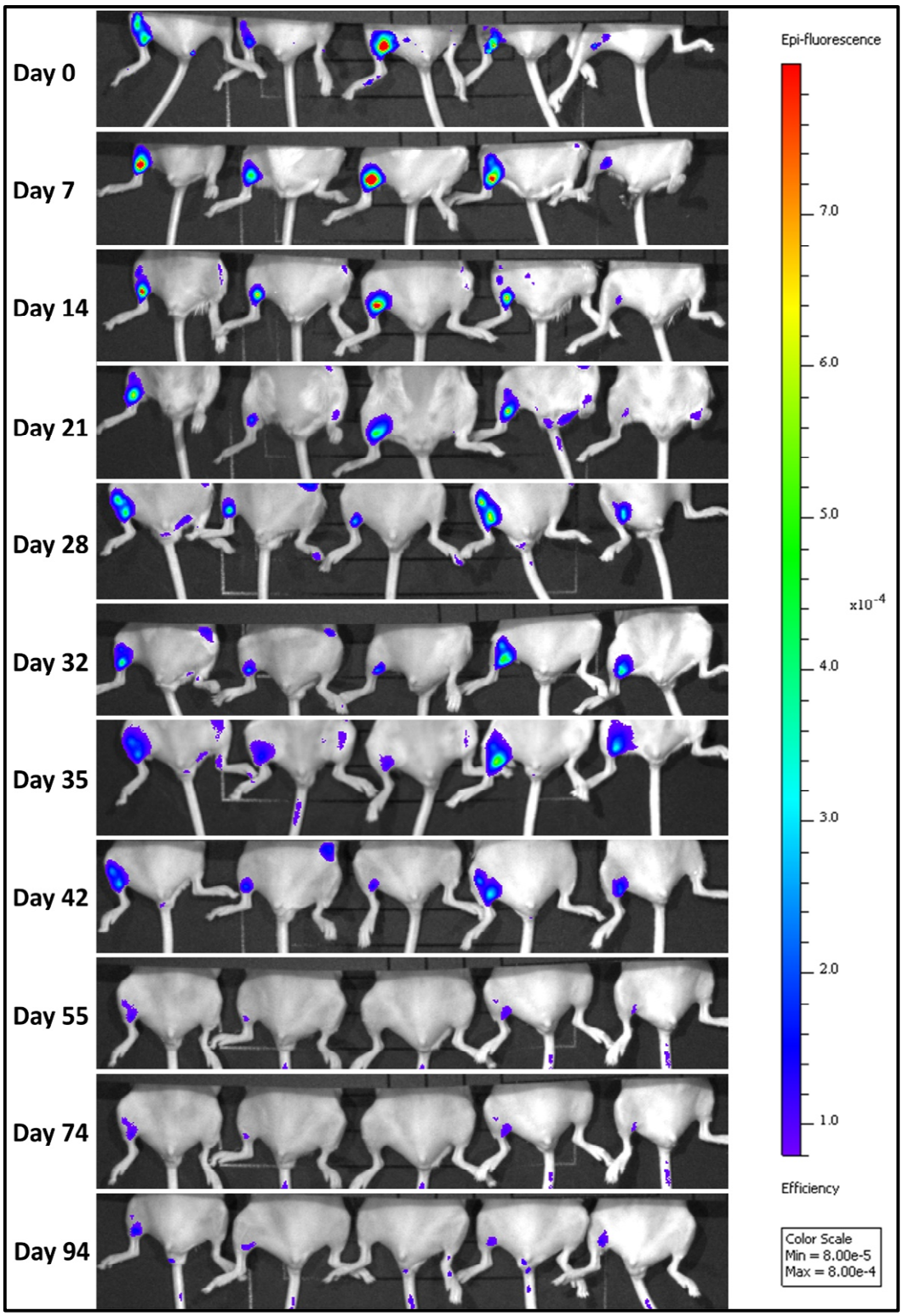

Figure 4-25: In vivo release kinetics of Medium formulation LCSS particles

BALB/c mice (n=5) were injected intramuscularly in the right tibialis muscle with LCSS particles loaded with 40kDa dextran-TRITC. The polymer used for the core shell was the Medium formulation (PLGA 54-69kDa Mw, 50:50 L:G). Images of the fluorescence from the encapsulated dextran-TRITC were taken at different timepoints using the IVIS. Scale colour bar identical for all images.

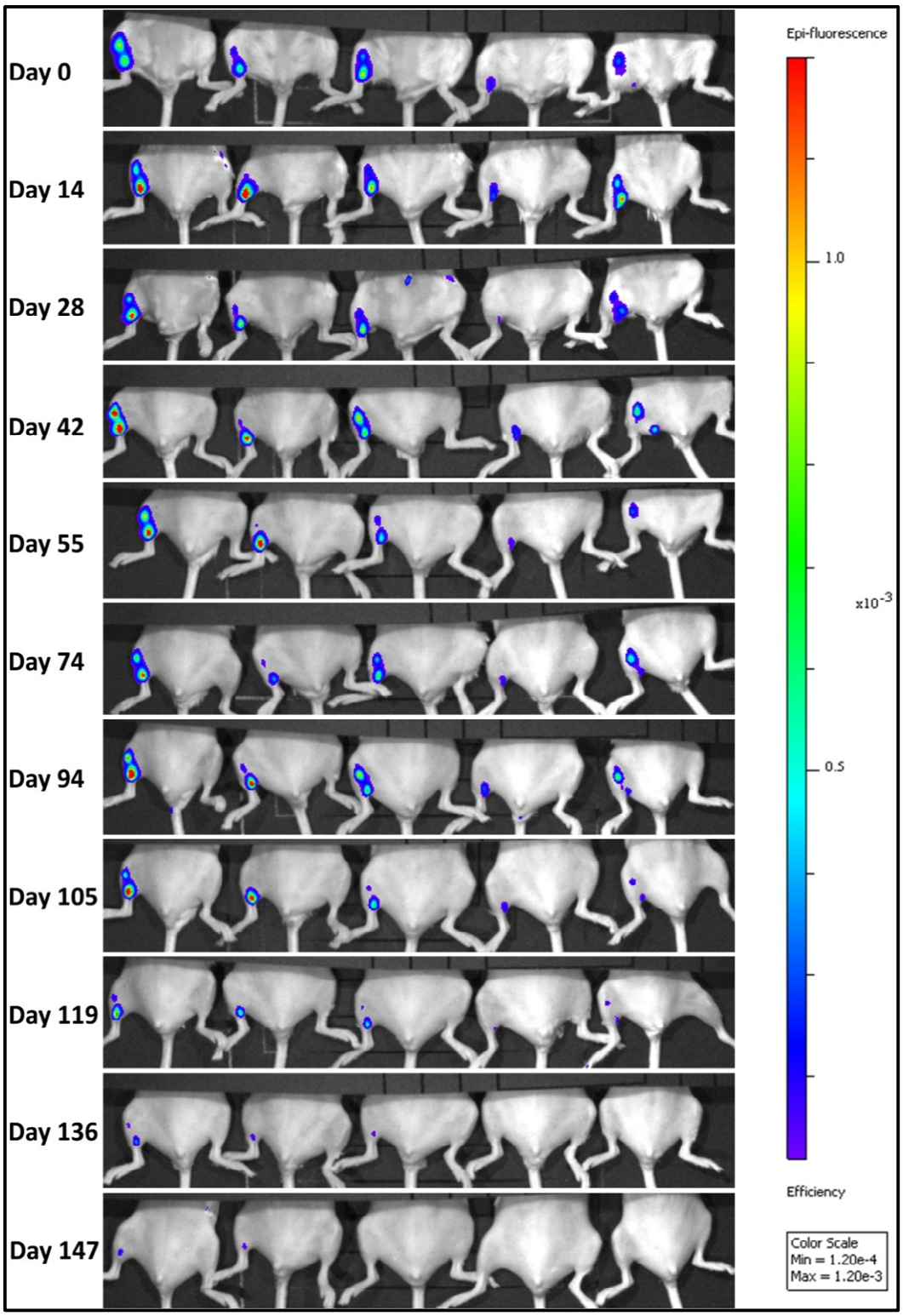

Figure 4-26: In vivo kinetic release of Long formulation LCSS particles

BALB/c mice (n=5) were injected intramuscularly in the right tibialis muscle with LCSS particles loaded with 40kDa dextran-TRITC. The polymer used for the core shell was the Long formulation (PLGA 24-38kDa Mw, 75:25 L:G). Images of the fluorescence coming from the encapsulated dextran-TRITC were taken at different timepoints using the IVIS. Scale colour bar identical for all images.

4.4 Discussion

In this chapter, particles produced by microfluidic emulsification were found to offer far superior control over payload release compared to particles made by BE. The LCSS architecture of the microfluidic particles prevented the early burst release and absence of a lag observed in BE particles. This burst release in BE particles was caused by material entrapped in the shell matrix [136]. In the case of LCSS particles, the clear separation of the liquid core content from the PLGA shell enabled the polymer to degrade by bulk heterogenous erosion and form a network of interconnected pores. These pores, ultimately forming a bridge between the internal cavity of the LCSS particle and the outside, provided a path for the loaded material to rapidly diffuse out after a certain time lag [47]. The resulting release at ~20 days for the lowest Mw PLGA studied (PLGA R502, 7-17kDa Mw, 50:50 L:G), was the result of this occurring simultaneously in a majority of particles. Because polymer degradation and pore formation are random processes, each particle has a certain probability of releasing its content at a given timepoint and a small fraction of particles remained loaded after 20 days for this formulation.

The thickness of the LCSS particle shell was found to be an important parameter controlling payload release. In thicker shells there was reduced diffusion of acidic by-products from the polymer degradation, thus maintaining the autocatalytic degradation for longer [137]. As a result, bigger pores were formed in thicker shell particles, increasing the chances of interconnection and the probability of bridge formation. Conversely, autocatalytic effects are reduced in Thin-shell particles, lowering the probability of forming bridges. Despite having a small fraction releasing at the same peak time of 20 days, most of the Thin-shell particle population

remaining loaded until complete degradation of the particle structure after 90 days. The conclusion is that the probability of connecting the inside to the outside of the LCSS particle, and hence the likelihood of earlier release, increased with the thickness of the shell.

Another consequence of the entrapment of acidic by-products in the thicker shells was a larger drop of pH in their cores. For LCSS particles, internal core pH reached a minimum just before peak release, before rising again to neutral pH after release. This rise was faster for thicker shell, indicating that the denser pore connection in thicker shells allowed for more exchange with the external media.

LCSS particle swelling was also found to be important for payload release. With degradation, the Mw of the polymer decreased, reducing chain entanglement, and ultimately enabling water penetration by osmosis [138], [139]. As the pores in the polymer matrix enlarge, so too does the whole particle, facilitating payload release. As a result, after the peak release, unloaded particles showed higher degree of swelling compared to the ones that had not released the payload.

Increasing the payload hydrodynamic radius, Rh, did not substantially increase the timing of the release, as the pores formed by the polymer shell degradation - the dominant factor controlling release kinetics - were much larger (micrometres) than the dextran molecules used as the payload (nanometres). However, this demonstrated that the diffusion through the PLGA matrix before peak release was also minimal for smaller payloads (4.4kDa dextran, 1.8 nm Rh), indicating that the system could be used for delivery of smaller molecules.

The lag before release could be substantially altered by changing the Mw of the PLGA or its L:G ratio, respectively increasing the peak timing by days, or weeks to

months. This property, in addition to the possibility of being refrigerated without altering the release properties, highlights the compatibility of these PLGA LCSS particles with application to vaccines. As most vaccines are injected intramuscularly (IM), particles would be exposed to an external pH lower than 7.4, induced by physical and metabolic activity [135]. Thus, a reduction of the incubation pH was assessed *in vitro*, demonstrating a significant delay in peak release time, due to a less dense pore network being formed in the shell. The lower external pH resulted in a more homogeneous polymer bulk erosion process at the surface of the particles explaining their smooth appearance and the absence of surface pitting [140].

Finally, a preliminary *in vivo* experiment in mice confirmed that the LCSS particles could be injected, were safe for in vivo administration, and remain loaded within the muscle for periods of time that varied with the particle formulation, in accordance with the observed *in vitro* release kinetics. The formulations resulting in different release lags were next used to encapsulate a malaria vaccine and tested in mice, to demonstrate the utility of the system in the context of vaccination. These results are presented in the following chapter.

5 *In vivo* use with R21 malaria vaccine

5.1 Introduction

5.1.1 The Case for Malaria as the target disease

Malaria is a deadly infectious disease caused by *Plasmodium* (*P.*) parasites and transmitted between humans by the carrier mosquito bites. In 2020 there were more than 241 million cases across the world and an estimated 627,000 deaths [141]. Of the five parasite species that can infect humans, *P. falciparum* poses the biggest threat. This is due to its ability to evade the immune system [142] and its prevalence in Africa, the region carrying the highest share of the malaria burden with more than 96% of the worldwide deaths.

The malaria infection is comprised of different stages: following the bite of a carrier mosquito, several tens of sporozoites may be injected into the dermis from where they migrate to the lymphatic system and/or the blood stream [143]. They are transported to the liver within 20-30 minutes, where they infect hepatocytes and undergo cycles of replication to form merozoites that are later released back into the bloodstream, initiating the blood stage of the infection. Merozoites invade circulating erythrocytes (Er), multiply, and are released by Er rupture to repeat the cycle. The clinical symptoms of malaria become visible from this stage, leading, if untreated, to anaemia and other pulmonary, renal or neurological complications [144].

Effective antimalarial drugs do exist [145], but *Plasmodium* parasites have developed resistance to the essential anti-malarial drug chloroquine [146], and their impact is limited by the bottleneck of diagnosis and access to treatment in low- and middle-income countries. Additional preventive strategies such as vaccines are therefore required. To date, two malaria vaccines have achieved significant success in large scale (Phase III-IV) trials: the RTS,S vaccine in AS01 adjuvant (RTS,S/AS01) developed by GSK, and the R21 vaccine developed by the Jenner Institute in Oxford in Matrix-M (MM) adjuvant owned by Novavax (R21/MM). They both target the same antigen, Circumsporozoite protein (CSP) displayed on the surface of *P. falciparum* sporozoites before the invasion of hepatocytes. Both vaccines have demonstrated significant efficacy in large clinical trials: 3 doses of RTS,S/AS01 showed a 56% [97.5%CI, 50.6-60.4] efficacy[147] in preventing the incidence of the first or only episode of clinical malaria during the 12 months follow-up, in a multi-site clinical trial for perennial use [147]. In comparison, 3 doses of R21/MM demonstrated up to 77% (95%CI, 67 – 84) efficacy against clinical malaria over 12 months in a separate study conducted at a single site in highly seasonal malaria transmission setting [148].

Both vaccines were administered intramuscularly in a 3-dose regimen with each injection separated by a month. The prime/multi-boost strategy is necessary to induce protective immunity but can result in non-completion of the vaccination course. Each trial reported various exclusions between the first and last vaccination (354/6000 people in [147]), including patients not receiving all vaccine doses (8/450 people in [148]). A single-shot approach could ease the roll-out of the malaria vaccine and greatly benefit future vaccination campaigns by reducing the logistical

burden and costs while improving compliance in regions with restricted access to health care.

5.1.2 The R21 vaccine and LMQ adjuvant

Similar to the RTS,S vaccine [149], the R21 vaccine is a fusion of two major fragments of the *P. falciparum* CSP protein with the hepatitis B surface antigen (HBsAg). The single DNA construct is expressed in *Pichia* yeast to form virus like particles (VLPs) ~22 nm in diameter [58]. The parts of the CSP protein included in the R21 vaccine, namely the NANP central repeat region (19 repeats of NANP sequence) and the C-terminal region (C-term, 105 amino acids long [150]), are known to contain protective B and T cell epitopes [151], [152], and antibody responses against these regions have been associated with protection in multiple RTS,S/AS01 clinical trials [153]–[156].

As mentioned above, R21 in combination with Matrix-M has shown good efficacy in both preclinical and clinical studies. Other adjuvants, such as LMQ (developed by the Vaccine Formulation Institute, VFI, in Geneva) have also been found to enhance immunogenicity in BALB/c mice [150]. LMQ is a liposome-based adjuvant containing QS-21 saponin and a TLR4 agonist (3D-6-acyl-PHAD) embedded into the liposomal membrane. Given in combination with R21 in a prime-boost regimen separated by 2 or 3 weeks, 80-100% protection against malaria was observed in a mouse challenge model 2 weeks following the booster injection (Reinke et al, manuscript under review).

Because of the VLP size, dispersibility in water, and promising efficacy in both animal models and human trials, R21 was selected to demonstrate the potential of

the LCSS particles produced by microfluidics as a delayed vaccine delivery system. This chapter focuses on the *in vivo* immunogenicity and efficacy results from BALB/c mice immunised with particles encapsulating R21 alone or adjuvanted with LMQ. The kinetics and magnitude of the clinically relevant ([154], [157]) NANP and Cterm-specific IgG responses with time are reported, along with the assessment of survival following malaria challenge.

5.2 Results

5.2.1 R21 immunogenicity is preserved when encapsulated inside particles

Firstly, the ability of R21 to elicit immunogenicity after being encapsulated and injected *in vivo* was assessed by immunising mice with the following regimens:

- **Prime:** a single injection of R21 alone (suspended) in PBS
- **Particle**: a single injection of R21 alone encapsulated in about 50,000 LCSS particles made with 7-17kDa MW, 50:50 L:G PLGA R502, also referred in this thesis as **Short** formulation
- **Prime + Particle:** a single injection of R21 alone in PBS combined with R21 encapsulated in about 50,000 LCSS **Short** formulation particles.
- **Prime/Boost:** two injections of R21 alone in PBS separated by 3 weeks (separate data kindly provided by Dr Reinke, titres only measured at week 5, the previously observed antibody peak titre)

Mice receiving the Particle or Prime + Particle regimens were injected with ~50,000 particles to match the soluble priming dose of R21 (1 µg), each particle containing only a fraction of the total dose. The different regimens were compared as shown in **Figure 5-1**.

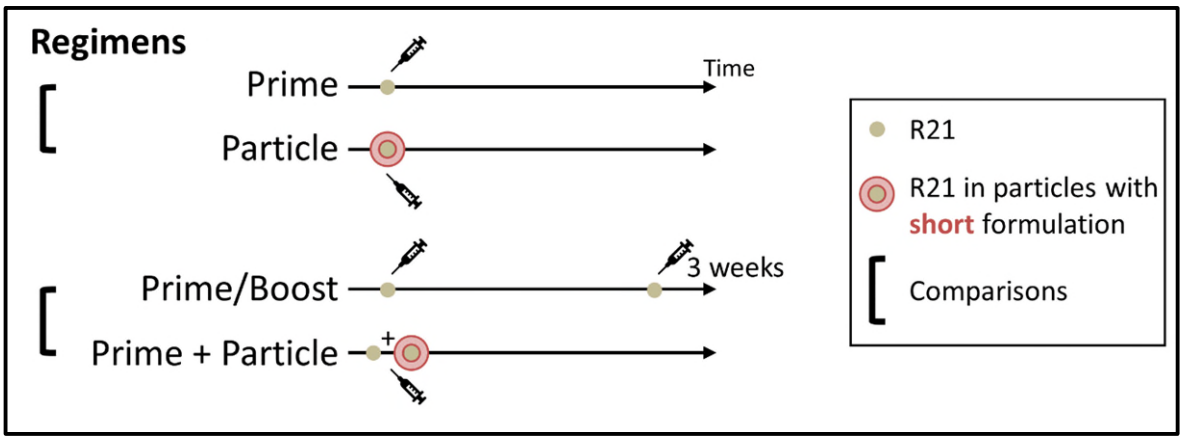

Figure 5-1: Design summary of the in vivo experiment testing for preservation of R21 immunogenicity following encapsulation.

BALB/c mice (n=8 per group) were immunised with four different regimens by intramuscular injection. Injections were performed using 100µL Hamilton glass syringes sterilised with ethanol and 25G needles. Injection volume was 50µL with 0.5% carboxymethylcellulose in PBS as a viscoenhancer agent to prevent LCSS particles aggregation in the syringe.

Immunogenicity was monitored by weekly blood sampling followed by IgG quantification by indirect ELISA using either a 6 repeat of the NANP fragment or a portion of the C-term fragment (pool of peptides covering 67 amino acids) as the antigen. Comparisons were performed on the peak antibody titre observed from the weekly monitoring for each mouse, and a threshold of 0.5-fold change in antibody titre was used to determine non-inferiority between groups.

The Particle and Prime + Particle regimens were compared to the Prime and Prime/Boost control regimens. The immune response kinetic profiles against the two immunogenic epitopes, Cterm and NANP, are shown in **Figure 5-2**. The profiles did not indicate any qualitative negative impact of the encapsulation process on the immune response. On the contrary, the response to the Cterm fragment appeared to be enhanced by the encapsulation when comparing the Prime regimen to the Particle regimen.

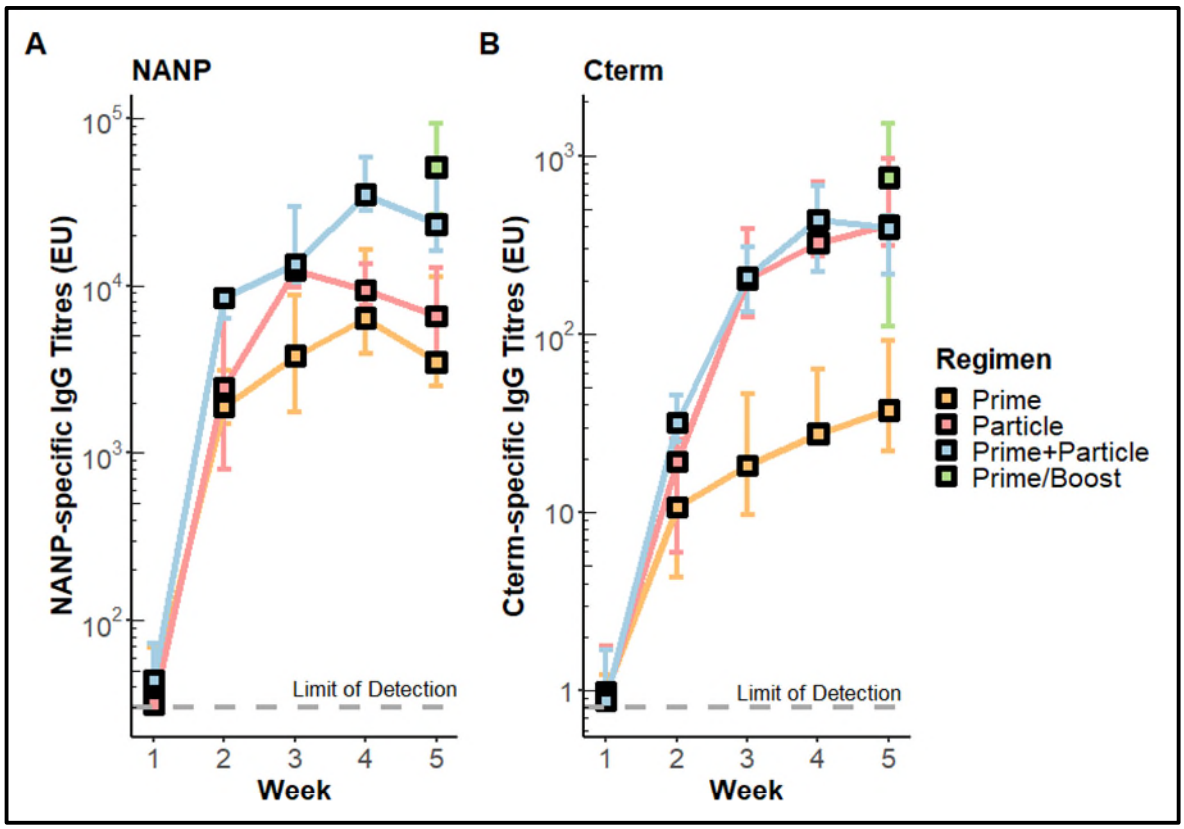

Figure 5-2: Immune response kinetics of vaccination regiments including encapsulated R21 compared to the unencapsulated vaccine.

Antigen-specific IgG titres were measured by ELISA against (A) NANP- (B) Cterm- epitopes of the R21 vaccine in BALB/c mice (n=8 per regimen) for each of the four regimens tested. Titres are measured from tail blood sampling every week following immunisation and represented by median and interquartile range.

The observed maximum IgG peak for each formulation and the fold change of the mean peak log titres between dose-matched soluble and encapsulated formulations are shown in **Figure 5-3**. Estimated geometric means and confidence intervals for the four regimens are reported in **Table 1-1**. Different regimens induced significantly different levels of NANP and Cterm specific IgG, as tested by permutation ANOVA (NANP p=0.0016, Cterm p=0.0002).

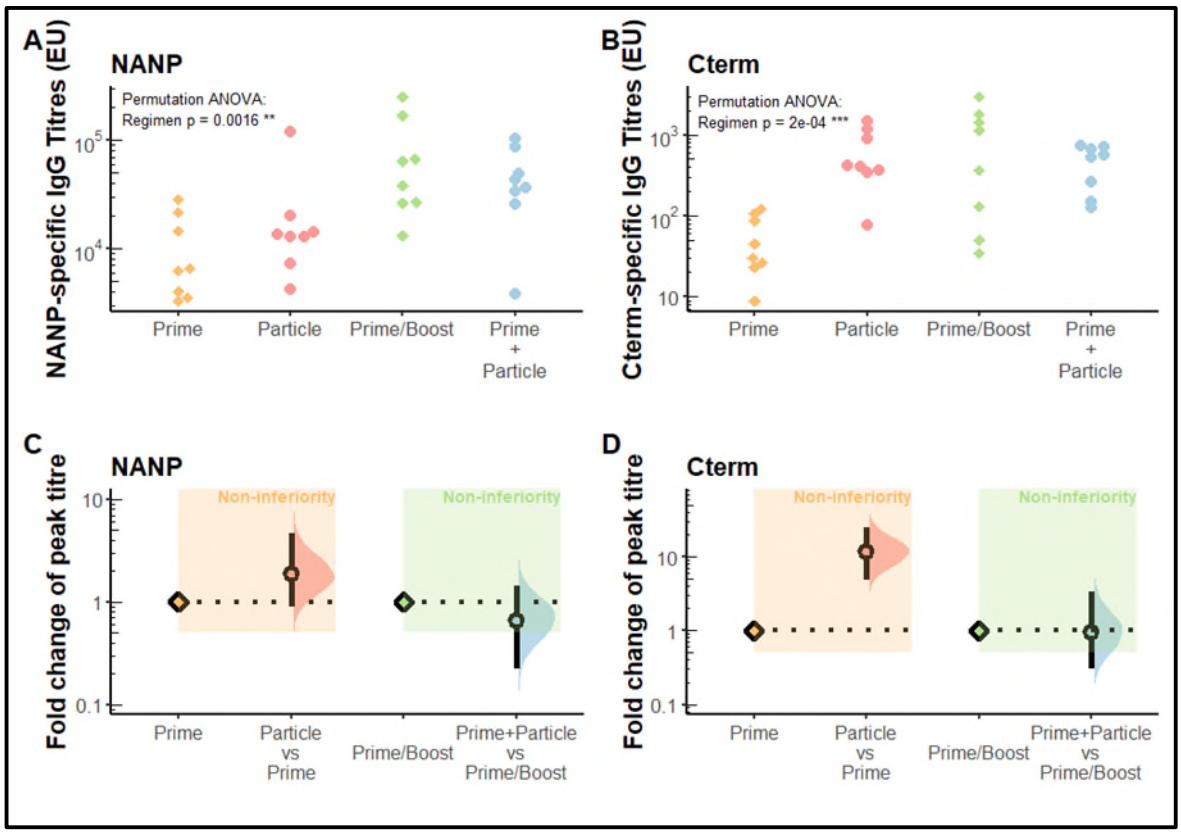

Figure 5-3: Peak antibody response of encapsulated non-adjuvanted R21 is non-inferior to the non-encapsulated vaccine.

Peak observed specific IgG against (A) NANP- (B) Cterm- epitopes are plotted for each mouse (n=8 per regimen). Fold change of the mean peak log titre for (C) NANP and (D) Cterm- specific responses are estimated by bootstrapping and reported as geometric mean fold change with 95% CI (error bars) and sampling distributions (density plots). Non-inferiority intervals at a 0.5-fold change threshold are displayed as faded rectangles for each comparison.

The encapsulation of R21 resulted in 1.9-fold higher (95% CI 0.9 – 4.7, p<0.05 for non-inferiority) and 11-fold higher (95% CI 4.8 – 25, p<0.05) levels of NANP- and Cterm-specific IgG titres respectively compared to the corresponding prime only control. In contrast, there was no sufficient evidence that the Prime + Particle regimen was non-inferior to the Prime/Boost regimen, with fold changes of 0.7 (95%CI 0.2 – 1.4, p>0.05) for the NANP response and 1 (95% CI 0.3 – 3.3, p>0.05) for the Cterm response.

Table 5-1: Geometric mean estimates of peak antibody titres for unadjuvanted R21 regimens.

Regimen	NANP specific IgG titres Geometric mean EU [95%CI]	Cterm specific IgG titres Geometric mean EU [95%CI]
Prime	**$8 \cdot 10^3$** $[4.9 \cdot 10^3 – 1.5 \cdot 10^4]$	**$4.1 \cdot 10^1$** $[2.2 \cdot 10^1 – 7.1 \cdot 10^1]$
Particle	**$1.5 \cdot 10^4$** $[9.2 \cdot 10^3 – 3.7 \cdot 10^4]$	**$4.7 \cdot 10^2$** $[2.3 \cdot 10^2 – 7.9 \cdot 10^2]$
Prime + Particle	**$3.5 \cdot 10^4$** $[1.4 \cdot 10^4 – 5.7 \cdot 10^4]$	**$3.9 \cdot 10^2$** $[2.2 \cdot 10^2 – 5.8 \cdot 10^2]$
Prime/Boost	**$5.3 \cdot 10^4$** $[3 \cdot 10^4 – 1.1 \cdot 10^5]$	**$4 \cdot 10^2$** $[1.2 \cdot 10^1 – 1.1 \cdot 10^3]$

5.2.2 Adjuvant effect of LMQ is maintained when co-encapsulated inside particles

Protein antigens require the addition of adjuvants to increase their immunogenicity. In this study, LMQ, a liposome-based adjuvant with saponin QS21 and a TLR-4 agonist integrated into the liposomal bilayer, was used. To assess retention of its adjuvant effect when co-encapsulated with R21 in LCSS particles, immune responses from the above Prime and Particle regimens were compared to immune responses to similar regimens, with the inclusion of the adjuvant. These are designated as Prime-Adj and Particle-Adj, respectively. For the Particle-Adj regimen the same Short formulation was used as for the Particle regimen.

Mice receiving the Particle-Adj regimen were injected with ~100,000 LCSS particles to match the soluble priming dose of R21 in the Prime-Adj regimen (total of 2 µg). The regimens and comparisons designed to evaluate preservation of adjuvant potency following encapsulation in Short formulation particles are summarised in **Figure 5-4**.

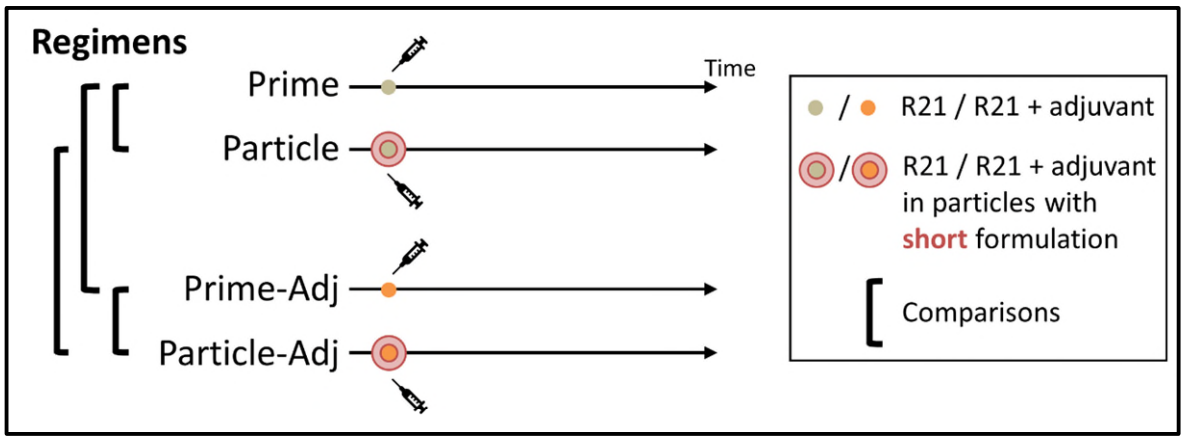

Figure 5-4: Summary of the in vivo experimental design to evaluate adjuvant potency following encapsulation.

BALB/c mice were immunised with different regimens (Prime-Adj n=16, otherwise n=8) by intramuscular injection. Injections were performed using 100µL Hamilton glass syringes sterilised with ethanol and 25G needles. Injection volume was 50µL with 0.5% carboxymethylcellulose in PBS as a viscoenhancer agent to prevent particle aggregation in the syringe.

As LMQ was supplied in a fixed concentration, and to avoid injection of excessive number of particles that would result in needle blockage, the amount of LMQ co-encapsulated with R21 was lower than the amount given in the unencapsulated regimen. Thus, mice in the Particle-Adj regimen received 1/7th of the standard LMQ dose. The resulting immune response kinetic profiles are shown in **Figure 5-5**.

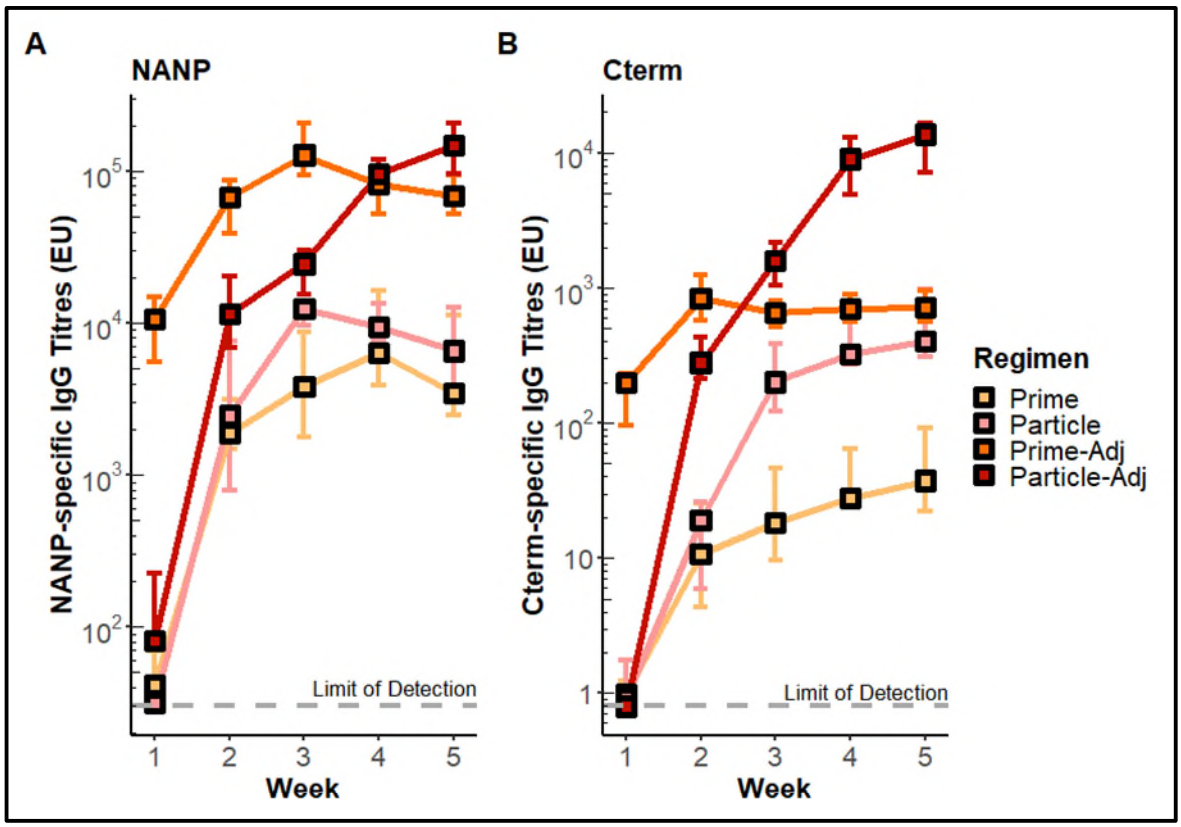

Figure 5-5: Effect of the addition of LMQ adjuvant on the immune response kinetics of encapsulated R21 regimens compared to unencapsulated controls.

Specific IgG are measured by ELISA against (A) NANP and (B) Cterm epitopes of the R21 vaccine in BALB/c mice (Prime-Adj n=16, other regimens n=8). Titres are measured from tail blood sampling every week following immunisation and represented by the Median and interquartile range.

The addition of the LMQ adjuvant provided an increase in the immune response against both epitopes in the Prime regimen from day 7 post-immunisation. Co-encapsulation of LMQ and R21 in LCSS particles resulted in a delay of the immune response against both epitopes compared to the Prime-Adj regimen. This is quantitatively analysed below.

The observed maximum IgG peak for each formulation and the fold change of the mean peak log titres between dose-matched soluble and encapsulated formulations are shown in **Figure 5-6**. Estimated geometric means and confidence intervals for

the different regimens are reported in **Table 5-2**. The addition of the LMQ adjuvant induced significantly different levels of NANP and Cterm specific IgG across encapsulated and nonencapsulated formulations, as tested by permutation ANOVA (NANP $p<2 \times 10^{-16}$, Cterm $p<2 \times 10^{-16}$). Encapsulation did not result in significantly different level of the NANP-specific response ($p=0.2$) across adjuvanted and nonadjuvanted formulations but did significantly affect the Cterm specific response ($p<2 \times 10^{-16}$). Finally, interactions between the effect of the encapsulation and the addition of adjuvant were not significant for either Cterm- or NANP-specific immune responses.

Encapsulation of R21 with the LMQ adjuvant either increased (C-term) or did not affect immunogenicity (NANP) compared to nonencapsulated controls, with a 1.1-fold change (95% CI 0.6 – 2, $p<0.05$ for noninferiority) in NANP-specific IgG titres and a 11-fold change (95% CI 7 – 17, $p<0.05$) in Cterm-specific IgG titres.

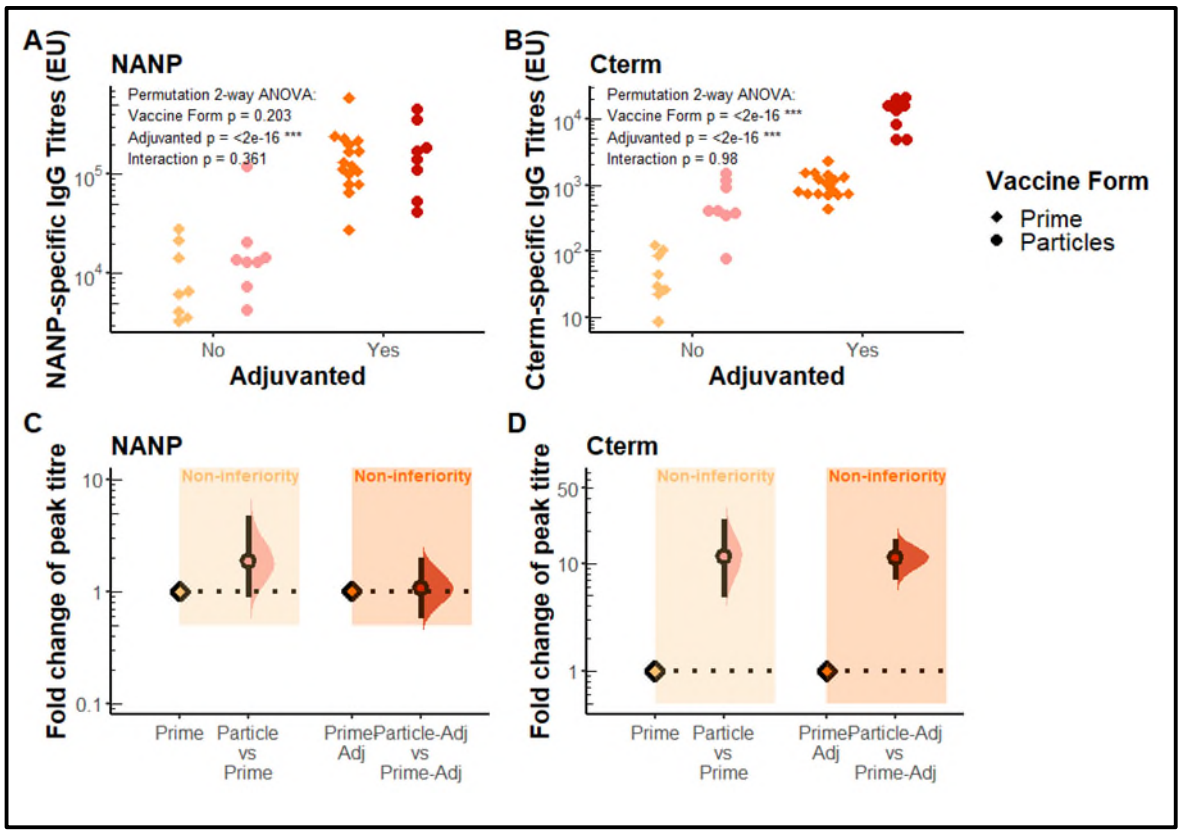

Figure 5-6: Peak antibody response of encapsulated R21 with LMQ adjuvant is noninferior to the unencapsulated control.

Peak observed titres of specific IgG against (A) NANP- (B) Cterm- epitopes are shown for each mouse (Prime-Adj n=16, other regimens n=8). Fold change of the mean peak log titre for (C) NANP- and (D) Cterm- specific responses are estimated by bootstrapping and reported as geometric mean fold change with 95% CI (error bars) and sampling distributions (density plots). Non-inferiority intervals at a 0.5-fold change threshold are displayed as shaded rectangles for each comparison.

***Table 5-2**: Geometric mean estimates of peak antibody titres for the adjuvanted R21 regimens.*

Regimen	NANP specific IgG titres Geometric mean EU [95%CI]	Cterm specific IgG titres Geometric mean EU [95%CI]
Prime – Adj	**$1.3 \cdot 10^5$** *[$9.6 \cdot 10^4$ – $1.8 \cdot 10^5$]*	**$1 \cdot 10^3$** *[$8.2 \cdot 10^2$ – $1.2 \cdot 10^3$]*
Particle – Adj	**$1.4 \cdot 10^5$** *[$8.1 \cdot 10^4$ – $2.4 \cdot 10^5$]*	**$1.1 \cdot 10^4$** *[$7.1 \cdot 10^3$ – $1.6 \cdot 10^4$]*

In the subsequent experiments, when co-encapsulated in Particle regimens, LMQ was used at 1/7th of the full dose.

5.2.3 Different particle formulations affect immunogenicity and immune response delay

In order to investigate the effect of encapsulation on immunogenicity and delay of the immune response with different particle formulations, data from Prime-Adj and Particle-Adj (Short formulation) regimens were combined with that from two additional formulations of particles co-encapsulating R21 and the fractional dose (1/7th) of LMQ. The immune response was monitored by weekly quantification of antibody titres. A summary of the regimens for each mouse and their designation in the figures is provided below:

- **Short:** a single injection of R21 and fractional LMQ dose encapsulated in LCSS particles made of 7-17kDa Mw, 50:50 L:G PLGA R502 with *in vitro* observed delay of 21 days.
- **Medium:** a single injection of R21 and fractional LMQ dose encapsulated in LCSS particles made of 54-69kDa Mw, 50:50 L:G PLGA R505 with *in vitro* observed delay of 33 days.
- **Long:** a single injection of R21 and fractional LMQ dose encapsulated in LCSS particles made of 24-38kDa Mw, 75:25 L:G PLGA R753S with *in vitro* observed delay of 77 days.
- **Prime:** a single injection of R21 and full standard LMQ dose in PBS.

Mice receiving Particle regimens were injected with ~100,000 LCSS particles to match the soluble priming dose of R21 (2µg here). The regimens and comparisons

designed to measure the immunogenicity delay induced by different particle formulations are summarised in **Figure 5-7**.

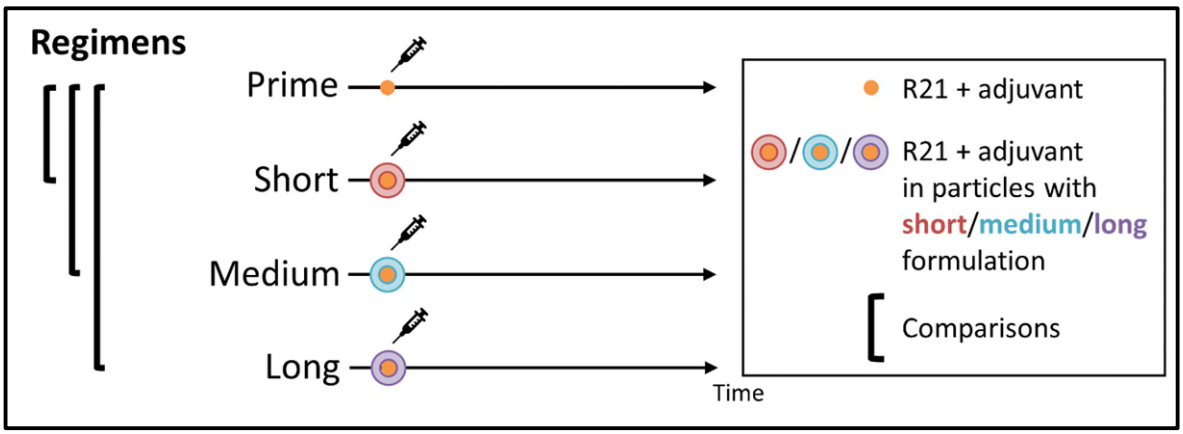

Figure 5-7: Design summary of the in vivo experiment testing the delay in immunogenicity induced by different particle formulations.

BALB/c mice were immunised with different regimens (Prime n=16, other regimens n=8) by intramuscular injection. Injections were performed using 100µL Hamilton glass syringes sterilised with ethanol and 25G needles. Injection volume was 50µL with 0.5% carboxymethylcellulose in PBS as a viscoenhancer agent to prevent particles aggregation in the syringe.

The longitudinal immune response kinetics profiles of the NANP and Cterm-specific responses are shown in **Figure 5-8** and **Figure 5-9** with the corresponding generalised additive model (GAM) fits performed on the log-transformed data as described in the Material and Methods chapter.

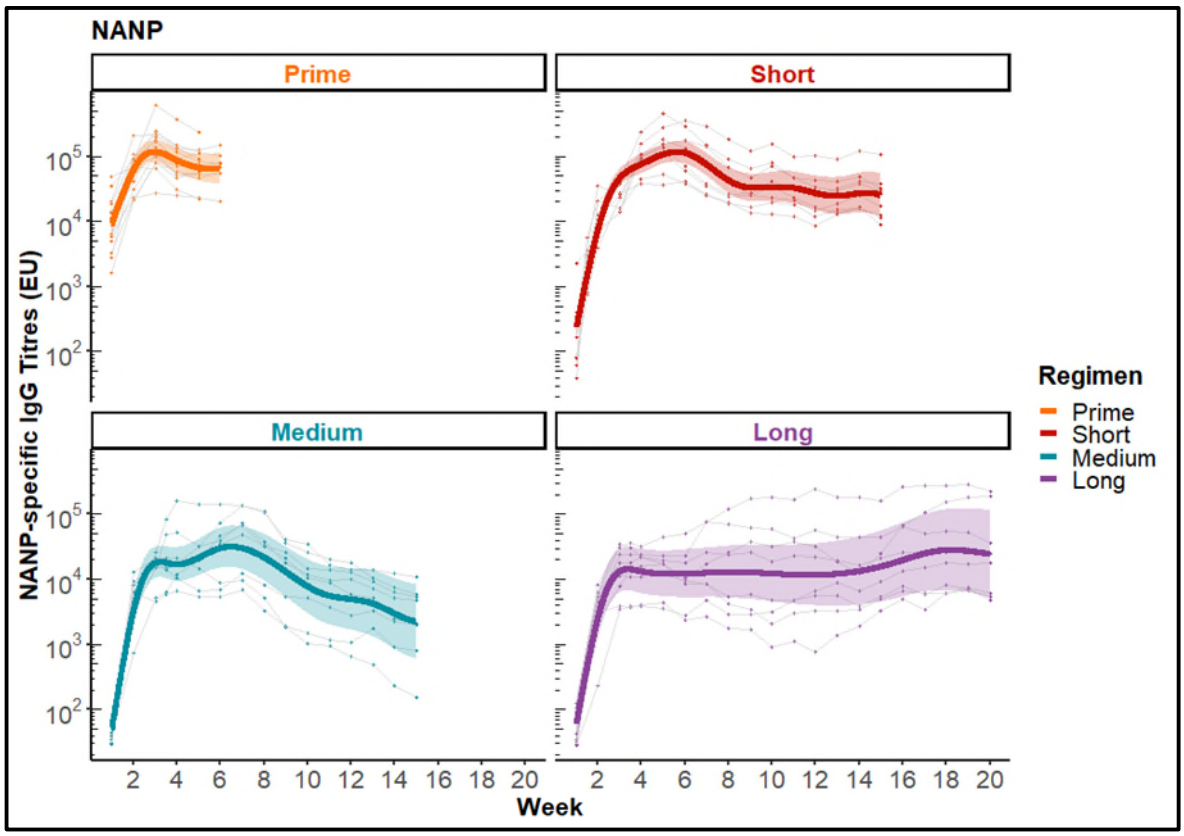

Figure 5-8: Longitudinal NANP-specific immune kinetic profiles for different LCSS particle formulations.

NANP-specific titres are measured by ELISA for adjuvanted R21, encapsulated in different LCSS particle formulations or nonencapsulated (Prime only n=16, other regimens n=8). Titres were measured weekly following immunisation, and data for individual mice are joined by grey lines. Group-level responses from generalised additive model (GAM) fits are displayed for each regimen as coloured lines, with the 95% CI represented by ribbons.

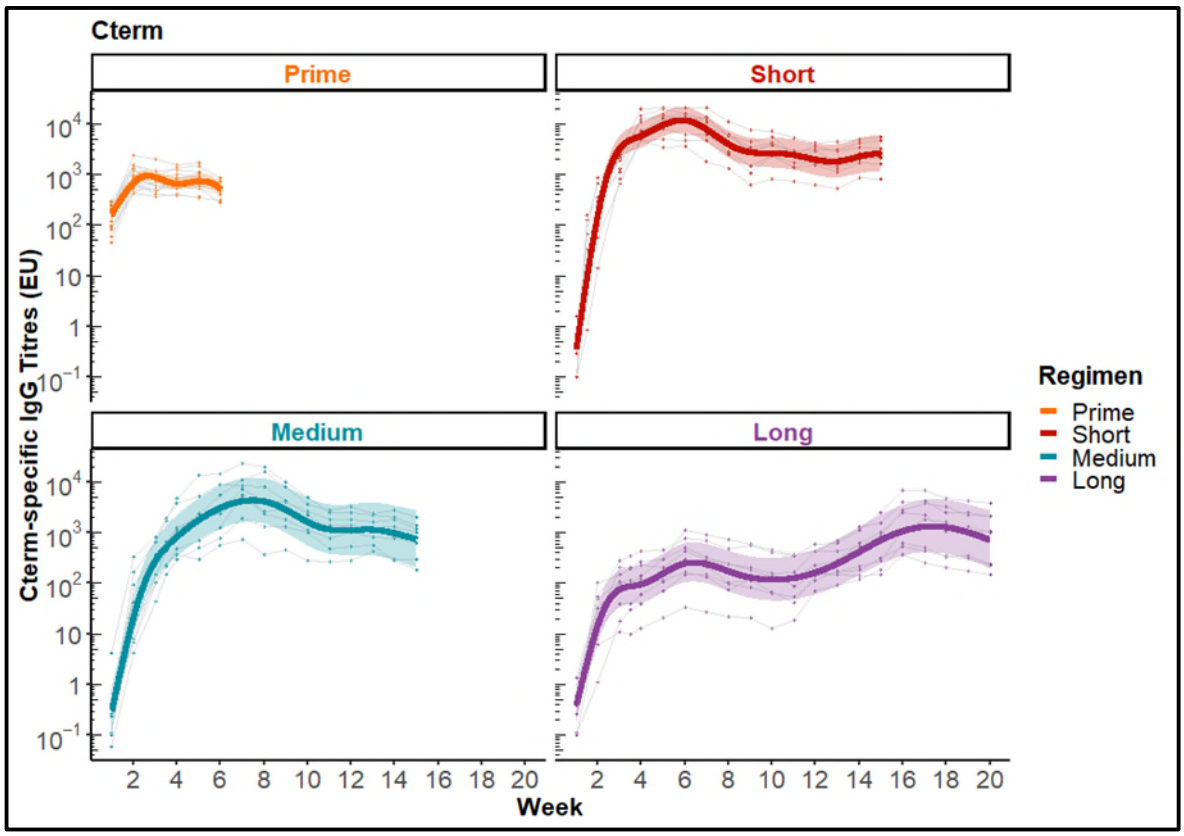

Figure 5-9: Longitudinal Cterm-specific immune kinetic profiles for different LCSS particle formulations.

Cterm-specific titres are measured by ELISA for adjuvanted R21, encapsulated in different LCSS particle formulations or nonencapsulated (prime only n=16, other regimens n=8). Titres are measured weekly following immunisation, and data for individual mice are joined by grey lines. Group-level responses from generalised additive model (GAM) fits are displayed for each regimen as coloured lines, with the 95% CI represented by ribbons.

The peak antibody titre and time to 50% of the peak titre, as estimated from the fit, are summarised with their 95% CI in **Table 5-3** and shown in **Figure 5-10**. The time taken to reach 50% of the peak titre (indicated by vertical bars) was chosen as

representative of the immune response delay, as 0.5-fold change was decided as the threshold for non-inferiority (see Material and Methods).

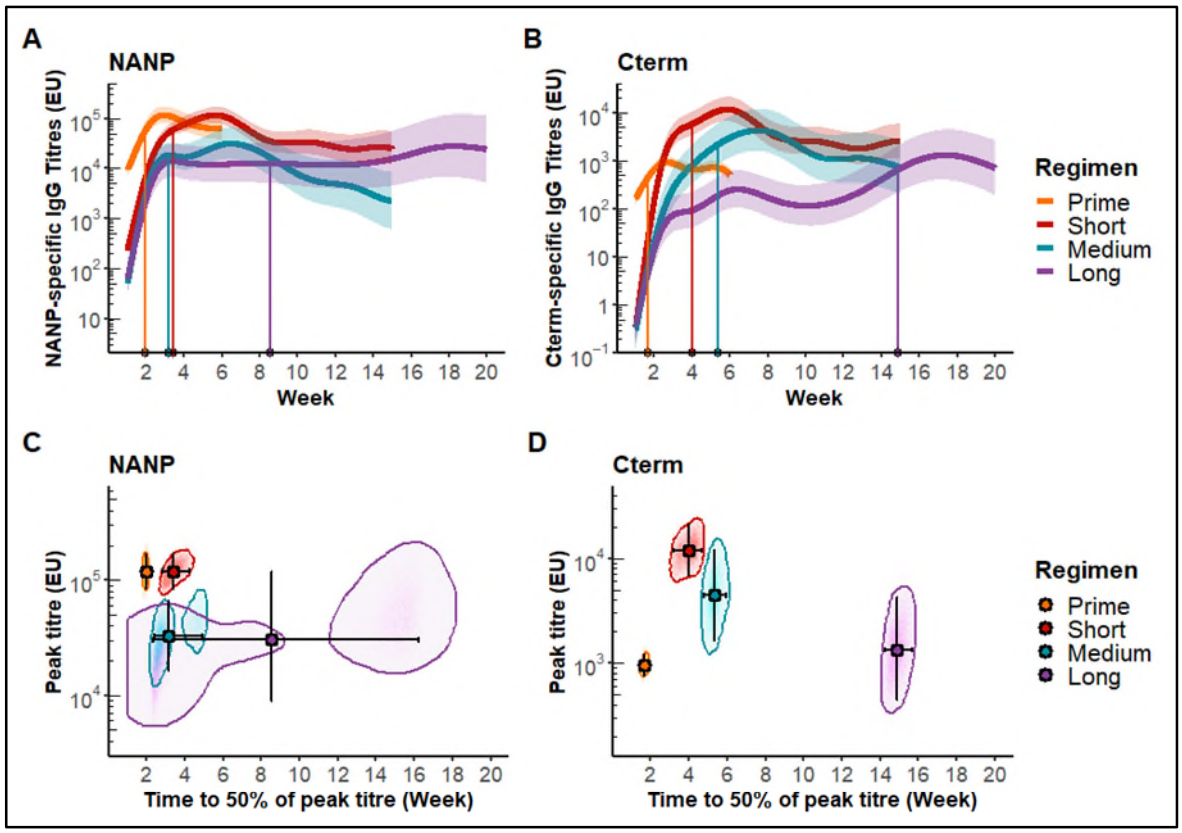

Figure 5-10: Estimates of the peak titre and time to 50% peak titre.

Group-level responses from generalised additive model (GAM) fits for (A) NANP-specific and (B) Cterm-specific IgG responses are displayed for each regimen as coloured lines, with the 95% CI represented by ribbons. Vertical lines indicate the time to 50% of peak titre. (C-D) Geometric mean peak antibody titre and mean time to 50% peak titre of the 10,000 simulated samples (faded dots for each simulated samples) with 95% confidence regions (shaded areas) and 95% marginal CI (error bars).

Table 5-3: Estimates of peak antibody titres and time to 50% peak titre for NANP-specific and Cterm-specific responses for the different particle formulations and the unencapsulated control.

Regimen	NANP		Cterm	
	Peak[a] EU *[95% CI]*	**Time to 50%Peak[b]** Weeks *[95% CI]*	**Peak[a]** EU *[95% CI]*	**Time to 50%Peak[b]** Weeks *[95% CI]*
Prime	**$1.2{\cdot}10^5$** *[$8.4{\cdot}10^4$ – $1.7{\cdot}10^5$]*	**2** *[1.9 – 2.1]*	**$9.5{\cdot}10^2$** *[$7.6{\cdot}10^2$ – $1.2{\cdot}10^3$]*	**1.7** *[1.6 – 1.8]*
Short	**$1.2{\cdot}10^5$** *[$8.4{\cdot}10^4$ – $1.7{\cdot}10^5$]*	**3.4** *[2.9 – 4.3]*	**$1.2{\cdot}10^4$** *[$6.8{\cdot}10^3$ – $2.1{\cdot}10^4$]*	**4** *[3.2 – 4.6]*
Medium	**$3.6{\cdot}10^4$** *[$1.6{\cdot}10^4$ – $6.5{\cdot}10^4$]*	**3.2** *[2.4 – 5]*	**$4.4{\cdot}10^3$** *[$1.7{\cdot}10^3$ – $1.2{\cdot}10^4$]*	**5.3** *[4.8 – 6]*
Long	**$3{\cdot}10^4$** *[$8.9{\cdot}10^3$ – $1.2{\cdot}10^5$]*	**8.6** *[2.4 – 16]*	**$1.7{\cdot}10^3$** *[$4.4{\cdot}10^2$ – $4.2{\cdot}10^3$]*	**15** *[14 – 16]*

[a]Geometric mean. [b]Mean.

As illustrated in **Figure 5-11**, the effect of encapsulation of R21 with LMQ adjuvant was tested for non-inferior immunogenicity (by comparison of the antibody peak titres of the encapsulated regimens to the Prime regimen, with a 0.5-fold threshold for non-inferiority) and a delay in onset of the immune response, indicating lag time in the release of the booster dose. The difference in immune response delay between the different particle formulations was then estimated.

In the Short formulation, as shown in section 5.2.2, encapsulation either increased or did not affect immunogenicity compared to the non-encapsulated control, with no fold change in NANP-specific peak antibody titres (95% CI 0.6 – 1.7, $p<0.05$ for noninferiority) and 12-fold higher (95% CI 6.8 – 23, $p<0.05$) Cterm-specific peak antibody titres. The encapsulation in Short particles extended the delay in the onset of immunogenicity compared to the nonencapsulated control, increasing the time to 50% of the peak titre by 1.5 weeks (95%CI 0.9 – 2.2, $p<0.05$) for the NANP-specific

antibody titres, and by 2.3 weeks (95%CI 1.5 – 3, $p<0.05$) for the Cterm-specific antibody titres (**Figure 5-11**).

In the Medium formulation, encapsulation led to increased Cterm-specific immunogenicity, with 4.6-fold higher (95% CI 1.7 – 13, $p<0.05$) Cterm-specific peak antibody titres. However, NANP-specific immunogenicity was significantly decreased by encapsulation, with a 0.3-fold change (95% 0.1 – 0.6, $p<0.05$) of antibody titre. The encapsulation in Medium particles extended the delay in the immunogenicity compared to nonencapsulated control, increasing the time to 50% of the peak titre by 1.2 weeks (95%CI 0.4 – 3, $p<0.05$) for the NANP-specific antibody titres, and by 3.7 weeks (95%CI 3.1 – 4.3, $p<0.05$) for the Cterm-specific antibody titres.

Finally, in the Long formulation, sufficient evidence was not found for the non-inferiority in immunogenicity compared to the nonencapsulated control, with 1.4-fold change (95% CI 0.4 – 4.5, $p>0.05$) in Cterm-specific peak antibody titres and a 0.3-fold change (95% 0.1 – 1.1, $p>0.05$) in NANP-specific peak antibody titres. However, the encapsulation in Long particles provided a significant extension of delay in the immunogenicity compared to nonencapsulated control, increasing the time to 50% of the peak titre by 6.6 weeks (95%CI 0.4 – 14, $p<0.05$) for the NANP-

specific antibody titres, and by 13 weeks (95%CI 13 – 14, p<0.05) for the Cterm-specific antibody titres.

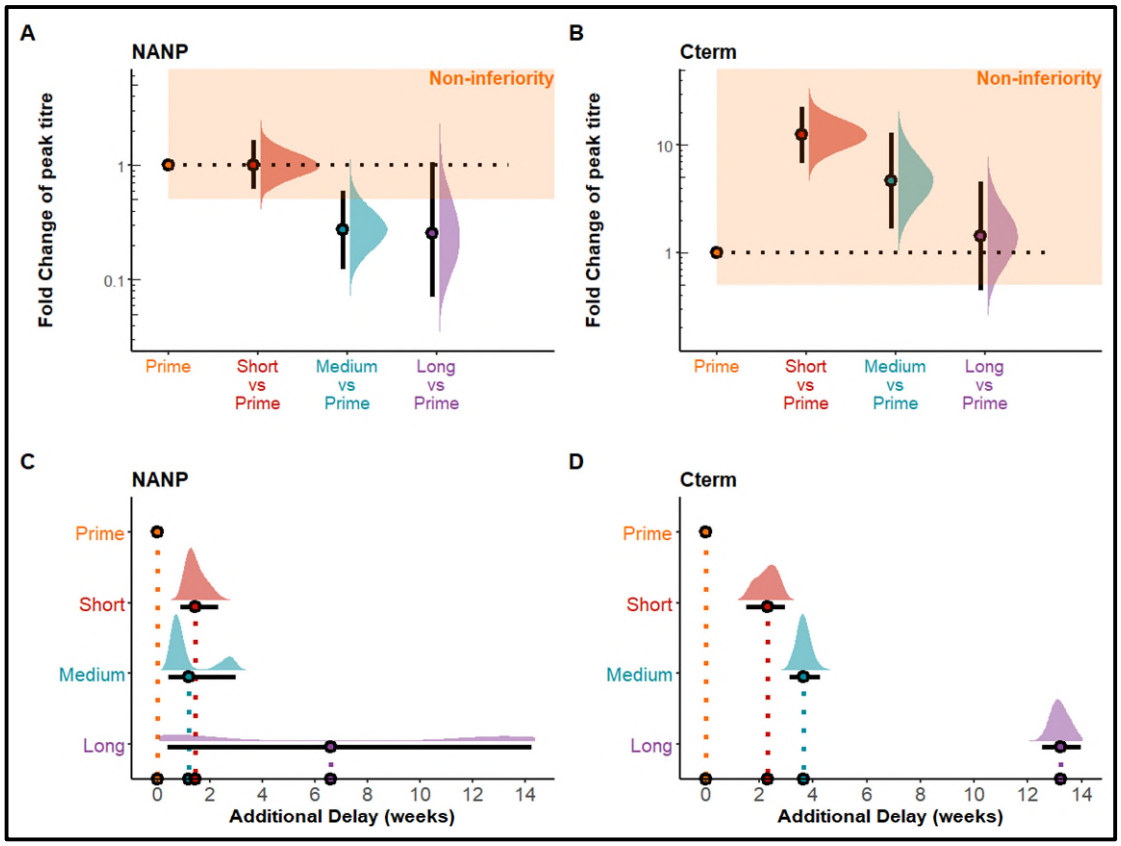

Figure 5-11: Fold change of peak antibody titres and additional immune response delay for different LCSS particle formulations compared to unencapsulated control.

Geometric mean fold change of (A) NANP- and (B) Cterm-specific peak antibody titre and mean additional delay in time to reach 50% (C) NANP- and (D) Cterm-specific peak titre for different LCSS particle formulations compared to unencapsulated control. Error bars represent 95% CIs, density plots represent the simulated sampling distributions. Non-inferiority intervals at a 0.5-fold change threshold are displayed as shaded rectangles.

The particle formulations studied here induced significantly different delays in Cterm-specific immune response compared to each other, similar to what was observed *in vitro* (see Chapter 4). Thus, compared to the Short particle formulation, the Medium particle formulation, made with higher Mw PLGA, increased the time to

50% of peak titre by 1.4 weeks (95%CI 0.5 – 2.3, p<0.05) for the Cterm-specific response. Similarly, the Long particle formulation, manufactured with a higher L:G ratio PLGA increased the time to 50% of peak titre by 9.5 weeks (95%CI 8.7 – 10, p<0.05) for the Cterm-specific response compared to the Medium particle formulation.

There was no conclusive evidence for an extended delay between different particle formulations for the NANP-specific response.

5.2.4 Prime + Particle formulation provides superior immunogenicity to Prime alone

The R21 vaccine in combination with the LMQ adjuvant has demonstrated high immunogenicity and protection in malaria challenge studies when given in a multi-injection regimen. To evaluate the potential benefit of co-injected prime and encapsulated doses (designated as the "**Prime + PAR"** regimen) over the single matched dose injection (designated as **"Prime"** regimen), both Short and Medium particle formulations were evaluated in parallel studies. For each study, BALB/c mice were injected with 3 different regimens, and immunogenicity and efficacy in a malaria challenge model were compared. The regimens were as presented below:

- **Prime:** a single injection of R21 and LMQ in PBS, matching the total amount received in the Prime + PAR regimens (2 full doses of R21, 1+1/7th dose of LMQ),
- **Prime/Boost:** a prime injection of R21 and LMQ in PBS, and a booster injection of R21 and LMQ in PBS. Booster was given two weeks after the prime for the Short study, and 3 weeks after prime for the Medium study.

- **Prime + Short PAR / Prime + Medium PAR:** a single injection of R21 and LMQ in PBS, and R21 with a fractional dose (1/7th) of LMQ co-encapsulated in either **Short** or **Medium** formulation LCSS particles,

Weekly blood samples were taken to follow the immune response until the malaria challenge session. Experimental design is illustrated in **Figure 5-12**.

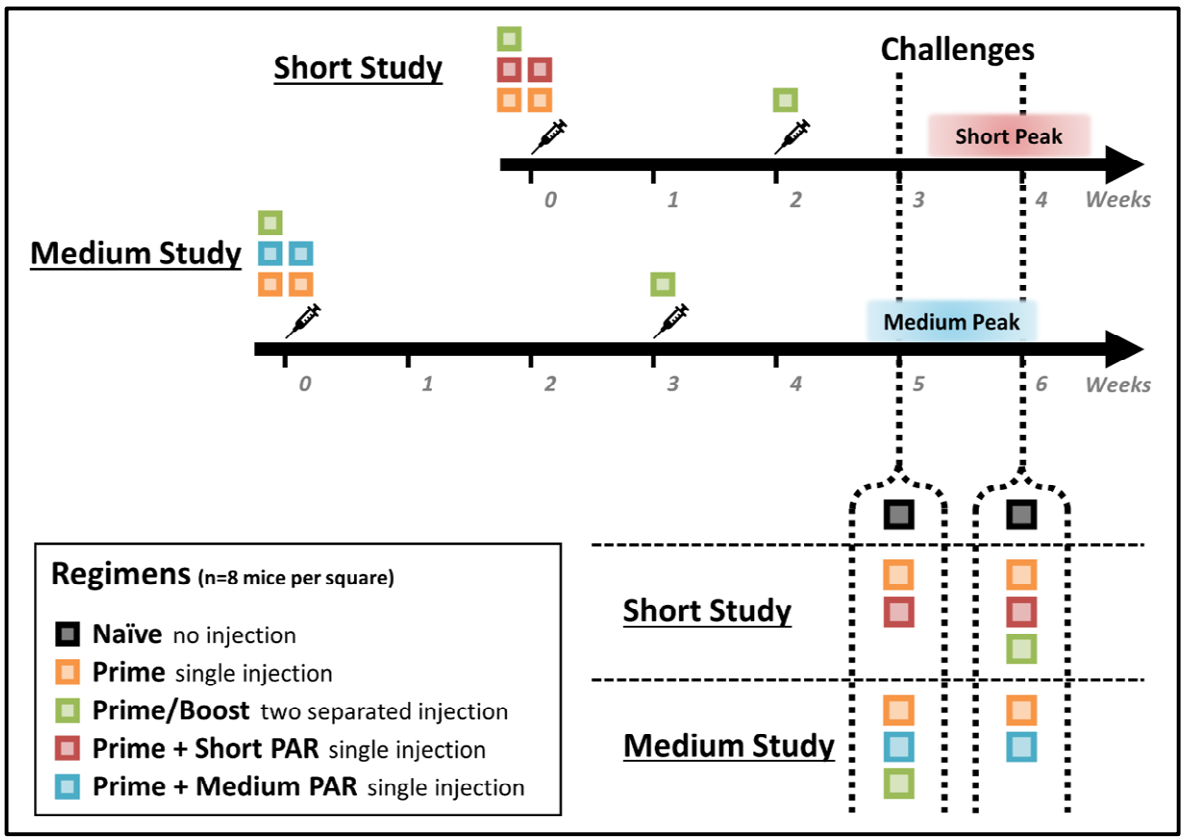

Figure 5-12: Design summary of the in vivo immunogenicity and malaria challenge experiment comparing the efficacy of the Prime + Particles regimen with Prime only.

BALB/c mice were immunised IM as illustrated. Injections were performed using 100µL Hamilton glass syringes sterilised with ethanol and 25G needles. Injection volume was 50µL with 0.5% carboxymethylcellulose in PBS as a viscoenhancing agent to prevent LCSS particle aggregation in the syringe. Challenge was performed in two challenges sessions, by IV injection (into the tail vein) of 1000 transgenic P. berghei sporozoites per mouse. Peak time windows displayed here correspond to the 95% CI of time to 50% of peak titre in Cterm-specific immunogenicity estimated in section 0.

5.2.4.1 Immunogenicity in the Short particle release study

As illustrated in **Figure 5-13**, all three regimens in the Short study had similar Cterm and NANP-specific immune response for the first 2 weeks. As expected, the booster dose produced a rise in antibody titres for the Prime/Boost regimen which was similar to the Prime + Short PAR regimen for the Cterm-specific antibody titres. The NANP-specific response in the Prime + Short PAR regimen remained at the same level as the Prime regimen. Both Cterm and NANP-specific responses in the Prime regimen reached a plateau after week 3.

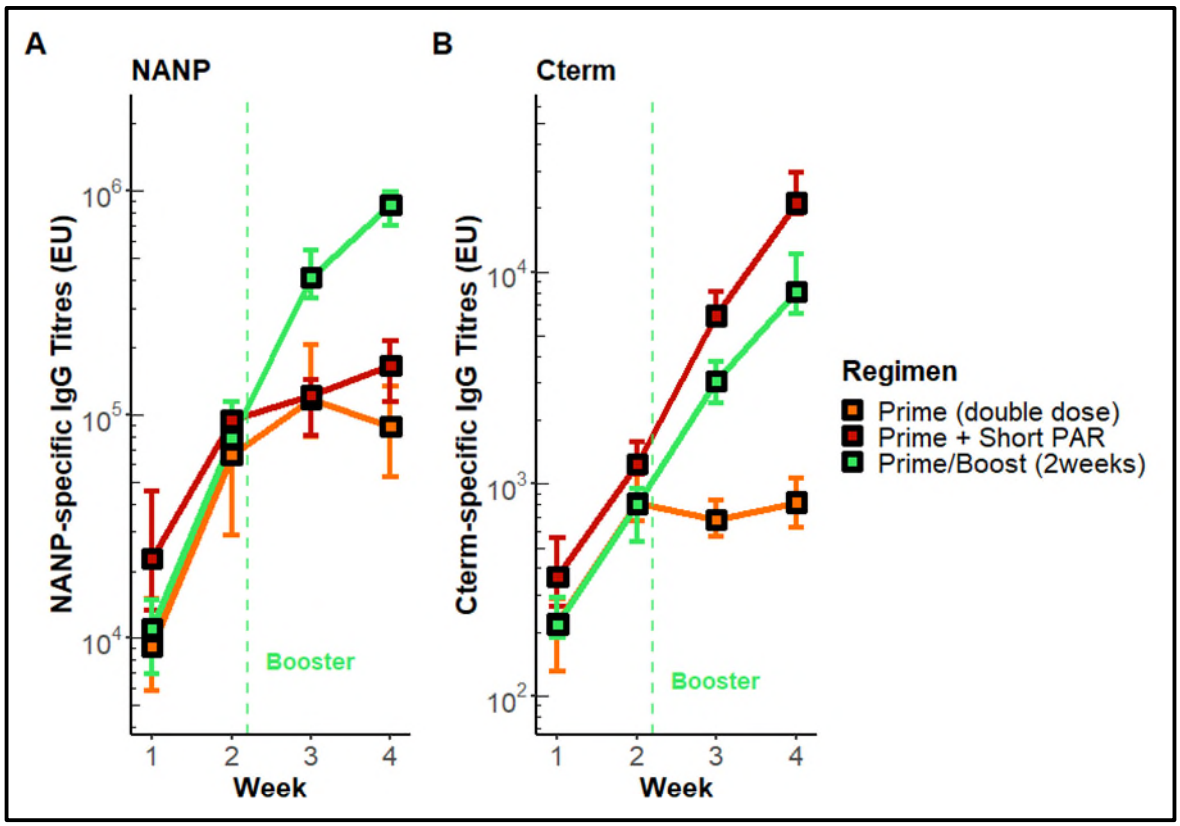

***Figure 5-13**: Immune response kinetics of different R21/LMQ regimens in the Short study challenge*

Specific IgG are measured by ELISA against (A) NANP – (B) Cterm epitopes of the R21 vaccine in BALB/c mice (Prime/Boost regimen n=8, other regimens n=16) for each of the three regimens tested. Titres are measured from tail blood sampling every week following immunisation until the challenge session and represented by the Median and interquartile range. Booster timing for the Prime/Boost regimen is represented by a vertical dashed line.

The observed maximum IgG peak for each regimen and the fold change of the mean peak log titres between encapsulated regimen and nonencapsulated controls are shown in **Figure 5-14**. Estimated geometric means and confidence intervals for the three regimens are reported in **Table 5-4**.

The Prime + Short PAR resulted in higher Cterm-specific immunogenicity compared to both the Prime, with 20-fold higher (95% CI, 12 – 28, $p<0.05$) antibody titres, and the Prime/Boost regimen, with 2.7-fold higher (95% CI, 1.7 – 4.3, $p<0.05$) antibody titres. In contrast, NANP-specific immunogenicity was lower in comparison with the Prime/Boost regimen, with a 0.2-fold reduction (95% CI, 0.1 – 0.3, $p<0.05$) in antibody titres. There was no significant difference in NANP-specific immunogenicity between the Prime + Short PAR regimen and single injection Prime, with a 1.7-fold change (95%CI 0.8 – 4.7, $p>0.05$) in antibody titres.

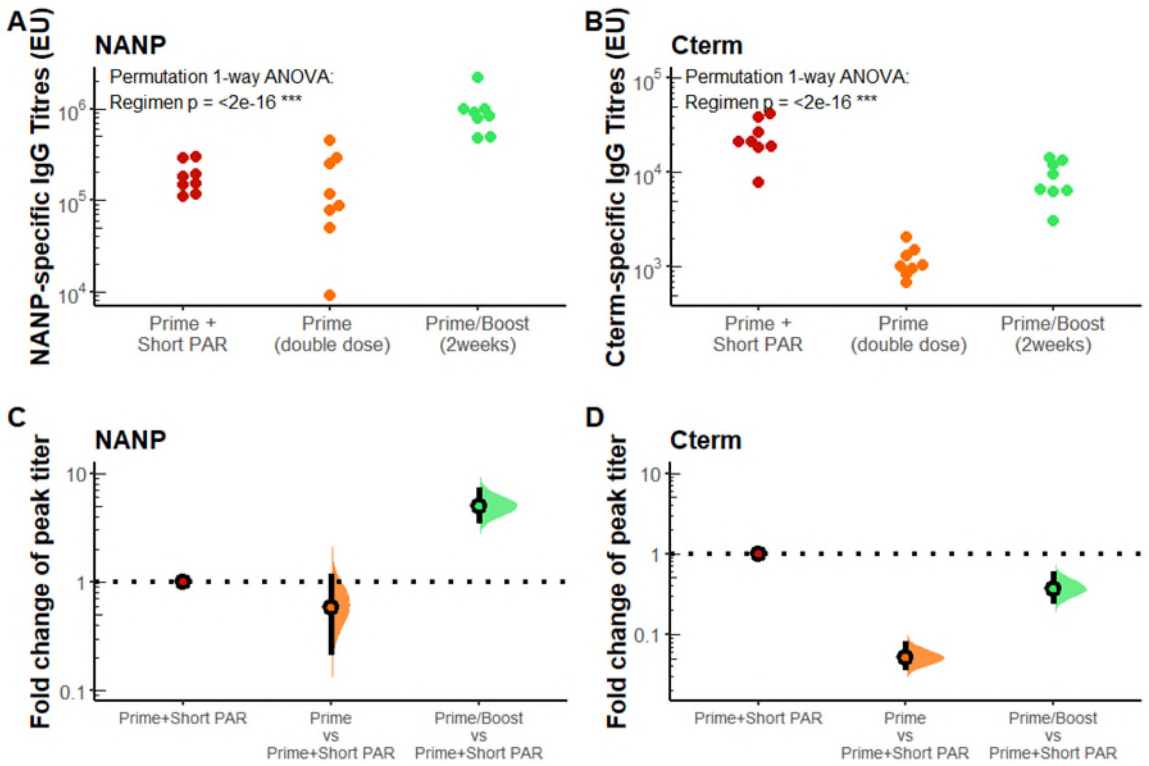

Figure 5-14: Peak antibody Cterm-specific response in the Prime and Short PAR regimen is superior to nonencapsulated Prime and Prime/Boost regimens.

Peak observed titres of specific IgG against (A) NANP – (B) Cterm epitopes are shown for each mouse (all regimens n=8). Fold change of the mean peak log titre for (C) NANP and (D) Cterm- specific responses are estimated by bootstrapping and reported as geometric mean fold change with 95% CI (error bars) and sampling distributions (density plots).

5.2.4.2 Immunogenicity in the Medium particle release study

The Prime + Medium PAR regimen generated a stronger immune response than the Prime regimen against both the NANP and Cterm epitopes (**Figure 5-15**). The kinetics however diverged after week 2, with titres in the Prime + Medium PAR group continuing to rise while those in the Prime regimen reached a plateau. The plateau

eventually reached by the Prime + Medium PAR regimen was between those for the Prime and Prime/Boost groups.

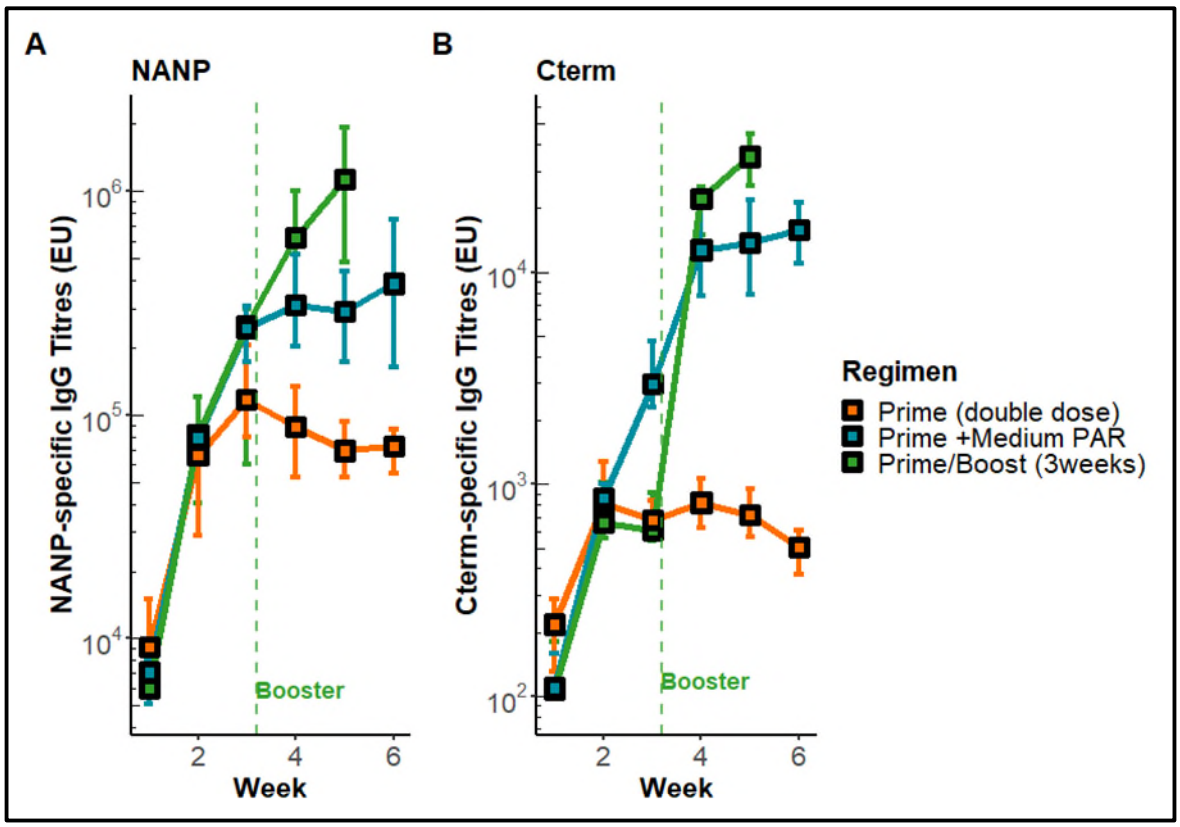

Figure 5-15: Immune response kinetics of different R21/LMQ regimens in the Short study challenge.

Specific IgG are measured by ELISA against (A) NANP – (B) Cterm epitopes of the R21 vaccine in BALB/c mice (Prime/Boost regimen n=8, other regimens n=16) for each of the three regimens tested. Titres are measured from tail blood sampling every week following immunisation until the challenge session and represented by the Median and interquartile range. Booster timing for the Prime/Boost regimen is represented by a vertical dashed line.

The observed maximum IgG peak for each regimen and the fold change of the mean peak log titres between encapsulated regimen and nonencapsulated controls are reported in **Figure 5-16**. Estimated geometric means and confidence intervals for the three regimens are reported in **Table 5-4**.

The Prime + Medium PAR induced higher immunogenicity against both NANP- and Cterm epitopes compared to Prime only, with 2.6-fold higher (95% CI, 1.6 – 4.2, $p<0.05$) NANP-specific, and 15-fold higher (95% CI, 11 – 21, $p<0.05$) Cterm-specific antibody titres. In contrast, Cterm-specific immunogenicity was lower in comparison with the Prime/Boost regimen, with a 0.4-fold change (95% CI, 0.3 – 0.6, $p<0.05$) in antibody titres. Sufficient evidence was not found for a significant difference on NANP-specific immunogenicity between the Prime + Medium PAR and the Prime/Boost regimen, with a 0.5-fold difference (95%CI 0.2 – 1.2, $p>0.05$) in antibody titres.

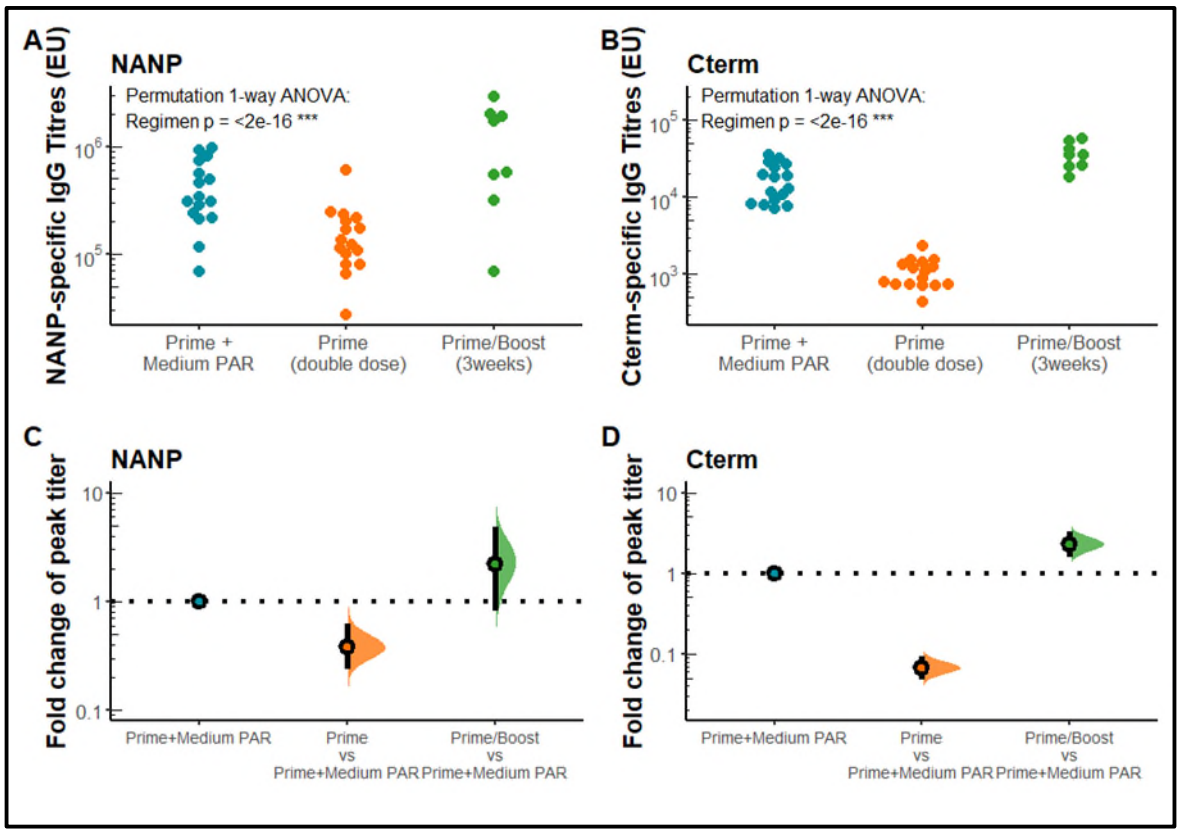

Figure 5-16: Peak antibody Cterm-specific response of Prime and Medium PAR regimen is superior to nonencapsulated Prime regimen.

Peak observed titres of specific IgG against (A) NANP – (B) Cterm epitopes are shown for each mouse (Prime/Boost regimen n=8, other regimens n=16). Fold change of the mean peak log titre for (C) NANP and (D) Cterm- specific responses are estimated by bootstrapping and reported as geometric mean fold change with 95% CI (error bars) and sampling distributions (density plots).

The estimated maximum observed peak titres for both the Short and Medium studies are summarised in **Table 5-4** below.

Table 5-4: Geometric mean estimates of peak antibody titres for Short and Medium formulations studies.

	Short Study		Medium Study	
Regimen	**NANP** EU *[95% CI]*	**Cterm** EU *[95% CI]*	**NANP** EU *[95% CI]*	**Cterm** EU *[95% CI]*
Prime	**$1{\cdot}10^5$** *[$3.9{\cdot}10^4$ – $2{\cdot}10^5$]*	**$1.1{\cdot}10^3$** *[$9.1{\cdot}10^2$ – $1.4{\cdot}10^3$]*	**$1.3{\cdot}10^5$** *[$9.5{\cdot}10^4$ – $1.8{\cdot}10^5$]*	**$1{\cdot}10^3$** *[$8.3{\cdot}10^2$– $1.2{\cdot}10^3$]*
Prime + PAR	**$1.7{\cdot}10^5$** *[$1.4{\cdot}10^5$ – $2.2{\cdot}10^5$]*	**$2.2{\cdot}10^4$** *[$1.5{\cdot}10^4$ – $2.9{\cdot}10^4$]*	**$3.5{\cdot}10^5$** *[$2.4{\cdot}10^5$ – $4.9{\cdot}10^5$]*	**$1.5{\cdot}10^4$** *[$1.2{\cdot}10^4$ – $2{\cdot}10^4$]*
Prime/Boost	**$8.6{\cdot}10^5$** *[$6.6{\cdot}10^5$ – $1.3{\cdot}10^6$]*	**$8{\cdot}10^3$** *[$5.3{\cdot}10^3$ – $1.1{\cdot}10^4$]*	**$7.7{\cdot}10^5$** *[$2.9{\cdot}10^5$ – $1.5{\cdot}10^6$]*	**$3.4{\cdot}10^4$** *[$2.6{\cdot}10^4$ – $4.4{\cdot}10^4$]*

5.2.5 Encapsulation improves the efficacy of a single vaccine dose

For each study, the animals in the Prime and Prime + PAR regimens were split into two groups of 8 mice to be challenged at two timepoints: at week 3 and 4 post immunisation in the Short study, and at week 5 and 6 post immunisation in the Medium study, sharing the challenge sessions between studies. This corresponds to the estimated time intervals covering their respective peak antibody titres following particle release (as described in section 5.2.3). Prime/Boost controls (n=8 per study) were only challenged once, 2 weeks after the boost. Naïve mice (n=8 per challenge session) were shared between the two studies. The challenge design is summarised in **Figure 5-12**.

Malaria challenge was performed by IV injection of 1000 transgenic *P. berghei* sporozoites. Development of parasitaemia was monitored from day 5 by assessing the presence and percentage of infected erythrocytes in peripheral blood using thin

blood smears. Animals that reached 1% parasitaemia were culled [148]. Animals that remained free from infection at day 12 were considered sterilely protected.

The effect of regimen on the time to infection was analysed by Cox regression and hazard ratios were computed, adjusted for the challenge session. The hazard ratio for a regimen of interest represents the instantaneous relative risk of infection at any given time, relative to the Prime regimen.

5.2.5.1 Short release delay particles

In this study the single injection of the Prime + Short PAR formulation conferred 25% protection (4/16 mice) while in the Prime only group 12.5% (2/16 mice) survived, for the mice in this study. The Prime + Short PAR formulation was more effective at delaying infection compared to the Prime only (**Figure 5-17**), with a hazard ratio of 0.4 (95% CI 0.2-0.9, p=0.02). The Prime/Boost regimen offered 87.5% protection (7/8 mice) and was also more effective than the Prime only, with a hazard ratio of 0.08 (95% CI 0.01-0.6, p=0.01).

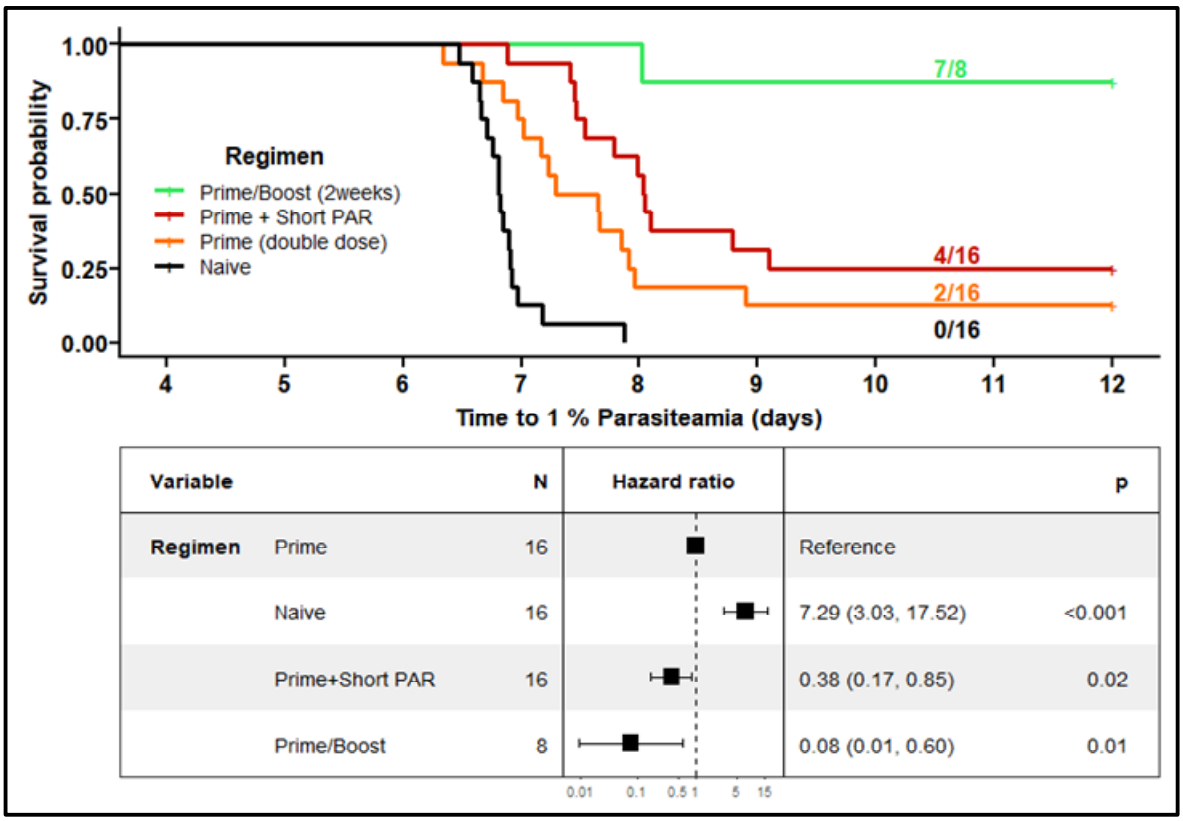

Figure 5-17: Prime + Short PAR is more protective and delays time to malaria infection compared to Prime only.

BALB/c mice were immunized with different regimens (n=8 for Prime/Boost, n=16 for others) and challenged by IV injection of 1000 sporozoites. Prime/Boost mice were challenged 2 weeks after the booster (4 weeks after the first) immunisation, whereas other regimens were challenged at either 3 or 4 weeks after immunisation in two challenge sessions, n=8 per regimen at each challenge session. Blood stage parasitaemia was monitored for a week starting from day 5 after challenge. Kaplan Meier curves for infection (1% parasitaemia) are plotted for each regimen, pooling data from the two challenge sessions. The table shows the hazard ratios (estimated by Cox regression) for each regimen compared to Prime. Hazard ratios are displayed with their respective 95% CI and p values.

5.2.5.2 Medium release delay particles

The single injection of the Prime + Medium PAR formulation conferred 43.8% (7/16 mice) sterile protection against malaria in comparison with 13.3% (2/15 mice) for the Prime only, observed for the mice in this study. The Prime + Medium PAR formulation was also significantly more effective at delaying infection compared to Prime only (**Figure 5-18**), with a hazard ratio of 0.4 (95% CI 0.2-0.9, p=0.026). The

Prime/Boost regimen resulted in 100% sterile protection (8/8 mice). In the absence of infection in the Prime/Boost regimen, the hazard ratio could not be estimated.

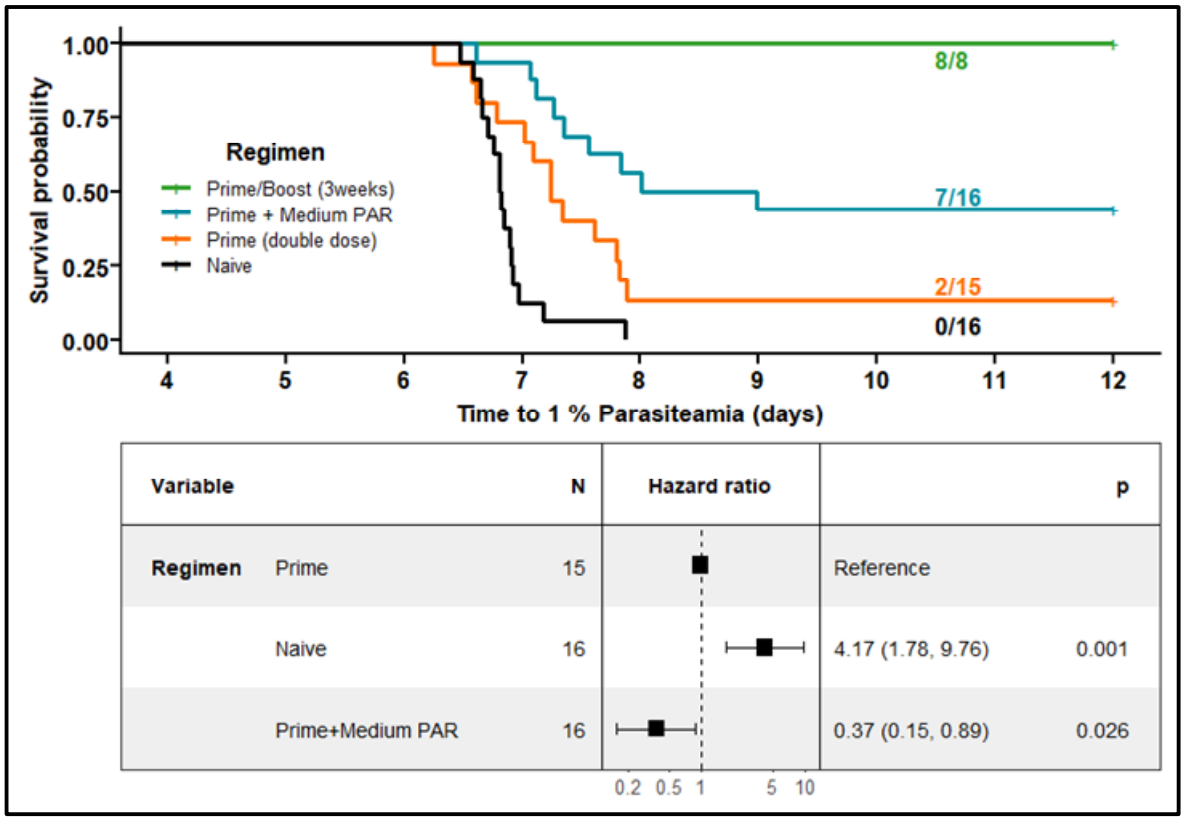

Figure 5-18: Prime + Medium PAR is more effective at delaying time to malaria infection compared to Prime only.

BALB/c mice were immunized with different regimens (n=8 for Prime/Boost, n=16 for others) and challenged by IV injection of 1000 sporozoites. Mice receiving the Prime/Boost regimen were challenged 2 weeks after the boost (5 weeks following the first immunisation) whereas other regimens were challenged at either 5 or 6 weeks after immunisation in two challenge sessions, n=8 per regimen at each challenge session. Blood stage parasitaemia was monitored from day 5 following challenge. Kaplan Meier curves for infection (1% parasitaemia) are plotted for each regimen pooling challenge sessions. The table shows the hazard ratios (estimated by Cox regression) for each regimen compared to Prime. Hazard ratios are displayed with their respective 95% CI and p values.

5.3 Discussion

5.3.1 R21 remains immunogenic following encapsulation

Short delay release formulation LCSS particles encapsulating the R21 vaccine resulted in non-inferior Cterm and NANP responses compared to the same dose of unencapsulated vaccine. This suggests that the microfluidic emulsification process and exposure to the low intraparticle pH (see Section 4.3.3) and physiological conditions *in vivo* following the injection of encapsulated R21 did not affect immunogenicity for either of the studied epitopes, demonstrating the utility of this technology with the malaria vaccine. The ability to retain of immunogenicity for payloads encapsulated inside LCSS particles could potentially be extended to any VLP, as they have demonstrated absence of morphological changes at low pH and physiological temperature. However, this may not hold for any immunogen used in a vaccination context. Thus, soluble proteins may lose their conformation in such conditions, as demonstrated for the tetanus toxoid, who loses 40% of its antigenicity after a week at 37°C [158]. Moreover, liposomes used for mRNA encapsulation are subjected to hydrolysis when kept at 37°C [159]. Such limitations could be overcome by the addition of excipients to reduce pH and temperature-induced aggregation of encapsulated antigens, thus improving their stability [160].

In our experiment, the response against the Cterm epitope was significantly higher in the Particle regimen compared to Prime, indicating that the kinetics of release and resulting delayed exposure to the booster vaccine dose increased the magnitude of the Cterm-specific immune response. The low immunogenicity of unadjuvanted R21 hindered the comparison of delays in generating immunogenicity

and relevant peak titre differences, as all previous preclinical work with R21 includes use of adjuvants [58], [150], [161].

Using LMQ as the adjuvant, co-encapsulation of R21 and a fractional dose of LMQ in Short delay release formulation particles demonstrated the same ability to maintain or improve immunogenicity compared to unencapsulated adjuvanted vaccine. NANP-specific response was non-inferior to Prime only, and Cterm-specific response was significantly increased by more than 12-fold, despite the 7-fold lower adjuvant dose.

5.3.2 Delay in the Cterm-specific response can be tuned by the LCSS particle formulation

Overall, the immunogenicity results suggest that the Cterm-specific response increases with repeated exposure to the R21 vaccine, as reported previously [162], [163]. Indeed, mice that only received a single Prime injection had the lowest Cterm-specific antibody titres, while mice that also received a booster, demonstrated a significant increase in Cterm-specific immunogenicity (**Figure 5-3**). In the case of LCSS particles, as observed *in vitro* (see Chapter 4), the kinetic of delivery of the encapsulated vaccine payload is the result of the cumulative release of each single particle. The individual releases happen after a lag slightly different for each particle resulting in a global release from all particles that can span from days to weeks depending on the LCSS particle formulation. Thus, multiple releases from different fractions of the total injected particles would result in multiple exposures to the vaccine *in vivo*, producing higher levels of Cterm-specific antibody response than the single exposure at a discrete time, as in Prime only regimens. Cterm immunogenicity monitoring can thus be used to detect delays in the vaccine release,

with the timing of the antibody peak titre indicating the end of exposure to the vaccine. Short, Medium and Long formulations of LCSS particles demonstrated the ability to induce significant delays in Cterm-specific peak response compared to a Prime only regimen, ranging from 2 additional weeks for the Short formulation, to 13 weeks for the Long formulation. The delay was consistent with the order of release observed *in vitro* (Short delay < Medium delay < Long delay, see Chapter 4) and expected from the PLGA composition of each formulation (increased Mw for Medium formulation, increased L:G for Long formulation), demonstrating the tuneability of this technology.

5.3.3 NANP-specific response from Particle only regimens is hindered with longer delay release formulations

Published research on the RTS,S vaccine, structurally very similar to R21, and including the same NANP and Cterm epitopes, found that the NANP-specific response reaches saturation after multiple boosters [163]. This is explained by a negative antibody feedback limiting the expansion of B cell responses against this immunodominant NANP target by epitope masking [162]. Indeed NANP-specific antibodies resulting from previous vaccinations are able to bind to the NANP region of the CSP antigen in subsequent boosters, which limits the memory B cell recruitment and differentiation, dampening the recall NANP-specific response. Cterm subdominant epitopes are not affected by this feedback mechanism and Cterm-specific IgG titres continuously increase with boosters [162], [163]. Thus, in the case of encapsulated regimen, the multiple exposure to the vaccine that results in increased Cterm-specific antibody titres would also explain the absence of increase in NANP-specific immunogenicity compared to the Prime only regimens.

Over the time required for a whole injected batch of Short formulation particles to release their content, the NANP-specific antibody produced by the early releasing particles would be expected to hinder the boost from the later releasing particles. Medium and Long formulation particles induced lower NANP-specific immunogenicity, consistent with the hypothesis of a negative antibody feedback as the release from these particles is more spread out across time than the Short formulation (see Chapter 4). As with the Short formulation particles, the subdominant Cterm-specific response with the Medium and Long formulations remained higher or similar to the Prime only control. Delays in the NANP-specific response compared to the Prime only were also observed for all particle formulations but, potentially due to the negative feedback mechanism, no delay differences were observed between different particles formulations. Indeed, Medium and Long formulation particle regimens displayed antibody titres detectable from the first week following immunisation. This could indicate a potential early release, due to physical breakage of the particles once injected *in vivo*, or a small initial burst release from a small fraction of particles, as observed with some formulations *in vitro* (see Chapter 4).

Another possible explanation for the reduced NANP-specific Ab titres in the longer delay particles regimen is the potential vaccine and/or adjuvant degradation when exposed for longer periods to 37°C and low pH inside the capsules once injected. VLPs like R21 have been found to be resistant to these ranges in temperature and pH [164], but liposomes (as LMQ) can be degraded by the hydrolysis of their constitutive phospholipids, with the hydrolysis rate increasing at higher temperature and lower pH [165]. This adjuvant degradation could also explain the observed decrease in Cterm-specific antibody peak titers with longer delay particles.

5.3.4 The addition of encapsulated booster to the Prime regimen increases both NANP and Cterm-specific immune responses

Despite the potential limitations in NANP-specific response, and long-term stability of the payload in the Particles only regimen, different immunogenic patterns were observed when co-injecting a standard priming vaccine dose with Short or Medium particle formulations containing the booster vaccine with a fractional (1/7th) dose of the adjuvant. The Prime + Medium PAR regimen induced 3-fold and 15-fold higher NANP- and Cterm-specific antibody titres respectively, compared to Prime only matched dose, regimens (**Figure 5-16**). The Prime + Short PAR regimen induced only 20-fold higher Cterm-specific Ab titres than the Prime only (**Figure 5-14**). This differences in NANP-specific immunogenicity between LCSS particle formulations when co-injected with the Prime, could be the result of the different delays induced by each formulation. Hence, the Short particles release the vaccine too soon after the priming dose, preventing the adequate boosting of the NANP-specific response. The Medium particles, for which complete release was delayed by an additional week (as defined using Cterm-specific response), resulted in a longer gap from the priming dose when combined with the Prime, driving the NANP-specific responses higher than the Prime only regimen.

5.3.5 Protection against malaria was increased by the addition of the encapsulated booster dose to a soluble prime

Regardless of their different immunogenicity profiles, the two Prime + Particle (Short and Medium) regimens provided a significant hazard ratio reduction in the malaria challenge experiments compared to Prime only, showing that booster dose

encapsulation can enhance protection against malaria in mice by more than 2.5-fold when administered as a single shot. The observed sterile protection of co-injected Prime and particle regimens was higher than Prime only, highlighting the additional benefit in efficacy provided by the particles in single injections. When Medium formulation particles were combined with a priming dose, 44% of the mice survived, a 2-fold higher protection than the Short formulation particles (25%) and a 3.3-fold higher protection than the Prime only (13%). The difference between Medium and Short particles could be the result of the increased NANP-specific immune response conferred only by the Prime + Medium PAR regimen.

The Prime/Boost regimen remained more protective compared to the Prime + Particle regimens. Multiple factors could explain efficacy. The adjuvant dose in the encapsulated booster was only $1/7^{th}$ of the standard dose, due to the fixed concentration of the available LMQ adjuvant. The NANP-specific antibody titres produced in Prime/Boost regimens were higher, potentially due to the intrinsic instantaneous availability of the vaccine and adjuvant in higher amounts during boosting in comparison to the Prime + Particle regimens that provided a prolonged exposure in smaller amounts. Finally, the timing of the delay induced by Short or Medium particle formulations is likely to be sub-optimal for this challenge model. It is known that optimal boosting in vaccination is achieved is the subsequent dose is given once the antibody responses from the previous vaccination have waned [166]. Since peak antibody titres are reached 2-3 weeks post-prime, release of the encapsulated dose within this time interval can be expected to result in suboptimal boosting.

Nonetheless, even though some of the formulation parameters would benefit from more optimisation, these results are the first demonstration of the benefit of an

injectable delayed delivery system in a disease challenge model, with a clinically relevant vaccine, in the context of single-dose vaccine development.

6 Concluding remarks

6.1 Summary of findings

LCSS particles can be produced by microfluidics emulsification: The addition of a step in the height of the channels of double emulsion microfluidic chips designs allowed the generation of well defined, monodispersed double emulsions with a PLGA and solvent middle phase in PDMS chips. Microfluidic emulsification in the stepped design was triggered by the cores passing and inducing Rayleigh-Plateau instabilities, ensuring a constant and systematic loading. The double emulsions were successfully converted into LCSS particles by solvent extraction, producing batches of particles with narrow size distributions (CV<4%) over long periods of production. The particle sizes were dependent on the flow pressures and their generation rate varied with the miscibility and interfacial properties between the organic middle phase and the aqueous outer phase. Overall, the microfluidic system developed achieved the production goals of monodispersity, injectable size and LCSS particle structure, allowing the evaluation of their utility in the context of single-dose vaccination.

Tuneable delayed release *in vitro* is achieved by LCSS particles: When evaluated *in vitro*, the LCSS particles were able to deliver their payload after a time lag varying from days to weeks depending on the Mw and L:G ratio of the PLGA used. This delayed kinetics of release was enabled by the LCSS structure of the particles, whereas particles made by batch emulsion exhibited immediate burst

release, inadequate to mimic the booster vaccination. Through autocatalysis, hydrolysis of the PLGA with time formed interconnected pores inside the particle shell, ultimately connecting the internal cavity to the outside, and enabling the release of the payload. The overall release of a batch of particles represented the combined release of individual particles mostly within a narrow time-window of a few days, after a lag time depending on the PLGA composition. The thickness of the particle shell played a role in the release behaviour, with thinner shell displaying a limited autocatalysed degradation, thus limiting the interconnection of pores. Different sizes of the payload could be encapsulated without significantly changing the lag time, and the particles can be kept refrigerated without influencing their kinetic of delivery, making the technology compatible with vaccine application.

LCSS particles improve the immunogenicity and efficacy of single-dose R21 regimen by delayed dose delivery: Encapsulating R21 and LMQ adjuvant in LCSS particles produced a delayed immune response in mice, lengthening with the increase in PLGA Mw and L:G ratio. The delays were consistent with the *in vitro* observations. The strength of the immune response was different for the two epitopes of interest, NANP and Cterm. In the case of NANP-specific antibodies, only the Short delay formulation exhibited an immune response non-inferior to the non-encapsulated Priming dose. However, Cterm-specific response was significantly higher in both Short and Medium delay particles, in comparison to a Prime only non-encapsulated dose. The differences between NANP and Cterm responses could be caused by the kinetics of release of the particles regimens, due to a longer exposure to the vaccine dose resulting from the cumulative release individual particles (~100,000/mice). In contrast to the Cterm, the NANP-specific response is prone to

antibody negative feedback, thus a longer exposure of smaller amounts of vaccine could explain the lower immunogenicity of particle regimens for this epitope. In addition, longer delay formulations exhibited lower immune response overall, potentially due to a degradation of the adjuvant when exposed to the physiological temperature and low pH inside particles.

When combined in a Prime + Particle regimen, the Medium delay formulation was significantly more immunogenic than a dose-matched Prime only regimen for both NANP and Cterm-specific responses. This translated into a 3-fold higher observed survival following malaria challenge, compared to the Prime only. The addition of particles significantly delayed the onset of parasitaemia in blood, decreasing the hazard ratio by 2.5-fold in the corresponding Cox regression model.

6.2 Limitations and future directions

6.2.1 Improving production reproducibility

The current microfluidic platform is based on a pressure-driven system, and consequently requires manual monitoring and tuning of the set pressures to achieve identical particles from different chips. This is because the sizes of microfluidic emulsions scale with flow rate [167]. The replacement of the chip and/or tubing, results in small variations of the fluidic resistance of the system, and hence the need to modify the flow rate for a given set pressure. To be achieve better reproducibility between production the production could be changed to flow rate-driven system, i.e., syringe pumps.

6.2.2 Increasing production rates

In the *in vivo* experiment presented in Chapter 5, ~4 mouse doses of encapsulated R21/LMQ per hour were produced by the system, at a droplet generation rate of 200Hz. The throughput could be increased for future larger pre-clinical and human clinical trials by adjusting:

Formulation: Fewer particles would be needed to encapsulate the total dose by increasing the payload concentration in the inner fluid, using ultra centrifugation or dialysis of the vaccine antigen.

Particle size: The volume of inner fluid encapsulated could be increased by increasing particles core diameters. In the thesis, the diameters of the core and particles were 45μm and 60μm respectively, to ensure a thickness of 7.5μm, crucial for release timing, as demonstrated in Chapter 4. Larger particles could be made, where an increase of 20μm of both core and particle diameters would result in a 3-fold higher volume of encapsulation.

Operating parameters: As demonstrated in chapter 3, changing the outer flow properties (salinity, surface tension with middle flow) and the position of the step resulted in increased droplet generation frequency. Further tuning could improve the throughput of the platform.

Parallelisation: As reported for other microfluidic emulsification processes [168], [169], multiple chips can be connected to the same fluid source and be run in parallel. A similar solution is compatible with the technology presented in this thesis and would multiply the throughput by the number of parallelised chips.

6.2.3 Exploration of new particle formulations

As demonstrated *in vitro* in Chapter 4, payload release was the result of the interconnection of the pore network, a random process for each particle, whose probability increased with shell thickness. The LCSS particles could benefit from the exploration of additional formulations and strategies to enhance the probability of the particle release happening, such as an osmotic active agent inside the core alongside the payload. Hence, with a biodegradable hydrogel or a sugar macromolecule with its corresponding enzyme encapsulated inside the core, a gradually increasing osmotic pressure environment could be established inside the core. This pressure would ultimately break the degraded PLGA shell after the lag phase, ensuring full release form all particles in a potential sharper release kinetic.

6.2.4 Potential for other routes of delivery

In this thesis, LCSS particles have only been tested *in vivo* using intramuscular injections, as it remains the preferred route of vaccination due to its ease of administration with minimal adverse effects [170]. The technology could be tested with other delivery routes. If the use of LCSS particles in aerosols is compromised as particles would need to be porous to achieve the small density required for lung deposition [171], defeating their purpose of keeping their payload loaded, other routes such as intradermal injection could be considered to improve immunogenicity of the encapsulated vaccines. Indeed, the skin being a region rich in antigen-presenting cells, it could provide a better environment for the induction of the immune response by a vaccine, while reducing the amount of antigen needed for an equivalent response with intramuscular injection [172]. However, such

administration routes are delicate to perform with the current needle-based methods, resulting in inconsistent vaccine administration [173]. Core-shell PLGA based transdermal microneedles have been recently developed [174] to provide an alternative solution for easier intradermal administration of the vaccine, while demonstrating the delayed release capability of core-shell PLGA architectures highlighted in this thesis. This delayed delivery intradermal system was able to match the efficacy provided by prime-boost injections of the Prevnar vaccine for prevention of infection by *Streptococcus Pneumonia*, despite suffering severe limitations in scale-up potential due to the delicate manufacturing involved (discontinuous, precise alignment required, delicate handling) due to the core-shell architecture [174]. Thus, the LCSS particles presented in this thesis could be used in combination with simple microneedles (non-core-shell), to be inserted intradermally and deliver their content after a delay, benefitting from the potential immunogenicity enhancement of delivery in the skin environment, while providing the continuous production advantage of the microfluidic process involved in the LCSS manufacturing (see Chapter 3).

6.2.5 *In vivo* release quantitative kinetics characterisation

The kinetics of the LCSS particles was characterised *in vitro*, under simulated conditions that is widely used in research but quite different from the real *in vivo* scenario. Thus, *in vivo*, the particles are not suspended in a liquid, they are exposed to mechanical stress in the muscle and potential changes in temperature [175] or pH [135] due to physical efforts. A quantitative follow-up of the IVIS work presented in Chapter 4, and histology studies to image the particle appearance and distribution

in the muscle at different timepoints would be useful to better understand the real kinetics of the particles *in vivo*. This could enable formulation of vaccine loaded particles without relying on the immune response as the indirect measure of the release kinetics.

6.2.6 Improvement of the single-dose R21 towards Prime/Boost equivalence

The *in vivo* study presented in Chapter 5 was not powered to compare accurately the Prime/Boost regimen to the Prime + Particle single injection regimen. However, the Prime/Boost regimen provided 2-fold higher immunogenicity and observed protection, compared to the Prime + Medium Particle regimen. Multiple adjustments could constitute points of improvement for a single dose R21 adjuvanted vaccine:

Adjuvant concentration: By concentrating the adjuvant by ultracentrifugation, the adjuvant dose inside the particles could be increased, probably improving the immunogenicity. A doubling in adjuvant dose has been reported to induce 2-fold higher titres of NANP-specific antibodies in human trials of R21/Matrix-M [148].

Protein stabilizers and antacids: Different excipients could be added inside the core of the particles to reduce the effect of the temperature on the antigen and adjuvants, such as trehalose or arginine, both reported as protein stabilisers and anti-aggregants in protein/PLGA delivery systems [160]. The addition of antacid, such as $Mg(OH)_2$, could also decrease the potential impact of the pH drop on the adjuvant stability [176].

Adjuvant replacement: The use of Matrix-M instead of LMQ as the encapsulated adjuvant could mitigate the effects of the physiological temperature and pH inside

the particle core, increasing the efficacy of the single-dose regimen. Indeed, LMQ is a liposome-based adjuvant, with lipids prone to hydrolysis at 37°C and acidic conditions. On the other hand, Matrix-M is a nanoparticle formed by spontaneous assembly of cholesterol phospholipids and saponin reported as stable for 3 months at 37°C or when exposed to a range of pH [177]. Furthermore, Matrix-M is currently in Phase III clinical trials with R21, demonstrating 77% protection in the field [178], making it highly relevant to the development of a single-dose malaria vaccine.

Particle formulation: NANP-specific immune response which has been associated with protection against malaria [153], seems affected by the kinetic of release (see Chapter 5). The timing of the release and its sharpness could be modified by particle formulation, to ensure a longer lag between the prime and the booster dose. Hence, the thickness of the particle could be increased to reduce the initial release at injection by reducing the risks of mechanical breakage of the particles. The addition of an osmotic agent inside the core could increase the release rate after the lag. Extended-release delays could be assessed to improve the immune response by changing the PLGA formulation of the particles.

6.3 Final Conclusion

This thesis describes the manufacturing of a LCSS particle-based delivery system and its application in single-dose vaccination. The R21 study demonstrated the beneficial effect of adding particles encapsulating a booster dose to a single injection regimen. The efforts will now be directed towards achieving the non-inferiority to a standard Prime/Boost regimen. The R21 malaria candidate vaccine, and the commercially available rabies vaccine will both be used in this objective. In

addition, the demonstration of an industrially viable manufacturing process will be key to providing a functional single-dose vaccine technology that could be evaluated in a first-in-man human trial.

References

[1] S. Pecetta *et al.*, “Vaccines for a sustainable planet,” *Sci Transl Med*, vol. 15, no. 685, Mar. 2023, doi: 10.1126/SCITRANSLMED.ADF1093.

[2] S. W. Roush *et al.*, “Historical Comparisons of Morbidity and Mortality for Vaccine-Preventable Diseases in the United States,” *JAMA*, vol. 298, no. 18, pp. 2155–2163, Nov. 2007, doi: 10.1001/JAMA.298.18.2155.

[3] F. Zhou *et al.*, “Economic Evaluation of the Routine Childhood Immunization Program in the United States, 2009,” *Pediatrics*, vol. 133, no. 4, pp. 577–585, Apr. 2014, doi: 10.1542/PEDS.2013-0698.

[4] G. Lien and D. L. Heymann, “The Problems with Polio: Toward Eradication,” *Infect Dis Ther*, vol. 2, no. 2, pp. 167–174, Sep. 2013, doi: 10.1007/S40121-013-0014-6/METRICS.

[5] “Weekly Epidemiological Record (WER), 30 November 2018, vol. 93, no. 48 (pp. 649–660) [EN/FR] - World | ReliefWeb.” https://reliefweb.int/report/world/weekly-epidemiological-record-wer-30-november-2018-vol-93-no-48-pp-649-660-enfr (accessed Feb. 26, 2023).

[6] H. H. Kyu *et al.*, “Mortality from tetanus between 1990 and 2015: findings from the global burden of disease study 2015,” *BMC Public Health*, vol. 17, no. 1, pp. 1–17, Feb. 2017, doi: 10.1186/S12889-017-4111-4/FIGURES/3.

[7] B. Greenwood, “The contribution of vaccination to global health: past, present and future,” *Philosophical Transactions of the Royal Society B: Biological Sciences*, vol. 369, no. 1645, Jun. 2014, doi: 10.1098/RSTB.2013.0433.

[8] I. J. Amanna and M. K. Slifka, “Successful vaccines,” *Curr Top Microbiol Immunol*, vol. 428, pp. 1–30, 2020, doi: 10.1007/82_2018_102/TABLES/1.

[9] B. Ashby and A. Best, “Herd immunity,” *Current Biology*, vol. 31, no. 4, pp. R174–R177, Feb. 2021, doi: 10.1016/J.CUB.2021.01.006.

[10] C. M. C. Rodrigues and S. A. Plotkin, “Impact of Vaccines; Health, Economic and Social Perspectives,” *Front Microbiol*, vol. 11, p. 1526, Jul. 2020, doi: 10.3389/FMICB.2020.01526/BIBTEX.

[11] C. Riumallo-Herl *et al.*, “Poverty reduction and equity benefits of introducing or scaling up measles, rotavirus and pneumococcal vaccines in low-income and middle-income countries: a modelling study,” *BMJ Glob Health*, vol. 3, no. 2, p. e000613, Apr. 2018, doi: 10.1136/BMJGH-2017-000613.

[12] P. S. Pannaraj *et al.*, “School-Located Influenza Vaccination Decreases Laboratory-Confirmed Influenza and Improves School Attendance,” *Clinical Infectious Diseases*, vol. 59, no. 3, pp. 325–332, Aug. 2014, doi: 10.1093/CID/CIU340.

[13] J. M. Okwo-Bele and T. Cherian, “The expanded programme on immunization: A lasting legacy of smallpox eradication,” *Vaccine*, vol. 29, no. SUPPL. 4, pp. D74–D79, Dec. 2011, doi: 10.1016/J.VACCINE.2012.01.080.

[14] “Immunization coverage.” https://www.who.int/news-room/fact-sheets/detail/immunization-coverage (accessed Feb. 28, 2023).

[15] J. L. Palgen *et al.*, “Optimize Prime/Boost Vaccine Strategies: Trained Immunity as a New Player in the Game,” *Front Immunol*, vol. 12, p. 554, Mar. 2021, doi: 10.3389/FIMMU.2021.612747/BIBTEX.

[16] F. Sallusto, A. Lanzavecchia, K. Araki, and R. Ahmed, “From Vaccines to Memory and Back,” *Immunity*, vol. 33, no. 4, p. 451, Oct. 2010, doi: 10.1016/J.IMMUNI.2010.10.008.

[17] “Immunization, Vaccines and Biologicals.” https://www.who.int/teams/immunization-vaccines-and-biologicals/policies/who-recommendations-for-routine-immunization---summary-tables (accessed Feb. 28, 2023).

[18] “Routine childhood immunisation schedule - GOV.UK.” https://www.gov.uk/government/publications/routine-childhood-immunisation-schedule (accessed Feb. 28, 2023).

[19] K. H. Nguyen *et al.*, “Parental Vaccine Hesitancy and Association With Childhood Diphtheria, Tetanus Toxoid, and Acellular Pertussis; Measles, Mumps, and Rubella; Rotavirus; and Combined 7-Series Vaccination,” *Am J Prev Med*, vol. 62, no. 3, p. 367, Mar. 2022, doi: 10.1016/J.AMEPRE.2021.08.015.

[20] M. E. Falagas and E. Zarkadoulia, “Factors associated with suboptimal compliance to vaccinations in children in developed countries: a systematic review,” *http://dx.doi.org/10.1185/03007990802085692*, vol. 24, no. 6, pp. 1719–1741, Jun. 2008, doi: 10.1185/03007990802085692.

[21] E. Dubé, J. Bettinger, W. Fisher, M. Naus, S. Mahmud, and T. Hilderman, “Improving Vaccination Rates: Vaccine acceptance, hesitancy and refusal in Canada: Challenges and potential approaches,” *Canada Communicable Disease Report*, vol. 42, no. 12, p. 246, Dec. 2016, doi: 10.14745/CCDR.V42I12A02.

[22] “Highlights from the 2019 childhood National Immunization Coverage Survey (cNICS) - Canada.ca.” https://www.canada.ca/en/public-health/services/publications/vaccines-immunization/2019-highlights-childhood-national-immunization-coverage-survey.html (accessed Feb. 28, 2023).

[23] H. R. Usman, S. Kristensen, M. H. Rahbar, S. H. Vermund, F. Habib, and E. Chamot, “Determinants of third dose of diphtheria–tetanus–pertussis (DTP) completion among children who received DTP1 at rural immunization centres in Pakistan: a cohort study,” *Trop Med Int Health*, vol. 15, no. 1, p. 140, Jan. 2010, doi: 10.1111/J.1365-3156.2009.02432.X.

[24] C. E. Gunning *et al.*, “Implementation and adherence of routine pertussis vaccination (DTP) in a low-resource urban birth cohort,” *BMJ Open*, vol. 10, no. 12, p. e041198, Dec. 2020, doi: 10.1136/BMJOPEN-2020-041198.

[25] V. Yelverton *et al.*, “Beyond coverage: Rural-urban disparities in the timeliness of childhood vaccinations in Tanzania,” *Vaccine*, vol. 40, no. 37, pp. 5483–5493, Sep. 2022, doi: 10.1016/J.VACCINE.2022.07.020.

[26] B. R. Bloom, “Vaccines for the Third World,” *Nature 1989 342:6246*, vol. 342, no. 6246, pp. 115–120, 1989, doi: 10.1038/342115a0.

[27] I. Preis and R. S. Langer, “A single-step immunization by sustained antigen release,” *J Immunol Methods*, vol. 28, no. 1–2, pp. 193–197, Jul. 1979, doi: 10.1016/0022-1759(79)90341-7.

[28] A. M. Dlugi, J. D. Miller, and J. Knittle, “Lupron depot (leuprolide acetate for depot suspension) in the treatment of endometriosis: a randomized, placebo-

controlled, double-blind study," *Fertil Steril*, vol. 54, no. 3, pp. 419–427, Sep. 1990, doi: 10.1016/S0015-0282(16)53755-8.

[29] T. K. Giri, C. Choudhary, Ajazuddin, A. Alexander, H. Badwaik, and D. K. Tripathi, "Prospects of pharmaceuticals and biopharmaceuticals loaded microparticles prepared by double emulsion technique for controlled delivery," *Saudi Pharmaceutical Journal*, vol. 21, no. 2, pp. 125–141, Apr. 2013, doi: 10.1016/J.JSPS.2012.05.009.

[30] R. S. Raghuvanshi, M. Singh, and G. P. Talwar, "Biodegradable delivery system for single step immunization with tetanus toxoid," *Int J Pharm*, vol. 93, no. 1–3, pp. R1–R5, May 1993, doi: 10.1016/0378-5173(93)90188-L.

[31] Y. Men, C. Thomasin, H. P. Merkle, B. Gander, and G. Corradin, "A single administration of tetanus toxoid in biodegradable microspheres elicits T cell and antibody responses similar or superior to those obtained with aluminum hydroxide," *Vaccine*, vol. 13, no. 7, pp. 683–689, Jan. 1995, doi: 10.1016/0264-410X(94)00046-P.

[32] D. T. O'Hagan, M. Singh, and R. K. Gupta, "Poly(lactide-co-glycolide) microparticles for the development of single-dose controlled-release vaccines," *Adv Drug Deliv Rev*, vol. 32, no. 3, pp. 225–246, Jul. 1998, doi: 10.1016/S0169-409X(98)00012-X.

[33] P. Johansen, B. Gander, H. P. Merkle, and D. Sesardic, "Ambiguities in the preclinical quality assessment of microparticulate vaccines," *Trends Biotechnol*, vol. 18, no. 5, pp. 203–211, May 2000, doi: 10.1016/S0167-7799(00)01437-2.

[34] A. A. Walters, C. Krastev, A. V. S. Hill, and A. Milicic, “Next generation vaccines: single-dose encapsulated vaccines for improved global immunisation coverage and efficacy,” *Journal of Pharmacy and Pharmacology*, vol. 67, no. 3, pp. 400–408, Mar. 2015, doi: 10.1111/JPHP.12367.

[35] S. Y. Tzeng *et al.*, “Thermostabilization of inactivated polio vaccine in PLGA-based microspheres for pulsatile release,” *Journal of Controlled Release*, vol. 233, pp. 101–113, Jul. 2016, doi: 10.1016/J.JCONREL.2016.05.012.

[36] Y. Tabata and Y. Ikada, “Effect of the size and surface charge of polymer microspheres on their phagocytosis by macrophage,” *Biomaterials*, vol. 9, no. 4, pp. 356–362, Jul. 1988, doi: 10.1016/0142-9612(88)90033-6.

[37] P. Johansen, H. Tamber, H. P. Merkle, and B. Gander, “Diphtheria and tetanus toxoid microencapsulation into conventional and end-group alkylated PLA/PLGAs,” *European Journal of Pharmaceutics and Biopharmaceutics*, vol. 47, no. 3, pp. 193–201, May 1999, doi: 10.1016/S0939-6411(98)00095-2.

[38] M. van de Weert, W. E. Hennink, and W. Jiskoot, “Protein instability in poly(lactic-co-glycolic acid) microparticles,” *Pharm Res*, vol. 17, no. 10, pp. 1159–1167, 2000, doi: 10.1023/A:1026498209874/METRICS.

[39] T. Estey, J. Kang, S. P. Schwendeman, and J. F. Carpenter, “BSA Degradation Under Acidic Conditions: A Model For Protein Instability During Release From PLGA Delivery Systems,” *J Pharm Sci*, vol. 95, no. 7, pp. 1626–1639, Jul. 2006, doi: 10.1002/JPS.20625.

[40] Y. Y. Yang, H. H. Chia, and T. S. Chung, “Effect of preparation temperature on the characteristics and release profiles of PLGA microspheres containing protein fabricated by double-emulsion solvent extraction/evaporation method,” *Journal of Controlled Release*, vol. 69, no. 1, pp. 81–96, Oct. 2000, doi: 10.1016/S0168-3659(00)00291-1.

[41] M. Ye, S. Kim, and K. Park, “Issues in long-term protein delivery using biodegradable microparticles,” *Journal of Controlled Release*, vol. 146, no. 2, pp. 241–260, Sep. 2010, doi: 10.1016/J.JCONREL.2010.05.011.

[42] E. Lagreca, V. Onesto, C. di Natale, S. la Manna, P. A. Netti, and R. Vecchione, “Recent advances in the formulation of PLGA microparticles for controlled drug delivery,” *Progress in Biomaterials 2020 9:4*, vol. 9, no. 4, pp. 153–174, Oct. 2020, doi: 10.1007/S40204-020-00139-Y.

[43] K. S. Jaganathan *et al.*, “Development of a single dose tetanus toxoid formulation based on polymeric microspheres: a comparative study of poly(d,l-lactic-co-glycolic acid) versus chitosan microspheres,” *Int J Pharm*, vol. 294, no. 1–2, pp. 23–32, Apr. 2005, doi: 10.1016/J.IJPHARM.2004.12.026.

[44] A. Giteau, M. C. Venier-Julienne, A. Aubert-Pouëssel, and J. P. Benoit, “How to achieve sustained and complete protein release from PLGA-based microparticles?,” *Int J Pharm*, vol. 350, no. 1–2, pp. 14–26, Feb. 2008, doi: 10.1016/J.IJPHARM.2007.11.012.

[45] S. Mohammadi-Samani and B. Taghipour, “PLGA micro and nanoparticles in delivery of peptides and proteins; problems and approaches,”

http://dx.doi.org/10.3109/10837450.2014.882940, vol. 20, no. 4, pp. 385–393, Jun. 2015, doi: 10.3109/10837450.2014.882940.

[46] K. J. McHugh *et al.*, “Fabrication of fillable microparticles and other complex 3D microstructures,” *Science (1979)*, vol. 357, no. 6356, pp. 1138–1142, 2017, doi: 10.1126/science.aaf7447.

[47] M. Sarmadi *et al.*, “Experimental and computational understanding of pulsatile release mechanism from biodegradable core-shell microparticles,” *Sci Adv*, vol. 8, no. 28, p. 5315, Jul. 2022, doi: 10.1126/SCIADV.ABN5315.

[48] I. Sadeghi *et al.*, “Micromolding of Thermoplastic Polymers for Direct Fabrication of Discrete, Multilayered Microparticles,” *Small Methods*, vol. 6, no. 9, p. 2200232, Sep. 2022, doi: 10.1002/SMTD.202200232.

[49] “IACUC Routes of Administration Guidelines | Office of the Vice President for Research.” https://research.umn.edu/units/rar/guidelines/routes-administration (accessed Mar. 02, 2023).

[50] M. Sarmadi *et al.*, “Modeling, design, and machine learning-based framework for optimal injectability of microparticle-based drug formulations,” *Sci Adv*, vol. 6, no. 28, Jul. 2020, doi: 10.1126/SCIADV.ABB6594.

[51] CDC and Ncird, “Vaccine Administration: Needle Gauge and Length”, Accessed: Mar. 02, 2023. [Online]. Available: www.cdc.gov/vaccines/hcp/acip-recs/general-recs/administration.html

[52] E. R. de Gioia *et al.*, “The Role of Needle Fear in Pediatric Flu Vaccine Hesitancy: A Cross-Sectional Study in Bologna Metropolitan Area,” *Vaccines*

(Basel), vol. 10, no. 9, p. 1388, Sep. 2022, doi: 10.3390/VACCINES10091388/S1.

[53] Y. C. Tan, V. Cristini, and A. P. Lee, “Monodispersed microfluidic droplet generation by shear focusing microfluidic device,” *Sens Actuators B Chem*, vol. 114, no. 1, pp. 350–356, Mar. 2006, doi: 10.1016/J.SNB.2005.06.008.

[54] J. C. Mcdonald *et al.*, “Fabrication of microfluidic systems in poly(dimethylsiloxane)”, doi: 10.1002/(SICI)1522-2683(20000101)21:1.

[55] T. Trantidou, Y. Elani, E. Parsons, and O. Ces, “Hydrophilic surface modification of PDMS for droplet microfluidics using a simple, quick, and robust method via PVA deposition,” *Microsystems & Nanoengineering 2017 3:1*, vol. 3, no. 1, pp. 1–9, Apr. 2017, doi: 10.1038/micronano.2016.91.

[56] A. S. Basu, “Droplet morphometry and velocimetry (DMV): a video processing software for time-resolved, label-free tracking of droplet parameters,” *Lab Chip*, vol. 13, no. 10, pp. 1892–1901, Apr. 2013, doi: 10.1039/C3LC50074H.

[57] N. Tottori, T. Hatsuzawa, and T. Nisisako, “Separation of main and satellite droplets in a deterministic lateral displacement microfluidic device,” *RSC Adv*, vol. 7, no. 56, pp. 35516–35524, Jul. 2017, doi: 10.1039/C7RA05852G.

[58] K. A. Collins, R. Snaith, M. G. Cottingham, S. C. Gilbert, and A. V. S. Hill, “Enhancing protective immunity to malaria with a highly immunogenic virus-like particle vaccine,” *Scientific Reports 2017 7:1*, vol. 7, no. 1, pp. 1–15, Apr. 2017, doi: 10.1038/srep46621.

[59] “Alexa Fluor™ 647 NHS Ester (Succinimidyl Ester).” https://www.thermofisher.com/order/catalog/product/A20006 (accessed Mar. 03, 2023).

[60] J. S. O’Donnell *et al.*, “Characterization and comparison of novel adjuvants for a prefusion clamped MERS vaccine,” *Front Immunol*, vol. 13, p. 4521, Sep. 2022, doi: 10.3389/FIMMU.2022.976968/BIBTEX.

[61] O. Qutachi *et al.*, “Improved delivery of PLGA microparticles and microparticle-cell scaffolds in clinical needle gauges using modified viscosity formulations,” *Int J Pharm*, vol. 546, no. 1–2, pp. 272–278, Jul. 2018, doi: 10.1016/J.IJPHARM.2018.05.025.

[62] A. M. Salman, C. M. Mogollon, J. W. Lin, F. J. A. Van Pul, C. J. Janse, and S. M. Khan, “Generation of transgenic rodent malaria parasites expressing human malaria parasite proteins,” *Methods in Molecular Biology*, vol. 1325, pp. 257–286, 2015, doi: 10.1007/978-1-4939-2815-6_21/FIGURES/4.

[63] R. J. Yetman *et al.*, “Concomitant administration of hepatitis A vaccine with measles/mumps/rubella/varicella and pneumococcal vaccines in healthy 12- to 23-month-old children,” *http://dx.doi.org/10.4161/hv.24873*, vol. 9, no. 8, pp. 1691–1697, Aug. 2013, doi: 10.4161/HV.24873.

[64] S. M. Garland *et al.*, “Noninferiority of antibody response to human papillomavirus type 16 in subjects vaccinated with monovalent and quadrivalent L1 virus-like particle vaccines,” *Clinical and Vaccine Immunology*, vol. 14, no. 6, pp. 792–795, Jun. 2007, doi: 10.1128/CVI.00478-06.

[65] J. Wei *et al.*, “Antibody responses and correlates of protection in the general population after two doses of the ChAdOx1 or BNT162b2 vaccines,” *Nature Medicine 2022 28:5*, vol. 28, no. 5, pp. 1072–1082, Feb. 2022, doi: 10.1038/s41591-022-01721-6.

[66] J. Wei *et al.*, “Antibody responses to SARS-CoV-2 vaccines in 45,965 adults from the general population of the United Kingdom,” *Nature Microbiology 2021 6:9*, vol. 6, no. 9, pp. 1140–1149, Jul. 2021, doi: 10.1038/s41564-021-00947-3.

[67] A. I. Mundo, T. J. Muldoon, and J. R. Tipton, “Generalized additive models to analyze non-linear trends in biomedical longitudinal data using R: Beyond repeated measures ANOVA and Linear Mixed Models,” *bioRxiv*, p. 2021.06.10.447970, Apr. 2022, doi: 10.1101/2021.06.10.447970.

[68] S. N. Wood, *Generalized additive models: An introduction with R, second edition*. CRC Press, 2017. doi: 10.1201/9781315370279/GENERALIZED-ADDITIVE-MODELS-SIMON-WOOD.

[69] K. Schroen *et al.*, “Droplet Microfluidics for Food and Nutrition Applications,” *Micromachines (Basel)*, vol. 12, no. 8, Aug. 2021, doi: 10.3390/MI12080863.

[70] L. Amirifar *et al.*, “Droplet-based microfluidics in biomedical applications,” *Biofabrication*, vol. 14, no. 2, p. 022001, Jan. 2022, doi: 10.1088/1758-5090/AC39A9.

[71] R. Noroozi, M. Mashhadi Kashtiban, H. Taghvaei, A. Zolfagharian, and M. Bodaghi, “3D-printed microfluidic droplet generation systems for drug delivery applications,” *Mater Today Proc*, vol. 70, pp. 443–446, Jan. 2022, doi: 10.1016/J.MATPR.2022.09.363.

[72] G. M. Whitesides, “The origins and the future of microfluidics,” *Nature 2006 442:7101*, vol. 442, no. 7101, pp. 368–373, Jul. 2006, doi: 10.1038/nature05058.

[73] B. E. Rapp, “Fluids,” *Microfluidics: Modelling, Mechanics and Mathematics*, pp. 243–263, Jan. 2017, doi: 10.1016/B978-1-4557-3141-1.50009-5.

[74] W. Li *et al.*, “Screening of the effect of surface energy of microchannels on microfluidic emulsification,” *Langmuir*, vol. 23, no. 15, pp. 8010–8014, Jul. 2007, doi: 10.1021/LA7005875.

[75] J. Guo, L. Hou, J. Hou, J. Yu, and Q. Hu, “Generation of Ultra-Thin-Shell Microcapsules Using Osmolarity-Controlled Swelling Method,” *Micromachines 2020, Vol. 11, Page 444*, vol. 11, no. 4, p. 444, Apr. 2020, doi: 10.3390/MI11040444.

[76] A. S. Utada, A. Fernandez-Nieves, J. M. Gordillo, and D. A. Weitz, “Absolute Instability of a Liquid Jet in a Coflowing Stream,” *Phys Rev Lett*, vol. 100, no. 1, p. 014502, Jan. 2008, doi: 10.1103/PhysRevLett.100.014502.

[77] B. Herranz-Blanco, E. Ginestar, H. Zhang, J. Hirvonen, and H. A. Santos, “Microfluidics platform for glass capillaries and its application in droplet and nanoparticle fabrication,” *Int J Pharm*, vol. 516, no. 1–2, pp. 100–105, Jan. 2017, doi: 10.1016/J.IJPHARM.2016.11.024.

[78] A. S. Utada, E. Lorenceau, D. R. Link, P. D. Kaplan, H. A. Stone, and D. A. Weitz, “Monodisperse double emulsions generated from a microcapillary device,” *Science (1979)*, vol. 308, no. 5721, pp. 537–541, Apr. 2005, doi: 10.1126/SCIENCE.1109164.

[79] R. K. Shah *et al.*, “Designer emulsions using microfluidics,” *Materials Today*, vol. 11, no. 4, pp. 18–27, Apr. 2008, doi: 10.1016/S1369-7021(08)70053-1.

[80] S. A. Nabavi, G. T. Vladisavljević, S. Gu, and E. E. Ekanem, “Double emulsion production in glass capillary microfluidic device: Parametric investigation of droplet generation behaviour,” *Chem Eng Sci*, vol. 130, pp. 183–196, Jul. 2015, doi: 10.1016/J.CES.2015.03.004.

[81] S. Rezvantalab and M. Keshavarz Moraveji, “Microfluidic assisted synthesis of PLGA drug delivery systems,” *RSC Adv*, vol. 9, no. 4, pp. 2055–2072, Jan. 2019, doi: 10.1039/C8RA08972H.

[82] D. Ding, B. Kundukad, A. Somasundar, S. Vijayan, S. A. Khan, and P. S. Doyle, “Design of mucoadhesive PLGA microparticles for ocular drug delivery,” *ACS Appl Bio Mater*, vol. 1, no. 3, pp. 561–571, Sep. 2018, doi: 10.1021/ACSABM.8B00041.

[83] F. Tu and D. Lee, “Controlling the stability and size of double-emulsion-templated poly(lactic- co -glycolic) acid microcapsules,” *Langmuir*, vol. 28, no. 26, pp. 9944–9952, Jul. 2012, doi: 10.1021/LA301498F.

[84] J. R. Anderson *et al.*, “Fabrication of Topologically Complex Three-Dimensional Microfluidic Systems in PDMS by Rapid Prototyping,” *Anal Chem*, vol. 72, no. 14, pp. 3158–3164, Jul. 2000, doi: 10.1021/AC9912294.

[85] Y. Xia and G. M. Whitesides, “SOFT LITHOGRAPHY,” *https://doi.org/10.1146/annurev.matsci.28.1.153*, vol. 28, no. 1, pp. 153–184, Nov. 2003, doi: 10.1146/ANNUREV.MATSCI.28.1.153.

[86] W. Lee, L. M. Walker, and S. L. Anna, “Role of geometry and fluid properties in droplet and thread formation processes in planar flow focusing,” *Physics of Fluids*, vol. 21, no. 3, p. 032103, Mar. 2009, doi: 10.1063/1.3081407.

[87] A. S. Utada, A. Fernandez-Nieves, H. A. Stone, and D. A. Weitz, “Dripping to jetting transitions in coflowing liquid streams,” *Phys Rev Lett*, vol. 99, no. 9, p. 094502, Aug. 2007, doi: 10.1103/PHYSREVLETT.99.094502/FIGURES/4/MEDIUM.

[88] A. S. Utada, L. Y. Chu, A. Fernandez-Nieves, D. R. Link, C. Holtze, and D. A. Weitz, “Dripping, jetting, drops, and wetting: The magic of microfluidics,” *MRS Bull*, vol. 32, no. 9, pp. 702–708, Jan. 2007, doi: 10.1557/MRS2007.145/METRICS.

[89] T. Fu, Y. Wu, Y. Ma, and H. Z. Li, “Droplet formation and breakup dynamics in microfluidic flow-focusing devices: From dripping to jetting,” *Chem Eng Sci*, vol. 84, pp. 207–217, Dec. 2012, doi: 10.1016/J.CES.2012.08.039.

[90] J. Yan, W. A. C. Bauer, M. Fischlechner, F. Hollfelder, C. F. Kaminski, and W. T. S. Huck, “Monodisperse Water-in-Oil-in-Water (W/O/W) Double Emulsion Droplets as Uniform Compartments for High-Throughput Analysis via Flow Cytometry,” *Micromachines 2013, Vol. 4, Pages 402-413*, vol. 4, no. 4, pp. 402–413, Dec. 2013, doi: 10.3390/MI4040402.

[91] M. Seo, C. Paquet, Z. Nie, S. Xu, and E. Kumacheva, “Microfluidic consecutive flow-focusing droplet generators,” *Soft Matter*, vol. 3, no. 8, pp. 986–992, Jul. 2007, doi: 10.1039/B700687J.

[92] A. Lashkaripour, C. Rodriguez, L. Ortiz, and D. Densmore, “Performance tuning of microfluidic flow-focusing droplet generators,” *Lab Chip*, vol. 19, no. 6, pp. 1041–1053, Mar. 2019, doi: 10.1039/C8LC01253A.

[93] J. Wu, S. Yadavali, D. Lee, and D. A. Issadore, “Scaling up the throughput of microfluidic droplet-based materials synthesis: A review of recent progress and outlook,” *Appl Phys Rev*, vol. 8, no. 3, p. 031304, Jul. 2021, doi: 10.1063/5.0049897.

[94] H. H. Jeong, V. R. Yelleswarapu, S. Yadavali, D. Issadore, and D. Lee, “Kilo-scale droplet generation in three-dimensional monolithic elastomer device (3D MED),” *Lab Chip*, vol. 15, no. 23, pp. 4387–4392, Nov. 2015, doi: 10.1039/C5LC01025J.

[95] M. B. Romanowsky, A. R. Abate, A. Rotem, C. Holtze, and D. A. Weitz, “High throughput production of single core double emulsions in a parallelized microfluidic device.,” *Lab Chip*, vol. 12, no. 4, pp. 802–807, Feb. 2012, doi: 10.1039/C2LC21033A.

[96] C. E. Rapier, K. J. Shea, and A. P. Lee, “Investigating PLGA microparticle swelling behavior reveals an interplay of expansive intermolecular forces,” *Sci Rep*, vol. 11, no. 1, Dec. 2021, doi: 10.1038/S41598-021-93785-6.

[97] L.-H. Hung, S.-Y. Teh, J. Jester, and A. P. Lee, “PLGA micro/nanosphere synthesis by droplet microfluidic solvent evaporation and extraction approaches”, doi: 10.1039/c002866e.

[98] A. R. Abate *et al.*, “Synthesis of Monodisperse Microparticles from Non-Newtonian Polymer Solutions with Microfluidic Devices,” *Advanced Materials*, vol. 23, no. 15, pp. 1757–1760, Apr. 2011, doi: 10.1002/ADMA.201004275.

[99] J. N. Lee, C. Park, and G. M. Whitesides, “Solvent Compatibility of Poly(dimethylsiloxane)-Based Microfluidic Devices,” *Anal Chem*, vol. 75, no. 23, pp. 6544–6554, Dec. 2003, doi: 10.1021/AC0346712.

[100] S. Hattori *et al.*, “Development of Microdroplet Generation Method for Organic Solvents Used in Chemical Synthesis,” *Molecules*, vol. 25, no. 22, Nov. 2020, doi: 10.3390/MOLECULES25225360.

[101] H. K. Makadia and S. J. Siegel, “Poly Lactic-co-Glycolic Acid (PLGA) as Biodegradable Controlled Drug Delivery Carrier,” *Polymers 2011, Vol. 3, Pages 1377-1397*, vol. 3, no. 3, pp. 1377–1397, Aug. 2011, doi: 10.3390/POLYM3031377.

[102] J. Petit, I. Polenz, J. C. Baret, S. Herminghaus, and O. Bäumchen, “Vesicles-on-a-chip: A universal microfluidic platform for the assembly of liposomes and polymersomes,” *The European Physical Journal E 2016 39:6*, vol. 39, no. 6, pp. 1–6, Jun. 2016, doi: 10.1140/EPJE/I2016-16059-8.

[103] S. Ma, J. M. Sherwood, W. T. S. Huck, and S. Balabani, “On the flow topology inside droplets moving in rectangular microchannels,” *Lab Chip*, vol. 14, no. 18, pp. 3611–3620, Aug. 2014, doi: 10.1039/C4LC00671B.

[104] S. Ma, J. M. Sherwood, W. T. S. Huck, and S. Balabani, “The microenvironment of double emulsions in rectangular microchannels,” *Lab Chip*, vol. 15, no. 10, pp. 2327–2334, May 2015, doi: 10.1039/C5LC00346F.

[105] S. Ma, W. T. S. Huck, and S. Balabani, “Deformation of double emulsions under conditions of flow cytometry hydrodynamic focusing,” *Lab Chip*, vol. 15, no. 22, pp. 4291–4301, Oct. 2015, doi: 10.1039/C5LC00693G.

[106] K. J. Humphry, A. Ajdari, A. Fernández-Nieves, H. A. Stone, and D. A. Weitz, “Suppression of instabilities in multiphase flow by geometric confinement,” *Phys Rev E Stat Nonlin Soft Matter Phys*, vol. 79, no. 5, p. 056310, May 2009, doi: 10.1103/PHYSREVE.79.056310.

[107] S. H. Kim, T. Y. Lee, and S. S. Lee, “Osmocapsules for Direct Measurement of Osmotic Strength,” *Small*, vol. 10, no. 6, pp. 1155–1162, Mar. 2014, doi: 10.1002/SMLL.201302296.

[108] W. H. Xie, W. Y. Shiu, and D. Mackay, “A review of the effect of salts on the solubility of organic compounds in seawater,” *Mar Environ Res*, vol. 44, no. 4, pp. 429–444, Dec. 1997, doi: 10.1016/S0141-1136(97)00017-2.

[109] R. P. F. Lanao, A. M. Jonker, J. G. C. Wolke, J. A. Jansen, J. C. M. van Hest, and S. C. G. Leeuwenburgh, “Physicochemical Properties and Applications of Poly(lactic-co-glycolic acid) for Use in Bone Regeneration,” *Tissue Eng Part B Rev*, vol. 19, no. 4, p. 380, Aug. 2013, doi: 10.1089/TEN.TEB.2012.0443.

[110] G. Bolognesi, A. Hargreaves, A. D. Ward, A. K. Kirby, C. D. Bain, and O. Ces, “Microfluidic generation of monodisperse ultra-low interfacial tension oil droplets in water,” *RSC Adv*, vol. 5, no. 11, pp. 8114–8121, Jan. 2015, doi: 10.1039/C4RA14967J.

[111] S. Ma, J. M. Sherwood, W. T. S. Huck, and S. Balabani, “The microenvironment of double emulsions in rectangular microchannels,” *Lab Chip*, vol. 15, no. 10, pp. 2327–2334, May 2015, doi: 10.1039/C5LC00346F.

[112] Z. Nie *et al.*, “Emulsification in a microfluidic flow-focusing device: Effect of the viscosities of the liquids,” *Microfluid Nanofluidics*, vol. 5, no. 5, pp. 585–594, Mar. 2008, doi: 10.1007/S10404-008-0271-Y.

[113] J. Wang, Z. Liu, Y. Pang, and M. Li, “Perturbations of liquid jets with an entering sphere in flow focusing,” *International Journal of Multiphase Flow*, vol. 147, p. 103914, Feb. 2022, doi: 10.1016/J.IJMULTIPHASEFLOW.2021.103914.

[114] A. Kamnerdsook *et al.*, “Formation of double emulsion micro-droplets in a microfluidic device using a partially hydrophilic–hydrophobic surface,” *RSC Adv*, vol. 11, no. 56, pp. 35653–35662, Nov. 2021, doi: 10.1039/D1RA06887C.

[115] I. C. Clark and A. R. Abate, “Microfluidic bead encapsulation above 20 kHz with triggered drop formation,” *Lab Chip*, vol. 18, no. 23, pp. 3598–3605, Nov. 2018, doi: 10.1039/C8LC00514A.

[116] S. A. Nabavi, G. T. Vladisavljević, and V. Manović, “Mechanisms and control of single-step microfluidic generation of multi-core double emulsion droplets,” *Chemical Engineering Journal*, vol. 322, pp. 140–148, Aug. 2017, doi: 10.1016/J.CEJ.2017.04.008.

[117] C. Zhang and P. Carloni, “Salt effects on water/hydrophobic liquid interfaces: a molecular dynamics study,” *Journal of Physics: Condensed Matter*, vol. 24, no. 12, p. 124109, Mar. 2012, doi: 10.1088/0953-8984/24/12/124109.

[118] E. M. Elmowafy, M. Tiboni, and M. E. Soliman, “Biocompatibility, biodegradation and biomedical applications of poly(lactic acid)/poly(lactic-co-glycolic acid) micro and nanoparticles,” *Journal of Pharmaceutical*

Investigation 2019 49:4, vol. 49, no. 4, pp. 347–380, Apr. 2019, doi: 10.1007/S40005-019-00439-X.

[119] H. K. Makadia and S. J. Siegel, “Poly Lactic-co-Glycolic Acid (PLGA) as Biodegradable Controlled Drug Delivery Carrier,” *Polymers (Basel)*, vol. 3, no. 3, p. 1377, Sep. 2011, doi: 10.3390/POLYM3031377.

[120] R. C. Mundargi, V. R. Babu, V. Rangaswamy, P. Patel, and T. M. Aminabhavi, “Nano/micro technologies for delivering macromolecular therapeutics using poly(d,l-lactide-co-glycolide) and its derivatives,” *Journal of Controlled Release*, vol. 125, no. 3, pp. 193–209, Feb. 2008, doi: 10.1016/J.JCONREL.2007.09.013.

[121] M. J. Dorta, A. Santoveña, M. Llabrés, and J. B. Fariña, “Potential applications of PLGA film-implants in modulating in vitro drugs release,” *Int J Pharm*, vol. 248, no. 1–2, pp. 149–156, Nov. 2002, doi: 10.1016/S0378-5173(02)00431-3.

[122] H. Ahmad, A. Arya, S. Agrawal, and A. K. Dwivedi, “PLGA scaffolds: building blocks for new age therapeutics,” *Materials for Biomedical Engineering: Hydrogels and Polymer-based Scaffolds*, pp. 155–201, Jan. 2019, doi: 10.1016/B978-0-12-816901-8.00006-7.

[123] M. Husmann, S. Schenderlein, M. Lü Ck, H. Lindner, and P. Kleinebudde, “Polymer erosion in PLGA microparticles produced by phase separation method,” *Int J Pharm*, vol. 242, pp. 277–280, 2002, Accessed: Nov. 15, 2022. [Online]. Available: www.elsevier.com/locate/ijpharm

[124] S. Boimvaser, R. N. Mariano, L. N. Turino, and J. R. Vega, “In vitro bulk/surface erosion pattern of PLGA implant in physiological conditions: a

study based on auxiliary microsphere systems," *Polymer Bulletin*, vol. 73, no. 1, pp. 209–227, Jan. 2016, doi: 10.1007/S00289-015-1481-6.

[125] J. A. Tamada and R. Langer, "Erosion kinetics of hydrolytically degradable polymers.," *Proceedings of the National Academy of Sciences*, vol. 90, no. 2, pp. 552–556, Jan. 1993, doi: 10.1073/PNAS.90.2.552.

[126] F. von Burkersroda, L. Schedl, and A. Göpferich, "Why degradable polymers undergo surface erosion or bulk erosion," *Biomaterials*, vol. 23, no. 21, pp. 4221–4231, Nov. 2002, doi: 10.1016/S0142-9612(02)00170-9.

[127] A. G. Ding and S. P. Schwendeman, "Acidic Microclimate pH Distribution in PLGA Microspheres Monitored by Confocal Laser Scanning Microscopy," *Pharm Res*, vol. 25, no. 9, p. 2041, Sep. 2008, doi: 10.1007/S11095-008-9594-3.

[128] J. Siepmann, K. Elkharraz, F. Siepmann, and D. Klose, "How autocatalysis accelerates drug release from PLGA-based microparticles: A quantitative treatment," *Biomacromolecules*, vol. 6, no. 4, pp. 2312–2319, 2005, doi: 10.1021/BM050228K.

[129] I. Mylonaki, E. Allémann, F. Delie, and O. Jordan, "Imaging the porous structure in the core of degrading PLGA microparticles: The effect of molecular weight," *Journal of Controlled Release*, vol. 286, pp. 231–239, Sep. 2018, doi: 10.1016/J.JCONREL.2018.07.044.

[130] R. A. Mensah, S. B. Kirton, M. T. Cook, I. D. Styliari, V. Hutter, and D. Y. S. Chau, "Optimising poly(lactic-co-glycolic acid) microparticle fabrication using a Taguchi orthogonal array design-of-experiment approach," *PLoS One*, vol. 14, no. 9, p. e0222858, Sep. 2019, doi: 10.1371/JOURNAL.PONE.0222858.

[131] Y. Xu, C. S. Kim, D. M. Saylor, and D. Koo, “Polymer degradation and drug delivery in PLGA-based drug–polymer applications: A review of experiments and theories,” *J Biomed Mater Res B Appl Biomater*, vol. 105, no. 6, pp. 1692–1716, Aug. 2017, doi: 10.1002/JBM.B.33648.

[132] T. J. Terpstra, “The asymptotic normality and consistency of kendall’s test against trend, when ties are present in one ranking,” *Indagationes Mathematicae (Proceedings)*, vol. 55, pp. 327–333, Jan. 1952, doi: 10.1016/S1385-7258(52)50043-X.

[133] M. Gümüşdereliog˘lu, G. Deniz, M. Menem¸, M. Gümü¸sderelio, G. Gümü¸sderelio, and Ï. Glu, “Sustained release of mitomycin-C from poly(DL-lactide)/poly(DL-lactide-co-glycolide) films,” *http://dx.doi.org/10.1163/156856200743562*, vol. 11, no. 10, pp. 1039–1050, 2012, doi: 10.1163/156856200743562.

[134] “Vaccine Administration Route and Site | CDC.” https://www.cdc.gov/vaccines/hcp/admin/administer-vaccines.html (accessed Dec. 01, 2022).

[135] D. Street, J. Bangsbo, and C. Juel, “Interstitial pH in human skeletal muscle during and after dynamic graded exercise,” *J Physiol*, vol. 537, no. Pt 3, p. 993, Dec. 2001, doi: 10.1111/J.1469-7793.2001.00993.X.

[136] J. Siepmann, N. Faisant, and J. P. Benoit, “A New Mathematical Model Quantifying Drug Release from Bioerodible Microparticles Using Monte Carlo Simulations,” *Pharmaceutical Research 2002 19:12*, vol. 19, no. 12, pp. 1885–1893, Dec. 2002, doi: 10.1023/A:1021457911533.

[137] K. Fu, D. W. Pack, A. M. Klibanov, and R. Langer, “Visual Evidence of Acidic Environment Within Degrading Poly(lactic-co-glycolic acid) (PLGA) Microspheres,” *Pharmaceutical Research 2000 17:1*, vol. 17, no. 1, pp. 100–106, 2000, doi: 10.1023/A:1007582911958.

[138] H. Gasmi, F. Danede, J. Siepmann, and F. Siepmann, “Does PLGA microparticle swelling control drug release? New insight based on single particle swelling studies,” *Journal of Controlled Release*, vol. 213, pp. 120–127, Sep. 2015, doi: 10.1016/J.JCONREL.2015.06.039.

[139] C. E. Rapier, K. J. Shea, and A. P. Lee, “Investigating PLGA microparticle swelling behavior reveals an interplay of expansive intermolecular forces,” *Scientific Reports 2021 11:1*, vol. 11, no. 1, pp. 1–12, Jul. 2021, doi: 10.1038/s41598-021-93785-6.

[140] B. S. Zolnik and D. J. Burgess, “Effect of acidic pH on PLGA microsphere degradation and release,” *J Control Release*, vol. 122, no. 3, pp. 338–344, Oct. 2007, doi: 10.1016/J.JCONREL.2007.05.034.

[141] “Malaria.” https://www.who.int/news-room/fact-sheets/detail/malaria (accessed Nov. 01, 2022).

[142] N. D. Pasternak and R. Dzikowski, “PfEMP1: An antigen that plays a key role in the pathogenicity and immune evasion of the malaria parasite Plasmodium falciparum,” *Int J Biochem Cell Biol*, vol. 41, pp. 1463–1466, 2009, doi: 10.1016/j.biocel.2008.12.012.

[143] R. Ménard, J. Tavares, I. Cockburn, M. Markus, F. Zavala, and R. Amino, “Looking under the skin: the first steps in malarial infection and immunity,”

Nature Reviews Microbiology 2013 11:10, vol. 11, no. 10, pp. 701–712, Sep. 2013, doi: 10.1038/nrmicro3111.

[144] P. Sinnis and D. A. Fidock, “The RTS,S vaccine—a chance to regain the upper hand against malaria?,” *Cell*, vol. 185, no. 5, pp. 750–754, Mar. 2022, doi: 10.1016/j.cell.2022.01.028.

[145] E. G. Tse, M. Korsik, and M. H. Todd, “The past, present and future of anti-malarial medicines,” *Malar J*, vol. 18, no. 1, Mar. 2019, doi: 10.1186/S12936-019-2724-Z.

[146] S. R. Bonam, L. Rénia, G. Tadepalli, J. Bayry, and H. M. S. Kumar, “Plasmodium falciparum Malaria Vaccines and Vaccine Adjuvants,” *Vaccines 2021, Vol. 9, Page 1072*, vol. 9, no. 10, p. 1072, Sep. 2021, doi: 10.3390/VACCINES9101072.

[147] “First Results of Phase 3 Trial of RTS,S/AS01 Malaria Vaccine in African Children,” *New England Journal of Medicine*, vol. 365, no. 20, pp. 1863–1875, Nov. 2011, doi: 10.1056/NEJMOA1102287.

[148] M. S. Datoo *et al.*, “Efficacy of a low-dose candidate malaria vaccine, R21 in adjuvant Matrix-M, with seasonal administration to children in Burkina Faso: a randomised controlled trial,” *The Lancet*, vol. 397, no. 10287, pp. 1809–1818, May 2021, doi: 10.1016/S0140-6736(21)00943-0.

[149] D. M. Gordon *et al.*, “Safety, immunogenicity, and efficacy of a recombinantly produced Plasmodium falciparum circumsporozoite protein-hepatitis B surface antigen subunit vaccine,” *J Infect Dis*, vol. 171, no. 6, pp. 1576–1585, 1995, doi: 10.1093/INFDIS/171.6.1576.

[150] K. Collins, “R21, a novel particle based vaccine for a multi-component approach to malaria vaccination”.

[151] S. Kumar *et al.*, “Cytotoxic T cells specific for the circumsporozoite protein of Plasmodium falciparum,” *Nature 1988 334:6179*, vol. 334, no. 6179, pp. 258–260, 1988, doi: 10.1038/334258a0.

[152] W. R. Ballou *et al.*, “Immunogenicity of Synthetic Peptides from Circumsporozoite Protein of Plasmodium falciparum,” *Science (1979)*, vol. 228, no. 4702, pp. 996–999, 1985, doi: 10.1126/SCIENCE.2988126.

[153] C. Dobaño *et al.*, “Concentration and avidity of antibodies to different circumsporozoite epitopes correlate with RTS,S/AS01E malaria vaccine efficacy,” *Nat Commun*, vol. 10, no. 1, p. 18, Dec. 2019, doi: 10.1038/S41467-019-10195-Z.

[154] T. Pholcharee *et al.*, “Structural and biophysical correlation of anti-NANP antibodies with in vivo protection against P. falciparum,” *Nature Communications 2021 12:1*, vol. 12, no. 1, pp. 1–14, Feb. 2021, doi: 10.1038/s41467-021-21221-4.

[155] S. Chaudhury *et al.*, “Breadth of humoral immune responses to the C-terminus of the circumsporozoite protein is associated with protective efficacy induced by the RTS,S malaria vaccine,” *Vaccine*, vol. 39, no. 6, pp. 968–975, Feb. 2021, doi: 10.1016/J.VACCINE.2020.12.055.

[156] N. Beutler *et al.*, “A novel CSP C-terminal epitope targeted by an antibody with protective activity against Plasmodium falciparum,” *PLoS Pathog*, vol. 18, no. 3, p. e1010409, Mar. 2022, doi: 10.1371/JOURNAL.PPAT.1010409.

[157] C. Dobaño *et al.*, “Concentration and avidity of antibodies to different circumsporozoite epitopes correlate with RTS,S/AS01E malaria vaccine efficacy,” *Nat Commun*, vol. 10, no. 1, p. 18, Dec. 2019, doi: 10.1038/S41467-019-10195-Z.

[158] P. Johansen, H. P. Merkle, and B. Gander, “Physico-chemical and antigenic properties of tetanus and diphtheria toxoids and steps towards improved stability,” *Biochimica et Biophysica Acta (BBA) - General Subjects*, vol. 1425, no. 2, pp. 425–436, Oct. 1998, doi: 10.1016/S0304-4165(98)00097-X.

[159] N. M. Payton, M. F. Wempe, Y. Xu, and T. J. Anchordoquy, “Long Term Storage of Lyophilized Liposomal Formulations,” *J Pharm Sci*, vol. 103, no. 12, p. 3869, 2014, doi: 10.1002/JPS.24171.

[160] L. Huang, S. Wang, and Z. Yin, “Study in the stabilization of proteins encapsulated in PLGA delivery system: Effects of additives on protein encapsulation, release, and stability,” *J Drug Deliv Sci Technol*, vol. 73, p. 103436, Jul. 2022, doi: 10.1016/J.JDDST.2022.103436.

[161] K. A. Collins *et al.*, “Ultra-low dose immunization and multi-component vaccination strategies enhance protection against malaria in mice,” *Scientific Reports 2021 11:1*, vol. 11, no. 1, pp. 1–15, May 2021, doi: 10.1038/s41598-021-90290-8.

[162] H. A. McNamara *et al.*, “Antibody Feedback Limits the Expansion of B Cell Responses to Malaria Vaccination but Drives Diversification of the Humoral Response,” *Cell Host Microbe*, vol. 28, no. 4, pp. 572-585.e7, Oct. 2020, doi: 10.1016/J.CHOM.2020.07.001.

[163] K. E. Kester *et al.*, “Efficacy of Recombinant Circumsporozoite Protein Vaccine Regimens against Experimental Plasmodium falciparum Malaria,” *J Infect Dis*, vol. 183, no. 4, pp. 640–647, Feb. 2001, doi: 10.1086/318534.

[164] S. F. Ausar, T. R. Foubert, M. H. Hudson, T. S. Vedvick, and C. R. Middaugh, “Conformational Stability and Disassembly of Norwalk Virus-like Particles: EFFECT OF pH AND TEMPERATURE,” *Journal of Biological Chemistry*, vol. 281, no. 28, pp. 19478–19488, Jul. 2006, doi: 10.1074/JBC.M603313200.

[165] M. Grit and D. J. A. Crommelin, “Chemical stability of liposomes: implications for their physical stability,” *Chem Phys Lipids*, vol. 64, no. 1–3, pp. 3–18, Sep. 1993, doi: 10.1016/0009-3084(93)90053-6.

[166] F. Castiglione, F. Mantile, P. De Berardinis, and A. Prisco, “How the interval between prime and boost injection affects the immune response in a computational model of the immune system,” *Comput Math Methods Med*, vol. 2012, 2012, doi: 10.1155/2012/842329.

[167] S. G. K. Calhoun *et al.*, “Systematic characterization of effect of flow rates and buffer compositions on double emulsion droplet volumes and stability,” *Lab Chip*, vol. 22, no. 12, pp. 2315–2330, Jun. 2022, doi: 10.1039/D2LC00229A.

[168] S. Nawar *et al.*, “Parallelizable microfluidic dropmakers with multilayer geometry for the generation of double emulsions,” *Lab Chip*, vol. 20, no. 1, pp. 147–154, Dec. 2019, doi: 10.1039/C9LC00966C.

[169] M. B. Romanowsky, A. R. Abate, A. Rotem, C. Holtze, and D. A. Weitz, “High throughput production of single core double emulsions in a parallelized microfluidic device,” *Lab Chip*, vol. 12, no. 4, pp. 802–807, Jan. 2012, doi: 10.1039/C2LC21033A.

[170] J. N. Zuckerman, “The importance of injecting vaccines into muscle : Different patients need different needle sizes,” *BMJ : British Medical Journal*, vol. 321, no. 7271, p. 1237, Nov. 2000, doi: 10.1136/BMJ.321.7271.1237.

[171] D. A. Edwards *et al.*, “Large porous particles for pulmonary drug delivery,” *Science (1979)*, vol. 276, no. 5320, pp. 1868–1871, Jun. 1997, doi: 10.1126/SCIENCE.276.5320.1868.

[172] Y. C. Kim, C. Jarrahian, D. Zehrung, S. Mitragotri, and M. R. Prausnitz, “Delivery Systems for Intradermal Vaccination,” *Intradermal Immunization*, vol. 351, no. 1, p. 77, 2012, doi: 10.1007/82_2011_123.

[173] P. H. Lambert and P. E. Laurent, “Intradermal vaccine delivery: Will new delivery systems transform vaccine administration?,” *Vaccine*, vol. 26, no. 26, pp. 3197–3208, Jun. 2008, doi: 10.1016/J.VACCINE.2008.03.095.

[174] K. T. M. Tran *et al.*, “Transdermal microneedles for the programmable burst release of multiple vaccine payloads,” *Nature Biomedical Engineering 2020 5:9*, vol. 5, no. 9, pp. 998–1007, Nov. 2020, doi: 10.1038/s41551-020-00650-4.

[175] G. P. Kenny, F. D. Reardon, W. Zaleski, M. L. Reardon, F. Haman, and M. B. Ducharme, “Muscle temperature transients before, during, and after exercise measured using an intramuscular multisensor probe,” *J Appl Physiol*, vol. 94, no. 6, pp. 2350–2357, Jun. 2003, doi: 10.1152/JAPPLPHYSIOL.01107.2002.

[176] J. Hajavi, M. Ebrahimian, M. Sankian, M. R. Khakzad, and M. Hashemi, “Optimization of PLGA formulation containing protein or peptide-based antigen: Recent advances,” *J Biomed Mater Res A*, vol. 106, no. 9, pp. 2540–2551, Sep. 2018, doi: 10.1002/JBM.A.36423.

[177] M. J. Pearse and D. Drane, “ISCOMATRIX® adjuvant for antigen delivery,” *Adv Drug Deliv Rev*, vol. 57, no. 3, pp. 465–474, Jan. 2005, doi: 10.1016/J.ADDR.2004.09.006.

[178] M. S. Datoo *et al.*, “Efficacy and immunogenicity of R21/Matrix-M vaccine against clinical malaria after 2 years’ follow-up in children in Burkina Faso: a phase 1/2b randomised controlled trial,” *Lancet Infect Dis*, vol. 22, no. 12, pp. 1728–1736, Dec. 2022, doi: 10.1016/S1473-3099(22)00442-X.

Appendix I

MATLAB custom script for image processing and feature measurement of double emulsions and core shell particles imaged in Brightfield and Fluorescence.

```
function
resMat=imageWeakAnalyzer(BF,Fluo,radiiCore,preciseCore,radiiParticle,preciseParticle,sensi
tivity,time,scale,Xgrid,Ygrid,visuDev)
%SCALE TO PIXEL%
%convert minCoreRadius and radii distances into pixel scale
radiiCore=round(radiiCore/scale);
radiiParticle=round(radiiParticle/scale);


% FILTERING %
%smooth the BF using a bilateral filter applying gaussian
%kernel while preserving edges
%For the fluo channel applies a gaussian filter to smooth the image
%particularly in case of strong noise due to long exposure
BF=imbilatfilt(BF);
Fluo=imgaussfilt(Fluo,4); %before 2


% BACKGROUND REMOVAL - FLUORESCENT IMAGE %
%uses flat field correction (gaussian filter to approximate the shadding)in
%case of a non-uniform illumination to increase the shadded objects
%the sigma of the gaussian filter is taken as lowest core radii
flatFluo=imflatfield(Fluo,radiiCore(1));


%CONTRAST ENHANCEMENT + THRESHOLD FOR DETECTION IMPROVEMENTS %
%adaptive thresholding on enhanced contrast to facilitate detection by
%hough circle and by thresholding
%imadjust to extend pixel value to whole range of image for BF (helps
%detection
%localcontrast to maintain edges while enhancing contrast, proven better
%than imsharpen, particularly usefull to enhance contrast of weak
%non-uniform fluorescent signal
%imsharpen to enhance contrast of Fluo channel
enhanceBF=imadjust(BF);%localcontrast(imadjust(BF),0.01,0.9);
enhanceFluo=flatFluo;%localcontrast(flatFluo,0.3,0.9);


% PARTICLE  DETECTION USING HOUGH TRANSFORM OR THRESHOLDING %
%use hough transform to detect circular shapes of particles with the user
%definer radii and sensitivity if hough activated
%detection performed on the adjusted image to enhance contrast
%and ease the detection of fading cores or particle shell with release and
%degradation
if preciseParticle %if detection is based on hough
```

```
[cB,rB]=imfindcircles(enhanceBF,radiiParticle,'ObjectPolarity','dark','Sensitivity',sensit
ivity); % find the particles
    mBF=createCirclesMask(BF,cB,rB); %create mask function using output from circle
detection of particles
    if isempty(cB) %if no particles is detected stop algorithm to save time
        resMat=[];
        return;
    end
else
    mBF=uint16(edge(BF,'sobel'));
    mBF=imdilate(mBF,strel('disk',10)); %dilate to connect potential dots created by
thresholding/edge detection
    mBF=imfill(mBF,'holes'); %fill potential holes created
    mBF=imerode(mBF,strel('disk',10)); %erode to reverse the dilatation process

end
    % MASK GENERATION %
    %creates two different masks for each channel (mBF, mFluo) using the circle detection,
segments them using
    %watershed function in case of touching circles, and remove the border ones
    %BrightField Channel
    mBF=watershedSeg(mBF,10,2); %watershed segmentation function to avoid touching
particle problem
    mBF=imclearborder(mBF,8); %clear borders with connectivity 8
    mBF=bwareaopen(mBF,round(pi*radiiParticle(1)^2)); %remove background noise object
detected using the min particle radius detection


%Fluorescent Channel
    if preciseCore %if precise detection of core (for late times where size is not
important, and core fades) is activated

[cF,rF]=imfindcircles(enhanceFluo,radiiCore,'ObjectPolarity','bright','Sensitivity',sensit
ivity); % find the cores even faded (weak signal, non even, or faded with degradation)
        if isempty(cF)
            mFluo=zeros(size(Fluo));
        else
            mFluo=createCirclesMask(Fluo,cF,rF); %create mask function using output from
circle detection of cores
        end
    else
        mFluo=uint16(edge(enhanceFluo,'sobel'));
        mFluo=imdilate(mFluo,strel('disk',3)); %dilate to connect potential dots created
by thresholding/edge detection
        mFluo=imfill(mFluo,'holes'); %fill potential holes created
        mFluo=imerode(mFluo,strel('disk',3)); %erode to reverse the dilatation process
    end
    mFluo=watershedSeg(mFluo,10,2); %watershed segmentation in case of touching
    mFluo=imclearborder(mFluo,8); %remove object connected to the borders (background and
out of field particles)
    mFluo=mFluo.*mBF;    %apply the brightfield mask to delimitate the detected particles
    mFluo=bwareaopen(mFluo,round(pi*radiiCore(1)^2)); %remove background noise object
detected using the definition of the min core size



% LABEL %
```

```
%label each diffent particles using the BF mask image
    if (max(mBF,[],'all')<1) %if no particle remained after border clear
        resMat=[];
        return;
    else
        labelParticle=bwlabel(mBF); %label the particles on the circular mask
        labelCore=labelParticle.*mFluo; %creates a labeled image for the core
corresponding
        emptyCore=false; %boolean to define if particles with no cores were detected in
the image
        if(max(labelParticle,[],'all')~=max(labelCore,[],'all')) %test if max label from
core is same as from particle
            %to make sure all particles are analyzed for presence of core or no, creation
of an temporary label on the top left corner that will be suppressed after
            %this prevent the creation of tables for the fluo signal of
            %different size than the table for the bf signal (due to
            %mismatch of number of particles vs cores)
            labelCore(1,1)=max(labelParticle,[],'all');
            emptyCore=true;
        end

        labelShell=labelParticle.*imcomplement(mFluo);
        emptyShell=false;%similar procedure as core
        if(max(labelParticle,[],'all')~=max(labelShell,[],'all')) %test if max label from
shell is similar to max label from particle
            labelShell(1,1)=max(labelParticle,[],'all');
            emptyShell=true;
        end

% MEASUREMENT %
%using labels, measure of global grey and fluo intensities and dimension
%parameters
%Global Particle

measureGlobalBF=regionprops('table',labelParticle,BF,'EquivDiameter','MeanIntensity','MaxI
ntensity','Centroid','Circularity');

measureGlobalFluo=regionprops('table',labelParticle,Fluo,'MeanIntensity','MaxIntensity','W
eightedCentroid');
%Core

measureCoreBF=regionprops('table',labelCore,BF,'EquivDiameter','MeanIntensity','Centroid')
;
        measureCoreFluo=regionprops('table',labelCore,Fluo,'Circularity','MeanIntensity');

%Shell
        measureShellBF=regionprops('table',labelShell,BF,'MeanIntensity','MaxIntensity');

measureShellFluo=regionprops('table',labelShell,Fluo,'MeanIntensity','MaxIntensity');



% OUTPUT PREPARATION %
%split centroids in 2 separate variables
        measureGlobalBF=splitvars(measureGlobalBF);
        measureGlobalFluo=splitvars(measureGlobalFluo);
        measureCoreBF=splitvars(measureCoreBF);
```

```
%Replace potential cell array created by max intesity measurement in
%missing shells  (no core or core filling particle)
        if(iscell(measureShellBF.MaxIntensity))
            if( isa(BF,'uint16'))

measureShellBF.MaxIntensity(cellfun('isempty',measureShellBF.MaxIntensity))={uint16(0)};
%replace [] cells by {0} cells to use cell2mat
            else

measureShellBF.MaxIntensity(cellfun('isempty',measureShellBF.MaxIntensity))={uint8(0)};
%replace [] cells by {0} cells to use cell2mat
            end
            measureShellBF.MaxIntensity=cell2mat(measureShellBF.MaxIntensity); %convert to
numerical array
        end
        if(iscell(measureShellFluo.MaxIntensity))
            if(isa(BF,'uint16'))

measureShellFluo.MaxIntensity(cellfun('isempty',measureShellFluo.MaxIntensity))={uint16(0)
}; %replace [] cells by {0} cells to use cell2mat
            else

measureShellFluo.MaxIntensity(cellfun('isempty',measureShellFluo.MaxIntensity))={uint8(0)}
; %replace [] cells by {0} cells to use cell2mat
            end
            measureShellFluo.MaxIntensity=cell2mat(measureShellFluo.MaxIntensity);
%convert to numerical array
        end


%remove the additional pixel used to label core and shell if used
        if(emptyCore)
            measureCoreBF(height(measureCoreBF),:)={NaN, NaN, 0, 0};
            measureCoreFluo(height(measureCoreFluo),:)={0,0};
        end
        if(emptyShell)
            measureShellBF(height(measureShellBF),:)={0,0};
            measureShellFluo(height(measureShellFluo),:)={0,0};
        end


%define adequate names

measureGlobalBF.Properties.VariableNames={'X','Y','Circularity','Diameter','meanGrey','max
Grey'};

measureGlobalFluo.Properties.VariableNames={'XfluoWeighted','YfluoWeighted','meanFluo','ma
xFluo'};

measureCoreBF.Properties.VariableNames={'coreX','coreY','coreDiameter','coreMeanGrey'};
        measureCoreFluo.Properties.VariableNames={'coreCircularity','coreMeanFluo'};
        measureShellBF.Properties.VariableNames={'shellMeanGrey','shellMaxGrey'};
        measureShellFluo.Properties.VariableNames={'shellMeanFluo','shellMaxFluo'};

%Extra calculations
        Eccentricity=(sqrt((measureGlobalBF.X-measureCoreBF.coreX).^2+(measureGlobalBF.Y-
measureCoreBF.coreY).^2)./(measureGlobalBF.Diameter./2-measureCoreBF.coreDiameter./2));
        weightedEccentricity=(sqrt((measureGlobalBF.X-
```

```
measureGlobalFluo.XfluoWeighted).^2+(measureGlobalBF.Y-
measureGlobalFluo.YfluoWeighted).^2)./(measureGlobalBF.Diameter./2-
measureCoreBF.coreDiameter./2));
        Thickness=(measureGlobalBF.Diameter-measureCoreBF.coreDiameter)/2;
        Time=repelem(time,size(measureGlobalBF,1))';
        Xgrid=repelem(Xgrid,size(measureGlobalBF,1))';
        Ygrid=repelem(Ygrid,size(measureGlobalBF,1))';


%Scaling
        measureGlobalBF.Diameter=measureGlobalBF.Diameter.*scale;
        measureCoreBF.coreDiameter=measureCoreBF.coreDiameter.*scale;
        Thickness=Thickness.*scale;
%OutPut
        resMat=[measureGlobalBF,measureGlobalFluo,...
                measureCoreBF,measureCoreFluo,...
                measureShellBF,measureShellFluo,...
                table(Eccentricity,weightedEccentricity,Thickness,Time,Xgrid,Ygrid)];
        resMat=fillmissing(resMat,'constant',0);

        if(visuDev)
            figure;
            imshow(BF,[]);
            viscircles([resMat.X,resMat.Y],resMat.Diameter./2./scale,'Color','r');

viscircles([resMat.coreX,resMat.coreY],resMat.coreDiameter./2./scale,'Color','b');
            figure;
            imshow(Fluo,[]);
            viscircles([resMat.X,resMat.Y],resMat.Diameter./2./scale,'Color','r');

viscircles([resMat.coreX,resMat.coreY],resMat.coreDiameter./2./scale,'Color','b');
        end
    end
end
```

Published with MATLAB® R2021b